

Interaction of magnetic and non-magnetic metals with graphene

D i s s e r t a t i o n

zur Erlangung des akademischen Grades

doctor rerum naturalium
(Dr. rer. nat.)

im Fach Physik

eingereicht an der

Mathematisch-Naturwissenschaftlichen Fakultät
der Humboldt-Universität zu Berlin

von

Dipl.-Phys. Hendrik Vita
geb. 20.04.1983 in Staaken

Präsident der Humboldt-Universität zu Berlin
Prof. Dr. Jan-Hendrik Olbertz

Dekan der Mathematisch-Naturwissenschaftlichen Fakultät
Prof. Dr. Elmar Kulke

Gutachter/innen:

1. Prof. Dr. Helmut Winter
2. Prof. Dr. Karsten Horn
3. Prof. Dr. Philip Hofmann

Tag der mündlichen Prüfung: 23.06.2015

Zusammenfassung

Diese Dissertation beschäftigt sich mit der Untersuchung der elektronischen Eigenschaften von sechs verschiedenen Graphen-Metall-Grenzflächen. Solche Systeme sind hochaktuell, aus fundamentaler Sicht als auch im Hinblick auf mögliche Anwendungen in elektronischen Bauteilen und anderen Bereichen. Die (111)-Oberfläche von Iridium wird wegen der schwachen Wechselwirkung zwischen den Partnern und der ausgezeichneten strukturellen Qualität als Vorlage für Graphenwachstum verwendet. Nach einer kurzen Einführung (Kapitel 1) werden die Eigenschaften von Graphen und der Graphen/Ir(111) Grenzfläche in Kapitel 2 behandelt. Die zugrunde liegende Physik der hier hauptsächlich genutzten experimentellen Methode, Photoemission und -Absorption, werden in Kapitel 3 und die Verfahren der Datenanalyse in Kapitel 5 beschrieben. Die Messplätze, an denen die Arbeiten durchgeführt wurden, sind in Kapitel 4 beschrieben, unter anderem eine „state-of-the-art“ Labor-Station welche von mir im Rahmen dieser Arbeit aufgebaut wurde. Kapitel 6 bis 10 berichten über Ergebnisse für Graphen auf Metallen, sowohl auf Volumenkristalloberflächen als auch auf zwischen Graphen und Ir(111) interkalierten Metallschichten, ausgehend von Ir(111) in Kapitel 6. Interkalierte Kupferschichten werden in Kapitel 7 behandelt; dies ist ein besonders wichtiges System, da der Einfluß der Hybridisierung zwischen Metall d -Zuständen und dem Graphen π -Band besonders klar zu beobachten ist und DFT-Rechnungen hier den Mechanismus der Öffnung der Bandlücke im Detail erklären können. Elektronische und magnetische Strukturuntersuchungen für interkalierte Kobaltschichten werden in Kapitel 8 vorgestellt. Der Transfer des magnetischen Moments auf die Graphen π Zustände wird durch Röntgenabsorptions-Dichroismus-Messungen

Zusammenfassung

an der Kohlenstoff-*K*-Kante detektiert. Die Entstehung von ferromagnetischer Ordnung in den Kobalt-Filmen wird beobachtet und durch einen Vergleich mit Theorie-Daten quantitativ erklärt. Interkalierte Ytterbium-Schichten (Kapitel 9) zeigen Ähnlichkeiten mit Kupfer, da in beiden Metallen die Region in der Nähe des Fermi-Niveaus ausschließlich von *s-p*-Zuständen besetzt ist. Analog zu Kupfer kann die Hybridisierung zwischen Metall und Graphenzustände auch hier deutlich verfolgt werden. Schließlich zeigt der Fall von interkalierten Mangan-schichten spezielle Eigenschaften. Einerseits existieren *d*-Zustände nahe der Fermi-Energie, welche mit Graphen wechselwirken; andererseits besteht aber nicht der starke Einfluss auf den sogenannten „Dirac cone“ des Graphen wie im Falle von Nickel und Kobalt (Kapitel 8). Die hier vorgestellten Ergebnisse zu den sechs Metallen ergeben ein konsistentes Bild der elektronischen Struktur von Metall-Graphen-Grenzflächen.

Abstract

This thesis deals with an investigation of the electronic properties of six examples of graphene-metal interfaces. Such systems are of great current interest, not only from a fundamental point of view, but also with respect to possible applications in electronic devices and other fields. The (111) surface of iridium is used as a template for graphene growth, in view of the weak interaction between the partners, and due to the excellent structural quality. After a brief introduction (chapter 1), the properties of graphene and the graphene/Ir(111) interface are described in chapter 2. My main experimental method within the thesis is photoemission and -absorption, hence chapter 3 deals with the underlying physics. The data analysis procedures are explained in chapter 5. The experimental stations on which the work was performed are described in chapter 4, including a state-of-the-art laboratory station that was built up within the work on this thesis. Chapters 6 through 10 then report on my findings for graphene on bulk and intercalated metals in between graphene and Ir(111), starting with Ir(111) in chapter 6. Intercalated copper layers are dealt with in chapter 7, a particularly important example since the signatures of hybridization between metal states and the graphene π band are especially clear, and the mechanism of band gap opening can be explained in detail on the basis of DFT calculations. Electronic and magnetic structure investigations for intercalated cobalt layers are covered in chapter 8. The transfer of magnetic moment onto the formerly paramagnetic graphene π states is evident from x-ray magnetic circular dichroism measurements at the carbon K edge. The emergence of ferromagnetic ordering in the cobalt films is reported and analyzed by recourse to theory. Intercalated ytterbium (chapter 9)

Abstract

is found to exhibit similarities with copper, since in both cases the region near the Fermi level is exclusively occupied by s - p -type states. Like in copper, hybridization between metal and graphene states can be clearly observed. Finally, the case of intercalated manganese is a special one: d -states are found to interact with graphene, but they do not seem to have the detrimental effect on the Dirac cone as observed for nickel and cobalt in chapter 8. Altogether, a consistent overview of metal-graphene interface electronic structure is given.

Publications

Publications covered in the thesis:

- I. S. Böttcher, H. Vita and K. Horn (2014). “Reversible photon-induced oxidation of graphene by NO₂ adsorption.”
Surface Science **621**: 117-122.
- II. H. Vita, S. Böttcher, K. Horn, E. N. Voloshina, R. Ovcharenko, Th. Kampen, A. Thissen and Yu. S. Dedkov (2014).
“Understanding the origin of band gap formation in graphene on metals: graphene on Cu/Ir(111).”
Scientific Reports **4**, Article number: 5704.
- III. H. Vita, S. Böttcher, P. Leicht, K. Horn, A. B. Shick and F. Máca (2014). “Electronic structure and magnetic properties of cobalt intercalated in graphene on Ir(111).”
Physical Review B **90**, Article number: 165432.
- IV. F. Bisti, G. Profeta, H. Vita, M. Donarelli, F. Perrozzi, P. Sheverdyayeva, P. Moras, T. Seyller, K. Horn and L. Ottaviano (2015). “Electronic and geometric structure of graphene/SiC decoupled by lithium intercalation.”
Physical Review B **91**, Article number: 245411.
- V. S. Böttcher, H. Vita and K. Horn (2015). “Photon-Induced Oxidation of Graphene/Ir(111) by SO₂ Adsorption.”
Surface Science **641**: 305-309.

Publications not covered in the thesis:

- VI. M. Ostler, R. J. Koch, F. Speck, F. Fromm, H. Vita, M. Hundhausen, K. Horn and T. Seyller (2012). “Decoupling the Graphene Buffer Layer from SiC(0001) via Interface Oxidation.”
Silicon Carbide and Related Materials 2011,
Pts 1 and 2 717-720: 649-652.
- VII. M. Ostler, F. Fromm, R. J. Koch, P. Wehrfritz, F. Speck, H. Vita, S. Böttcher, K. Horn and T. Seyller (2014). “Buffer layer free graphene on SiC(0001) via interface oxidation in water vapor.”
Carbon **70**: 258-265.

List of talks and posters

- I. Poster, 2nd International Symposium on Graphene Devices, Tohoku University Sendai, Japan (2010).
H. Vita, M. Weser, S. Böttcher, Yu. S. Dedkov, K. Horn, M. Sicot, Ph. Leicht, A. Zusan, and M. Fonin
“Graphene on lattice-mismatched metal surfaces.”
- II. Poster, 2nd Joint BER II and BESSY II Users Meeting, Berlin, Germany (2010).
H. Vita, M. Weser, S. Böttcher, A. Generalov, Yu. S. Dedkov, K. Horn, M. Sicot, Ph. Leicht, A. Zusan and M. Fonin
“Graphene on lattice-mismatched metal surfaces.”
- III. Talk, DPG-Frühjahrstagung Dresden, Germany (2011).
H. Vita, A. Generalov, M. Weser, Yu. S. Dedkov, K. Horn, M. Sicot, Ph. Leicht, A. Zusan and M. Fonin
“Graphene on lattice-mismatched metal surfaces: STM and ARPES studies.”

- IV. Poster, Meeting of the DPG Priority Programme "Graphene" SPP 1459 at Zerkana-Hütte, Mittelberg, Austria (2011).
H. Vita, M. Weser, S. Böttcher, Yu. S. Dedkov and K. Horn
"Graphene on lattice-matched and mismatched metal surfaces."

- V. Poster, DPG-Frühjahrstagung Berlin, Germany (2012).
H. Vita, S. Böttcher, M. Weser, Yu. S. Dedkov and K. Horn
"Interaction of manganese and nickel with epitaxial graphene on Ir(111)."

- VI. Talk, DPG-Frühjahrstagung Regensburg, Germany (2013).
H. Vita, S. Böttcher, Yu. S. Dedkov and K. Horn
"Intercalated thin films on Graphene/Ir(111)."

- VII. Talk, Ringberg-Meeting on Physical Chemistry, Tegernsee, Germany (2013).
H. Vita, S. Böttcher, Yu. S. Dedkov and K. Horn
"Intercalated metal thin films on graphene/Ir(111)."

- VIII. Poster, Graphene Week Chemnitz, Germany (2013).
H. Vita, S. Böttcher, P. Leicht, M. Fonin, A. Preobrajenski and K. Horn
"Electronic and magnetic properties of cobalt intercalated in graphene on Ir(111)."

- IX. Poster, 5th Joint BER II and BESSY II Users Meeting Berlin, Germany (2013).
H. Vita, S. Böttcher, E. N. Voloshina, Th. Kampen, A. Thissen, Yu. S. Dedkov and K. Horn
"Electronic structure of graphene on the pseudomorphic Cu/Ir(111) substrate."

Publications

- X. Poster, 5th Joint BER II and BESSY II Users Meeting Berlin, Germany (2013).
H. Vita, S. Böttcher, P. Leicht, M. Fonin, A. Preobrajenski and K. Horn
“Electronic and magnetic properties of cobalt intercalated in graphene on Ir(111).”
- XI. Talk, DPG-Frühjahrstagung Dresden, Germany (2014).
H. Vita, S. Böttcher and K. Horn
“Electronic and magnetic properties of cobalt interaction with graphene on Ir(111).”
- XII. Talk, DPG-Frühjahrstagung Berlin, Germany (2015).
H. Vita, S. Böttcher, Yu. S. Dedkov and K. Horn
“Manganese Intercalation in Graphene/Ir(111): electronic structure.”

Prizes

- I. Poster Award
5th Joint BER II and BESSY II Users Meeting Berlin, Germany (2013). “Electronic structure of graphene on pseudomorphic Cu/Ir(111)”

Contents

Zusammenfassung	i
Abstract	iii
Publications	v
1 Introduction	1
2 Background – isolated graphene and graphene on Ir(111)	7
2.1 Crystallographic structure in real and reciprocal space	7
2.2 Classification of graphene/metal systems; possible graphene applications	13
3 Photoelectron and x-ray absorption spectroscopy	19
3.1 Fundamentals of photoelectron spectroscopy	19
3.1.1 Theoretical description of ARPES and three-step-model	21
3.1.2 One-particle spectral function	28
3.2 X-ray absorption spectroscopy and x-ray magnetic circular dichroism	30
3.2.1 Absorption of x-rays	30
3.2.2 X-ray absorption spectroscopy	35
3.2.3 X-ray magnetic circular dichroism	37

4	Experimental set-up and preparation of graphene	41
4.1	The hemispherical electron analyser – PHOIBOS . . .	42
4.2	Experimental considerations for ARPES and XPS . .	46
4.3	Synchrotron radiation	48
4.4	The ARPES station at BESSY II	51
4.5	The XMCD/NEXAFS station at MAX-lab II	57
4.6	New laboratory experiment for combined ARPES/XPS	59
4.7	Preparation of graphene	64
4.8	Graphene/Ir(111) – a lattice mismatched system . . .	65
4.9	Growth and intercalation of transition metals on graphene	68
5	Data analysis	75
5.1	Analysis of ARPES data	75
5.2	XPS spectra analysis	78
5.3	NEXAFS and XMCD analysis	80
6	Experimental investigations of graphene/Ir(111)	85
6.1	First studies at the new laboratory ARPES station . .	85
6.2	Measurements at the ARPES station at BESSY II . .	93
6.3	Rotational domains	105
6.4	Line shape analysis on graphene/Ir(111)	108
7	Modification of graphene/Ir(111) by copper intercalation	111
7.1	Preparation and spectroscopic methods	114
7.2	Results and electronic structure calculations	115
7.3	Discussion	126
8	Graphene/Ir(111) – intercalation of cobalt and nickel	133
8.1	Intercalation of nickel	135
8.2	Intercalation of cobalt	141
8.3	Electronic structure calculations	155
	8.3.1 Monolayer Co/Ir(111) and graphene/Co/Ir(111)	155
	8.3.2 Graphene/2 ML Co/Ir(111)	157
8.4	Conclusions	162
9	Intercalation of ytterbium in graphene/Ir(111)	163
9.1	Experimental results	163

10 Manganese as intercalate in graphene/Ir(111)	177
10.1 Intercalation of manganese – trigonal phase	179
10.2 The high temperature phase	187
11 Conclusions and outlook	199
Appendix	201
Bibliography	209
List of Abbreviations	235
Acknowledgments	241

Chapter 1

Introduction

It is now about ten years ago that a discovery induced a storm of activities in the field of solid state physics: a method to prepare graphene, the single atomic layer of hexagonally coordinated carbon atoms, and single atomic layers of other layered materials [1], and to characterize them using electronic transport measurements. Graphene in particular has been at the focus of attention, since it is related to 0-dimensional fullerenes, 1-dimensional carbon nanotubes, and 3-dimensional graphite. The single layer graphene had been studied by theoretical means for about 60 years, starting with the work of Wallace in 1947 [2]; however, that this material exhibits very special properties that are unlike any other material was only realized in 1984 [3, 4] when it became clear that it provides a solid state analogue of quantum electrodynamics, with its charge carriers behaving as quasiparticles with zero effective mass. Since the very existence of a 2D material was thought to be forbidden by virtue of theorems formulated by Peierls [5] and Landau [6], these considerations were thought to be purely Gedanken experiments. All this changed when single layers of graphene were prepared in what is an extremely simple method, micromechanical exfoliation, also known as the “scotch tape method” [1]. These one-atomic layer films, being “all surface and no bulk” were deposited on an oxidized silicon wafer. Subsequently, contacts are attached to the layer, and with the use of the silicon

substrate as a gate electrode, a field effect transistor (FET) or Hall bar could be prepared. This opened the path to unleash the arsenal of (magneto-) transport experiments. Surprisingly, the mechanically transferred graphene films turned out to be of extremely high quality, permitting ballistic transport of their charge carriers over micron-size distance.

In two back-to-back papers [7, 8] in 2005, the groups of Geim (Manchester University) and Kim (Columbia University, New York) showed quantum Hall data that convincingly proved that the charge carriers indeed behave as though they have zero effective mass; the integer quantum Hall effect “ladder” is replaced by a half-integer one. This development culminated with the Nobel Prize in Physics “for groundbreaking experiments regarding the two-dimensional material graphene” bestowed on Geim and Novoselov in 2010 [9]. The charge carriers are Fermions that are thus not described by the Schrödinger equation, but by the Dirac equation for massless particles. However, they still interact through their charges. By virtue of its specific band structure discussed in chapter 2.1, with linearly dispersing bands that cross at a point on the Brillouin zone boundary where the density of states vanishes, creating the so-called Dirac “cone”, the carrier type and concentration can be tuned continuously between electron- and hole-type by the electric field effect, with carrier concentrations up to $1 \times 10^{13} \text{ cm}^{-2}$ and mobilities reach $100\,000 \text{ cm}^2 \text{ V}^{-1} \text{ s}^{-1}$ at room and more than $250\,000 \text{ cm}^2 \text{ V}^{-1} \text{ s}^{-1}$ at low temperature. These and other findings, such as the extremely high electrical and thermal conductivities, impermeability to gases *etc.* have sparked an enormous interest and research effort from a fundamental as well as applications-oriented point of view, with many expectations for this “wonder material” yet to be demonstrated in practice. The storm of activities has led to tens of thousands of publications, hundreds (if not more) of scientists involved in studies of the basic science and possible applications of graphene, and the funding agencies have launched programmes such as the “Graphene Flagship” [10] at a level not seen in condensed matter physics and material science before.

From a fundamental physics point of view, the fact that graphene’s charge carriers are quasiparticles that obey the Dirac equation and thus enable quantum electrodynamics in a table-top experiment is

the most important aspect. Relativistic massless particles that move through the 2D “solid” with a reduced “speed of light”, and an extra “pseudospin quantum number” that describes the sublattice they are moving in (chapter 2.1) can be used to study quantum electro dynamics phenomena such as Klein tunneling where the particles can traverse high potential barriers. This effect, already predicted in 1929, was only verified experimentally in 2009 in graphene-based devices. One of the advantages of graphene is that not only the single atomic layer can be examined: by stacking two or more layers on top of one another, the transition from purely 2D to quasi-2D to the 3D bulk can be investigated. The charge carriers in the bilayer, for example, are massive Dirac Fermions that are described by a Hamiltonian that combines aspects of the Dirac and Schrödinger equation, an effect that can immediately be seen in the difference in the quantum Hall ladder.

The discovery of how to prepare single layers of graphene by means of micromechanical exfoliation has recently been adapted to the preparation of other, van-der-Waals binded materials such as hexagonal boron nitride, transition metal dichalcogenides, for which the expression “graphene-related materials” (GRM) has been coined. Not only may these serve to encapsulate graphene and thus preserve its unique properties in harsh environments, but they can also be used in their own right, for applications where a specific property, for example fundamental band gap, sadly missing in graphene, is important, such as in digital switching devices. It should also be mentioned that several of the attractive features such as the extreme strength and Young’s modulus of graphene and its very high thermal conductivity do not arise from the special nature of its charge carriers, but from the strong in-plane σ -bond.

Given the intriguing properties, what are the applications envisaged? High frequency transistors and even low level analog integrated circuits have already been made at the laboratory level. The use of graphene as a transparent conductive electrode to replace the standard indium tin oxide has been demonstrated on a laboratory scale in smart phone displays; here graphene flexibility may come in useful. Graphene is used as a saturable absorber for the cost-effective production of ultrafast pulsed laser operation over a wide wavelength range. In metrology, graphene serves as a transferable resistance standard which

can be operated with closed cycle refrigerators. Photodetectors with a broad wavelength range and very high sensitivity have also been produced. Clearly, there are many opportunities for applications, and the question of how many of these will eventually lead to workable devices will soon be answered, given the intense research effort.

This thesis examines the interaction of graphene with metallic substrates and metallic intercalated layers. One may well ask why such systems are important, given that the metal by necessity “short-circuits” all the novel and exciting electronic properties of graphene? There are several important reasons why the metal-graphene interface is an important one and needs in-depth studies from an experimental and theoretical point of view. First, any graphene-based device needs metallic contacts for its functionality, and issues such as doping through the contact material, destruction of the Dirac cone, reduction of mobility *etc.* are important. Secondly, and equally important from a fundamental point of view, an interface between graphene and a ferromagnetic metal may act as a spin filter [11, 12] as discussed in chapter 2.2, possibly paving the way for the use of graphene in spintronic devices and quantum computing, or even the investigation of entangled states [13]. Finally, at present the only viable pathway towards large scale mass production of graphene appears to be through chemical vapor deposition of hydrocarbons on metal surfaces, and an understanding of the process that lead to high quality growth, and transfer processes to other substrates is very important. Graphene may be used as protecting layer of reactive surfaces and a kind of surfactant for intercalated layers, possibly yielding interesting applications in thin film technology.

The interaction between graphene and a range of metals is studied in this thesis: iridium, copper, ferromagnetic cobalt, manganese, and ytterbium. All of these exhibit different aspects of graphene-metal interaction. The thesis is organized as follows. After a brief survey, in chapter 2, of the properties of graphene, in particular its electronic structure both as a free-standing layer and epitaxially grown on a substrate are discussed. The experimental methods employed in the thesis, *i. e.* photoemission, -absorption, and x-ray magnetic circular dichroism are treated in chapter 3. The experimental details (analyzers, vacuum chambers, beamlines *etc.* , and preparation protocols) are

described in chapter 4, and data analysis procedures in chapter 5. Chapters 6 through 10 then present the experimental results and interpretation in the following sequence: as a basis for the intercalation processes of Cu, Ni, Co, Yb, and Mn in between graphene and the Ir(111) surface, the properties of graphene/Ir(111) with its specific moiré structure are treated in chapter 6. The intercalation of Cu (ch. 7) is a particularly important example, not only because the electronic structure information is revealed in great clarity experimentally, but also since density functional calculations reveal the Cu *d*/graphene *p* state hybridization process that induce a band gap opening at the “Dirac” crossing point of valence and conduction bands; conclusions drawn from this interpretation can be applied to other metal/graphene interfaces. For cobalt, electronic structure information is complemented in chapter 8 by a determination of the magnetic moments present in a bilayer, and its partial transfer onto the carbon atoms in graphene, and these are compared to state-of-the-art calculations of magnetic moments in this system. The intercalation of ytterbium and manganese is dealt with in chapters 9 and 10; Yb is a case closely related to Cu, in that the hybridization between metal and graphene states is reflected in detail in valence level photoemission, while manganese exhibits, beyond an intercalated layer that adapts to the structure of the Ir (111) substrate a second phase that consists of a surface alloy which strongly influences the structure of graphene. On the basis of these five examples, a comprehensive picture of the general properties of metal/graphene interfaces emerges.

Background – isolated graphene and graphene on Ir(111)

It is well known that carbon atoms are able to form different allotropes (Fig. 2.1), due to the different configuration of their valence electrons.

The most common ones are diamond and graphite. Diamond is formed by sp^3 – hybridized orbitals leading to the diamond cubic crystal structure. Graphite, on the other hand, consists of stacked carbon sheets bonded by weak van der Waals forces. The sheets are arranged in a honeycomb lattice formed by sp^2 – hybridized orbitals. In recent years, graphene – a two dimensional single layer of carbon atoms arranged in a honeycomb lattice – has attracted much interest [7, 8, 16–18] as discussed in the introduction.

2.1 Crystallographic structure in real and reciprocal space

Graphene has been described theoretically by various authors [19–23]. Early theoretical work on graphene by Wallace [2] dates back to 1947, he studied a one-atom thick sheet of graphite to gain insight into the electronic properties of the three-dimensional graphite system, already grasped the electronic behavior of the π band, showing a

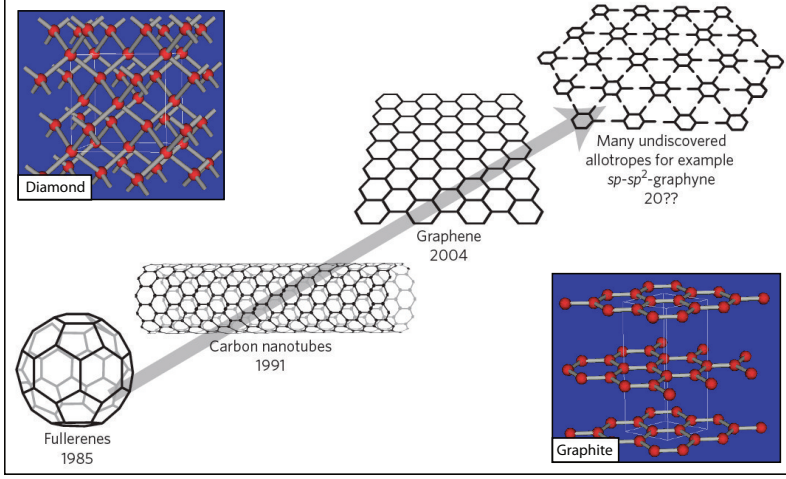


Figure 2.1: Carbon allotropes, taken from Hirsch [14] and Gross [15]. Apart from the classic allotropes like graphite and diamond, there are also more exotic ones. These include fullerenes, carbon nanotubes and the two dimensional material graphene.

linear dispersion near the K point. The aim of this chapter is the derivation of the electronic structure of graphene in the framework of the tight-binding approximation, which I outline in a few steps based on the work of Aoki and Dresselhaus [21] and Atienza [23]. The crystal structure of graphene has a two-atom basis (A, B) with the following lattice vectors:

$$\vec{a}_1 = a(1, 0) \quad (2.1)$$

$$\vec{a}_2 = a\left(-\frac{1}{2}, \frac{\sqrt{3}}{2}\right) \quad (2.2)$$

with $a \approx 2.46 \text{ \AA}$ being the graphene lattice constant. The shortest distance between two carbon atoms – $a_{CC} = a/\sqrt{3} \approx 1.42 \text{ \AA}$ – is the carbon-carbon bond length. Each atomic position A and B (Fig. 2.2) alone form a hexagonal Bravais lattice in the forms of a separate sublattice A, B. The relation between the trigonal lattice vectors \vec{a}_1 and \vec{a}_2 in real space and the related reciprocal space with the

corresponding reciprocal lattice vectors \vec{b}_1 and \vec{b}_2 is given by the following equation:

$$\vec{b}_1 = \frac{2\pi}{a}(1, \frac{1}{\sqrt{3}}) \quad (2.3)$$

$$\vec{b}_2 = \frac{2\pi}{a}(0, \frac{2}{3}) \quad (2.4)$$

The crystal structure and the corresponding Brillouin zone for graphene are shown in Fig. 2.2 (a) and (b). The corners of the hexagonal Brillouin zone are defined by two inequivalent points – K and K' – since they are not connected by a reciprocal lattice vector. The coordinates in reciprocal space of these points are

$$\vec{K} = \frac{2\pi}{a}(\frac{1}{3}, \frac{1}{\sqrt{3}}) \quad (2.5)$$

$$\vec{K}' = \frac{2\pi}{a}(0, \frac{2}{\sqrt{3}}) \quad (2.6)$$

Covalent bonds are formed due to sp^2 hybridization, connecting the carbon atoms in the graphene plane and involving the atomic orbitals $2s$, $2p_x$ and $2p_y$. The $2p_z$ orbitals can be treated separately since they are oriented perpendicular to the plane, having zero overlap with the other orbitals. Hence the $2p_z$ orbitals form the π bonds in graphene, while the $2s$, $2p_x$ and $2p_y$ form the σ bond. One can formulate a trial wavefunction Ψ by superposition of Bloch functions [26, 27], taking into account one $2p_z$ orbital per atomic site, composing the π band of graphene. Since each graphene unit cell consists of two atoms A and B , the model uses two Bloch functions Φ_A and Φ_B :

$$\Psi(\vec{r}) = \frac{1}{\sqrt{N}} \sum_{\vec{R}_A} e^{i\vec{k}\vec{R}_A} \phi(\vec{r} - \vec{R}_A) + \frac{1}{\sqrt{N}} \sum_{\vec{R}_B} e^{i\vec{k}\vec{R}_B} \phi(\vec{r} - \vec{R}_B) \quad (2.7)$$

$$= C_A \Phi_A(\vec{r}) + C_B \Phi_B(\vec{r}) \quad (2.8)$$

with $\phi(\vec{r})$ being the wavefunction of the $2p_z$ orbital of the isolated carbon atom and N being the number of unit cells. The summation is taken over all vectors of the graphene lattice. Any pair of atoms

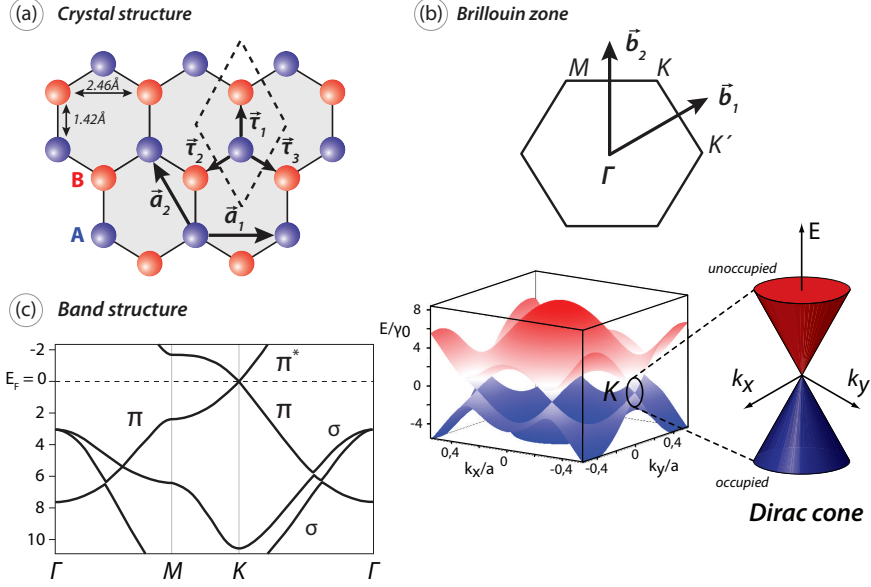


Figure 2.2: Crystallographic structure of graphene in real and reciprocal space. (a) Crystal structure with two sublattices (red and blue) and two carbon atoms per unit cell. (b) The corresponding Brillouin zone for graphene. (c) Band structure of free-standing graphene obtained by means of DFT taken from Dedkov et al. [24] – π , π^* , σ bands are indicated (left). Band structure of the π band solely in the framework of tight-binding calculations [2, 4, 25] (right).

from a unit cell can be labeled by the vectors: $\vec{R}_A = n_1 \vec{a}_1 + n_2 \vec{a}_2$; $\vec{R}_B = n_1 \vec{a}_1 + n_2 \vec{a}_2 + \vec{\tau}_1$ with n_1 and n_2 being integer values.

The vectors following the path along the carbon-carbon bonds are: $\vec{\tau}_1 = a(0, 1/\sqrt{3})$; $\vec{\tau}_2 = a(-1/2, -1/2\sqrt{3})$; $\vec{\tau}_3 = a(1/2, -1/2\sqrt{3})$; With the Schrödinger equation $\hat{H}\Psi = E\Psi$, and using the Dirac notation, one can obtain the transfer integral matrix $H_{ij} = \langle \Phi_i | H | \Phi_j \rangle$ and the overlap integral matrix $S_{ij} = \langle \Phi_i | \Phi_j \rangle$. By solving the secular equation $\det[\hat{H} - ES] = 0$ the dispersion relation $E(k)$ is obtained. Considering that in graphene the atoms in the A and B sublattice are the same, the related matrix elements H_{AA} and H_{BB} are also the same, which implies $H_{AB} = H_{BA}^*$. Using in the following the assumption that the

overlap between wave functions centered at different atoms is zero ($S_{AB} = S_{BA} = 0$), and the normalization $S_{AA} = S_{BB} = N$, the secular equation is given by

$$E_{\pm} = H_{AA} \pm |H_{AB}| \quad (2.9)$$

with E_+ being the eigenvalue for a symmetric combination of the wave functions forming the bonding π energy band (valence band) and E_- for the anti-symmetric combination (anti-bonding π^* band). The diagonal elements in the matrix become constant terms since the atoms A interact only with themselves and the three neighboring B atoms (nearest neighbor tight-binding approximation). Thus the diagonal elements represent the energy of the electron on the carbon $2p_z$ orbital $H_{AA} = E_{2p}$. For the graphene system, solely consisting of atoms of the same kind, the on-site energy E_{2p} is always the same, thus making $E_{2p} = E_F = 0$. A different situation occurs for the off-diagonal elements $H_{AB} = \langle \Phi_A | H | \Phi_B \rangle$ for which one obtains:

$$H_{AB} = \sum_{\vec{R}_A} \sum_{\vec{R}_B} e^{i\vec{k} \cdot (\vec{R}_A - \vec{R}_B)} \langle \phi(\vec{r} - \vec{R}_A) | H | \phi(\vec{r} - \vec{R}_B) \rangle \quad (2.10)$$

$$= \gamma_0 \sum_{l=1}^3 e^{i\vec{k} \cdot \vec{\tau}_l} \quad (2.11)$$

$$= \gamma_0 e^{i\vec{k} \cdot (\vec{a}_1 - \vec{a}_2)/3} [1 + e^{i\vec{k} \cdot \vec{a}_2} + e^{-i\vec{k} \cdot \vec{a}_1}] \quad (2.12)$$

$$= \gamma_0 \left[\exp\left(i \frac{k_y a}{\sqrt{3}}\right) + 2 \cos \frac{k_x a}{2} \exp\left(-i \frac{k_y a}{2\sqrt{3}}\right) \right] \quad (2.13)$$

with γ_0 being the tight-binding integral. The substitution of the equation above into the secular equation yields the energy dispersion relation of graphene in the tight-binding approximation with eigenenergies E_{\pm}

$$E_{\pm}(k_x, k_y) = E_F \pm \gamma_0 \sqrt{1 + 4 \cos \frac{ak_x}{2} \cdot \cos \frac{\sqrt{3}ak_y}{2} + 4 \cos^2 \frac{ak_x}{2}} \quad (2.14)$$

Especially interesting is the region around $E_{\pm} = 0$ where valence and conduction band meet, which happens at the K and K' points.

The $2p_z$ orbital forming the π band is half occupied for graphene, thus the Fermi energy lies in the middle of both bands. The energy dispersion described above can be approximated by a linear form in the vicinity of K and K' .

$$E_{\pm} = \pm \hbar v_F |\vec{k}| \quad (2.15)$$

$$v_F = \frac{\sqrt{3} a \cdot \gamma_0}{2 \hbar} \quad (2.16)$$

This relation has a conical behavior around E_F , forming the so-called Dirac cone (Fig. 2.2 (c) – right). Furthermore, a constant Fermi velocity v_F of $\approx 1 \times 10^6 \text{ m s}^{-1}$ is found using parameters of $a = 2.46 \text{ \AA}$ and $\gamma_0 \approx 3 \text{ eV}$, according to DiVincenzo and Mele [4] and Reich et al. [25]. The scientific breakthrough happened when experiments on the quantum-hall effect by two different groups (Novoselov et al. [7] and Zhang et al. [8]), proved the massless behavior of the charge carriers, hence a linear energy dispersion around K and K' . Interestingly, the experimental results in this work obtained by ARPES on graphene/Ir(111), described in chapter 6, confirm the value given for the Fermi velocity in agreement with studies by Kralj et al. [28]. The general Dirac operator of the free electron has in the limit of vanishing mass ($m \rightarrow 0$) the following structure according to Nolting [29]:

$$\hat{H}_D = c \cdot \hat{a} \cdot \hat{p} \quad (2.17)$$

with the Dirac-matrices $\hat{a} = \begin{pmatrix} 0 & \sigma \\ \sigma & 0 \end{pmatrix}$ and the momentum operator $\hat{p} = (-i\hbar\nabla)$. From the eigenenergies in equation (2.15) one can assume a similar operator describing electrons and holes in graphene near the K point as relativistic massless particles. Hence the physical system can be understood as a Dirac equation in the limit of vanishing mass [21],

$$\hat{H}_D = \pm \hbar v_F \sigma \cdot (-i\hbar\nabla) \quad (2.18)$$

with $\sigma = (\sigma_x, \sigma_y)$ being the vector of the two-dimensional Pauli matrices. The electrons near the K point move with the constant Fermi velocity $v_F \approx c/300$ replacing the speed of light. As described by

Ohlsson [30], this operator leads to two two-dimensional Weyl equations showing the same structure in the energy-momentum relation as derived in equation (2.15). According to the above described similarity to the Dirac equation, the zone corners of graphene in reciprocal space are called Dirac points (K , K' point) with the dispersion of electrons showing a linear behavior near these Dirac cone, and the charge carriers in graphene are called Dirac Fermions.

Using the framework of the tight-binding approximation above, the findings of equation(2.14) are implemented and calculated using the software Igor Pro [31]. With the parameters mentioned above one can derive the band structure for the π band (Fig. 2.2 (c) – right). The band structure of so-called free-standing graphene – thus including the σ bands – can be obtained by means of DFT, taken from Dedkov et al. [24] – π , π^* and σ bands are indicated (Fig. 2.2 (c) – left).

2.2 Classification of graphene/metal systems; possible graphene applications

Graphene itself has many possible applications. Due to its high charge carrier mobility [32] electronic based applications were proposed [17, 33], potentially replacing silicon in electronic components. Other possible applications, *e. g.* spintronics, use the electron spin degree of freedom in graphene [34] and exploit the spin transport at room temperature and the long spin diffusion lengths of several μm as reported by Tombros et al. [35]. The mechanical properties of graphene with its high Young's modulus [36] could be exploited *e. g.* for applications in flexible electronics [37, 38]. In order to actually use graphene in devices, the material needs to get, at some point, in contact with metals. A main challenge is to understand how the electronic structure of graphene is influenced by the metal. Graphene-metal interfaces are of special importance to possible applications in devices which could relate to the transport of charge or spin. For graphene/metal systems a classification is used, as discussed by Voloshina and Dedkov [39], distinguishing into two cases – “weakly” and “strongly” bonding graphene to the underlying metal substrate. These two cases show a different behavior concerning their electronic band structure. On the one hand,

it has been shown that in the case of a “strong” bonding situation, the Dirac cone is modified by low lying metal valence band states and basically not preserved, as in the case of graphene/Ni(111) [12, 40–42]. On the other hand, “weakly” interacting systems as graphene/Ir(111) show an intact Dirac cone with a linearly dispersing π band [43–45]. Other properties could affect the electronic structure like doping of π band effectively shifting the Dirac cone; opening of band gaps between π and π^* states; hybridization between the π states of graphene and low lying transition metal $3d$ states. These effects can be generated by specific modification of graphene/Ir(111) using intercalation of metal thin films (chapter 7 – 10). Following the work of Voloshina and Dedkov [39], graphene placed on the (111)-surface of (*sp*)-metals, leads to a shift of the Dirac cone below the Fermi energy (n-doping). The Dirac cone is preserved and no band gap opening is observed. A possible explanation for the shift of the π band is that the *sp*-metal acts as electron donor subsequently occupying the π^* states. This behavior is depicted in Fig. 2.3 (a), suggesting a “weak” interaction between graphene and the *sp* metal. A different situation occurs if graphene is placed on *d*-metals with an partially open *d* shell as in the case of Ni or Co (ch. 8). Additional effects of $\pi - d$ band hybridization emerge beyond the initial doping effects. This hybridization leads to the formation of so-called interface- or hybrid-states [40], effectively destroying the Dirac cone (Fig. 2.3 (b) and chapter 8.2). This case would suggest a rather “strong” interaction between graphene and open *d* shell metals.

However, there is an interesting intermediate case, as for graphene on *d*-metals with a closed shell (Cu). Again the graphene π band is n-doped, shifting the Dirac cone towards lower binding energy. From Fig. 2.3 (c) it is apparent that a band gap is opened directly at the K point. This behavior was experimentally verified using ARPES, XPS and LEED (ch. 7). Voloshina and Dedkov [39] draw the conclusion that this is due to hybrid states, which emerge from the $2p_z$ orbitals of graphene from the two different sublattices, interacting with the Cu $3d$ states, thus forming an symmetry-induced band gap. Hybridization affects also the π band dispersing through the lower lying Cu $3d$ states. At the intersections, additional hybridization gaps are induced. A detailed discussion on graphene/Cu(111) is found in chapter 7.

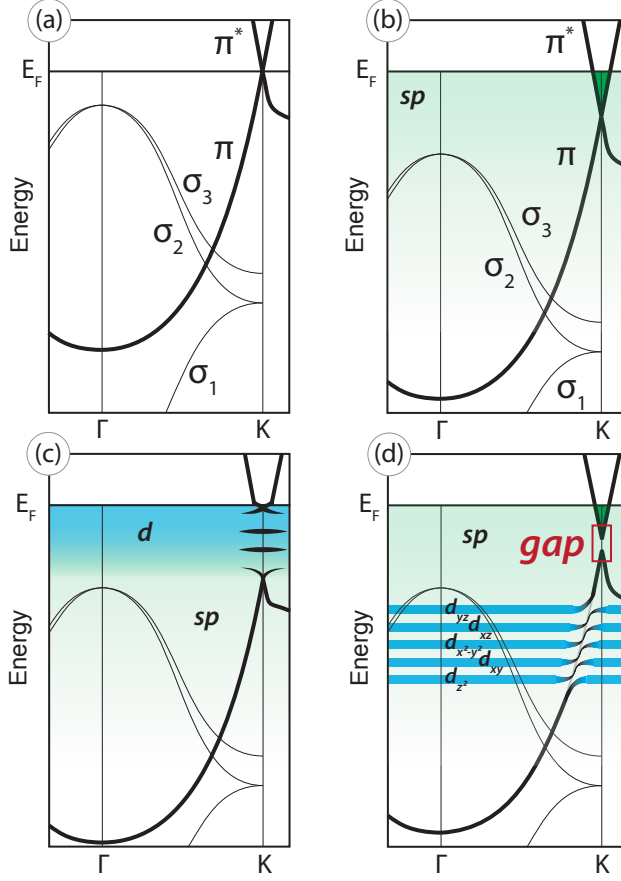


Figure 2.3: Schematic band structure for graphene on different metal substrates, with kind permission from Voloshina and Dedkov [39]. (a) Free-standing graphene exhibits a linear dispersion near the Dirac point. (b) Graphene/*sp*-metal: n-doped graphene, with preserved linear dispersion near the Dirac point. (c) Graphene/open-*d*-shell-metal: initial n-doped graphene; subsequently $\pi - d$ hybrid states emerge which affect the band structure by a massive rearrangement of bands. (c) Graphene/closed-*d*-shell-metal: initial n-doped graphene; hybrid states emerge at energies far below E_D accompanied by the opening of a band gap at E_D .

Spintronic applications

Spin polarized electron physics and spin electronics, summarized under the term “spintronics”, refers to the manipulation of the electron spin degree of freedom instead, or in addition to the electron charge, which I outline in the following section. In order to exploit spin properties, effects like spin relaxation time and spin transport in metals and semiconductors needs to be considered. A device that

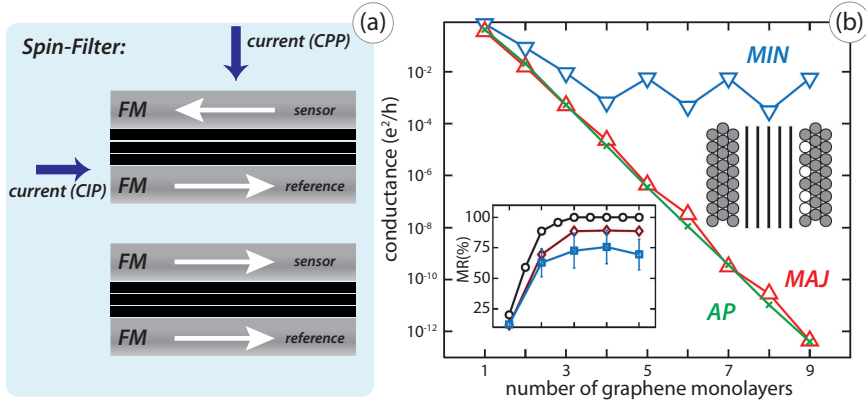


Figure 2.4: Effect of spin-filtering via graphene layers separating two ferromagnetic materials, taken from Karpan et al. [11]. (a) Schematic representation of parallel and anti-parallel orientations of magnetizations of ferromagnetic electrodes in a junction – spin-filter in CPP and CIP geometry. (b) Conductance as a function of number of graphene layers for minority and majority electrons for parallel and anti-parallel configurations of an ideal Ni/graphene/Ni junction, measured in CPP geometry. (Inset) The respectively calculated magnetoresistance, indicating effective spin filtering by four orders of magnitude for 3 monolayers of graphene and beyond. (circles) ideal junctions; (diamonds) junctions where the surface layer is a disordered NiCu alloy; (squares) junctions where the top layer of one of the electrodes is rough with only half of the top layer sites occupied (sketch on the right).

is already in use in industry is the spin valve GMR-sensor which is a sandwich based structure exploiting the “giant-magnetoresistance effect” (GMR) in an current-perpendicular-to-plane (CPP) or current-

in-plane (CIP) structure (Fig. 2.4 (a)). The GMR effect, discovered independently by Fert et al. [46] and Grünberg et al. [47] which led to the award of the Nobel Prize in Physics in 2007 [48], is observed for sandwich-based structures of two ferromagnetic layers separated by a non-magnetic spacer layer (*e.g.* Cu). The observed effect is apparent, according to Stöhr [49], when electrons in the “sensor” layer travel with spin orientation anti-parallel or parallel relative to the spin in the underlying “reference” layer, and a drop in the electric resistivity on the order of 10 % is observed in such a device. Fast changing small external magnetic fields cause the magnetization in the sensor layer to switch. This structure is used as read head for data stored on magnetic media. The written bit pattern on the hard disk rotates under a read head while the sudden change in the GMR signal is used to read the pattern.

According to Karpan et al. [11] it is possible to further enhance this effect by using a certain number of graphene layers as spacer layer in a spin-filter device. The authors predict perfect spin filtering for interfaces between graphite and (111) fcc or (0001) hcp Ni or Co surfaces. They calculate a distinct difference in the drop in the conductance of minority and majority carriers resulting in effective spin-filtering of the junction for 3 monolayers of graphene and beyond. Hence perfect spin filtering is presumed for interfaces between graphite and (111) fcc Ni, or (0001) hcp Co surfaces. Further arguments concerning the functionality of such a device are that the in-plane lattice constants of graphene (2.46 Å) and (0001) Co (2.506 Å); or (111) Ni (2.492 Å) [11] match almost completely, with only a small lattice mismatch of 1.3 % in the case of Ni. The electronic states of graphene are, in the vicinity of the Fermi level, solely found around the K-point. Co and Ni have in this region only electronic states of minority spin character; majority spin states are largely absent. This behavior is shown in Fig. 2.5, where the Fermi surface projections for majority and minority spin states are depicted for Co and Ni with respect to Cu and graphene. The authors conclude that perfect spin filtering is expected for several layers of graphene on top of a flat Ni or Co (111) surface. However, the major drawback up to now is that a single graphene sheet adsorbed on open 3d-shell transition-metals like Ni and Co undergoes chemical bonding to the metal [40], and its

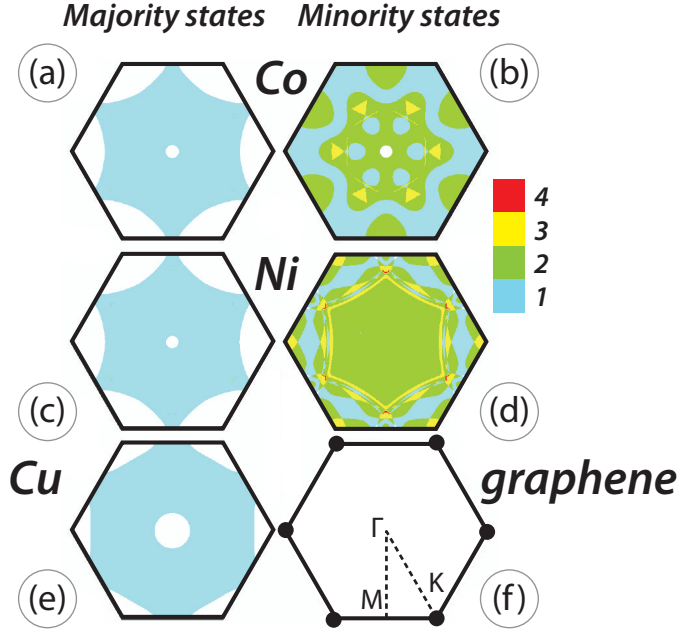


Figure 2.5: Fcc Fermi surface projections onto a plane perpendicular to the (111) direction for Co, Ni, Cu, and graphene, taken from Karpan et al. [11]. The color bar indicates the number of Fermi surface sheets. Only the minority electrons take part in electron transport, since majority electrons are largely absent.

characteristic electronic structure, the Dirac cone at the K points, is destroyed (ch. 8). A possible route towards avoiding this detrimental effect may involve intercalation of Cu or Au, which is known to restore the Dirac cone [41, 50, 51].

Photoelectron and x-ray absorption spectroscopy

3.1 Fundamentals of photoelectron spectroscopy

For the description of photoemission spectroscopy (PES), I follow the comprehensive literature sources [52–56]. Photoemission spectroscopy utilizes the photoelectric effect which was discovered already in 1887 by Hertz [57]. For the first photoemission experiments, monochromatic light was used, which was focused on a sample of alkali metal. In order to determine the maximum kinetic energy of the photoelectrons, Lenard [58] applied a counter potential until the current was fully suppressed. The theoretical explanation for this effect was given in 1905 by Einstein [59], who explained the photoelectric effect as an expression of the quantum nature of light, with electrons being able to absorb photons and using the gained energy to be ejected from the bulk material.

$$eU = E_{kin,max} = h\nu - \Phi \quad (3.1)$$

According to equation (3.1), the energy of the photons $h\nu$ is related to the kinetic energy of the photoelectrons in vacuum E_{kin} and a material-dependent constant Φ . By varying the excitation frequency ν one obtains a linear relationship between voltage and frequency, making

it possible to extract Planck's constant h . For current experiments gas discharge lamps and x-ray sources are used on a laboratory scale as a source of photons. Complementary, on a larger scale synchrotron radiation produced by particle accelerators is used. Photoemission spectroscopy may be divided into different regimes: "valence level" PES which is also known as ultraviolet photoemission spectroscopy (UPS) in the regime 5 – 100 eV [52]. "Core level" PES, which may be also called x-ray photoemission spectroscopy (XPS), uses higher photon energies in order to obtain information from core level electrons.

The "Fermi energy", abbreviated E_F is used as a reference in solid state physics, hence the energetically lower lying occupied states with the binding energy E_B are referred to E_F . The electrons escaping into the vacuum need to overcome the energy difference between E_F and the vacuum level, which is called "work function" Φ , which is the same as in equation (3.1).

$$E_{kin} = h\nu - \Phi_{sample} - |E_B| \quad (3.2)$$

The experimental setup, which is in contact with the sample, must be considered in this equation. The alignment of the Fermi energies between sample and detector leads to an energy shift in the detected spectra, by the difference of the work functions $\Delta\Phi = \Phi - \Phi_{Det}$ [60]. The measured energy of the electron corresponds to:

$$E_{kin,Det} = h\nu - \Phi_{Det} - |E_B| \quad (3.3)$$

This process is shown in Fig. 3.1. Equation (3.3) plays an important role in the determination of the Fermi edge by reference measurements, for example on noble metal surfaces, and to gain information about the energy resolution of the experiment. By utilizing photoemission spectroscopy it is not only possible to determine electron energies, but also electron emission angles can be measured. This expansion leads to "angular resolved photoemission spectroscopy", abbreviated ARPES. The angular dependent detection of photoelectrons is shown in Fig. 3.2. For a fixed known photon energy $h\nu$ and detected kinetic energy of the photoelectrons, one can gain information about the binding energy. With the determination of the polar angle ϑ under which the

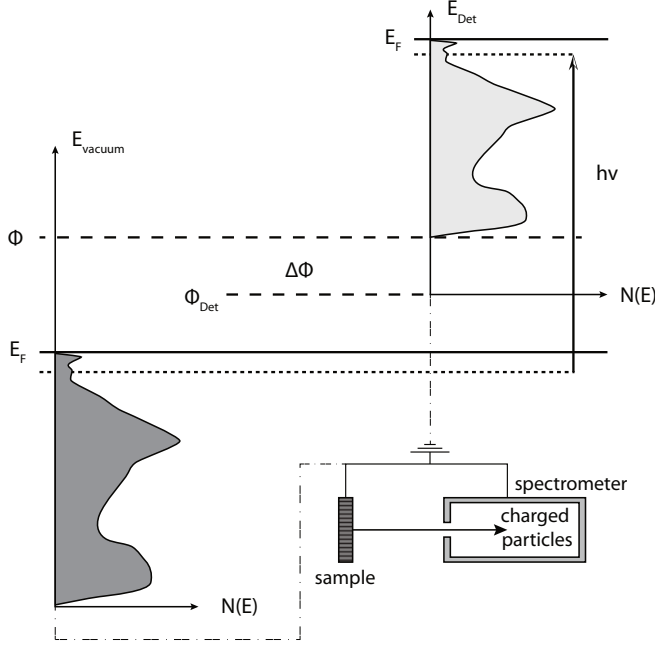


Figure 3.1: The Photoemission process for $\Phi_{sample} > \Phi_{det}$, after [55, 56, 61]. The energy scale of the free electron above the sample surface in vacuum is related to the energy scale of the detector by $\Delta\Phi = \Phi - \Phi_{Det}$. The maximum energy of the electrons in the spectrum is determined by $h\nu$ and Φ_{Det} , using equation (3.3). The minimum energy in the spectrum is set by Φ_{Det} . For this case there is a cut off in the spectrum, since $\Phi > \Phi_{Det}$.

electrons leave the solid, the crystal momentum of the electrons can be determined.

3.1.1 Theoretical description of ARPES and three-step-model

In the following part the theoretical aspects of ARPES are described relying on [52] and [54]. One approach to describe the photoemission process is by using the three-step-model, proposed by Berglund and Spicer [62]. Following this model, the photoemission process is rather artificially split up into three single steps:

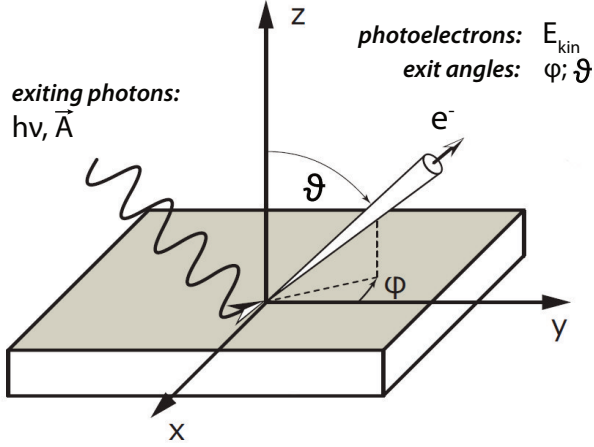


Figure 3.2: Schematic description of the angular resolved photoemission spectroscopy (ARPES), inspired by [52]. The incoming electromagnetic wave causes the emission of electrons from the sample with kinetic energy E_{kin} and angles ϑ, φ , detected by the analyzer.

- I. Excitation of electrons in the solid by photons with energy $h\nu$. The electrons pass from the initial state $|\vec{k}_i\rangle$ to the final state $|\vec{k}_f\rangle$.
- II. Transfer of the excited electrons to the surface of the crystal.
- III. Transmission of the excited electrons through the crystal surface into the vacuum.

The separate steps of the three-step-model are described in Fig. 3.3. In order to apply this model one needs to use approximations, such as negligence of many-body-effects (“independent particle picture”) and the relaxation of the system during the photoemission process (“sudden approximation”). Because of these simplifications, the three-step-model represents more of a descriptive form of the photoemission process and is not exact.

First step: photoabsorption

The incoming photons can be described as electromagnetic radiation field with vector potential \vec{A} , which interacts with the electrons in the crystal. Energy and momentum need to be conserved during this process:

$$\begin{aligned} E_f &= E_i + h\nu \\ \vec{k}_f &= \vec{k}_i + \vec{k}_{\text{photon}} + n\vec{G} \end{aligned} \quad (3.4)$$

with E_i being the initial state energy of an electron in an occupied state and E_f the final state energy of the unoccupied state. Photoemission becomes possible if the final state of the electron lies above the vacuum level (Fig. 3.3 (a)). To obtain momentum conservation in this process,

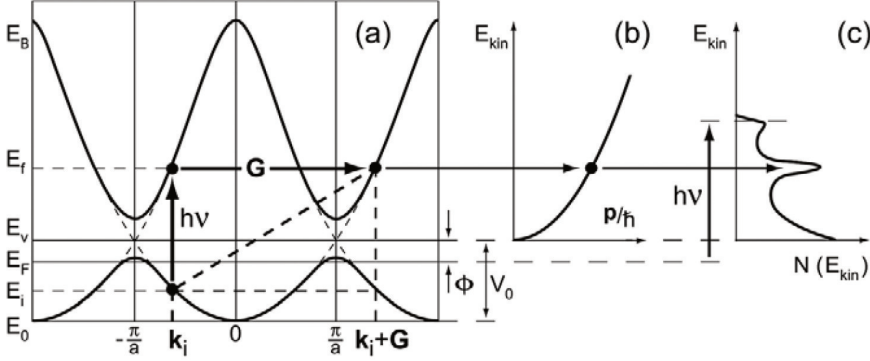


Figure 3.3: The photoemission process depicting the separate steps of the three-step-model, taken from [54]. a) Electrons are excited by photons with energy $h\nu$ with regard to energy and momentum conservation. Subsequently transport of the electrons to the surface. b) Transition of the electron through the surface with the repulsive potential V_0 into the vacuum with description as free-electron state. c) Measured photoelectron spectrum by the analyser.

an additional reciprocal lattice vector \vec{G} becomes necessary, because comparing the momentum of non-relativistic electrons to the photon momentum shows that in the range of low photon energies (UPS) the photon momentum \vec{k}_{photon} is insignificantly small – exiting electrons with a photon energy of 21.21 eV by He-I $_{\alpha}$ radiation one obtains for

the light a negligible photon-momentum of:

$$k = \frac{2\pi}{\lambda} \approx 8 \times 10^{-5} \text{ \AA}^{-1} \quad (3.5)$$

Hence, this excitation process represents a direct transition in the reduced zone scheme. The process of photoabsorption can be treated by perturbation theory. A one-particle-Hamiltonian is used as ansatz, which represents the ground state of the system.

$$\hat{H}_0 = -\frac{\hbar^2}{2m}\Delta + V \quad (3.6)$$

An electron in a electromagnetic field is described as

$$\hat{H} = \frac{1}{2m_e}(-i\hbar\nabla - e\vec{A})^2 - e\phi \quad (3.7)$$

with m_e the electron rest mass, considering the interaction of the electron (momentum $\hat{\vec{p}} = -i\hbar\nabla$) with the field of the electromagnetic radiation \vec{A} as perturbative term. Using the following approximations according to Hüfner [52] and Damascelli [54]: the gauge $\phi = 0$ of the scalar potential is chosen; terms of higher order are neglected; the dipole approximation is used, with the vector field \vec{A} being constant over atomic distances (hence $\nabla \cdot \vec{A} = 0$), one obtains the following relation:

$$\hat{H}_{int} = -\frac{e}{2m_e}(\vec{A} \cdot \hat{\vec{p}} + \hat{\vec{p}} \cdot \vec{A}) - e\phi + \frac{e^2}{2m_e}(\vec{A} \cdot \vec{A}) \approx \frac{e}{m_e}(\vec{A} \cdot \hat{\vec{p}}) \quad (3.8)$$

According to Fermi's golden rule [29] and Dirac's notation the transition probability $w_{f \rightarrow i}$ from a ground state $|\vec{k}_i\rangle$ into an excited state $|\vec{k}_f\rangle$ is defined as:

$$w_{f \rightarrow i} = \frac{2\pi}{\hbar} \left| \langle \vec{k}_f | \vec{A} \cdot \hat{\vec{p}} | \vec{k}_i \rangle \right|^2 \delta(E_f - E_i - h\nu) \quad (3.9)$$

The conservation of energy in equation (3.8) is guaranteed by the Dirac delta function. Using the sum of possible states $|\vec{k}_i\rangle$ and $|\vec{k}_f\rangle$, the current of excited electrons is derived from the following relation:

$$I \propto \sum_{\vec{k}_i, \vec{k}_f} \left| \langle \vec{k}_f | \vec{A} \cdot \hat{\vec{p}} | \vec{k}_i \rangle \right|^2 \delta(E_f - E_i - h\nu) \quad (3.10)$$

where the transition-matrix-element between ground state and excited state is represented by the term $\left| \langle \vec{k}_f | \vec{A} \cdot \hat{\vec{p}} | \vec{k}_i \rangle \right|^2 = |M_{i,f}|^2$.

Second step: transfer of the electron to the surface

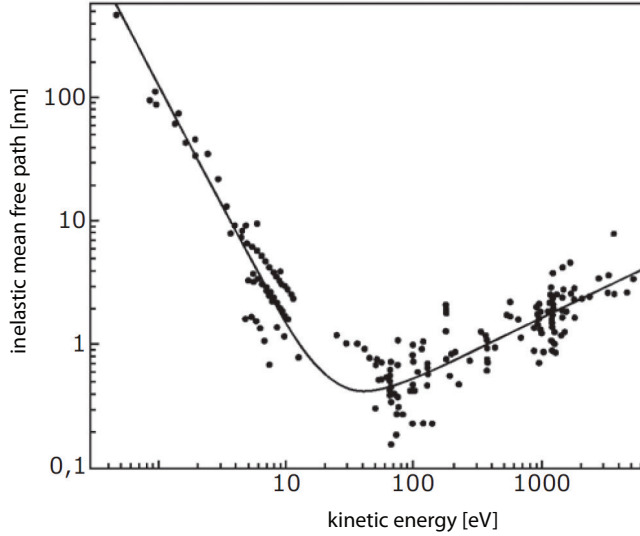


Figure 3.4: Relation of the inelastic mean free path of photoelectrons versus the kinetic energy, taken from [63].

The electron is affected by several scattering mechanisms before it reaches the surface of the crystal. The main scattering mechanism is inelastic electron-electron scattering inside the solid. Due to the loss of energy of these electrons, a so-called inelastic background emerges at higher binding energy in the measured spectra. The incoming photons penetrate the crystal up to a depth of several 100 Å, exciting photoelectrons along the path. Due to the scattering processes and the related energy loss, the free path of the electrons measures only

several monolayers. The behavior of the “inelastic mean free path” of the electrons, abbreviated IMFP, as a function of their kinetic energy can be determined empirically [63] and gives rise to the so called “universal curve” (Fig. 3.4). The described behavior holds for most of the common materials. Moreover, the high surface sensitivity of photoemission spectroscopy as a scientific technique, is based on the broad minimum over the range of 5 – 100 eV, where the IMFP is a few nm and less.

Third step: transmission through the surface into vacuum

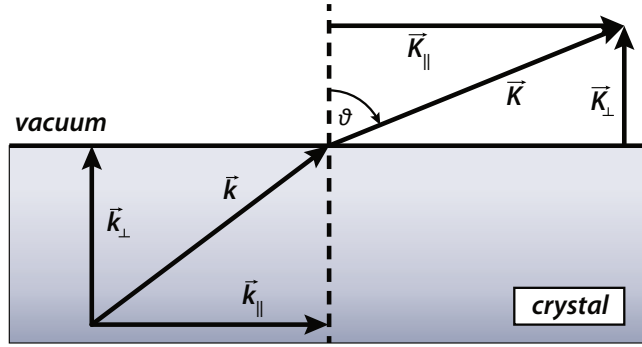


Figure 3.5: Schematic drawing of the refraction of electrons at the solid–vacuum interface. The momentum vector inside the crystal is described by \vec{k} and in the vacuum by \vec{K} .

Consider now the electrons inside the crystal which behave as free particles in a potential box of depth E_0 (free-electron model). The corresponding dispersion relation yields

$$E_f(\vec{k}) = \frac{\hbar^2}{2m} \vec{k}^2 + |E_0| \quad (3.11)$$

The excited electron can leave the crystal structure if the kinetic energy of the electron is larger than the potential barrier. The same holds for the momentum vector \vec{k} , which will be separated into a perpendicular \vec{k}_{\perp} and parallel component \vec{k}_{\parallel} of the sample

surface. The criterion for transmission of the electron through the surface depends on the valence band minimum E_0 and the vacuum level E_V (Fig. 3.3 (a)).

$$\frac{\hbar^2}{2m} \vec{k}_\perp^2 \geq E_V - E_0 \quad (3.12)$$

The transmission process can be understood as refraction of the electrons at the crystal surface. This behavior is described in Fig. 3.5, showing the change in the components of the momentum vector. On the one hand, overcoming the potential barrier leads to a reduction of the perpendicular component \vec{k}_\perp of the momentum vector. On the other hand, the parallel component \vec{k}_\parallel is conserved, because of the constant crystal potential along the sample surface. In the framework of the reduced zone scheme one obtains:

$$\vec{k}_\parallel = \vec{K}_\parallel = \sqrt{\frac{2m}{\hbar^2} E_{kin}} \sin \vartheta \quad (3.13)$$

The electrons are emitted into the vacuum within a cone under the polar and azimuthal angles ϑ , ϕ and are detected by an analyzer as described in Fig. 3.2. Besides E_{kin} and \vec{k}_\parallel , also the perpendicular component \vec{k}_\perp needs to be considered to obtain a complete understanding of the photoemission process. Here the inner potential $V_0 = |E_0| + \Phi$ needs to be considered, consisting of the work function Φ and the minimum E_0 of the nearly free electron parabola (shown schematically in Fig. 3.3 (a)).

$$E_f = E_{kin} + V_0 = \frac{\hbar^2}{2m} (\vec{k}_\parallel + \vec{k}_\perp)^2 - V_0 \quad (3.14)$$

$$\vec{k}_\perp = \sqrt{\frac{2m}{\hbar^2} (E_{kin} \cos^2 \vartheta + V_0)} \quad (3.15)$$

For the determination of \vec{k}_\perp according to equation (3.14), the exact knowledge about the inner potential of the studied system is necessary.

We obtain under consideration of all single steps of the three-step-model for the total photoelectron current:

$$I(E_{kin}, \vartheta, \phi) \propto \sum_{\vec{k}_i; \vec{k}_f} |M_{i,f}|^2 \cdot \delta(E_f - E_i - h\nu) \cdot \delta(\vec{k}_f - \vec{k}_i) \delta(E_{kin} - E_f) \quad (3.16)$$

The electronic structure of graphene can be regarded as two-dimensional, since the electrons are confined to the two-dimensional structure in real space. We can therefore restrict ourselves to the parallel component of the crystal momentum:

$$\vec{k}_{\parallel} = \frac{\vec{p}_{\parallel}}{\hbar} = \sqrt{2mE_{kin}} \cdot \sin \vartheta \approx 0.512 \cdot \sqrt{E_{kin}(\text{eV})} \cdot \sin \vartheta \quad (3.17)$$

3.1.2 One-particle spectral function

In the following part I introduce the one-particle spectral function, using the argumentation of Damascelli et al. [64] and Johnson and Valla [65]. The one-particle spectral function is a model for the description of the photoemission process going beyond the three-step-model. The three-step-model, being rather phenomenological, disregards several aspects such as damping processes and energetic shifts [66]. ARPES measures directly the one-particle spectral function [54, 65, 67], which I outline in the following. In many-electron theory a Green's function can be formulated in the framework of non-interacting particles as described by Raimis [68] and Johnson and Valla [65], which represents the spectral function

$$A_0(\vec{k}, \omega) = \text{Im } G_0(\vec{k}, \omega) = \frac{1}{\omega - \epsilon_{\vec{k}_0} - i\eta} \quad (3.18)$$

with η being a small positive constant and $\epsilon_{\vec{k}_0}$ representing the dispersion of the bare band, hence the single electron dispersion in the absence of corrections.

Including effects of hypothetical many-body interactions this equation evolves into

$$A(\vec{k}, \omega) = \text{Im } G(\vec{k}, \omega) = \frac{1}{\omega - \epsilon_{\vec{k}_0} - \Sigma(\vec{k}, \omega)} \quad (3.19)$$

with $\Sigma(\vec{k}, \omega) = \Sigma_1(\vec{k}, \omega) + i\Sigma_2(\vec{k}, \omega)$ being the complex self energy. The real part Σ_1 and the imaginary part Σ_2 represent information on the energy corrections in relation to the bare band dispersion – renormalization and associated mass enhancement – and changes in the lifetime of the electron propagating in the many-body system. The one-particle spectral function has then the following form [54, 64, 65, 67, 69]

$$A(\vec{k}, \omega) \propto \frac{\Sigma_2(\vec{k}, \omega)}{[\omega - \epsilon_{\vec{k}_0} - \Sigma_1(\vec{k}, \omega)]^2 + (\Sigma_2(\vec{k}, \omega))^2} \quad (3.20)$$

In the framework of this model the total photoelectron current is represented as

$$I(\vec{k}, \omega) = |M|^2 A(\vec{k}, \omega) f(\omega) \quad (3.21)$$

with $|M|^2$ being the transition matrix element as described in equation (3.9). The Fermi function $f(\omega)$ is used to consider the limitation to occupied states in photoemission spectroscopy. In the following the momentum distribution curve (MDC) method – an intensity cut at constant energy – is considered as will be explained in chapter 4.2. Hence the spectral function takes the simple form

$$A(\vec{k}, \omega) = \frac{\Sigma_2(\omega_0)}{[\omega_0 - \epsilon_{\vec{k}_0} - \Sigma_1(\omega_0)]^2 + (\Sigma_2(\omega_0))^2} \quad (3.22)$$

In graphene the bare dispersion can be approximated near the Fermi energy as a linear form $\epsilon_{\vec{k}_0} = v_0(k - k_F)$, with v_0 being the bare velocity. Kaminski et al. [70] and Valla et al. [71] show that the MDC takes in this case the form of a simple Lorentzian located at $k_m = k_F + [\omega_0 - \Sigma_1(\omega_0)]/v_0$ and the FWHM of $\Delta k = 2\Sigma_2(\omega_0)/v_0$. Hence, it is possible to extract information on the self energy from the FWHM of MDC spectrum evaluated at any binding energy. Further information

can be gained by evaluation of the energy dispersion curve (EDC) – an intensity cut at constant momentum – which takes also the form of a Lorentzian. The EDC has a FWHM of $\Delta E = v\Delta k = 2\Sigma_2/(1+\lambda)$. The measured dispersion corresponds to the renormalized velocity $v = v_0/(1+\lambda)$, with λ representing the so-called coupling constant. In chapter 6 I will use MDC data analysis to investigate the magnitude of the Fermi velocity and scattering mechanisms in graphene on Ir(111) and other metals.

3.2 X-ray absorption spectroscopy and x-ray magnetic circular dichroism

3.2.1 Absorption of x-rays

For the description of “x-ray absorption spectroscopy” (XAS) and “x-ray magnetic circular dichroism” (XMCD), I follow Refs. [49, 72–75]. Materials which are irradiated by x-rays attenuate the x-ray signal, through absorption and scattering in the material. The attenuation of x-rays with intensity I_0 by an amount of dI in a material of thickness dx follows an exponential decay law. The attenuation coefficient $\mu(E) = \mu_a + \mu_s$ as a function of the incident photon energy is composed additively of contributions from absorption μ_a and elastic and inelastic scattering μ_s .

$$dI = -\mu I_0 dx \rightarrow I(x) = I_0 \cdot e^{-\mu(E)x} \quad (3.23)$$

The overview of the cross section $\sigma = \mu(E)/n$, with n being the density of atoms, is shown exemplary for copper in Fig. 3.6 plotted against the photon energy. Three processes are mainly responsible for x-ray absorption. The photoelectric effect, also called photoionization, occurs mainly at low photon energies. For higher energies around 1×10^5 eV the Compton effect dominates, and for even higher energies $> 1 \times 10^7$ eV electron pair production takes over. During photoionization, the photon transmits the total amount of energy $h\nu$ to an electron with binding energy E_B inside an atom. To utilize this process, the energy of the photon must exceed the binding energy of the electron in the sample. Whenever the incident x-ray photon energy surpasses

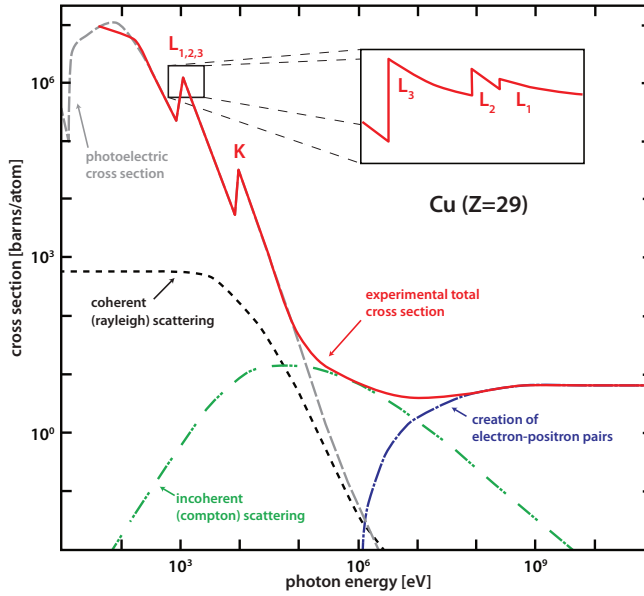


Figure 3.6: Overview of the cross section regimes for a copper sample taken at different photon energies and depicted on a double logarithmic scale, taken from Hubbell et al. [76].

the characteristic binding energy in the term scheme, the absorption increases rapidly as more electrons are accessible to photoionization. This behavior gives rise to the increase in the absorption coefficient μ_a . Different energy levels in the term scheme are related to different absorption edges. For electrons which are excited from a ground state with main quantum number of $n = 1$ are called $K \hat{=} 1s$ edge. Electrons from quantum numbers $n = 2$ are called L edges and are subdivided into $L_3 \hat{=} 2p_{3/2}$, $L_2 \hat{=} 2p_{1/2}$ and $L_1 \hat{=} 2s$ edges according to the quantum numbers (l, j) of the absorbing electron. Electrons from higher quantum numbers $n \geq 3$ are called M, N, \dots edges *etc.* This behavior leads to the characteristic edge-like-structure for the absorption coefficient of metals with K –, L – and M – absorption edges, as described by the experimental cross section (red curve) in Fig. 3.6. The red curve indicates the behavior of the experimental cross section for photon energies from 100 eV to about 1 GeV. Since the binding energies in

the term scheme are unique for each element, XAS can be used as an element selective spectroscopic tool (Manne Siegbahn, Nobel Prize in Physics 1924 [77]). The L edge shows a fine structure, separating it into L_3, L_2 and L_1 edges. This behavior is exploited by XMCD on metal L -edges, as explained in chapter 8.2 for cobalt at the Co $L_{2,3}$ -edge to obtain information about the magnetic coupling of the charge carriers.

The absorption of x-rays describing the transition of electrons from core level states into empty valence states can be understood in the framework of quantum mechanics. Hence, a transition probability $w_{i \rightarrow f}$ can be formulated from an initial state $|i\rangle$ into an final state $|f\rangle$ according to Fermi's Golden rule [29] as used earlier in equation (3.9).

The electric field vector $\vec{E} = \partial \vec{A} / \partial t$ is described as the derivative of the vector potential \vec{A} . In the following I assume the electromagnetic waves as plane waves $\vec{A} = A_0 \vec{\varepsilon} e^{i(\vec{k} \cdot \vec{r} - \omega t)}$ with $\vec{\varepsilon}$ being the polarization vector. Using the electric dipole approximation one obtains

$$\vec{A} \approx A_0 \vec{\varepsilon} e^{-i\omega t} (1 - i \vec{k} \cdot \vec{r} + \dots) \quad (3.24)$$

which is truncated after the first term. Hence the transition probability is given as

$$w_{f \rightarrow i} = \frac{2\pi}{\hbar} \frac{e^2}{m_e^2} |A_0|^2 \left| \langle f | \hat{\vec{\varepsilon}} \cdot \hat{\vec{p}} | i \rangle \right|^2 \delta(E_f - E_i - h\nu) \quad (3.25)$$

Using the commutator relation for the momentum operator $\hat{\vec{p}} = -i\hbar \nabla = m/i\hbar [\hat{\vec{r}}, \hat{H}_0]$ yields

$$w_{f \rightarrow i} = \frac{2\pi}{\hbar} e^2 |A_0|^2 \frac{(E_f - E_i)^2}{\hbar^2} \left| \langle f | \hat{\vec{\varepsilon}} \cdot \hat{\vec{r}} | i \rangle \right|^2 \delta(E_f - E_i - h\nu) \quad (3.26)$$

The absorption cross section σ is defined as $\sigma = \frac{w_{f \rightarrow i} \cdot h\nu}{I_{ph}}$, the ratio of the rate at which energy is removed from the photon beam by the photoelectric effect, divided by the rate of energy in the photon beam crossing the unit area perpendicular to its propagation direction [72]. Using $I_{ph} = 2\varepsilon_0 c |A_0|^2 \omega^2$ for the photon flux [72], one obtains for the absorption cross section

$$\sigma(\nu) = \alpha 4\pi^2 E \left| \langle f | \hat{\vec{\epsilon}} \cdot \hat{\vec{r}} | i \rangle \right|^2 \delta(E_f - E_i - h\nu) \quad (3.27)$$

with $\alpha = e^2/4\pi\epsilon_0\hbar c = 1/137$ being the fine structure constant and the energy difference between initial state and final state $E = E_f - E_i$. To obtain the total absorption cross section of the sample, we integrate over the absorption cross section. Hence the resonant x-ray absorption intensity depends only on the polarization of the incoming light and the photon energy.

$$I_{res} = \alpha 4\pi^2 E \left| \langle f | \hat{\vec{\epsilon}} \cdot \hat{\vec{r}} | i \rangle \right|^2 \quad (3.28)$$

What is left is the calculation of the matrix elements $\langle f | \hat{\vec{\epsilon}} \cdot \hat{\vec{r}} | i \rangle$, which is outlined following the argumentation of Stöhr [49]. The transition matrix elements involve the tensor operator $\hat{\vec{\epsilon}}_q \cdot \hat{\vec{r}}$ consisting of the electron position vector $\vec{r} = x\hat{e}_x + y\hat{e}_y + z\hat{e}_z$ and the electric field vector. For circularly polarized light $\hat{\vec{\epsilon}}_{q=\pm 1} = \mp \frac{1}{\sqrt{2}}(\hat{e}_x \pm i\hat{e}_y)$ and for linear polarized light $\hat{\vec{\epsilon}}_{q=0} = \hat{e}_z$ is used. The result using the spherical harmonics $Y_l^m(\vartheta, \varphi)$ [78] is described for the different polarizations used in the experiments as

$$\text{right circular polarization} \quad \frac{1}{\sqrt{2}}(x + iy) = r\sqrt{\frac{4\pi}{3}}Y_1^1 \quad (3.29)$$

$$\text{left circular polarization} \quad \frac{1}{\sqrt{2}}(x - iy) = r\sqrt{\frac{4\pi}{3}}Y_1^{-1} \quad (3.30)$$

$$\text{linear polarization} \quad z = r\sqrt{\frac{4\pi}{3}}Y_1^0 \quad (3.31)$$

In the following I briefly outline the so-called “single-electron model”, proposed by Erskine and Stern [79] which is used to describe transitions of $2p$ core level states into $3d$ valence states [80]. The initial state can be expressed as core atomic orbital and the final state by a valence orbital according to Cohen-Tannoudji et al. [81]:

$$|f\rangle = |R_{n',l'}(r); l'; m'_l, s', m'_s\rangle = R_{n',l'}(r) Y_{l',m'_l}(\vartheta, \varphi) \chi_{s',m'_s} \quad (3.32)$$

where $R_{n',l'}(r)$ is the radial part, $Y_{l',m'_l}(\vartheta, \varphi)$ the angular component and χ_{s',m'_s} the spin component. The following quantum numbers with their eigenvalues are used: n principal-; l, m_l angular-; and s, m_s spin quantum number. The formulation of the initial state takes spin-orbit coupling of the core levels into account, hence m_l and m_s are no longer good quantum numbers. Therefore the additional operators $\hat{J} = \hat{L} \pm \hat{S}$; \hat{M} with the eigenvalues $j = l \pm s$; m_j needs to be used [81]. The initial state can be formulated as

$$\begin{aligned} |i\rangle &= |R_{n,l}(r); j; m_j, l, s\rangle \\ &= \sum_{m_l, m_s} |R_{n,l}(r); l, m_l; s, m_s\rangle \langle l, m_l; s, m_s | j, m_j \rangle \end{aligned} \quad (3.33)$$

with the Clebsch-Gordan coefficients $C_{l,m_l} = \langle l, m_l; s, m_s | j, m_j \rangle$. For the calculation of the matrix elements $\langle f | \vec{\varepsilon} \cdot \hat{\vec{r}} | i \rangle$, the following result is obtained with factorized spin, radial and angular contributions [49]:

$$\begin{aligned} \langle f | \vec{\varepsilon} \cdot \hat{\vec{r}} | i \rangle &= \langle R_{n',l}(r); l, m_l; s, m'_s | \vec{\varepsilon} \cdot \hat{\vec{r}} | R_{n,c}(r); c, m_c; s, m_s \rangle \\ &= \underbrace{\delta(m'_s, m_s)}_{\text{spin part}} \cdot \underbrace{\langle R_{n',l}(r) | r | R_{n,c}(r) \rangle}_{\text{radial part}} \cdot \underbrace{\langle l, m_l | \frac{\vec{\varepsilon} \cdot \hat{\vec{r}}}{r} | c, m_c \rangle}_{\text{angular part}} \end{aligned} \quad (3.34)$$

$$(3.35)$$

here c refers to the core shell angular momentum and l the unfilled valence shell angular momentum. Hence the dipole operator describing the polarization dependence solely acts on the angular part. The spin part is not affected, only allowing spin preserving transitions. The radial part describes the angle integrated transition strength. The separate evaluation of the above described spin, radial and angular parts yield the important dipole selection rules for transitions between $|n, l, m_l, s, m_s\rangle$ states which I state in the following [49]:

- spin quantum number not affected by the transition, hence $\Delta s = 0$; $\Delta m_s = 0$.

- orbital quantum number l differs by one to give contributions to transition matrix element, hence $\Delta l = l' - l = \pm 1$.
- $\Delta m_l = m'_l - m_l$ needs to take the following values:
 $\Delta m_l = -1$ (left circular polarized light); $\Delta m_l = +1$ (right circular polarization) and $\Delta m_l = 0$ (linear polarization).

3.2.2 X-ray absorption spectroscopy

X-ray absorption spectroscopy is used to characterize the interaction between x-rays and matter near absorption edges. XAS measures the x-ray absorption as a function of the photon energy. X-ray excitations in the near-edge region, which refers to about 10 eV below and about 30 eV above the absorption edge, are connected to transitions from core level states to empty valence band states. Spectroscopic measurements in this region defines the “near edge x-ray absorption fine structure”, abbreviated NEXAFS. Outside the near-edge region, excitations of the photoelectron into free electron-like continuum states take place, which is called “extended x-ray absorption fine structure” – EXAFS. Fig. 3.7 shows in a schematic picture how NEXAFS spectra are obtained by the use of synchrotron radiation.

In order to employ XAS in experiments different processes can be used. One possible way would be the measurement of the absorbed photons in a transmission experiment. This method cannot be used for the experiments on strongly absorbing bulk samples as done in the framework of this thesis. Another opportunity is the detection of the generated photoelectrons which is described in the following. In this case, additional secondary processes yielding Auger- and secondary electrons play a role. The experiments conducted in this thesis use the detection of the so-called XAS total electron yield (TEY) and XAS partial electron yield (PEY). The TEY detection mode collects all electrons, including these generated by secondary processes, while the PEY mode uses a MCP-detector with a retardation potential, which suppresses electrons with low kinetic energy from the absorption spectrum. Since these slow electrons are involved in scattering processes in the bulk, the PEY mode has a higher surface sensitivity than the TEY mode.

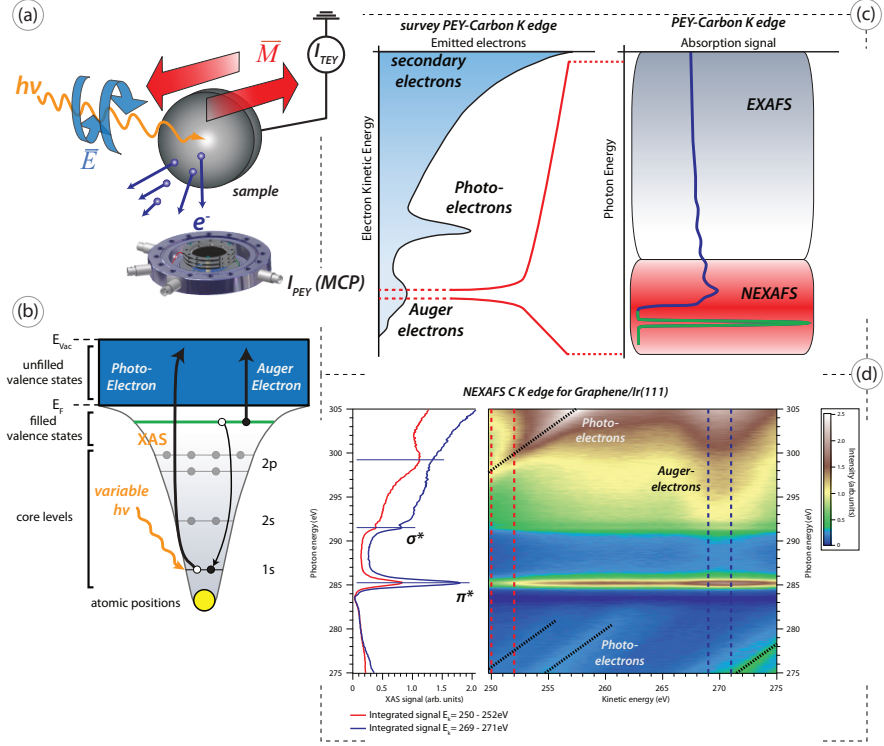


Figure 3.7: Overview of the XAS and XMCD mechanism inspired by [82]. (a) The MCP-detector is positioned directly under the sample, which can be magnetized either in-plane or out-of-plane and illuminated by photons of different helicity. Partial electron yield (PEY) and total electron yield (TEY) are measured simultaneously. (b) Schematic description of the energy levels of a carbon atom. Excitation of photoelectrons and Auger electrons by incoming photons. (c) Detection of the emitted electrons relative to their kinetic energy yields a characteristic spectrum of Auger electrons, photoelectrons and secondary electrons. For a fixed kinetic energy in the region of Auger emission, the MCP detector yields an absorption spectrum with characteristic absorption behavior around the absorption edge. (d) NEXAFS spectra for graphene/Ir(111) are measured over a certain photon energy range for different kinetic energies of the detected electrons.

3.2.3 X-ray magnetic circular dichroism

In general, “dichroism” describes the dependence of photon absorption on polarization. XMCD is a special type of dichroism which depends on charge and spin distribution [49]. Figure 3.7 (a) shows the principal setup for XMCD spectroscopy, used at beamline D1011 in MAX-lab (ch. 4.5), with the sample exposed to different magnetization directions while photons of different helicity excite photoelectrons. By employing XMCD one can probe magnetic effects due to dipole-allowed $2p - 3d$ transitions and gain insight into the properties of the $3d$ valence electrons which are responsible for the magnetic behavior of the transition metals.

The XMCD effect is described as the difference of the $p \rightarrow d$ transition intensities as a function of the photon energy, obtained with negative (I^-) and positive (I^+) helicity for circular polarized light [49].

$$\Delta I(E) = I^-(E) - I^+(E) \quad (3.36)$$

The mechanism behind XMCD is shown exemplary for the $L_{2,3}$ edges of a magnetic metal in Fig. 3.8 and can be understood in the framework of a two-step process.

First, the incoming photons of either positive or negative helicity, transfer its angular momentum to an excited photoelectron during the absorption process (conservation of angular momentum). This electron is excited, *e. g.* from a $2p_{3/2}$ spin-orbit split core level. According to equation (3.28) and the above described dipole selection rules for the transition matrix elements, spin-orbit coupling leads to a preferred excitation of electrons of one spin direction, yielding spin-polarized photoelectrons. Hence, spin-down [spin-up] electrons are excited preferentially by photons of negative [positive] helicity from the $2p_{3/2}$ levels and vice versa from the $2p_{1/2}$ levels, since they have opposite spin-orbit coupling ($l + s$ and $l - s$, respectively). Stöhr [49] gives ratios of 62.5 % spin-down electrons, compared to 37.5 % spin-up electrons for the L_3 edge (negative helicity), and respectively 25 % spin-down and 75 % spin-up electrons at the L_2 edge (negative helicity).

In a second step the electrons fill the unoccupied $3d$ states which has unequal spin-up and spin-down populations (formation of majority and

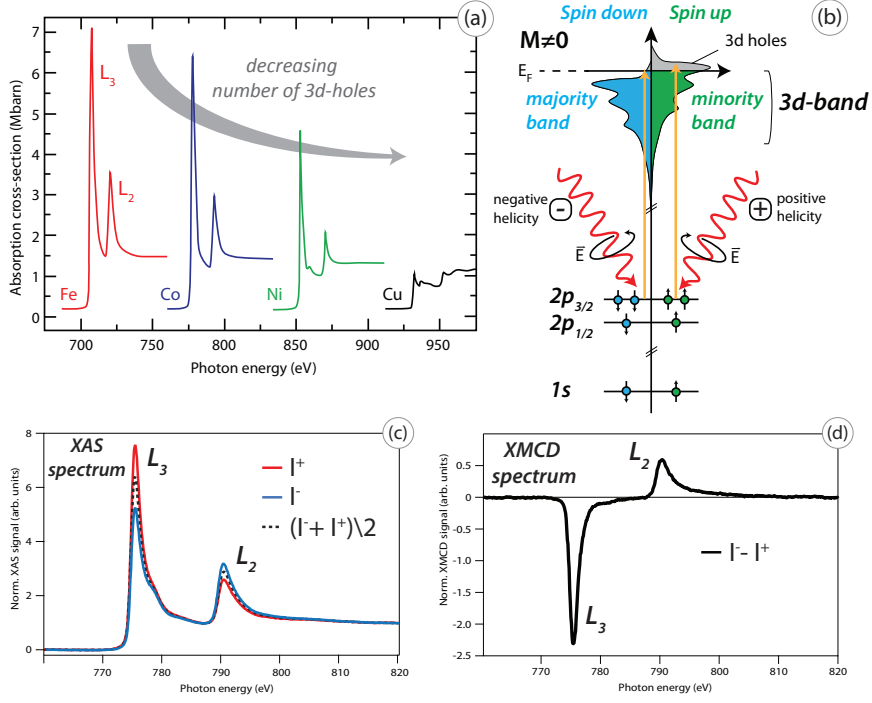


Figure 3.8: (a) $L_{2,3}$ edge XAS spectra of different 3d transition metals, plotted against the absorption cross section, taken from [49]. (b) Schematic description of the XMCD mechanism for a magnetic metal at the $L_{2,3}$ edges. Only spin-up electrons are excited, since the majority states are fully occupied. (c) XAS spectra at the Co $L_{2,3}$ absorption edge measured with circular polarized light of different helicity I^+ [red]; I^- [blue] and the “white line” spectrum $(I^- + I^+)/2$. (d) Show the corresponding XMCD spectrum.

minority states due to exchange splitting – Stoner model [49]). The transition needs to take place with respect to the dipole selection rules. Thus, the unoccupied 3d states act as “detector” for the spin state of the photoelectrons, with an optimal effect when the magnetization of the sample is aligned to the photon spin. The schematic description in Fig. 3.8 (b) indicates, that only the excitation of spin-up electrons from the $2p$ core level to the partially unfilled spin-up 3d valence shell is allowed, since the spin quantum number needs to be conserved during

transitions (dipole selection rule $\Delta s = 0$; $\Delta m_s = 0$ forbids spin-flips). The XMCD effect is shown exemplary for data of graphene/Co/ Ir(111), taken at the Co $L_{2,3}$ edges in Fig. 3.8 (c) and (d). The two absorption edges emerge due to $p_{3/2}$ state to valence band transitions (L_3 edge), and $p_{1/2}$ to valence band transitions (L_2 edge). The difference of these two spectra also called XMCD spectrum $\Delta I = I^- - I^+$ and is directly proportional to the atomic magnetic moment [49], hence contains the magnetic part of the signal. On the other hand, the nonmagnetic part is obtained by the “white line” spectra $(I^- + I^+)/2$, which is obtained as intensity averaged XAS spectra for negative and positive helicity, or different directions of magnetization. Two equivalent ways to obtain a XMCD spectrum are possible: on the one hand, by changing the direction of the photon spin and the associated angular momentum for a fixed magnetization of the sample.

On the other hand, it is equally possible to use a fixed helicity and switch the magnetization of the sample [83]. In general the “white-line” intensity is directly proportional to the number of $3d$ states above the Fermi level and is described by the different absorption cross section of Fe, Co and Ni in Fig. 3.8 (a). Finally, utilizing synchrotron light of different circular helicity one gains not only information on the quantity of the orbital and spin magnetic moments, it is also possible to gain insight into the direction of the magnetic moment and the coupling type between different magnetic materials. To extract quantitative values for the magnetic moment out of XMCD spectra, so-called “sum rules” (Carra et al. [84], Thole et al. [85] and Schütz et al. [86]) are used. The sum rules are discussed with respect to the experimental data in chapter 5.3.

Integrals over the L_3 and L_2 edges are obtained from the XMCD spectrum and the white line, after subtracting a step function (ch. 5.3):

$$\Delta A_i = \int_{L_i} \Delta I \, dE, \quad i = 2, 3 \quad (3.37)$$

$$A_i = \int_{L_i} \left(\frac{(I^- + I^+)}{2} - I_{step} \right) dE, \quad i = 2, 3 \quad (3.38)$$

For $L_{2,3}$ and K edges following sum rules used throughout the thesis. A detailed derivation of these sum rules is found elsewhere [74].

$$M_L = -\frac{2}{3} \frac{n_h \mu_B}{P_{circ} \cos \phi} \frac{\Delta A_3 + \Delta A_2}{A_3 + A_2} \quad (3.39)$$

$$M_S = -\frac{n_h \mu_B}{P_{circ} \cos \phi} \frac{\Delta A_3 - 2\Delta A_2}{A_3 + A_2} \quad (3.40)$$

with P_{circ} the degree of circular polarization of the incoming photons. The angle ϕ is defined by the geometry of the experiment, with the direction between the photon angular momentum and the magnetic moment. The number of holes is given by n_h . Finally, the ratio of the orbital and spin moment – $R_{L,S} = \frac{M_L}{M_S}$ – can be derived, which does not require magnetic saturation of the sample.

At K edges, spin polarization is not possible, due to zero orbital moment in the initial states ($1s \rightarrow 2p$). Hence employing sum rules for K edge absorption, can only derive values for orbital moments, as shown by Huang et al. [87].

$$M_L = -\frac{1}{3} \frac{n_h \mu_B}{P_{circ} \cos \phi} \frac{\Delta A}{A} \quad (3.41)$$

Experimental set-up and preparation of graphene

In my work I used three different experimental set-ups. Large parts of the measurements were performed at a dedicated ARPES station at the double-branch undulator beamline UE56/2 operated by the Max Planck Society at the BESSY II electron storage ring of the Helmholtz Zentrum Berlin (chapter 4.4). A detailed description of the set-up is depicted in Fig. 4.1. The sample is mounted on a molybdenum sample holder, suitable for annealing treatment, which is mounted on a spring-loaded molybdenum counterpart on a 6-axis-manipulator. The manipulator permits movement of the sample along the three translational axes – (x, y, z) – and also a movement around the rotational axes – $(\vartheta, \varphi, \beta)$. A hemispherical analyzer of the PHOIBOS 100/150 type, equipped with a MCP detector, collects the photoelectrons with respect to their take-off angle and kinetic energy. A CCD camera records the images of the illuminated MCP/phosphor screen combination. The generated single data files are collected by the measurement software and stored as a complete data packet.

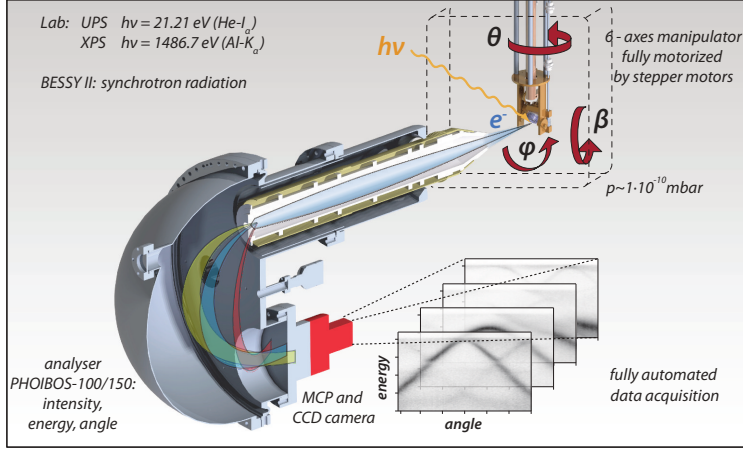


Figure 4.1: Principal layout of an ARPES station. Incoming photons, generated either by a helium discharge lamp or a synchrotron radiation source, excite photoelectrons emerging from the sample. The sample is mounted on a sample holder, which is placed on a 6-axis-manipulator. A hemispherical analyzer, equipped with a MCP detector collects the photoelectrons with respect to their emission angle and their kinetic energy. The CCD camera records the images of the phosphor screen behind the MCP and is read out by software.

4.1 The hemispherical electron analyser – PHOIBOS

Within the last few years, ARPES has undergone several improvements. Historically, ARPES was measured by stepwise rotation of the analyzer mounted on a goniometer inside the vacuum chamber. This procedure was very inefficient since only electrons leaving the sample under a certain angle were detected. The breakthrough came with the development of the so-called “angle-mode” by Mårtensson et al. [88], which allows the simultaneous detection of a range of take-off angles and kinetic energies of the electrons [53]. The ARPES measurements in this thesis were obtained with a modern hemispherical analyzer – PHOIBOS 100/150 – from SPECS Surface Nano Analysis GmbH.

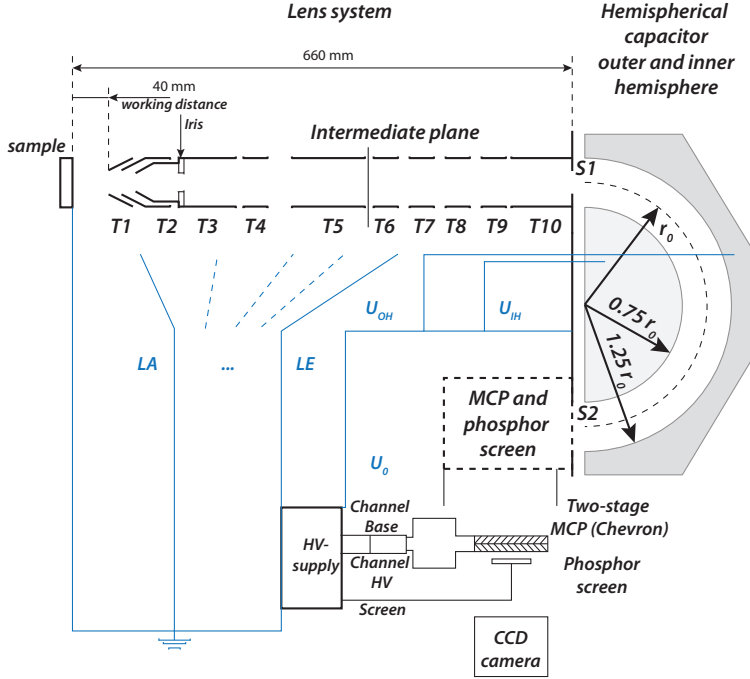


Figure 4.2: Principal layout of the PHOIBOS analyzer according the data sheet [61].

I outline in the following the principle of operation of the analyzer using Refs. [53, 61]. A schematic picture of the hemispherical analyzer PHOIBOS is depicted in a cutaway view in Fig. 4.2. The analyzer consists of the following main components:

- Input lens system for receiving charged particles.
- 180° hemispherical analyzer (HSA) with 100/150 mm nominal radius for spectroscopic energy measurements.
- Detector assembly – MCP and phosphorous screen.
- Slit Orbit mechanism with straight and curved slits.
- Iris aperture.

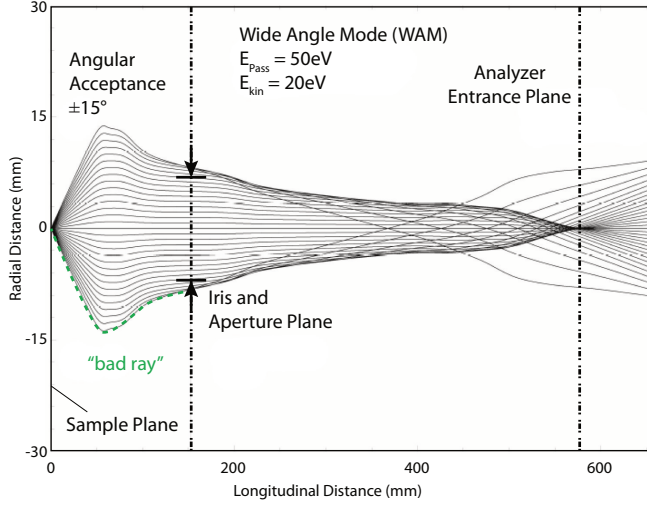


Figure 4.3: Trajectories of electrons in WAM mode, taken from [89] and described by SPECS data sheet [61].

The electron lens system consists of ten electrostatic lens tubes (T1 – T10 in Fig. 4.2), which enable the lens system to operate in different modes. The analyzer can be set to various angular resolved modes for ARPES studies, bending the electrons according to their take-off angle. The acceptance angle of the electrons can range from $\pm 3^\circ$ in the HAD-mode up to $\pm 13^\circ$ for the WAM-mode. Spatially resolved modes are preferentially used for XPS measurements. In this case the electrons are bend with respect to their position on the sample. An overview of the various lens modes can be found in Table 4.1. indicated are the used lens modes throughout this thesis – WAM, LAD, MAD for ARPES-measurements and HM and MA for XPS studies. The electrons are retarded or accelerated towards the so-called “pass energy” – E_{pass} by the lens system and focused onto the entrance slit S1 of the hemispheres. In the next step the electrons are guided through the capacitor by a radial electrostatic field applied between the inner and outer hemisphere and thus analyzed according to their energy (Fig. 4.2).

Table 4.1: Mode of operation of the PHOIBOS analyser according to [61]. The parameter M refers to the magnification of the hemispherical analyser. The used lens modes in this thesis are indicated [blue].

Lens mode	Acceptance area	Acceptance angle	Application
Spatially resolved			
High Magnification (HM-mode)	M = 10	up to $\pm 9^\circ$	Small area XPS
Medium Magnification (MM-mode)	M = 5	up to $\pm 6^\circ$	Small area XPS
Low Magnification (LM-mode)	M = 2	up to $\pm 3^\circ$	Small area XPS
Transmission optimized			
Large area (LA-mode)	spot size 5 mm	up to $\pm 5^\circ$	Large area XPS
Medium area (MA-mode)	spot size 2 mm	up to $\pm 7^\circ$	Large area XPS
Small area (SA-mode)	spot size 0.1 mm	up to $\pm 9^\circ$	Large area XPS
Angular resolved			
High angular dispersion (HAD-mode)		$\pm 3^\circ$	ARPES
Medium angular dispersion (MAD-mode)		$\pm 4^\circ$	ARPES
Low angular dispersion (LAD-mode)		$\pm 7^\circ$	ARPES
Wide angle mode (WAM)		$\pm 13^\circ$	ARPES

The theoretical energy resolution of hemispherical analyzers is described by Polaschegg [90].

$$\Delta E_A = E_{Pass} \cdot \left(\frac{s}{2r_0} + \frac{\alpha}{4} \right) \quad (4.1)$$

with s being the slit width and r_0 the mean radius of the electron path through the hemispheres. For a useful approximation the second term with the acceptance angle α can be neglected. For ARPES measurements, straight entrance slits are used, which are selected via a slit orbit mechanism. Straight slits produce a curved distortion in the ARPES raw data which needs to be corrected as discussed in chapter 5.1. Curved slits do not affect the shape of the spectra in this way. However, the photoelectrons would emerge from a curved line in k space which is not desired. A iris aperture located between lens tubes T2 and T3 at the head of the lens system can be used for the suppression of “bad rays” on undesirable trajectories leading to artificial intensity changes on the MCP (Fig. 4.3). Another useful aspect of the iris is for the alignment of the sample in front of the analyzer, by decreasing the iris diameter. Finally the electrons are projected onto the “multi-channel-plate” (MCP). Here the electrons are multiplied and illuminate a phosphorous screen. A CCD camera records images of the screen illuminated by the photoelectrons.

4.2 Experimental considerations for ARPES and XPS

For a given photon energy $h\nu$, the detector records the intensities $I(E_{kin}, k)$ of incoming photoelectrons as a function of their kinetic energy E_{kin} and their take-off angle – ϑ, φ – with respect to the sample surface, which relates to the momentum in reciprocal space (Fig.4.4). The geometry of the setup defines an energy dispersive axis and perpendicular to it an angle dispersive axis. To be able to analyze detailed information from the recorded images it is useful to extract lines of constant energy - “momentum distribution curve” (MDC), and of constant momentum - “energy distribution curve” (EDC) from the dataset. MDC spectra display intensities in dependence of the

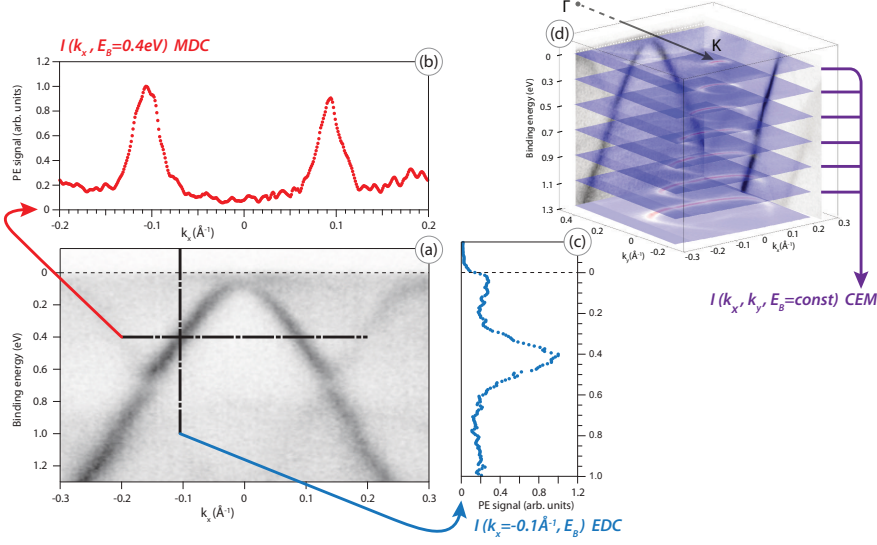


Figure 4.4: Example for a 2-D- k -space dataset of graphene/Ir(111) measured by ARPES at the station at BESSY II using $h\nu = 65 \text{ eV}$. (a) shows a valence spectrum taken by the PHOIBOS analyzer with the angle dispersive axis perpendicular to ΓK . Extracted MDC [$I(k_x, E_B = 0.4 \text{ eV})$] and EDC [$I(E_B, k_x = -0.1 \text{ \AA}^{-1})$] spectra are depicted in (b) and (c). By recording a large number of valence spectra, each at different flip-angle β , yields a dataset $I(k_x, k_y, E_B)$ from which it is possible to extract CEM spectra.

momentum $I(k)_{E_{kin}; h\nu = \text{const}}$ [Fig. 4.4 (b)], whereas EDC spectra display intensities as a function of the kinetic energy of the measured photoelectrons $I(E_{kin})_{k; h\nu = \text{const}}$ [Fig. 4.4 (c)]. From a range of separate MDC spectra for different k -values, it is possible to extract surfaces of constant energy – “constant energy map” (CEM) – $I(\vec{k})_{E_{kin}; h\nu = \text{const}}$. Of special interest are the CEM maps obtained by using different k_{\parallel} values. The implementation of the variation of k_{\parallel} is realized by tilting the sample surface – β -flip – or rotating it around the azimuth – φ . An exemplary illustration can be found in Fig. 4.4 (d) showing a dataset of graphene/Ir(111), measured by ARPES. The image is composed of several single spectra measured near the K-point of graphene, utilizing the β -flip of the sample, to map a certain area of the Brillouin zone. For the case of graphene/Ir(111), as explained in chapter 2, the

distances between the high symmetric points of the Brillouin zone of graphene become important. During experiments at the synchrotron the relevant tilt angles – β – are calculated using equation (3.17). For a photon energy of $h\nu = 65\text{ eV}$ and $\Phi = 4.9\text{ eV}$ [91] one obtains the following values:

$$\begin{aligned}\Gamma - K &= 1.71\text{ \AA}^{-1} \rightarrow \beta_K \approx 25.5^\circ \\ \Gamma - M &= 1.47\text{ \AA}^{-1} \rightarrow \beta_M \approx 21.7^\circ\end{aligned}\tag{4.2}$$

Considering experiments using He-I radiation ($h\nu = 21.21\text{ eV}$) the angular values increase significantly: $\beta_K \approx 55.8^\circ$; $\beta_M \approx 45.3^\circ$.

4.3 Synchrotron radiation

For the description and instrumentation of synchrotron radiation as a spectroscopic tool, I follow in broad outlines references [15, 56, 83, 92, 94–96]. A synchrotron is a circular-accelerator for charged particles, which are in most of the cases electrons. As a example, a schematic layout of the main components of BESSY II is shown in Fig. 4.5. Synchrotron radiation is generated by deflection of electrons traveling near the speed of light ($v/c \approx 1$). The electron beam is bent by a magnetic field which is oriented perpendicular to the beam direction. Undergoing radial acceleration, the electrons dissipate continuous “Bremsstrahlung”, which is called in this special case “Synchrotron Radiation”. In the following, I explain the generation of synchrotron radiation by taking the example of bending-magnet radiation, as described in Fig. 4.5(c). In detail, the electrons in a synchrotron are generated by an electron-gun and pre-accelerated by a racetrack microtron. From this first accelerating stage, the electrons are subsequently guided into the booster synchrotron for final acceleration up to 1.7 GeV by microwave resonators (“cavities”). Finally, the electrons are injected into the storage ring, where they circulate and emit synchrotron radiation at “insertion devices” (IDs) – wigglers and undulators. A certain part of the electrons are lost due to scattering processes, giving rise to an exponential decay of the ring current. This is compensated by replacing the electron-bunches,

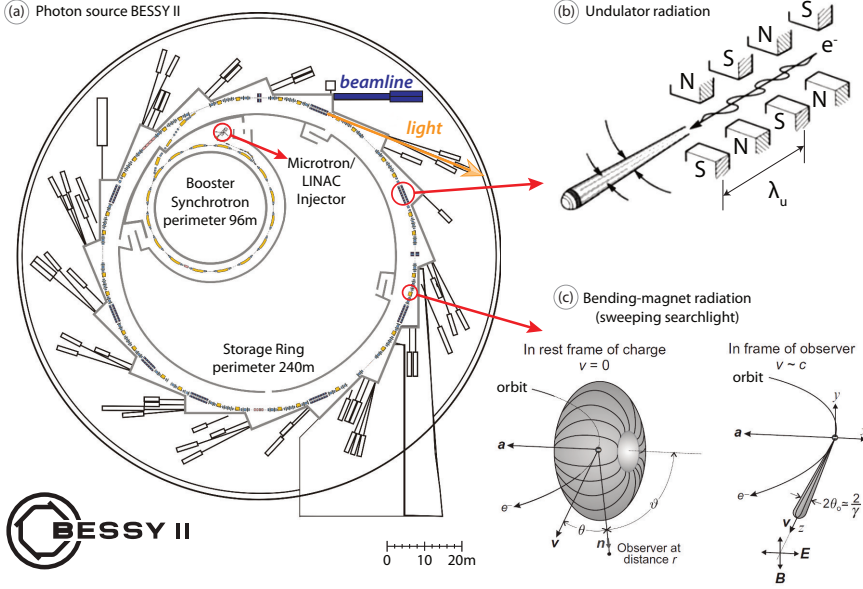


Figure 4.5: Schematic layout of the Synchrotron BESSY II at the Helmholtz Zentrum Berlin. Left side: (a) Top-view of the synchrotron with microtron/LINAC and the booster synchrotron ring situated inside the storage ring. The storage ring contains straight undulator sections alternating with sections for dipole magnets, after [92] Right side: (b) Sketch of an undulator section which consists of several bending magnets, after [83]. c) Synchrotron radiation produced by relativistic electrons which travel on a curved path, after [49].

for example every eight hours (“injection”). While the arc sections in an synchrotron are used for focusing and bending magnets, the straight sections are mainly used for insertion devices, *i. e.* wigglers and undulators. Wigglers and undulators consist of linear arrays of vertically oriented magnets with alternating polarity. The electrons undergo a sinusoidal trajectory in the horizontal plane, for linear polarized radiation which leads to emission of synchrotron radiation. For undulators, small deflection of the electron path in the device leads to overlapping radiation cones, giving rise to coherently accumulating radiation. While the radiation spectrum emitted by wigglers and bending magnets has a rather broad shape, the radiation of undulators is

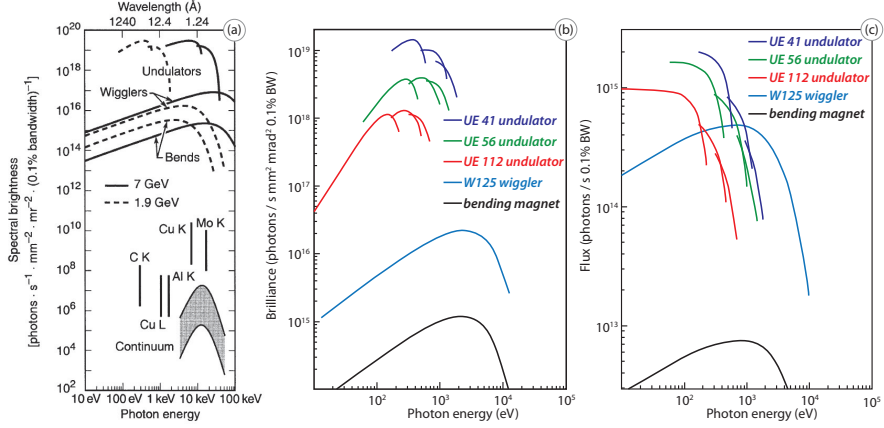


Figure 4.6: Layout of the characteristic parameters of synchrotron radiation sources. (a) Depicted is the key parameter of synchrotron sources – spectral brightness vs. photon energy in comparison to conventional x-ray sources like $\text{AlK}\alpha$ according to [93]. (b) and (c) Comparison of characteristic parameters, with the brilliance being equivalent to the spectral brightness of different devices – bending magnets, wigglers and undulators – for some IDs of BESSY II at the Helmholtz Zentrum Berlin [92], with the used beamline UE56 labeled in green.

sharply peaked for a certain photon energy. In the course of implementation of the BESSY II “top-up operation mode” in 2012 it became mandatory to exchange the racetrack-microtron for a new pre-injector linear particle accelerator (LINAC) [97]. Several advantages came with the new top-up-mode, compared to the conventional decay-mode. In the top-up-mode, electrons are injected to the storage ring within very short time intervals (every 30 to 60 seconds), yielding an almost constant ring current. Hence, a higher and more stable photon flux becomes available. Moreover, the thermal stability of the storage ring and monochromator optical components is improved, resulting in a more stable electron beam orbit and photon beam position at the user end stations [96]. Thus, the whole experimental working process at the end station could be optimized and became more flexible, independent of the former shut-down times during injection every eight hours. Most of the datasets presented in this thesis were measured

in top-up-mode operation. BESSY II belongs to the 3rd generation of synchrotron light sources, which were developed to achieve higher brightness, by using storage rings with many straight sections for insertion devices [98]. This results in low electron beam emittance and high spectral brightness of up to 10^{20} photons /s/mm²/mrad²/0.1 % BW – defined as photon flux per unit source area and per angle into which the light is emitted. This is about 10^{12} times higher than radiation emitted by conventional x-ray tubes, as depicted in Fig. 4.6 (a). A comparison of the key parameter of synchrotron light sources – spectral brightness or brilliance versus photon energy – is depicted for some IDs of BESSY II in Fig. 4.6 (b) and Fig. 4.6 (c). The exceptional high spectral brightness of undulators is also connected to high spatial resolution, since a large number of photons can be focused into a single spot on the sample surface.

4.4 The ARPES station at BESSY II

In the following, I will give a detailed overview of the ARPES set-up in conjunction with the used beamline UE56/2-PGM-1 of the Max Plack Society at BESSY II, based on the description found in Sawhney et al. [99] and Follath and Senf [100]. The layout of the beamline is shown in Fig. 4.7, in top-view (a) and side-view (b). The insertion device UE56/2 of the Sasaki-type [101], which is also called APPLE-type (abbreviation for Advanced Planar Polarized Light Emitter), is built up of two identical modules $U1$ and $U2$ in Fig. 4.7, each of them having a period length of 56 mm and consisting of 31 periods. Using an APPLE-type undulator makes it possible to change the helicity of the synchrotron light, which can be shifted in direction and type of polarization between linear horizontal/vertical and circular left/right. The beamline consisting of two undulators is used here in a mode which allows to treat the emission from the two undulators as one undulator with twice the length. The synchrotron radiation produced by the undulator has a fairly narrow spectral range within a single harmonic, but still too wide for direct use in the experiments. So the photon beam needs to be monochromatized. The beam is focused by a toroidal mirror M1 and subsequently monochromatized by a plane grating

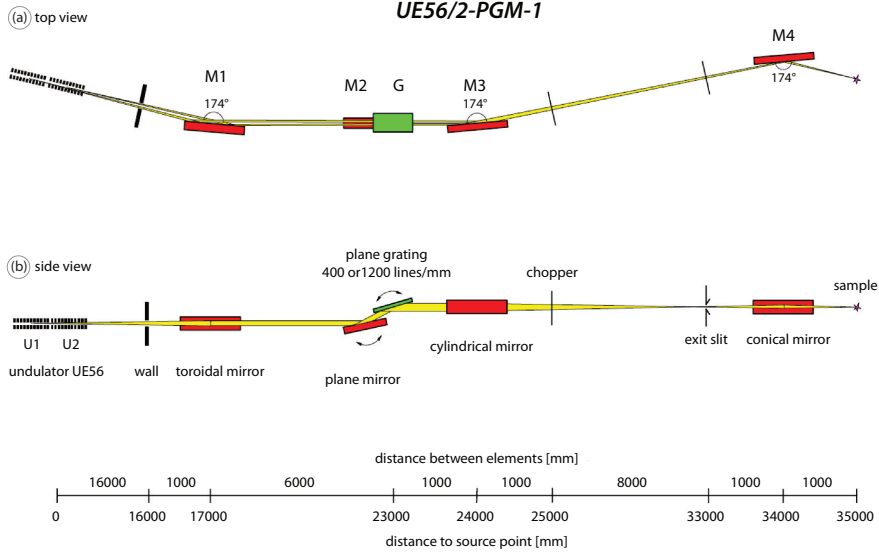


Figure 4.7: Optical layout of the undulator beamline UE56/2-PGM-1. (a) Topview and (b) sideview, the optical path of the photons passing different optical elements, after [99].

(PGM), consisting of a planar mirror and grating, which are rotated against each other to select different wavelengths [100]. In order to obtain information on the performance of the beamline UE56/2-PGM-1, flux measurements with an GaAs-Diode were obtained (Fig. 4.8). For most of the measurements throughout the thesis, the $1200 \frac{1}{\text{mm}}$ grating was used, yielding a maximum flux for photon energies around 120 eV and still acceptable intensities at higher photon energies around the region 600 eV–1000 eV, in contrast to the $400 \frac{1}{\text{mm}}$ grating, which shows a strong decrease of flux for high photon energies. A certain dip in the flux curve around 260 eV–300 eV is visible, resulting from absorption due to carbon contamination of the optical elements of the beamline. Thus, careful reference measurements are necessary if XAS spectra are obtained in the same range, as for the C *K*-edge of systems under study. The schematic layout of the dedicated ARPES endstation mounted at UE56/2-PGM-1 is shown in Fig. 4.9. The set-up is a two-chamber design with a separate main and preparation

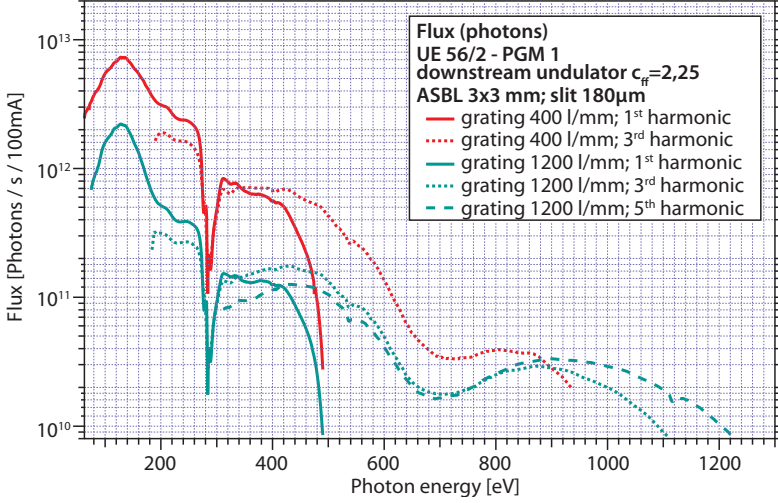


Figure 4.8: Measured flux at beamline UE56/2-PGM-1. The data were recorded by inserting a GaAs-Diode in the optical path in front of the experimental station. Data from Willy Mahler [102].

chamber. The main chamber is made from μ -metal (material with high magnetic permeability) used for magnetic shielding and equipped with a hemispherical analyzer PHOIBOS-100 from SPECS Surface Nano Analysis GmbH, Berlin. The sample is mounted on an stepper-motor controlled 5-axis manipulator with an additional retractable, manually operated axis for sample rotation along the azimuthal axis. Additionally, the manipulator holds a filament for radiative heating of the sample from the back side and a quartz-microbalance to estimate the thickness of deposited thin films. For certain preparation steps *e. g.* , the recovery of the C 1s core level intensity during intercalation of transition metals under graphene/Ir(111), it is desirable to measure the evolution of particular features in real time. Hence, the chamber is equipped with two gate valves for insertion of evaporators in a geometry which allows to use the analyzer for ARPES or XPS during the deposition of thin films. Further components of the main chamber are a mass spectrometer for residual gas analysis and a pinhole/fluorescence screen combination for precise alignment of the whole station with respect to the beamline spot. To evaluate the sample orientation, which

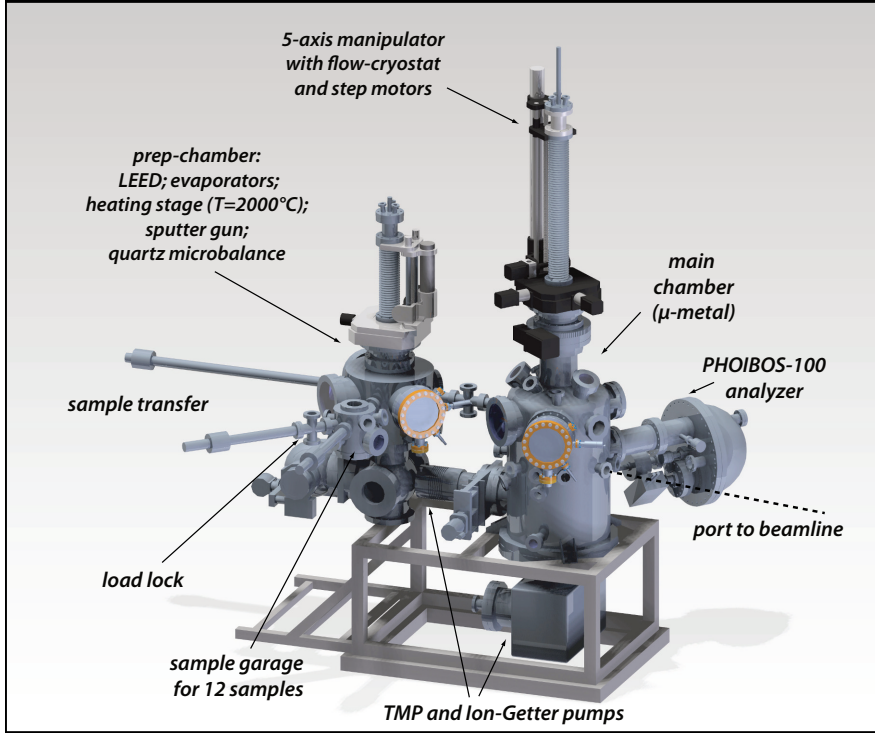


Figure 4.9: Schematic layout of the ARPES endstation at BESSY II with the essential components. The main chamber is equipped with a hemispherical analyzer PHOIBOS-100 from SPECS Surface Nano Analysis GmbH. The sample is mounted on an step-motor controller 5-axis manipulator with an additional retractable axis for sample rotation along the azimuthal axis. A second separate chamber is equipped with several techniques for sample preparation (heating stage, sputter gun, ports for evaporators). Both chambers are equipped with LEED optics to have precise control over separate preparation steps or effects like sample degradation.

becomes important for ARPES measurements, the main chamber is equipped with a LEED optics. A separate preparation chamber is equipped with several techniques for sample treatment. These include an e-beam heating stage, a sputter-gun for sample cleaning, two gate valves for insertion of evaporators, LEED optics and leak valves to feed in partial pressures of different gases, *e. g.* , for propylene cracking

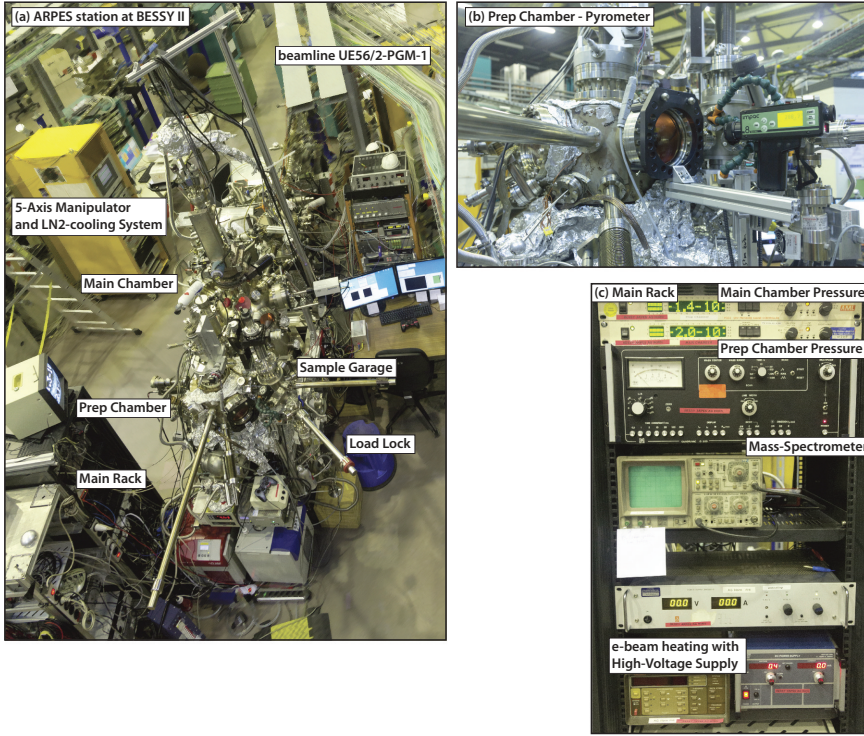


Figure 4.10: Image of the ARPES station at BESSY II mounted at undulator beamline UE56/2-PGM-1. Left side: (a) top-view of the station showing the essential components. Right side: (b) and (c) Preparation chamber with mounted pyrometer for control of annealing temperatures of the sample and main rack with several instruments for vacuum gauges, mass spectrometer and electron beam heating.

or annealing in an oxygen atmosphere. A sample garage for storage of up to 12 samples under UHV conditions and a fast entry load lock for efficient sample exchange complete the set-up of the endstation. An overview of the mounted endstation at beamline UE56/2-PGM-1 is given in Fig. 4.10 (a). A commercial pyrometer of the type *IMPAC IGA 8 pro* [103] is mounted on the preparation-chamber – Fig. 4.10 (b) – and used for measurement of the sample temperatures during annealing and flashing steps of the sample. For simple surveillance of

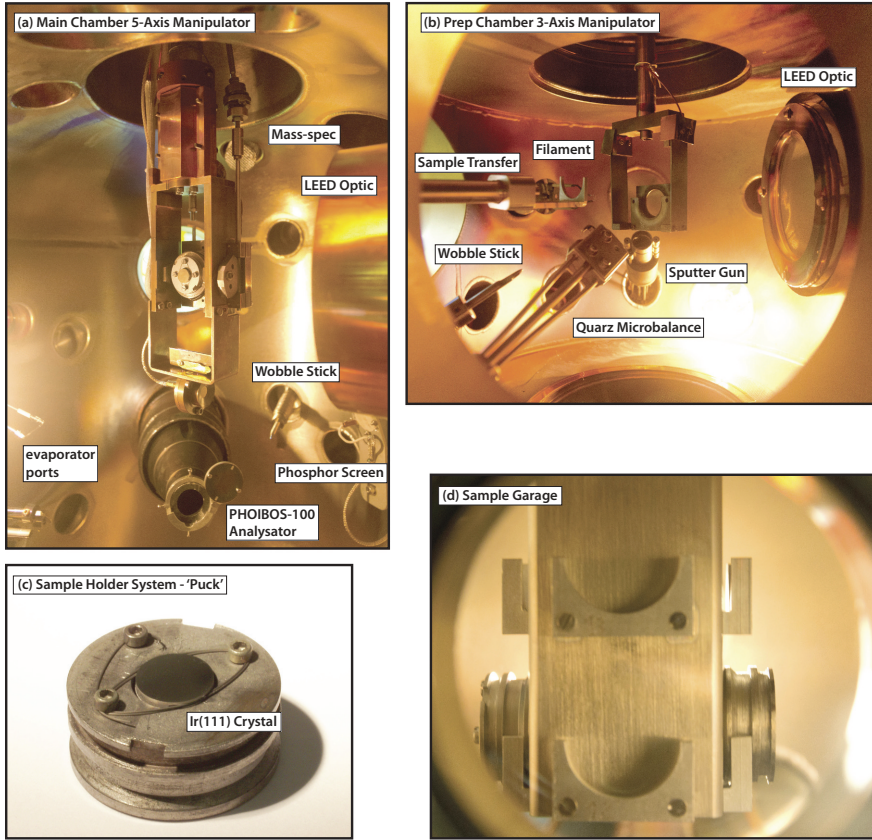


Figure 4.11: Images of the ARPES station at BESSY II showing the interior of the chambers. Left side: (a) Main chamber with PHOIBOS-100 analyzer, 5-axis-manipulator, LEED optic, wobble stick and phosphorous screen for alignment of the station. Right side: (b) Preparation chamber with essential components: high temperature resistant manipulator, filament for e-beam heating, sputter gun, LEED optics, quartz micro-balance and wobble stick. Bottom: (c) Ir(111) single-crystal fixed by tungsten wires on sample holder in “puck” design, made from molybdenum (d) sample holders mounted in the garage.

the vacuum pressure of the separate chambers during the experiment, the controllers of the different vacuum gauges are integrated in one rack – Fig. 4.10 (c), which also accommodates the high-voltage control of the e-beam heating and the controller of the mass-spectrometer.

To obtain a more detailed impression of the layout of the end station, an interior view of the main and preparation chambers is depicted in Fig. 4.11. Shown are in (a) the 5-axis manipulator with the additional retractable, manual operated axis for sample rotation along the azimuthal axis. The arrangement of the components in the preparation chamber is visible in (b). Fig. 4.11 (c) shows the “puck”-design of the sample holder, made from molybdenum to permit high temperature treatment during sample preparation steps. Finally, Fig. 4.11 (d) shows the sample garage, which was constructed in the framework of this thesis, and accommodates up to 12 samples.

4.5 The XMCD/NEXAFS station at MAX-lab II

Based on references Nyholm et al. [104] and Vinogradov [105], I will give a short overview of the principle of operation of the XMCD and NEXAFS station at the D1011 beamline at the MAX II synchrotron in Lund, Sweden. The D1011 beamline is a bending magnet beamline. As described in Fig. 4.5, bending magnets have a lower brilliance than undulator beamlines. On the other hand, less intense radiation per unit area illuminates the optical elements. Absorption on the optical elements due to contaminations, *e. g.* , at the C *K*-edge are thus usually less severe than for undulator beamlines. This can be seen from a comparison of the measured photon flux, given in Fig. 4.13 for the bending magnet beamline D1011 at MAX II, and Fig. 4.8 for the undulator beamline UE56/2-PGM-1 at BESSY II. Thus the bending magnet beamline D1011 is optimally suited for applications where the photon energy is swept during the experiment as in XAS, NEXAFS and XMCD studies. For NEXAFS and XMCD studies it becomes necessary to have precise control over the polarization of the emitted radiation. The type and degree of polarization of the generated synchrotron light is controlled at the D1011 beamline by quadrupole magnets, tilting the beam-orbit inside the magnet.

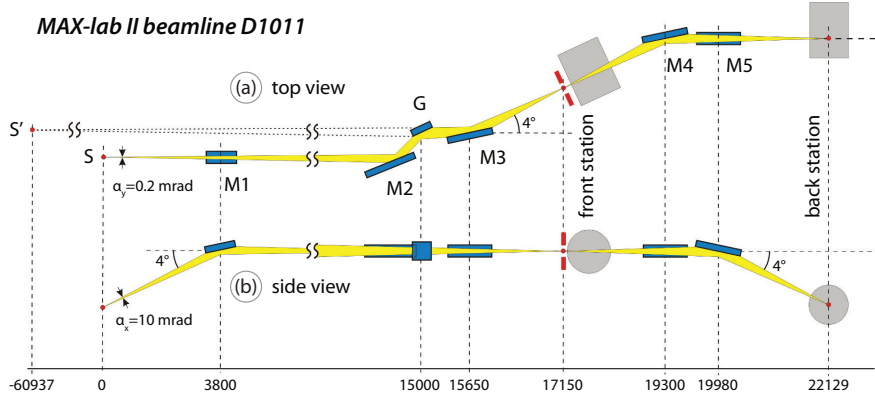


Figure 4.12: Optical layout of the dipole beamline D1011 at MAX II in Lund, Sweden. Shown are in (a) from top view and (b) side view, the optical path of the photons passing different optical elements, M1 – spherical mirror, M2 – rotatable plane mirror, G – plane grating and M3 – vertically focusing plane elliptical mirror, illuminating the sample in the “front station”, after [106]. Additional elements – M4, M5 – vertically and horizontally refocusing spherical mirrors guide the beam into the “back station”.

An overview of the different endstations at beamline D1011 is given in Fig. 4.14 (c). The front station is equipped with a hemispherical analyzer SCIENTA SES-200 for ARPES measurements, a separate MCP detector for partial yield measurements (PEY), LEED optics and mass-spectrometer [Fig. 4.14 (a)]. The separate preparation chamber of the front station is additionally equipped with a permanent magnet, so the sample can be magnetized in the out-of-plane and in-plane directions for measurements in remanence, with a static magnetic field of 500 Oe. The back station is likewise equipped with a separate MCP detector for partial yield measurements and a LEED optics, but lacks a dedicated photoelectron analyzer. On the other hand, the back chamber is equipped with an electromagnetic coil system for the creation of magnetic fields of up to 700 Oe [Fig. 4.14(b)]. Hence, the back chamber is preferentially used for hysteresis measurements of bulk magnetic samples. All preparation techniques described in chapter 4.7 were performed in the same way at MAX II as for samples prepared at the BESSY II station and the new laboratory ARPES station.

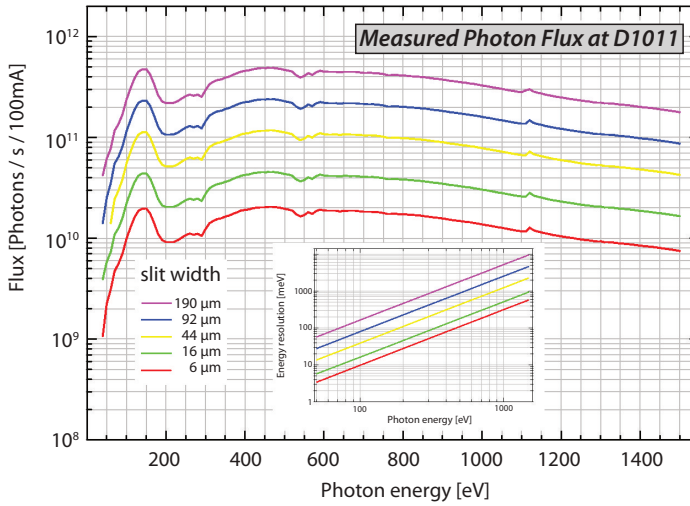


Figure 4.13: Measured flux at beamline D1011 at MAX II, taken from [106]. A slit width of 92 μm was used throughout the measurements. The data show a significantly reduced “dip” in the spectra around 275 – 325 eV, indicating less absorption on optical elements due to contaminations. Thus the beamline is exceptionally well suited for absorption experiments like NEXAFS and XMCD near the C K -edge.

4.6 New laboratory experiment for combined ARPES/XPS

In the following, I will give a detailed description of the new laboratory ARPES station, which was built-up and commissioned in this thesis. The new set-up is a further development of the previous photoemission machine which consisted only of a single UHV chamber, lacked an x-ray source and a dedicated heating stage for high-temperature annealing of metal single crystals. Hence, several improvements were made to optimize the capabilities of the experiment. In order *e. g.*, to prepare experiments for upcoming beamtimes or to test new sample preparation techniques, the construction and installation of a new laboratory photoemission experiment became necessary. Further, experiments with substances like pyridine, which are “problematic” for the usage in

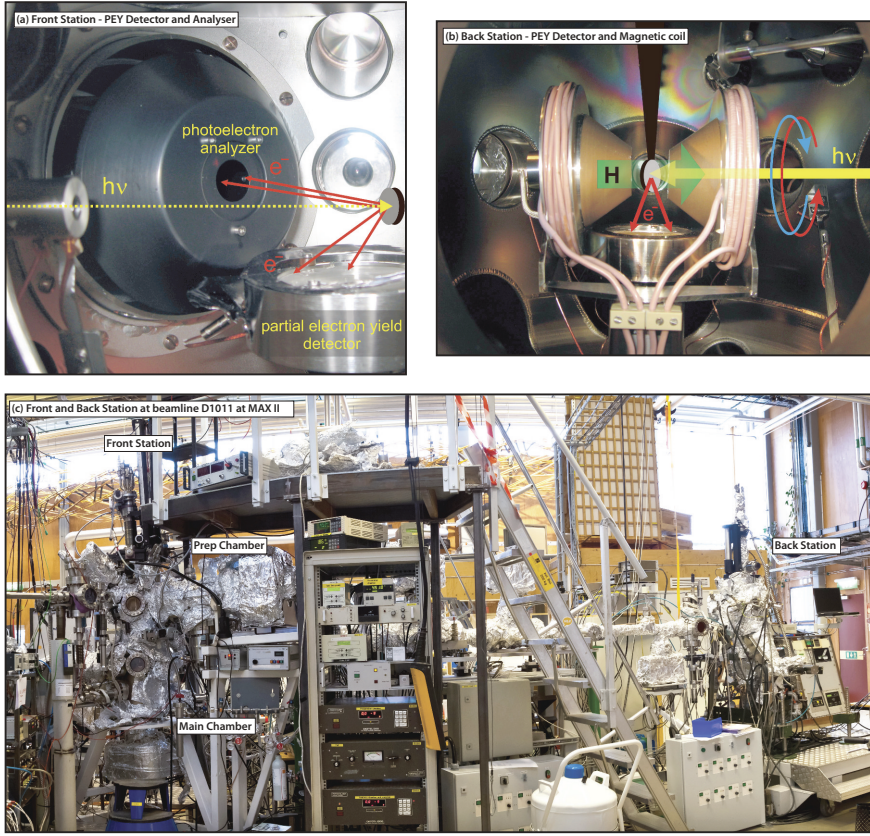


Figure 4.14: Layout of the endstation at the dipole beamline D1011 at MAX II, courtesy of Hirsimäki [107] and MAX IV Laboratory [106]. Shown are in (a) front station with hemispherical analyser SCIENTA-200 and PEY detector; (b) back station with PEY detector and magnetic coil for hysteresis measurements.

UHV systems (sticking on surfaces generates long term degassing), can easier be realized on the laboratory scale. The new machine consists of two separate UHV chambers, with a preparation chamber which can be used for several surface preparation techniques. The main chamber is made from μ -metal, to shield the earths magnetic field. The set-up incorporates a novel 6-axis manipulator design with three translational

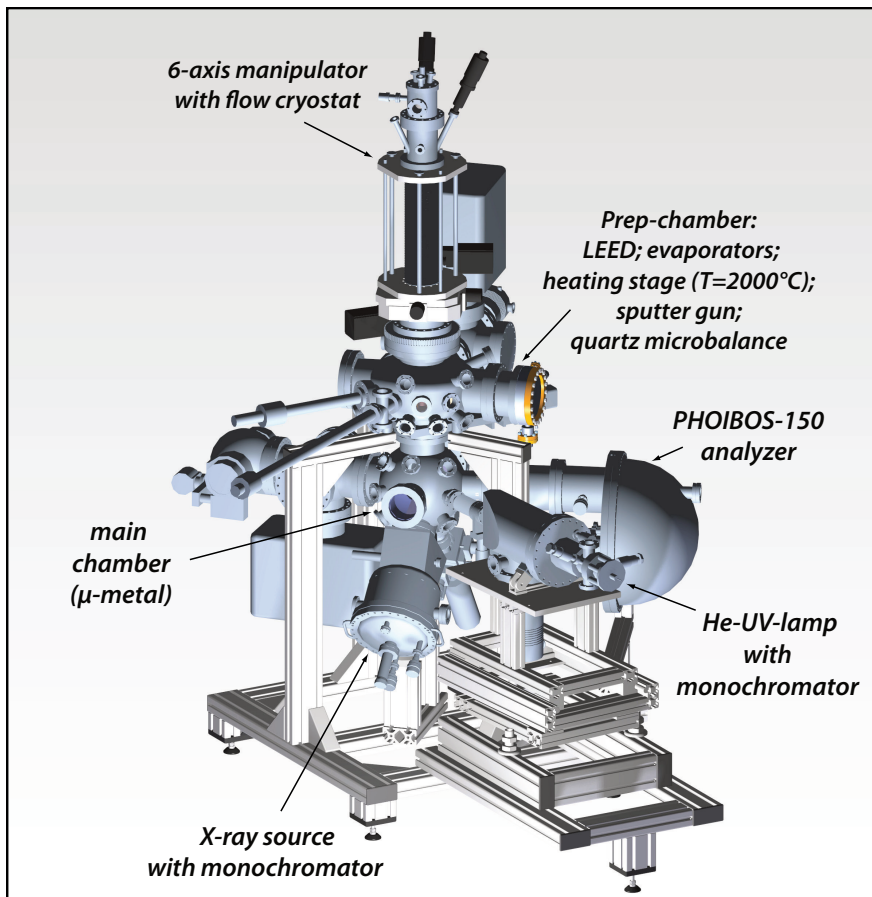


Figure 4.15: Design of the novel laboratory ARPES station. The set-up employs a novel 6-axis manipulator, which has three translational axis (x, y, z) and full control over three rotational axis – ($\vartheta, \beta, \varphi$) – for sample manipulation. The main chamber is made from μ -metal and uses an PHOIBOS-150 hemispherical analyzer from SPECS Surface Nano Analysis GmbH. The separate preparation chamber is used for surface preparation techniques under UHV conditions. A monochromatic x-ray source is used for quantitative sample characterization by XPS, additionally to an monochromatic He lamp, which is used as source for ARPES in the UPS-regime.

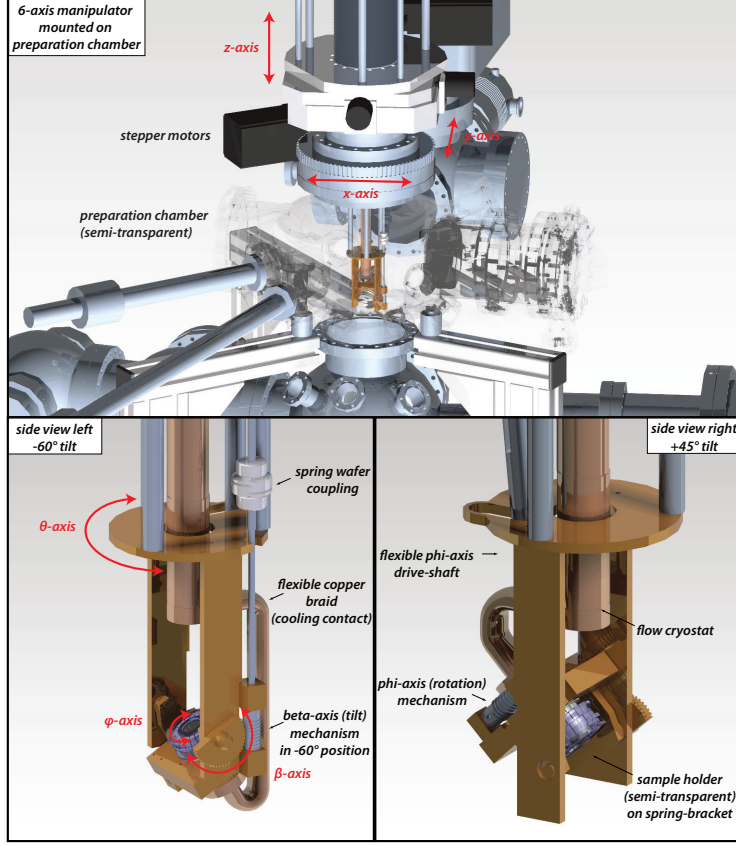


Figure 4.16: Design of the 6-axis manipulator developed within this thesis. Top: Installation of the 6-axis manipulator on the preparation chamber with indication of the three translational axis (x,y,z). Bottom: Design of the manipulator head, indicating the three rotational axis ($\vartheta, \beta, \varphi$). The possible angular range of the β -axis (tilt) is -60° (left side) up to $+45^\circ$ (right side), thus covering a large range for ARPES measurements of the entire Brillouin zone of graphene samples employing He-I as excitation source.

axes – (x,y,z) – and three rotational axes – ($\vartheta, \beta, \varphi$) –, with the β - and φ -axis being actuated by worm drives, integrated in the manipulator head, as shown in Fig. 4.16. The accuracy of the β -axis was verified by an angle-calibration-device shown in Fig. 4.17, with an accuracy

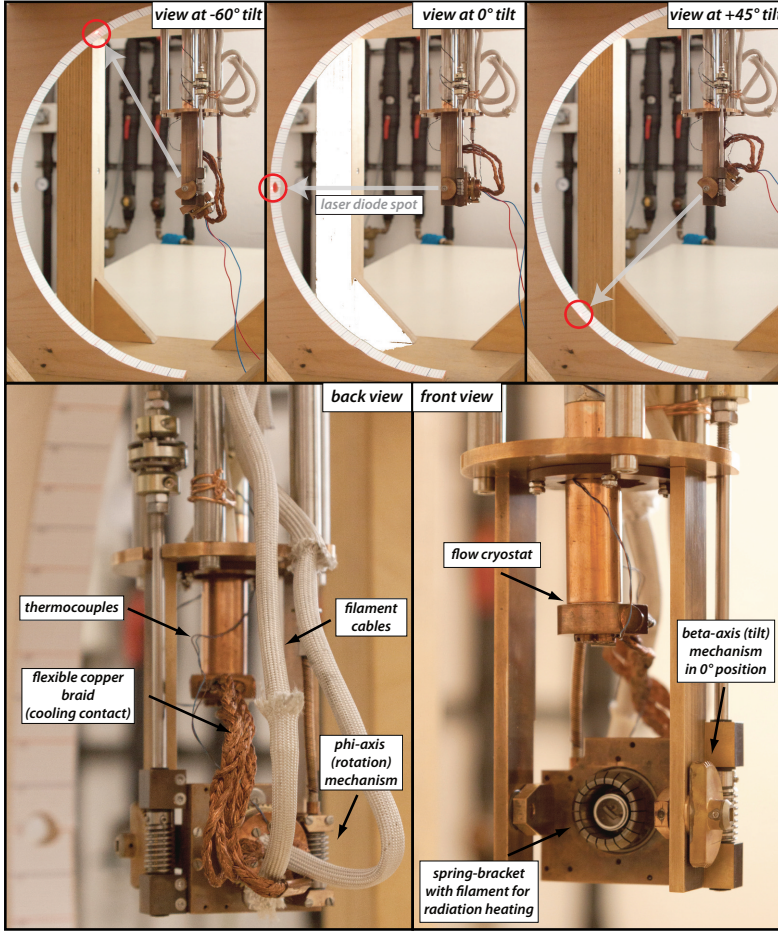


Figure 4.17: Novel design of the 6-axis manipulator. Top: 6-axis manipulator mounted on the angle calibration device for verification of accuracy of the tilt angle (β). Indicated are from left to right the positions -60° , normal and $+45^\circ$. Bottom: Front and back view of the manipulator head with attached filament, thermocouples and copper braids for connection to flow cryostat.

better than 0.1° prior to mounting the manipulator on the chamber. The y-axis of the three translational axis is oriented in such a manner that when the sample is positioned with the surface normal parallel to the direction of the lens system (ϑ = normal emission) in front of the analyzer, the distance between sample normal and the axis of the lens cone (“working distance”) can be varied without changes in orientation of the x-axis. With the new 6-axis manipulator, both tilt and azimuthal scans are possible. Having precise control over the β -axis (tilt), and at the same time the φ -axis (azimuth) by stepper motors is a further advantage compared to manual sample alignment by a wobble stick or transfer rod. The machine has a low energy electron diffraction optics (LEED), a sputter gun, a newly designed dedicated heating stage for temperature up to 2000°C , ports for evaporators and a quartz microbalance. In addition to a monochromatized He-lamp, which is used as source for ARPES in the UPS-regime, a monochromatized x-ray source was installed for the use in the XPS regime. First results obtained on the new experiment are presented in chapters 6.1 and 11.

4.7 Preparation of graphene

The growth of graphene on top of a single crystal Ir(111) surface is accomplished by chemical vapor deposition (CVD). Prior to the growth of graphene, the Ir(111) single crystal is cleaned by repeated cycles of annealing under an oxygen atmosphere ($p_{\text{O}_2} = 1 \times 10^{-6}$ mbar; $T = 1400^\circ\text{C}$) and flashing up to 1800°C for $t = 20$ s. The graphene samples were prepared under ultra high vacuum (UHV) conditions in a separate preparation chamber inside the ARPES experiments, according to the recipe given in detail in [108–110]. Annealing of the Ir(111) crystal and subsequently cracking of propylene molecules C_3H_6 on the heated surface by thermal decomposition happens under the following conditions: $T = 1300^\circ\text{C}$; $p_{\text{C}_3\text{H}_6} = 5 \times 10^{-7}$ mbar; $t = 30$ min, as shown in Fig. 4.18. This procedure leads to single-domain graphene layer on Ir(111) of very high quality which is verified by means of Low Energy Electron Diffraction (LEED) and scanning tunneling microscopy (STM). The preparation of graphene/Ni/W(110) follows standard procedures, described in [42, 51, 111, 112].

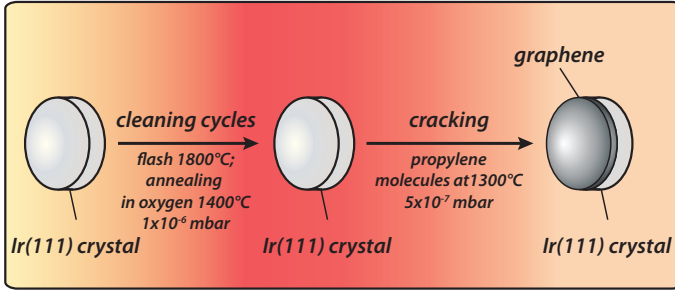


Figure 4.18: The preparation of graphene/Ir(111). The crystal is cleaned beforehand by repeated cycles of annealing under oxygen atmosphere and flashing (middle). The graphene growth is accomplished by cracking of propylene (right).

Prior to sample preparation, the W(110) crystal is cleaned by repeated steps of flashing and annealing in an oxygen atmosphere as described above for Ir(111). However, due to the significantly higher melting point of tungsten ($T_{MP} = 3410^\circ\text{C}$ [113]) other parameters are used: ($p_{\text{O}_2} = 1 \times 10^{-6}$ mbar; $T = 1400^\circ\text{C}$) and flashing up to 2000°C for $t = 15$ s. Subsequently, about 200 \AA of Ni are deposited on W(110). Due to the epitaxial growth of thicker Ni films on W(110) a Ni(111) surface is obtained. After an annealing step, heating the sample to about 400°C for several minutes to remove defects formed during growth, propylene molecules are cracked on the heated sample via thermal decomposition using the following parameters: $T = 500^\circ\text{C}$; $p_{\text{C}_3\text{H}_6} = 1 \times 10^{-6}$ mbar; $t = 30$ min.

4.8 Graphene/Ir(111) – a lattice mismatched system

Graphene/Ir(111) is a lattice-mismatched system. Different lattice constants of C (2.46 \AA) and Ir (2.72 \AA) lead to a lattice mismatch of 9.6% [114]. Therefore a super-structure is formed illustrated by positioning the atoms approximately in a C (10×10)/Ir(9×9) lattice (Fig. 4.19). To obtain a better understanding of the structural prop-

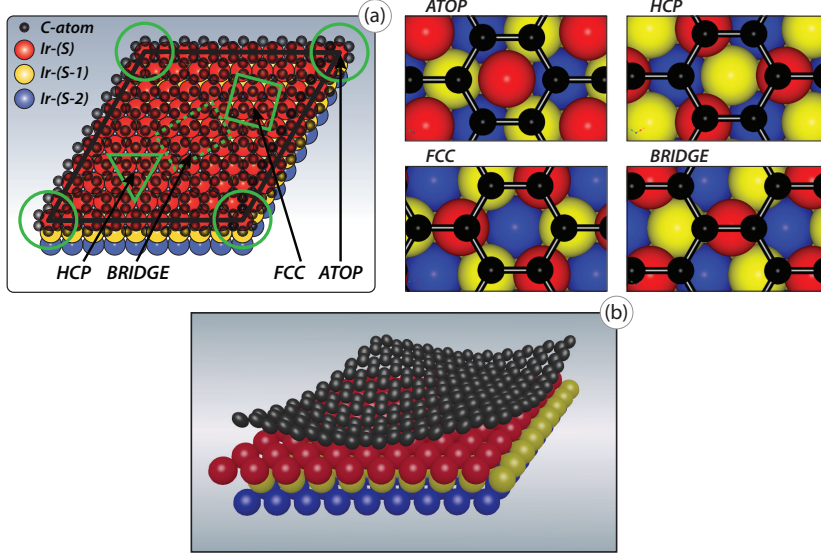


Figure 4.19: (a) Top-view of the graphene/Ir(111) lattice – graphene [black], Ir surface (S) [red] and the underlying Ir layers (S-1) [yellow] and (S-2)[blue] – which form the moiré structure. Different atomic positions – ATOP, FCC-, HCP-hollow and bridge – emerge and are shown enlarged to emphasize the structural arrangement (right). (b) Three dimensional Sketch of the moiré lattice. The vertical corrugation of the carbon atoms is exaggerated to emphasize the different atomic positions discussed above.

erties of graphene/Ir(111) N'Diaye et al. [108, 115] carried out STM and LEED measurements, reporting a incommensurate super-structure resembling a so-called moiré-lattice with a moiré repeat distance of $(25.3 \pm 0.3 \text{ \AA})$ in length, equaling (9.32 ± 0.15) times the Ir nearest neighbor distance. For the arrangement of the graphene sheet on top of Ir(111), different high-symmetry stacking positions can be found. I follow the nomenclature used by Dedkov et al. [116] to describe these positions:

- ATOP (*hcp*–*fcc*) position. A hexagon of carbon atoms surround the metal atom of the top layer (S). Another way to describe this situation is using the positions of the atoms above *hcp*- and *fcc* hollow sites of Ir(111) stacked above the (S-1) and (S-2)

underlying Ir layers (circle in Fig. 4.19 (a)). This nomenclature is used throughout the thesis.

- FCC (*top* – *hcp*) position. A hexagon of carbon atoms surround the *fcc* hollow site of the Ir(111) surface layer (S). Hence, the carbon atoms are positioned above *top* and *hcp* hollow sites of the Ir(111) surface stacked above the (S-1) and (S-2) underlying Ir layers (rhombus in Fig. 4.19 (a)).
- HCP (*top* – *fcc*) position. A hexagon of carbon atoms surround the *hcp* hollow site of the Ir(111) surface layer (S). The carbon atoms are positioned above *top* and *fcc* hollow sites of the Ir(111) surface stacked above the (S-1) and (S-2) underlying Ir layers (triangle in Fig. 4.19 (a)).
- BRIDGE position. This site lies in between the FCC and HCP sites with the carbon atoms being bridged by the Ir atom of the top layer (S) (rectangle in Fig. 4.19 (a)).

Due to the lattice-mismatch of graphene/Ir(111) a buckling of the graphene sheet is observed. This is illustrated in Fig. 4.19 (b) showing a three dimensional sketch of the moiré structure. The vertical corrugation is exaggerated to emphasize the various atomic positions of the carbon atoms of the graphene sheet. The amount of corrugation is determined by STM measurements reported by several authors [108, 110, 116, 117]. However, the obtained values yield slightly different results of $\approx 0.14 - 0.32 \text{ \AA}$ depending to a certain amount on the tunneling conditions as discussed by Dedkov et al. [116]. The authors observe a inversion of the imaging contrast at certain tunneling conditions and assign this partially to the formation of so-called interface states formed between graphene $2p_z$ and Ir $5d_{z^2}$ states. The vertical corrugation of the graphene sheet can also be estimated by using LEED I-V curves [118]. The authors find slightly larger values for the corrugation $\approx 0.42 - 0.56 \text{ \AA}$ as reported by Ref. [116].

4.9 Growth and intercalation of transition metals on graphene

The deposition of thin films of transition metals onto graphene covered Ir(111) is realized in general by physical vapor deposition (PVD), under UHV conditions, as shown schematically in Fig. 4.20. PVD describes the process of thin film deposition by condensation of vaporized material. The technique is also known as molecular beam epitaxy (MBE) ; Cho and Arthur [119] describe the method as preparation and condensation of clean thin films at low deposition rates, leading to epitaxial growth of the material onto a substrate.

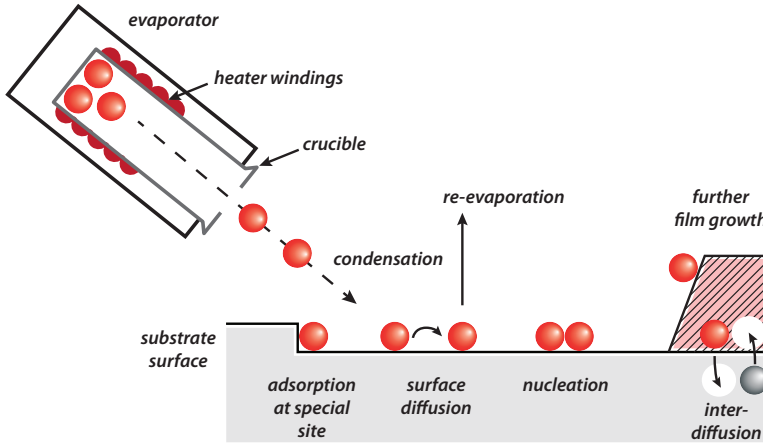


Figure 4.20: Schematics of different mechanisms involved in thin film deposition, taken from [120]. For further description see text.

In order to carefully control the deposition process and minimize degassing of the evaporator, low deposition rates of $0.2 - 0.6 \text{ \AA min}^{-1}$ are used during the experiments. As described in Fig. 4.20, the material is heated inside a crucible until thermal evaporation is reached. The vaporized material beam subsequently hits the surface of the substrate, where different mechanisms related to the deposited atoms are possible: condensation, adsorption, surface diffusion or nucleation towards further film growth. Since the deposited material and the substrate – Ir(111) – are of a different kind, the process is heteroepitaxial, with

different lattice constants of adsorbate and substrate involved, possibly giving rise to a certain degree of lattice mismatch. Depending on the vapor pressure and the associated temperatures during evaporation of the material [121], different types of evaporators are used. For rather low temperatures, as for low melting metals such as manganese (507 °C at 1.3×10^{-8} mbar), ytterbium (520 °C at 1.3×10^{-8} mbar), and copper (727 °C at 1.3×10^{-8} mbar) – values from [113] – Knudsen-type evaporators are used in a configuration of molecular beam effusion cells, and pyrolytic boron nitride is used as crucible. On the other hand, for metals with higher melting temperatures, like Ni (927 °C at 1.3×10^{-8} mbar) and Co (850 °C at 1.3×10^{-8} mbar), an electron beam evaporator becomes mandatory.

In this type of evaporator, the material is heated by electron bombardment inside tantalum or molybdenum crucibles, or directly from a solid rod. In both cases, the evaporators are cooled and thermally stabilized by a water-cooling system, in order to prevent overheating and therefore degassing of the whole evaporator assembly during operation. Either self-built e-beam evaporators, consisting of a crucible with a high-voltage-proof filament beneath it, or commercially available e-beam evaporators (Omicron UHV Evaporator EFM3 [122]) are used. In order to control the deposition rate before the experiment, a quartz microbalance is used in front of the sample. The EFM3 evaporator additionally supports a flux monitor giving a measure for the deposition rate during the experiment. Further, a calibration method described as “overlayer method” [52] is used during the deposition of metal thin films. Here, the photoemission intensity of a substrate core-level I_s is monitored as the thickness t of the overlayer increases.

$$I_s = I_s^0 \cdot \exp\left(\frac{-t}{\lambda_s \cos \vartheta}\right) \quad (4.3)$$

This method can be used to calibrate the deposition rate of the e-beam evaporator in “real-time” by using photoemission. In a sample geometry of electron detection measured normal to the surface ($\vartheta = 0$) this relation simplifies to

$$I_s = I_s^0 \cdot \exp\left(\frac{-t}{\lambda_s}\right) \quad (4.4)$$

with I_s^0 being the photoemission signal from the substrate without the overlayer. For the calibration on clean Ir(111), an inelastic mean free path of $\lambda_s = 6.6$ is used, whereas for graphene covered samples $\lambda_s = 4.6$ is used [123]. Different growth modes as a function of film thickness Θ are possible. These different growth modes are: layer-by-layer growth

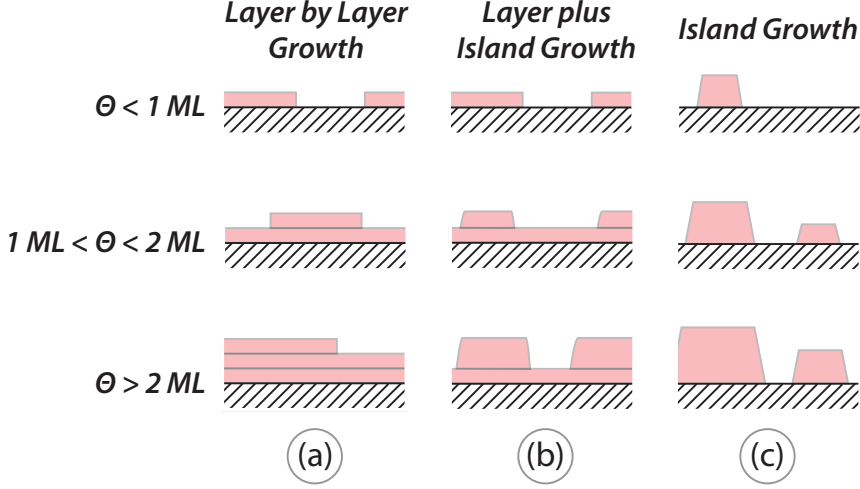


Figure 4.21: Schematics of growth modes for different coverages Θ in monolayers (ML). Shown in (a) is the layer-by-layer growth (Frank-van der Merve). (b) Shows the layer-plus island growth (Stranski-Krastanov). (c) Island growth mode (Vollmer-Weber), taken from [120]

(“Frank-van der Merve”), Fig. 4.21 (a), which describes a process where the formation of a second layer only starts once the growth of the first layer is completed. The reason for this behavior is that the interaction between substrate adatoms is rather strong, but relatively weak considering inter-atomic interactions between the adatoms. The opposite scenario with large interaction between the adatoms leads to the formation of islands on the substrate surface, as shown in Fig. 4.21 (c) “Volmer-Weber” growth. Hence, clusters of adatoms pile up in certain spots without completing a closed layer. The combination of these two growth modes, layer plus island “Stranski-Krastanov” growth, Fig. 4.21 (b), yields a closed first or second overlayer, with subsequent

formation of islands on top. The deposition of various transition metals on top of graphene/Ir(111) leads mostly to the formation of islands (Volmer-Weber growth), following an argument of Sicot et al. [124], who showed by STM measurements that the deposition of Ni adatoms of different thicknesses (0.25 and 1.5 ML) onto graphene/Rh(111) leads to the formation of small size nanoclusters on the graphene film.

In the present study, the Ni adatoms are deposited on the surface, while keeping the sample at temperatures of 110 K, effectively suppressing the surface mobility of the clusters and leading to a random occupation of the different sites of the graphene/Ir(111) supercell. A different scenario is realized by deposition of Ni onto graphene/Rh(111), while the substrate is kept at room temperature. This leads to the formation of large epitaxial triangular-shaped islands, aligned to the Ir substrate, rather than an ordered arrays of clusters [124]. In order to obtain equal initial conditions for the intercalation process of the deposited thin film under graphene/Ir(111), the deposition at low temperature is preferred throughout this thesis. To modify the electronic

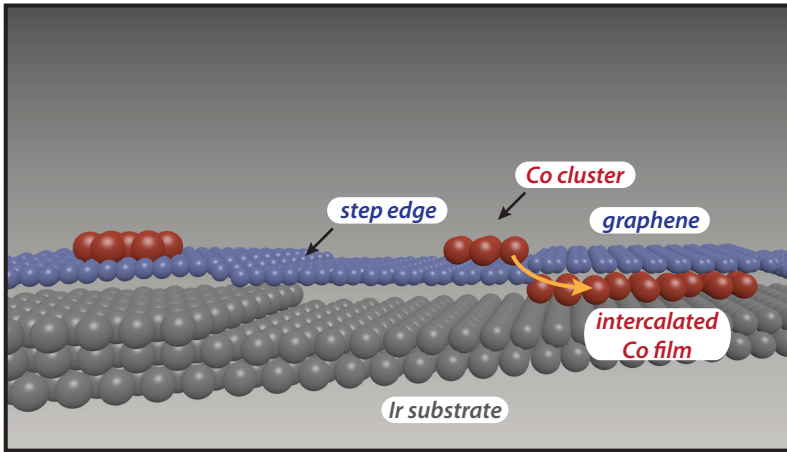


Figure 4.22: Schematics of intercalation of metal thin films under graphene/Ir(111). A possible intercalation path is the penetration of the graphene layer by mobile atom clusters at wrinkles of the graphene film formed *e. g.* at step edges of the underlying substrate.

properties of the graphene film, the deposition of the transition metal thin film is followed by annealing of the sample. The thermal energy thus supplied mobilizes the adatom clusters and a subsequent intercalation of the material with formation of an epitaxial layer underneath the graphene sheet becomes possible. Petrović et al. [125] studied the intercalation of Cs atoms underneath graphene/Ir(111) by LEEM, LEED and STM, proposing that the intercalation of adatoms occurs at wrinkles of the graphene film probably formed at steps edge of the underlying Ir substrate. This behavior is shown schematically for the intercalation of Co atoms underneath graphene/Ir(111) in Fig. 4.22. Adatom clusters of Co are partially still on top of the graphene sheet, whereas other atoms have migrated to a step edge and subsequently intercalate under the graphene film, forming an epitaxial thin film between graphene and the Ir substrate. In order to have a precise control over the rather complex intercalation process, it is instructive to monitor the evolution of the whole process by recording C1s-XPS spectra incrementally, after annealing the sample step by step, in a separate preparation chamber. Another, far better procedure is to intercalate the sample while taking C1s-XPS spectra in “real-time”. The temperature window in which the intercalation occurs can change with respect to the adsorbed atom species: Yb, Ni, Co and Mn intercalate at quite low temperatures of about 300 °C, while for Cu and Mn in the (2×2) phase much higher temperatures of around 550 °C are needed (Table 4.2).

Table 4.2: Overview of the intercalation temperatures T_{int} for the different atomic species used throughout this thesis.

Material	Yb	Mn-trigonal	Ni	Co	Mn- (2×2)	Cu
T_{int} (°C)	250	300	400	400	550	550

Therefore one would like to know exactly when the intercalation process is initiated and when it is finished. Over-annealing of the sample leading to re-evaporation of the deposited atoms, for example and has to be avoided.

By taking C 1s-XPS spectra in “real-time”, a characteristic decrease in the C 1s core level intensity is observed during the deposition of the metal thin film on top of graphene/Ir(111). The following annealing of the sample is performed by a gradual ramp up of the sample temperature. As soon as the temperature is high enough to initiate the intercalation, the C 1s intensity increases, due to the diffusion of the overlying metal film. The carbon atoms of the graphene film are no longer covered by the metal thin film. The annealing procedure is stopped as soon as the intensity in the C 1s core level stabilizes. The formation of an ordered metal thin film underneath the graphene layer is verified by LEED, after the completed intercalation process. For studies on intercalated Cu underneath graphene/Ir(111), as described in chapter 7, the sample was transferred through air and further analyzed in a separate STM experiment.

Data analysis

5.1 Analysis of ARPES data

In this section I describe the approach for the evaluation of the measured ARPES images with graphene/Ir(111) as example dataset. The ARPES images are measured by the PHOIBOS-100/150 electron analyzer, as described in chapter 4.1 and 4.2.

$I_{el}(E_B \text{ (eV)}, \text{angle (pixel)}, \beta \text{ (degree)})$ datasets are obtained by automatically tilting the sample by small increments over an angular range, thus covering a certain area of the Brillouin zone, and contain several hundred raw spectra – $I_{el}(E_B \text{ (eV)}, \text{angle (pixel)})_{\beta=\text{const}}$. Raw images are shown in Fig. 5.1(a) and Fig. 5.1(c), for two different tilt angles β at 20° and 29° . The images of the illuminated MCP are recorded by a CCD camera, with (640×480) pixel resolution. Therefore, the unit of the angular axis is given in (pixel) , as shown in Fig. 5.1. Since the photon energy and the work function are well known, we can relate the kinetic energy of the electrons E_{kin} to their binding energy. This is done by the measurement software internally, relating E_B to the work function of the analyzer and shown in Fig. 5.1 (a) and (c).

$$E_{kin,Det} = h\nu - \Phi_{Det} - |E_B| \quad (5.1)$$

In a further step, the energy scale is shifted to match $E_B = 0$ at the Fermi energy of the metallic sample under study. For insulating samples showing a band gap around E_F , a gold plate positioned under the sample holder is taken for reference. These steps are depicted in Fig. 5.1(d) and Fig. 5.1(f) and further described in the following part. A stepwise description of the data analysis is given below, yielding a 2D-k-space dataset $I_{el}(E_B(\text{eV}), k_x(\text{\AA}^{-1}), k_y(\text{\AA}^{-1}))$.

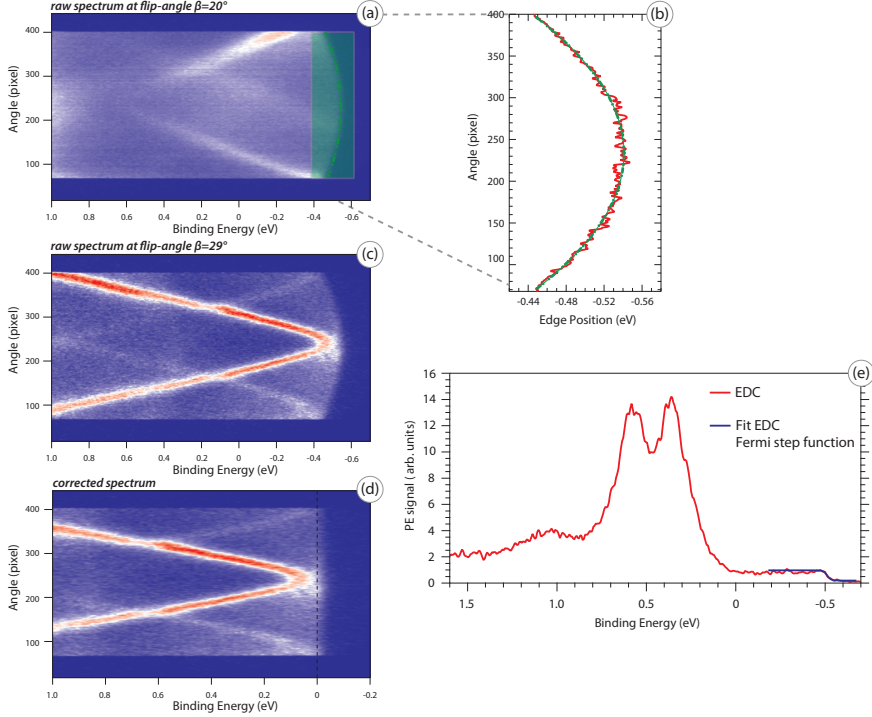


Figure 5.1: Analysis of the ARPES raw data using graphene/Ir(111) for calibration. For further information see text.

First Step: Straight entrance slits are used for ARPES measurements, as discussed in chapter 4.1 (labeled S1 in Fig. 4.2). Hence the electrons bent through the hemispherical shaped analyzer produce a curved image on the MCP detector. The raw datasets obtained in this manner show a curved distortion of the ARPES spectra [Fig. 5.1 (a)

and (c)]. The image of graphene/Ir(111) measured at the tilt angle $\beta = 20^\circ$ (a), is dominated near E_F by featureless Ir bulk contributions, whereas at $\beta = 29^\circ$ (c) it shows contributions of π states near E_F . Hence the image shown in (a) is used in order to correct this distortion. A MDC spectrum is extracted, integrating over homogeneous contributions in a range near the Fermi energy, and is fitted to a third order polynomial [Fig. 5.1 (b)]. This curve is then given as an input in a trapezoidal distortion correction procedure, which corrects the $I_{el}(E_B(\text{eV}), \text{angle}(\text{pixel}))$ spectrum in two single steps along the energy and angle axis, leading to the final spectrum [Fig. 5.1 (d)]. This correction is applied to the complete dataset for all measured tilt angles $\beta(\text{degree})$.

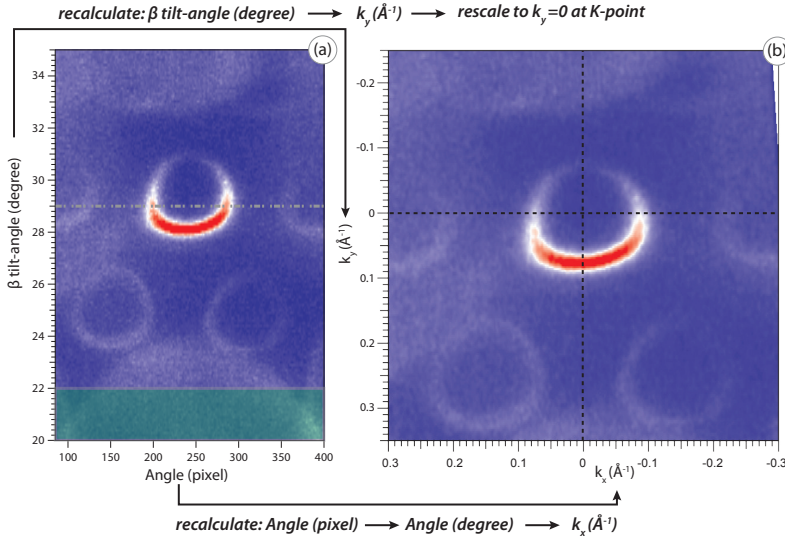


Figure 5.2: Description of the recalculation of the angular scales of the ARPES spectra. The current dataset indicates the Dirac cone of graphene/Ir(111) as example.

Second Step: The scale of the energy axis is related to the work function of the analyzer. It differs slightly from the exact binding energy scale of the sample under study. This deviation is corrected by a constant shift, referring the binding energy E_B of the measured

ARPES spectra, per definition as positive numbers to the Fermi level, as described by Hüfner [52]. In detail, this is done by fitting the extracted EDC spectrum, as shown in Fig. 5.1(e), to a Fermi-step-function. The shifted image is shown in Fig. 5.1(d), accordingly matching the Fermi energy at $E_B = 0$ of the graphene/Ir(111) sample under study. This correction is applied to the whole dataset for all tilt-angles β (degree), using an automated routine.

Third Step: Recalculation of the angular axis from *pixel* to *degree* values, according to the different lens modes of the analyzer, as described in chapter 4.1. In order to compare *e. g.*, datasets obtained using different angular resolved modes, or spectra measured for various photon energies, the spectra are rescaled to reciprocal space (Fig. 5.2(a) and (b)), to k_x/k_y (\AA^{-1})-values using

$$\vec{k}_{\parallel} = \frac{\vec{p}_{\parallel}}{\hbar} = \sqrt{2mE_{kin}} \cdot \sin \vartheta \approx 0.512 \cdot \sqrt{E_{kin}(\text{eV})} \cdot \sin \vartheta \quad (5.2)$$

as described in chapter 3.1.1. The K-point of graphene/Ir(111) is located, according to the geometry of the measurement, at $k_x = 0 \text{ \AA}^{-1}/k_y = 1.71 \text{ \AA}^{-1}$. The k_y -value at the K-point is rescaled to zero, in order to simplify the comparison of different datasets.

5.2 XPS spectra analysis

The shape of x-ray photoemission spectra is affected by inelastic energy loss contributions, nearby peaks and secondary electrons, termed background, as described by Hüfner [52], and outlined in the description of photoemission spectroscopy using the framework of the three-step-model in chapter 3.1.1. In order to extract information from the original spectrum $I(E)$, it becomes helpful to model a background function $T_B(E)$, which is subtracted from the spectrum. The resulting spectrum is called primary spectrum $P(E)$. There are several ways to describe the background signal, depending on the shape of the signal, *e. g.*, by constant, linear or polynomial functions, which yield a better or worse representation of the primary spectrum [52]. A background function using a universal loss function is proposed by Tougaard and Jorgensen [128] for transition metals.

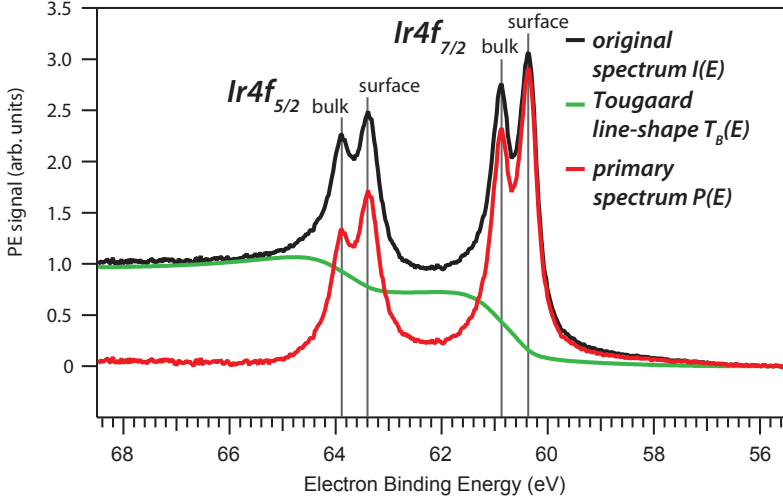


Figure 5.3: Description of the Tougaard background shown for Ir $4f_{5/2}$ and Ir $4f_{7/2}$ spectra of graphene/Ir(111) measured at the BESSY ARPES station, with $h\nu = 120$ eV radiation. Both core level lines have components originating from inside the bulk and from the surface [126, 127].

The Tougaard background model [128–131] is used in the framework of a four parameter inelastic electron scattering cross section [132] as described in the following.

$$T_B(E) = \lambda(E) \int_E^{\infty} K(E, T) M(E') dE' \quad (5.3)$$

and

$$\lambda(E) K(E, T) = \frac{BT}{(C + C'T^2)^2 + DT^2} \quad (5.4)$$

with λ being the inelastic mean free path and E the kinetic energy of the electrons. B , C , C' and D are parameters described elsewhere [129, 132]. The parameters are optimized to the spectrum such that the primary spectrum vanishes at about 10 eV above the main line. $T = E - E'$ is the energy loss and $K(E, T)$ the probability for electrons with energy E of losing energy T during the traveled path through the solid. The

resulting $\lambda(E)K(E, T)$ is called the inelastic electron scattering cross section. The primary spectrum is thus obtained as:

$$P(E) = I(E) - T_B(E) \quad (5.5)$$

As pointed out by Hüfner [52], it is essential to record data points in a energy window large enough before and after the region of interest, to match the shape of the background properly to the original spectrum $I(E)$. As shown in Fig. 5.3, the inelastic signal in the spectrum is well described by the background function using the Tougaard model. In order to quantitatively analyze the positions of the prominent peaks in the extracted primary spectrum, the peaks are fitted using line shapes of Voigt- and Doniach-Sunjić-profiles [133]. The software Igor Pro uses the Levenberg-Marquardt nonlinear least squares optimization [134] for peak fitting.

5.3 NEXAFS and XMCD analysis

The method for the evaluation of NEXAFS data is essential for a detailed analysis of XMCD spectra as described in chapter 8.2. In order to correct the primary NEXAFS spectra – $I_{sample}(h\nu)$ – for contributions due to the x-ray optics of the beamline, background contributions from the substrate, intensity variations due to instabilities of the electron beam in the storage ring *etc.*, it is mandatory to normalize the spectra as described in detail by Stöhr [136] and Schöll et al. [137]. There are various ways to normalize the spectra, *e. g.* by using a photodiode inside the chamber as reference $I_{Diode}(h\nu)$, the photon flux curve of the beamline $I_0(h\nu)$ [102] before or by measuring additional spectra of the clean substrate $I_{substrate}(h\nu)$, directly after the actual NEXAFS spectrum of the sample in question is obtained.

For NEXAFS spectra measured at the ARPES station at BESSY II, this is illustrated for the clean substrate as reference in Fig. 5.4, indicating the primary NEXAFS spectrum of graphene/Ir(111) in Fig. 5.4(a). The additional spectrum, shown in Fig. 5.4(b), is taken directly afterwards for the clean Ir(111) substrate.

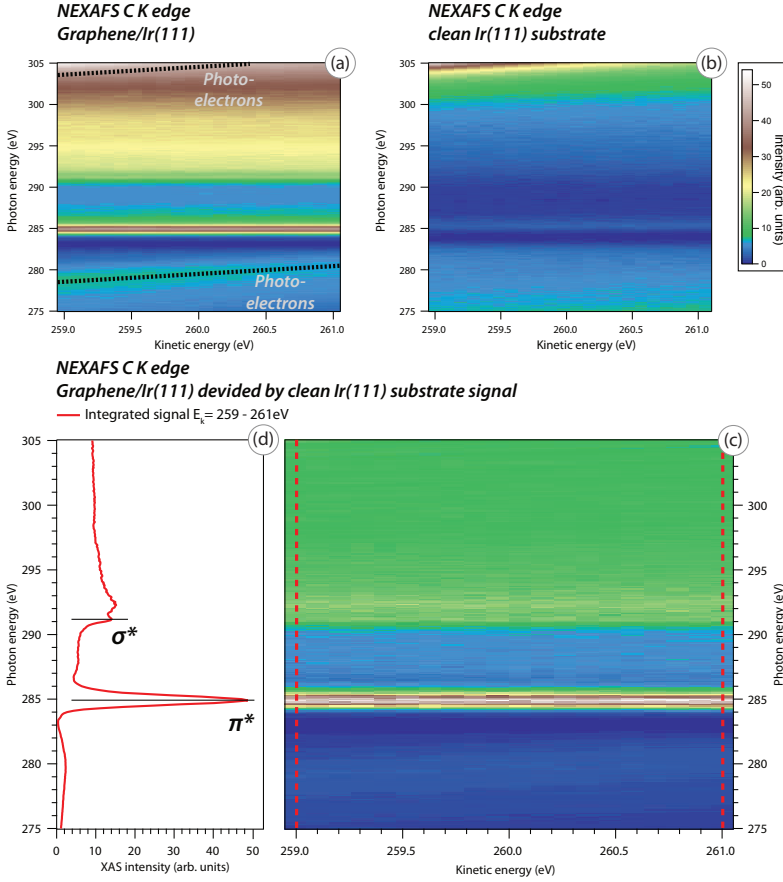


Figure 5.4: Analysis of NEXAFS spectra measured at the ARPES station at BESSY II. (a) Measured CK-edge spectra for graphene/Ir(111). (b) CK-edge spectra for the clean substrate Ir(111) as reference. Weak signals of photoelectrons, linearly dispersing with kinetic energy are visible. (c) By forming the quotient of the two spectra, a spectrum is obtained with contributions from the π^* and σ^* unoccupied states. (d) The integrated spectrum, obtained in the Auger yield mode, compares well to NEXAFS data of graphene/SiO₂ by Pacilé et al. [135].

For the corrected spectrum the following equation is used, according to Schöll et al. [137],

$$I(h\nu) = c \cdot \left[\frac{I_{sample}(h\nu)}{I_{substrate}(h\nu)} - f \right] \quad (5.6)$$

with $I(h\nu)$ the normalized spectrum, f being an attenuation factor which is treated as a free parameter, and c as a prefactor. As described in detail in chapter 3.2.3, XMCD spectra are obtained in two equivalent ways: on the one hand, by changing the direction of the photon spin and the associated angular momentum for a fixed magnetization of the sample. It is equally possible to use a fixed helicity of the photons and switch the magnetization of the sample [83]. In order to understand the magnetic coupling of a specific graphene/ferromagnet sample, spectra of the metal $L_{2,3}$ -edges and carbon K -edge are evaluated. This yields either parallel or anti-parallel magnetic order if the XMCD spectra show the same, or opposite signs. Utilizing XMCD, for example at the Co $L_{2,3}$ and C K edges it is possible to gain quantitative insight into the magnetic behavior of the graphene/Co/Ir(111) system as described in detail in chapter 8.2.

The NEXAFS intensity as raw spectra at the Co $L_{2,3}$ edge were taken with right and left [I^+ and I^- , (red) and (blue) in Fig. 5.5 (a)], circularly polarized light, respectively. The raw spectra are normalized as described by equation (5.6) to the reference spectrum of the clean Ir(111) sample. Due to low signal strength at the Co $L_{2,3}$ -edge for the clean substrate, the Co L spectra in Fig. 5.5 (a) are normalized to the reference spectrum of the photodiode, whereas the C K spectra are referenced to clean Ir(111). As described by Chen et al. [138] the spectra need to be further normalized to the edge jump by subtraction of a double-Fermi-step function taken at the center of the L_3 and L_2 edges [Fig. 5.5 (b)], indicated as gray line.

In order to evaluate magnetic moments using the sum rules, the integral $A_3 + A_2$, shown as black curve in Fig. 5.5 (b) is evaluated by integrating the averaged NEXAFS intensity $\frac{(I^+ + I^-)}{2}$, over the whole range of photon energy in the spectrum. The indices 2,3 indicate the ranges of photon energy of the Co $L_{2,3}$ edge. The XMCD spectrum [black line in the lower part of Fig. 5.5 (c)] is obtained by calculating

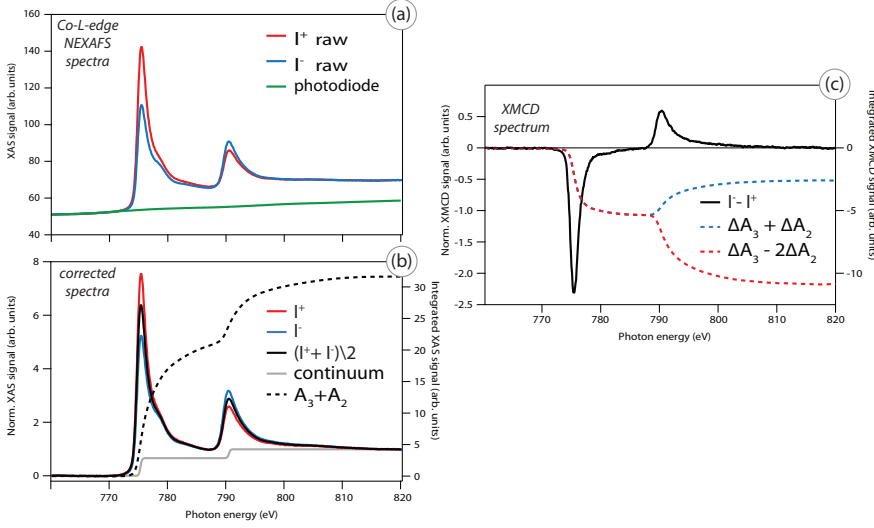


Figure 5.5: (a) NEXAFS raw spectra measured at the Co $L_{2,3}$ absorption edge for the graphene/Co/Ir(111) system. The traces show the absorption spectra measured with circularly polarized light for two opposite directions [red and blue]. As reference spectra for normalization, the clean Ir(111) substrate or photodiode measurements are used [green]. (b) show the corrected NEXAFS spectra at the Co $L_{2,3}$ absorption edge. Shown is also the edge jump, which is corrected by subtraction of a double-Fermi-step function [gray] and the averaged NEXAFS intensity $\frac{(I^+ + I^-)}{2}$ [black]. (c) show the recorded XMCD spectra, and additional integrated spectra [dashed lines].

the difference $\Delta I = I^- - I^+$, leading to a negative result at the Co L_3 edge. The integrals $\Delta A_3 + \Delta A_2$ and $\Delta A_3 - 2\Delta A_2$ are formed by integrating the XMCD signal over the range of photon energies in the spectrum. To extract quantitative values for the magnetic moment from of the XMCD spectra, sum rules, as described in detail in chapter 3.2.3, according to Carra et al. [84] and Thole et al. [85] are used.

$$M_L = -\frac{2}{3} \frac{n_h \mu_B}{P_{circ} \cos \phi} \frac{\Delta A_3 + \Delta A_2}{A_3 + A_2} \quad (5.7)$$

$$M_S = -\frac{n_h \mu_B}{P_{circ} \cos \phi} \frac{\Delta A_3 - 2\Delta A_2}{A_3 + A_2} \quad (5.8)$$

with P_{circ} the degree of circular polarization of the incoming photons. The angle ϕ is defined by the geometry of the experiment, with the direction between the photon angular momentum and the magnetic moment. For geometries where the magnetization of the sample and the \vec{k} vector of the incident photons are collinear, as for out-of-plane measurements, the factor $\cos \phi$ yields unity. The number of holes is given by n_h . Finally, the ratio of the orbital and spin moment – $R_{L,S} = \frac{M_L}{M_S}$ – can be derived, which does not require magnetic saturation of the sample.

A error bar of 10 % for the orbital moment and 20 % for the spin moment is usually assumed [75, 139], due to several theoretical approximations used in the sum rules (dipol approximation, neglecting electron – hole interactions in final states [140], assuming final states as pure d states). At K edges, spin polarization is not possible, due to zero orbital moment in the initial states ($1s \rightarrow 2p$). Hence employing sum rules for K edge absorption, one can only derive values for orbital moments, as shown by Huang et al. [87].

$$M_L = -\frac{1}{3} \frac{n_h \mu_B}{P_{circ} \cos \phi} \frac{\Delta A}{A} \quad (5.9)$$

Experimental investigations of graphene/Ir(111)

In this chapter I will present the results obtained on the system graphene/Ir(111), which is used as a starting point for further modifications of graphene by intercalation of magnetic and non-magnetic metals. All spectroscopic data are obtained either at the laboratory ARPES station, at the ARPES station at BESSY II synchrotron (beamline UE56/2-PGM-1/2) and at the front station at beamline D1011 at the MAX II synchrotron.

6.1 First studies at the new laboratory ARPES station

Using XPS in combination with ARPES is exceptionally useful *e.g.* , for the preparation of graphene/metal samples, since it becomes possible not only to obtain access to the band structure and the related electronic properties of the system, but also to gain quantitative insight into the chemical composition of the system under study. After my successful completion of the new laboratory station, commissioning was necessary to check that all components work properly. Further, it is essential to evaluate the energy and k-space resolution in the

spectra ($\Delta E, \Delta k$) measured by the PHOIBOS-150 analyzer. In order to validate this, I use the system graphene/Ir(111) as reference. On the one hand, graphene's linearly dispersing π -band around the K-point is well suited for the evaluation of the mode of operation of the analyzer in conjunction with the β -flip and φ -rotation of the manipulator. On the other hand, the core level lines of graphene/Ir(111), especially when probed with x-rays of higher energy (in this case $h\nu = 1486.7 \text{ eV} - \text{Al } K_\alpha$), are nearly unaffected by graphene coverage and similar to the Ir(111) system [141].

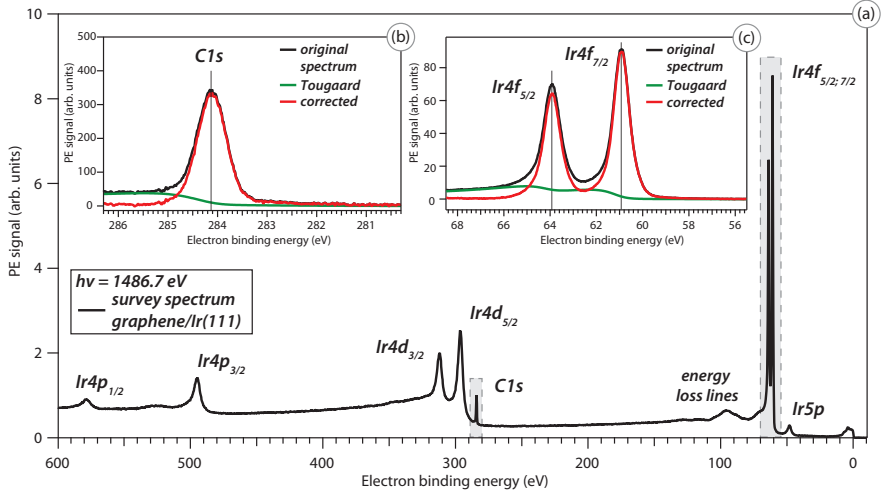


Figure 6.1: XPS spectra of graphene/Ir(111) measured by a monochromatic x-ray source at the laboratory ARPES station with the sample kept at room temperature. (a) XPS survey spectra, using the Al K_α anode with excitation energy $h\nu = 1486.7 \text{ eV}$ and $E_{pass} = 20 \text{ eV}$. Apparent are the characteristic Ir 5p, 4f, 4d and 4p core level lines from the Ir bulk and the related (plasmonic) energy loss lines situated at about 30 eV higher values compared to the respective core level, in agreement with [142]. Additionally, the C 1s core level of the overlaying graphene sheet is clearly distinguishable. (b) and (c) Detail spectra of the C 1s core level and the spin-doublet Ir 4f_{5/2,7/2} obtained at $E_{pass} = 5 \text{ eV}$.

A main reason for this observation is the fact that the interaction between graphene and Ir(111) is quite weak, thus resulting in negligible

modifications of the electronic properties caused by charge transfer or hybridization. Core level spectra of graphene/Ir(111) are shown in Fig. 6.1. For comparison, the data are always obtained in the same geometry: $\vartheta = 20^\circ$ – off normal emission. The analyzer is set to high magnification lens mode, (HM mode) as described in table 4.1 in chapter 4.1, to measure spatially resolved XPS spectra. It is instructive to collect “survey spectra” with coarse energy resolution (in this case $\Delta E \approx 400$ meV) by choosing a large pass energy and large step size (250 meV), if an unknown sample is investigated or specific contaminations are suspected.

Shown in fig. 6.1(a) is the survey spectrum of graphene/Ir(111) for the range 600 – 0 eV binding energy with the characteristic Ir 5*p*, Ir 4*f*, Ir 4*d* and Ir 4*p* core level lines, stemming from the Ir bulk and additionally the C 1*s* core level of the overlying graphene sheet. Also visible is the gradually increasing contribution from inelastically scattered electrons leading to an enhanced signal for larger binding energies. To gain detailed information about the structure of the core level lines and to assign precise peak locations it is instructive to collect “detail scans” with enhanced energy resolution (in this case $\Delta E \approx 100$ meV) by choosing a lower pass energy and small step-size (20 meV), as shown in Fig. 6.1(b) and (c) for the C 1*s* and Ir 4*f*_{7/2} core level lines.

To extract information from the detail scans in Fig. 6.1 (b) and (c), a lineshape analysis is applied. A secondary electron background of Tougaard shape [52, 128, 130], as described in chapter 5, is assumed. The C 1*s* spectra of graphene/Ir(111) is evaluated using a single Voigt profile [144] yielding a peak position of 284.110(3) eV and a FWHM of 680 meV, in agreement with Lacovig et al. [141]. A value of 3σ is taken for the error bar resulting in a negligible deviation from the peak positions. For the Ir 4*f*_{5/2,7/2} core levels I extract line positions of 63.91 eV and 60.91 eV by using Doniach-Sunjic-profiles [133], with FWHM of 820 meV and 850 meV, respectively, in agreement with Moulder et al. [142]. Valence band spectra of graphene/Ir(111) are measured by using monochromatic He-I ($h\nu = 21.21$ eV) radiation and the LAD mode (table 4.1), to capture a specific region around the K-point of graphene. The following geometry is used: $\vartheta = \text{normal emission}$; variation of $\beta = 40 - 60^\circ$; $\Delta\beta = 0.4^\circ$.

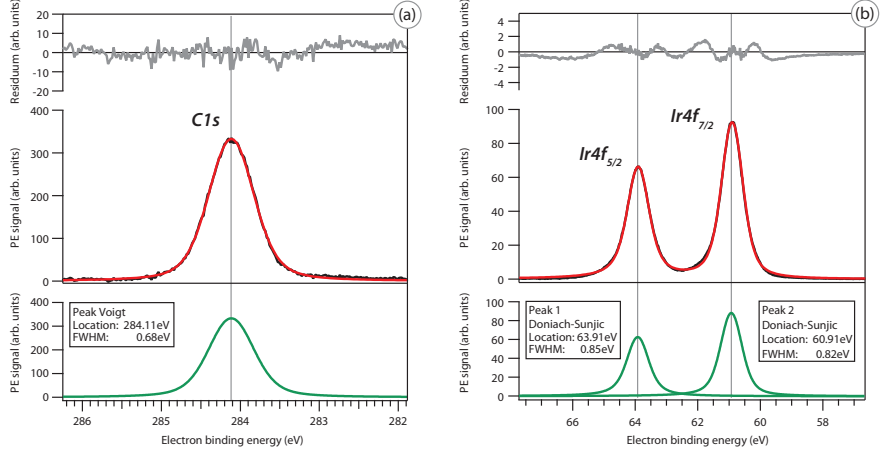


Figure 6.2: Detailed analysis of certain prominent core level spectra of graphene/Ir(111). (a) and (b) Lineshape analysis of the spectra reveals the position of the C 1s core level at 284.11 eV and the spin-doublet Ir $4f_{5/2,7/2}$ core level at 63.91 eV and 60.91 eV in agreement with [141–143].

In order to extract detailed information on the shape of the band structure and to examine the energy resolution of the setup, it is desirable to reduce the thermal broadening affecting the spectra, by measuring at low sample temperatures of $T \approx 135$ K achieved by liquid nitrogen cooling. Energy resolution measurements are normally done on systems like evaporated polycrystalline gold films. Since not only information on the energy resolution (ΔE) needs to be obtained but also on the k-space resolution (Δk_x ; Δk_y), graphene/Ir(111) exhibiting sharp π states near E_F is used as benchmark sample.

An overview of the spectroscopic data in 2D-k-space is shown in Fig. 6.3. The Dirac cone is observed at the K point (Fig. 6.3 (a)), derived by evaluating constant energy maps at $E_B = 0.3$ eV. The shape is circular along the $\Gamma - K$ -direction but slightly asymmetric in the intensity distribution, leading to a rotated “dark corridor”. This is in agreement with ARPES measurements on graphene at comparatively low photon energies. Gierz et al. [145] also observed a slightly rotated Dirac cone by using linear horizontal radiation of $h\nu = 35$ eV. This behavior is compared to spectra taken with higher photon energies

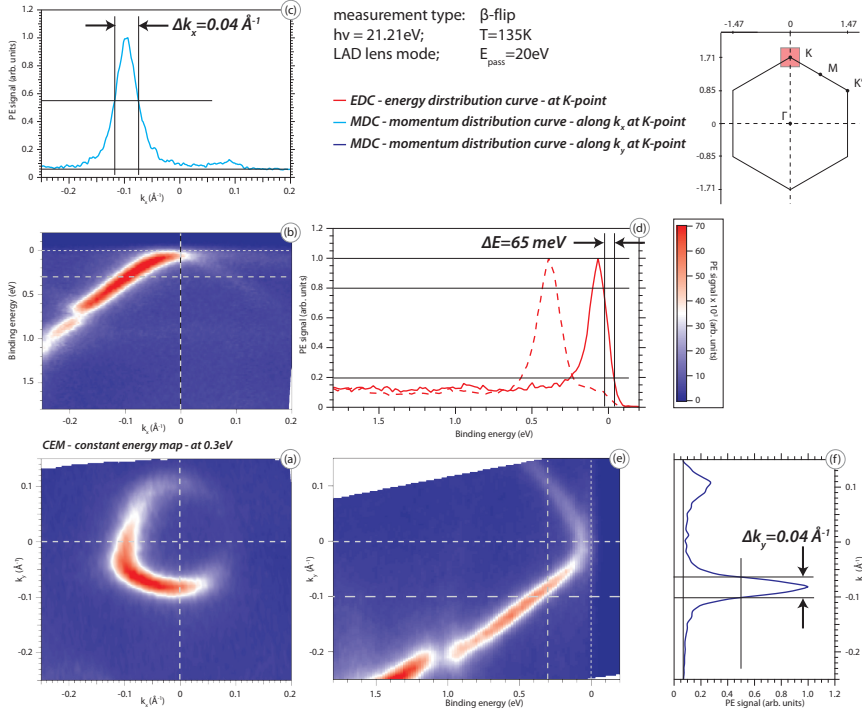


Figure 6.3: 2D-k-space ARPES data from graphene/Ir(111) measured by employing the β -flip-axis at the new laboratory ARPES-station, using He-I radiation. (a) Constant energy map extracted at energies of 0.3 eV below the Fermi level. (b) and (e) Valence band spectra at the K-point along the k_x and k_y directions in k-space, with main contributions from the π -band of graphene. (d) EDC at the K-point, and at $k_y = -0.1 \text{ \AA}^{-1}$, indicating a experimental resolution of about 65 meV, measured at a sample temperature of about 135 K. (c) and (f) MDC spectra extracted at the K-point. The according FWHM of the π -band yields an experimental k-space resolution of about $\Delta k_x = 0.04 \text{ \AA}^{-1}$, $\Delta k_y = 0.04 \text{ \AA}^{-1}$, which could be smaller because of the lifetime broadening in the band.

($h\nu = 65 \text{ eV}$) at BESSY II where no rotation of the dark corridor is observed. As described in chapter 4.2 it is instructive to use lines of constant momentum – EDC’s – at the K-point in order to extract more detailed information on the occupied states. Since the underlying substrate – Ir – is metallic it is possible to use the width of the Fermi

edge as evidence for the overall energy resolution of the setup, is determined by the width of the first derivative (FMHM) of the EDC at the Fermi edge, or assuming the FWHM from the width of the spectra at 20 % – 80 % peak intensity. In order to verify that the intense signal of the π -band does not interfere with the width of the background signal at E_F , an additional EDC at -0.1 \AA is evaluated, giving the same result of $\Delta E = 65 \text{ meV}$.

$$\Delta E = \sqrt{(\Delta E_A)^2 + (3.5k_B T)^2 + (VUV)^2} \quad (6.1)$$

According to equation (6.1) the total energy resolution ΔE of the setup is derived by the convolution of single FWHM's of Gaussian linewidth from the partial terms in energy resolution ΔE_A of the electron analyzer, $3.5k_B T$ the thermal broadening and VUV intrinsic contributions from the excitation source [61, 146]. From the total energy resolution of $\Delta E = 65 \text{ meV}$ and temperature measurements using a thermocouple at the back of the sample holder, one can conclude that the thermal broadening amounts to 42 meV and the partial energy resolution of the hemispherical analyzer to $\Delta E_A = 50 \text{ meV}$. The value for ΔE_A is slightly larger than values approximating the theoretical energy resolution of hemispherical energy analyzers described by equation (4.1) [90]. Contributions in the broadening of the lineshape due to the helium gas discharge lamp are of the order of 2 meV [146] and are therefore negligible. For the k-space resolution, values of $\Delta k_x = 0.04 \text{ \AA}^{-1}$, $\Delta k_y = 0.04 \text{ \AA}^{-1}$ can be extracted from Fig. 6.3 (c) and (f). In order to classify these values we compare them with benchmark-spectra of quasi free-standing monolayer graphene (QFMLG) which were measured at the ARPES-station at BESSY, performed by the group of Seyller et al. [147], shown in table 6.1. In order to evaluate the performance of the azimuth-axis (φ) of the sample of the 6-axis manipulator, valence band spectra of graphene/Ir(111) were obtained at room temperature in the following geometry: $\vartheta = 60^\circ$ – off normal emission, and a variation of $\varphi = 2 - 22^\circ$; in $\Delta\varphi = 0.4^\circ$ step size. To access a larger range around the K-point, the WAM lens mode (see chapter 4.1) is used, as shown in Fig. 6.4. Due to the larger acceptance angle of the WAM mode, parts of the replica cones are accessible as shown in Fig. 6.4 (a).

Table 6.1: Evaluation of energy and k-space resolution for ARPES, measured at the lab machine compared to the BESSY machine (benchmark QFMLG). The slit refers here to the entrance slit of the hemispherical analyzer. The modes of operation of the detector are explained in table 4.1 of chapter 4.1.

	BESSY QFMLG β -scan	Lab G/Ir β -scan	Lab G/Ir φ -scan
slit [mm]	0.1	0.2	0.2
detector mode	HAD	LAD	WAM
E_{pass} [eV]	10	20	40
T_{sample} [K]	110	135	300
ΔE [meV]	45	65	100
$3.5k_B T$ [meV]	33	42	91
Δk_x [\AA^{-1}]	0.031	0.040	0.040
Δk_y [\AA^{-1}]	0.026	0.040	0.040

Due to the lattice mismatch of the graphene/Ir(111) interface and the associated buckling of the graphene sheet, back-folded “replica bands” of the π -band emerge. The shape of the measured main Dirac cone is circular and symmetric to the k_x axis, which is different from measurements using the β -flip axis in Fig. 6.3(a). This observation suggests that the rotation of the dark corridor is related to a “geometric effect”. For the φ -ARPES measurements presented here, the linear horizontal polarization of the light has always the same orientation with respect to the sample surface. This is not the case for the earlier shown β -ARPES measurements, where for successively larger flip-angles up to ($\beta = 60^\circ$) the orientation of the light compared to the sample surface changes significantly. Hence, using the additional rotational axis (φ) of the 6-axis manipulator seems preferential for ARPES measurements using low photon energy ($h\nu = 21.21$ eV). The extracted EDC and MDC spectra yield broader structures compared to measurements shown in Fig. 6.3 due to thermal broadening (sample kept at room temperature) and the use of the WAM mode. The obtained energy and k-space resolution are $\Delta E = 100$ meV and $\Delta k_x = 0.040 \text{ \AA}^{-1}$, $\Delta k_y =$

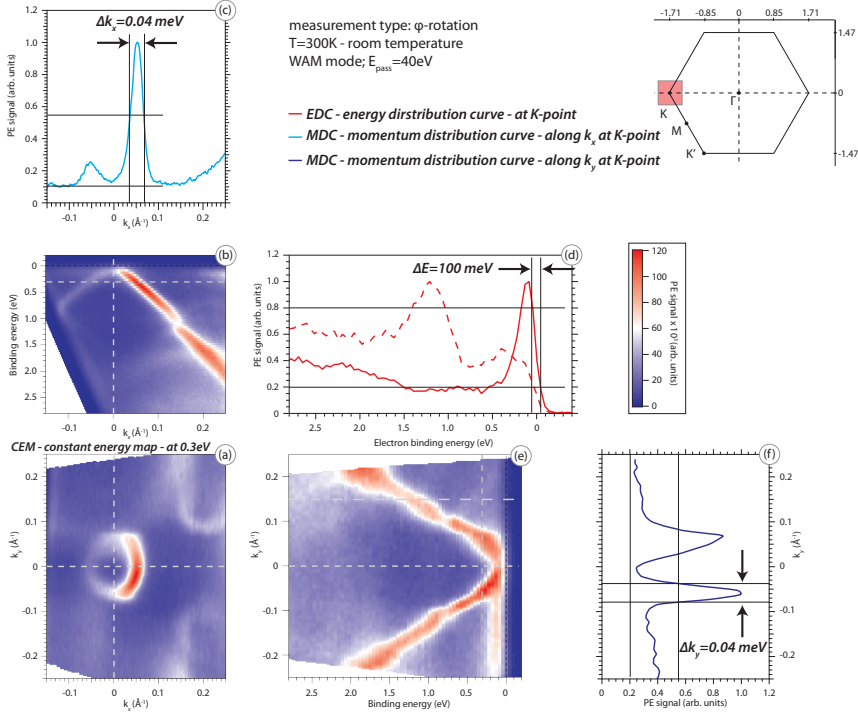


Figure 6.4: 2D-k-space ARPES data from graphene/Ir(111) measured at the laboratory ARPES station, using He-I radiation and employing the φ -rotation. (a) Constant energy map extracted at energies of 0.3 eV below the Fermi level. (b) and (e) Valence band spectra at the K-point along the k_x and k_y directions in k-space, with main contributions from the π -band of graphene and associated replica bands. (d) EDC at the K-point, and at $k_y = 0.15 \text{ \AA}^{-1}$, indicating an experimental resolution of about 100 meV, with the sample kept at room temperature. (c) and (f) MDC extracted at the K-point. The according FWHM of the π -band yields an experimental k-space resolution of about $\Delta k_x = 0.040 \text{ \AA}^{-1}$, $\Delta k_y = 0.040 \text{ \AA}^{-1}$.

0.040 \AA^{-1} . In order to evaluate the performance of the laboratory machine, a summary of the achieved resolution is shown in table 6.1. The main reason for the poorer energy resolution of the spectra shown in Fig. 6.4 are the relatively large thermal broadening with the sample kept at room temperature, and the use of higher E_{pass} .

However, there is still good agreement with the benchmark-spectra of “quasi-free-standing graphene” (QFMLG) , by the group of Seyller *et al.* [147], at the ARPES station at BESSY II. The term QFMLG is used here for graphene on 6H-SiC(0001) prepared by intercalation of hydrogen under the buffer layer. QFMLG is known to exhibit only negligible interaction with the substrate, hence being efficiently decoupled from the substrate [148].

6.2 Measurements at the ARPES station at BESSY II

In the following chapter I describe XPS and ARPES spectra of the system graphene/Ir(111), measured at the synchrotron source BESSY II. Core level spectra of graphene/ Ir(111) using a photon energy of $h\nu = 400\text{ eV}$ are shown in Fig. 6.5. The survey spectrum (Fig. 6.5 (a)) is collected for the range $330 - 0\text{ eV}$ binding energy with the characteristic core level lines of Ir $5p$, Ir $4f$ from the Ir bulk and additionally the C $1s$ core level of graphene. Also visible is the gradually increasing contribution from inelastically scattered electrons leading to an enhanced signal for larger binding energies. Detail scans are collected with a smaller energy step size ($\Delta E = 25\text{ meV}$), as shown in Fig. 6.5(b) and (c) for the C $1s$ and Ir $4f_{7/2}$ core level lines, and detailed information from the core level spectra is extracted using a lineshape analysis (Fig. 6.6). The value obtained for the position of the C $1s$ core level at $284.170(2)\text{ eV}$ is in good agreement to spectra obtained at the laboratory machine described in chapter 6.1, using a conventional x-ray source. A value of 3σ is taken for the error bar resulting in a negligible deviation from the peak positions. However, the FWHM is, with 190 meV , significantly narrower due to better resolution. For the Ir $4f_{5/2,7/2}$ core levels line positions of 63.91 eV and 60.90 eV are extracted by using Doniach-Sunjic-profiles [133], with FWHM of 590 meV and 510 meV respectively, in exact agreement with measurements performed at the laboratory machine. Furthermore, the lineshape of the Ir $4f_{5/2,7/2}$ core levels shows significant contributions of a second component at lower binding energies at each line of the doublet. These additional contributions stem from the Ir surface underneath the

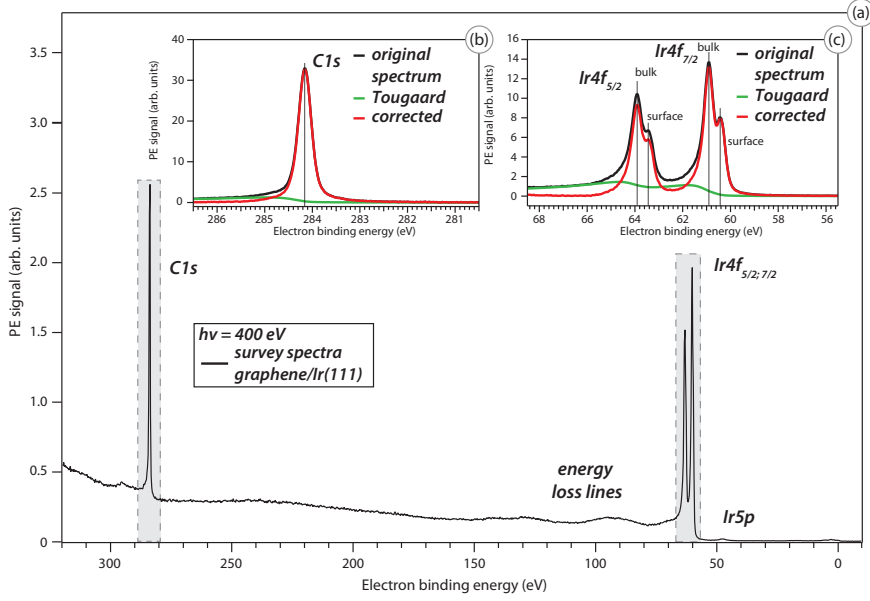


Figure 6.5: XPS spectra of graphene/Ir(111) measured at the BESSY ARPES station, using the UE56/2-PGM-1 undulator beamline at $h\nu = 400 \text{ eV}$ radiation. Normal emission geometry – $\vartheta = 0^\circ$; $E_{pass} = 20 \text{ eV}$ and high magnification lens mode, (HM mode). (a) XPS survey spectra with coarse step size of $\Delta E = 250 \text{ meV}$. Apparent are the characteristic core level lines at Ir $5p$ and Ir $4f$ from the Ir bulk and the related (plasmonic) energy loss lines situated at about 30 eV higher values compared to the respective core level, in agreement with [142]. (b) and (c) Detail spectra of the C $1s$ core level and the spin-doublet Ir $4f_{5/2,7/2}$ core level obtained with a smaller step size of $\Delta E = 25 \text{ meV}$.

graphene sheet, accessible due to the enhanced surface sensitivity of the photoelectrons excited with 400 eV compared to spectra measured with $h\nu = 1486.7 \text{ eV}$ in Fig. 6.2. Especially if the graphene/Ir(111) interface is modified *e.g.* by “intercalation” of transition metals underneath the graphene sheet, as discussed in chapter 4.9, it is worth while to study the behavior of the surface components, which are detectable in the Ir $4f_{5/2,7/2}$ core level spectra of Fig. 6.6 (b). To have a even more detailed view on the Ir $4f_{5/2,7/2}$ core levels of graphene/Ir(111) spectra

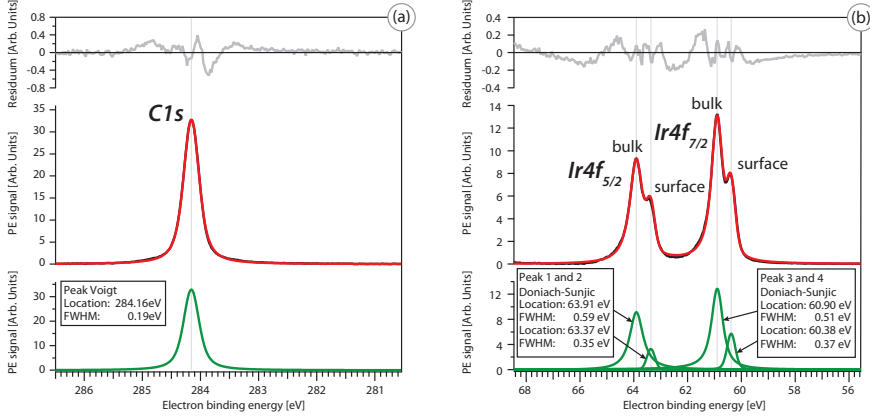


Figure 6.6: Detailed analysis of certain prominent core level spectra of graphene/Ir(111) using a photon energy of 400 eV. (a) and (b) Lineshape analysis of the spectra reveal the position of the C 1s core level at 284.17 eV the spin-doublet Ir $4f_{5/2,7/2}$ core level at 63.91 eV and 60.90 eV in agreement with [141–143] and the measured spectra shown in the previous chapter 6.1 obtained with photon energy of $h\nu = 1486.7$ eV.

are measured with extreme surface sensitivity at a lower photon energy of $h\nu = 120$ eV. The surface components on the Ir $4f_{5/2,7/2}$ core levels at 63.91 eV and 60.90 eV, measured with photon energy of $h\nu = 400$ eV, as shown in Fig. 6.5, are even more prominent with $h\nu = 120$ eV. Fig. 6.7 (a) shows the survey spectra and (b) indicates the Ir $4f_{5/2,7/2}$ core levels with the associated surface components. A subsequent analysis of the spectra using Doniach-Sunjić line shapes [133] yield values of 63.38 eV and 60.37 eV, for the positions of the surface components, being separated from the bulk-related lines (63.87 eV and 60.89 eV) by about 490 meV and 520 meV. These values are close to those by Varykhalov et al. [127]. Comparing ARPES spectra measured by, *e. g.*, a helium discharge lamp with photon energy of 21.21 eV on the laboratory machine with spectra obtained using synchrotron light shows that the latter has several benefits. The main advantage lies in the tunable photon energy, which expands the experimentally accessible range of ARPES. Since the distances in reciprocal units scales with the inverse of the square root of the kinetic energy of the measured photoelectrons

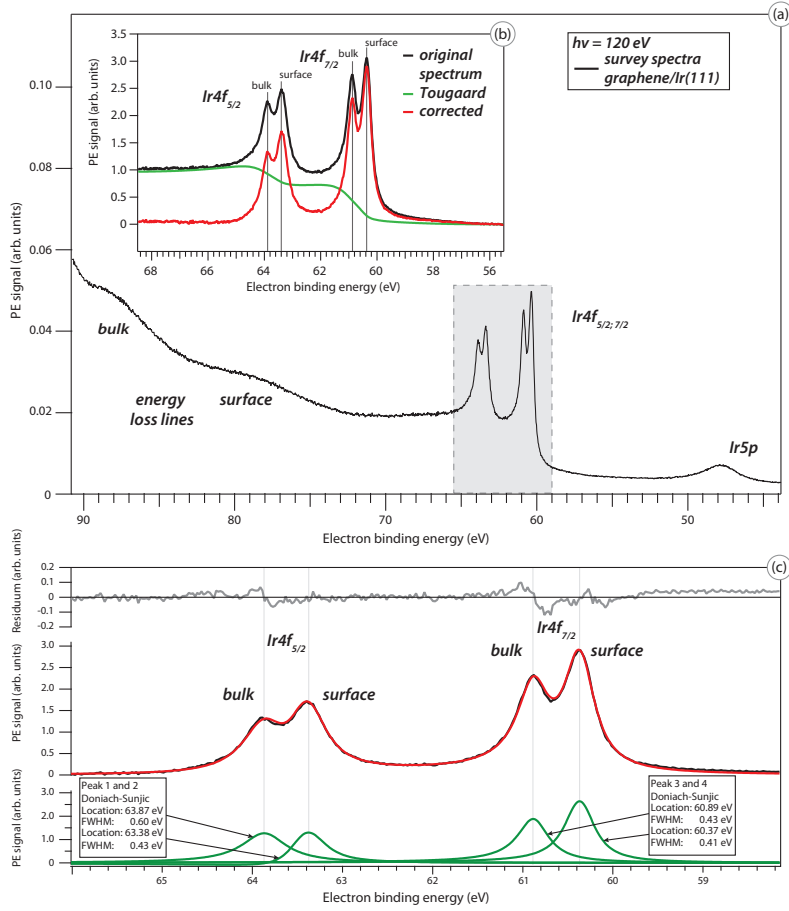


Figure 6.7: XPS spectra of graphene/Ir(111) measured at the ARPES station at BESSY II, with $h\nu = 120$ eV. (a) XPS survey spectra with $E_{pass} = 20$ eV. Apparent are the characteristic core level lines at Ir 5p and Ir 4f from the Ir bulk and the related (plasmonic) energy loss lines, situated at about 30 eV higher values compared to the respective core level. (b) Detail spectra of the spin-doublet Ir 4f_{5/2,7/2} core level. (c) Lineshape analysis of the corrected Ir 4f_{5/2,7/2} core level with subtracted Tougaard background.

(equation (5.2)), large areas of the first Brillouin zone of the studied system become accessible. For graphene/Ir(111) measured in the WAM

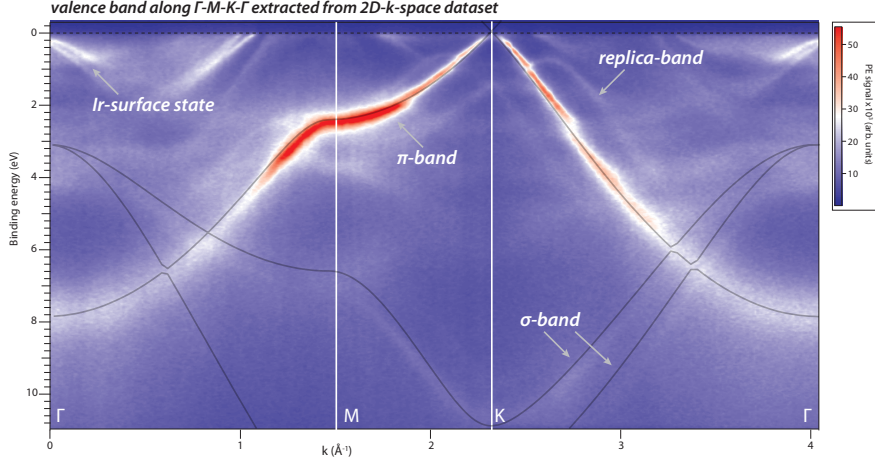


Figure 6.8: Valence band structure of graphene/Ir(111) measured by ARPES. Intensity maps acquired along the $\Gamma - M - K - \Gamma$ direction of the first Brillouin zone of graphene using a photon energy of $h\nu = 65$ eV. The gray line shows a calculated band structure for a free-standing graphene layer using DFT calculations [149].

mode, the entire band structure of the system is detectable in one β -sweep. The main advantage in the spectroscopic measurement of 2D- k -space spectra is that arbitrary directions in k_x/k_y -direction can be traced and evaluated, independently of the geometric orientation of the sample. For the graphene/Ir(111) system, the valence band along the high symmetric directions is especially interesting. Evaluation of the 2D- k -space data shown in Fig. 6.9, yield the band structure along specific directions, with the positions of the π band at symmetric points collected in table 6.2.

The measured band structure along $\Gamma - M - K - \Gamma$ is depicted in Fig. 6.8, showing a survey of the graphene π -band dispersing from 7.8 eV at the Γ -point towards the K-point. Additionally, spectral features of the underlying Ir substrate – surface states – are visible near E_F at the Γ -point. Further features are faint signals of the bottom of the σ -band at 10.6 eV at the Γ -point. As shown in Fig. 6.8, back-folded

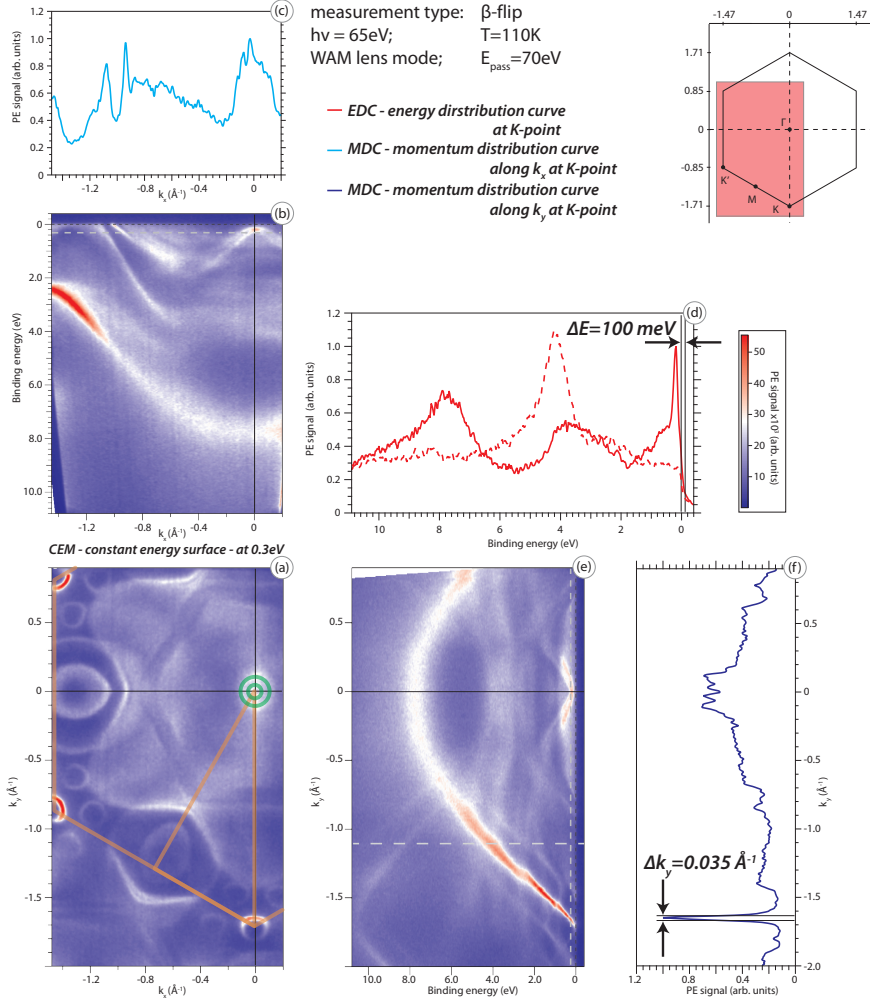


Figure 6.9: 2D-k-space ARPES data from graphene/Ir(111) measured at the BESSY ARPES station, using the UE56/2-PGM-1 undulator beamline. (a) Constant energy map extracted at energies of 0.3 eV below the Fermi level. (b) and (e) depict the valence band image at the K-point along k_x (b) and k_y (e) directions in k-space, with main contributions from the π -band of graphene and associated replica-bands. (d) EDC at the Γ -point, and at $k_y = -1.1\text{ \AA}^{-1}$, indicating an experimental resolution of about 100 meV. (f) MDC along the Γ -K direction. The FWHM of the π -band yields an experimental k-space resolution of about $\Delta k_y = 0.035\text{ \AA}^{-1}$.

Table 6.2: Overview of characteristic positions of graphene’s π -band for high symmetric points of the Brillouin zone, of graphene on different substrates.

	G/Ir(111)	G/Ni/W(110)	G/H/SiC (QFMLG)
Γ	7.8 eV	10.1 eV	8.0 eV
M	2.6 eV	4.8 eV	2.7 eV
K	−0.1 eV	2.8 eV	−0.2 eV

bands of the π -band – replica bands – emerge, which are related to the lattice mismatch of the graphene/Ir(111) interface and the associated buckling of the graphene sheet as discussed in (Fig. 6.11). In order to have a detailed view on the band structure around the K-point of graphene, it is instructive to take high resolution spectra in a narrow range around K. The analyzer is set to the angular resolved MAD mode, which gives a good trade-off between transmission and thus intensity of the obtained signal, and adequate k-space resolution. Further, the acceptance angle is large enough to capture features of the replica bands. The resolution of graphene/Ir(111) samples measured at the BESSY-machine is evaluated in the same spirit as described in section 6.1 for the laboratory ARPES-machine and summarized in table 6.3. The values obtained for the energy resolution measured with graphene/Ir(111) are still slightly larger than the reference values for QFMLG samples. On the one hand, using the HAD mode for graphene/Ir(111) does not cover the replica structures in one scan, because of the limited angular acceptance of HAD and thus the MAD detection mode is used, offering larger acceptance angles (see chapter 4.1). Comparing the values obtained from graphene/Ir(111) to the benchmark QFMLG, as shown in table 6.3, indicates that a reduction in pass energy E_{pass} below 20 eV yields slight improvements in the overall energy resolution. This behavior indicates clearly that for $E_{pass} = 10$ eV, the improved energy resolution of the electron analyzer is masked by the thermal broadening, being the dominating factor in the overall spectral broadening. Regarding the k-space resolution, significant improvements are observable when comparing the MAD

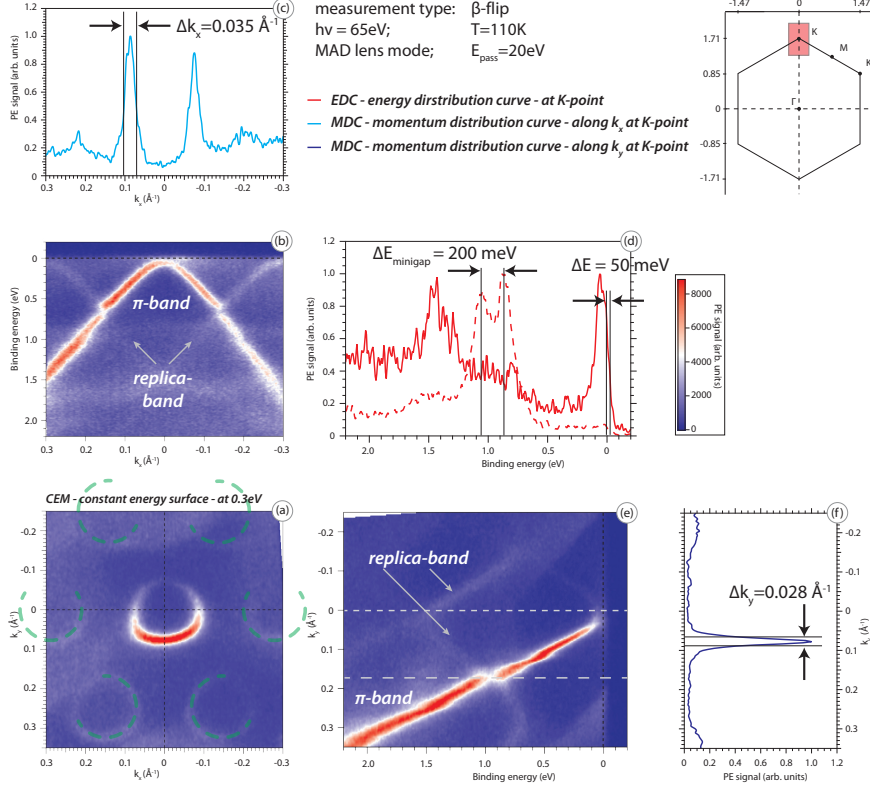


Figure 6.10: 2D-k-space ARPES data from graphene/Ir(111) measured at the BESSY ARPES station, using the UE56/2-PGM-1 undulator beamline. (a) Constant energy maps extracted at energies of 0.3 eV below the Fermi level. The arrangement of the replica cones is indicated by dashed lines (green). (b) and (e) depict the valence band spectra at the K-point along k_x (b) and k_y (e) directions in k-space, with main contributions from the π -band of graphene and associated replica-bands. (d) EDC at the K-point, and at $k_y = 0.17 \text{ \AA}^{-1}$, indicating a experimental resolution of about 50 meV, and a minigap of 200 meV. (c) and (f) MDC, extracted at the K-point. The according FWHM of the π -band indicates an experimental k-space resolution of about $\Delta k_x = 0.035 \text{ \AA}^{-1}$ and $\Delta k_y = 0.028 \text{ \AA}^{-1}$.

Table 6.3: Evaluation of energy and k-space resolution for ARPES, measured at the BESSY-machine compared to the benchmark QFMLG measurements, performed by Seyller et al. [147]. The slit refers here to the entrance slit of the hemispherical analyser.

	QFMLG β -scan	G/Ir β -scan	
entrance slit [mm]	0.1	0.1	0.1
detector mode	HAD	MAD	WAM
E_{pass} [eV]	10	20	70
T_{sample} [K]	110	110	110
ΔE [meV]	45	50	100
$3.5k_B T$ [meV]	33	33	33
Δk_x [\AA^{-1}]	0.031	0.035	0.044
Δk_y [\AA^{-1}]	0.026	0.028	0.035

mode to the WAM mode, as shown in table 6.3. However, the choice of the correct analyzer mode and pass energy is a trade-off depending on the strength of the spectral features/sample survival time, the position of the band structures relative to the Fermi edge and the analyzer transmission. Therefore, it is instructive to obtain survey spectra covering large areas of the Brillouin zone with medium energy and k-space resolution. Measurements with highest resolution are reasonable only for sharp spectral features such as the Dirac cone formed by graphene's π -band, in a small range of the Brillouin zone. At the intersection of bands of the same symmetry character – as for replica bands with the main π -band – avoided crossings lead to the formation of so-called minigaps. A minigap splitting of 200 meV can be extracted from the spectra in Fig. 6.10(c) and (d). This is an improvement over the measurements by Pletikosić et al. [43], who state a width of the minigap in the range of 0.1 – 0.2 eV, depending on the position in k-space where the EDC is evaluated. The minigaps arise from an interaction of the bands in the primary cone with those occurring due to the lattice mismatch because of the additional reciprocal lattice vectors.

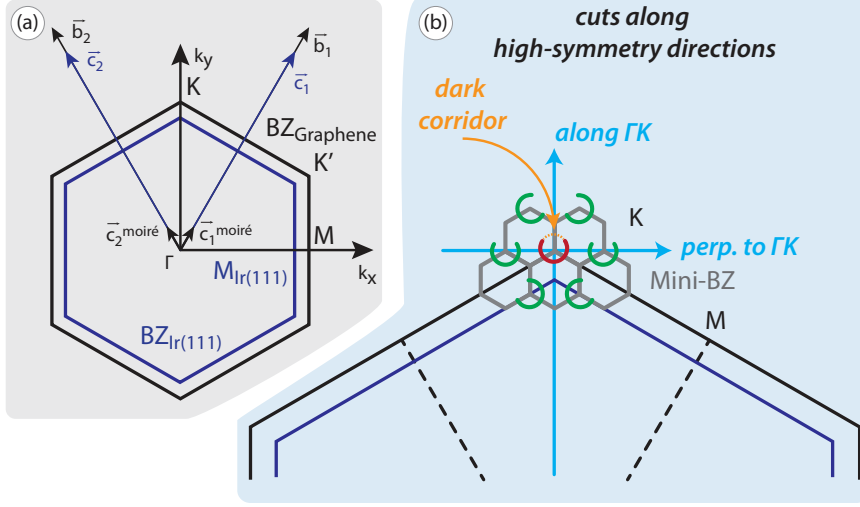


Figure 6.11: (a) Brillouin zone of graphene (black) and Ir(111) (blue) with the corresponding reciprocal lattice vectors \vec{b}_1, \vec{b}_2 and \vec{c}_1, \vec{c}_2 , taken from Pletikosić et al. [43]. The difference in the reciprocal lattice vectors $-\vec{c}_1^{\text{moiré}}, \vec{c}_2^{\text{moiré}}$ forms the so-called mini-Brillouin zone (mini-BZ). (b) Sketch of the area around the K point. Indicated is the position of the main Dirac cone at the K point (red) and additional replica cones (green) positioned at the borders of the mini-BZ (gray) and the dark corridor (orange). ARPES data are taken along high-symmetric directions along and perpendicular to ΓK (blue).

The structural formation of the moiré-lattice has effects on the electronic structure of graphene/Ir(111) as well. The lattice vectors of graphene and Ir (\vec{b}_1, \vec{b}_2 and \vec{c}_1, \vec{c}_2) are depicted in reciprocal space in Fig. 6.11 (a), showing the Brillouin zones of graphene in relation to that of Ir(111). The difference in the reciprocal lattice vectors gives rise to a moiré lattice vector $-\vec{c}_1^{\text{moiré}}, \vec{c}_2^{\text{moiré}}$ forming the so-called mini-Brillouin zone. Pletikosić et al. [43], find that graphene/Ir(111) exhibits a linear dispersing π band, forming a Dirac cone at the K point, comparable to pristine graphene. The term “pristine graphene” is in this context also used as “free standing graphene” by the community, which considers an isolated graphene layer with the physical properties described in chapter 2.1.

However, the π band in graphene/Ir(111) shows minor deviations from pristine graphene, as the Dirac point is located at 0.10 ± 0.02 eV slightly above E_F [43]. Since the unoccupied states are not accessible by photoemission spectroscopy, the authors extrapolated the location of the Dirac cone, making the system p-doped by 0.1 eV. The authors suggest a possible band gap opening at the K point, which is estimated by Rusponi et al. [45] with about 70 meV. Interestingly, six additional

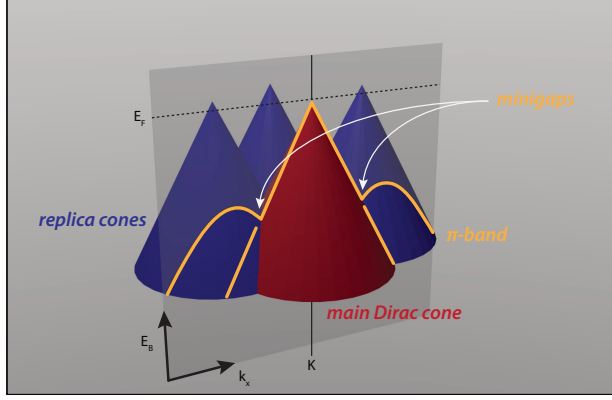


Figure 6.12: Artistic view of the band structure with the graphene Dirac cone formed by the π band (red) in the proximity of the K-point, and surrounding replica cones (blue), inspired by Pletikosić et al. [43]. Indicated is the plane along the high symmetry direction $\Gamma - K - M$ (gray). At the intersection of the main Dirac cone with the replica cones the opening of “minigaps” is observed.

Dirac cones emerge in the band structure, observed near the zone border around the K point. These cones can be understood as replicas of the main Dirac cone at K, called “replica cones” [43, 45, 91]. It is suggested that the existence of a periodic potential, induced by the moiré lattice, is responsible for the replicas [43]. Furthermore, the π band near E_F forming the Dirac cone exhibits a horseshoe-shaped suppression in intensity along the direction ΓK , shown schematically in Fig. 6.11 (b). This effect is denoted by Gierz et al. [145] as “dark corridor” and can be understood as interference effects of the photoelectrons emitted from the two sublattices A , B of the graphene unit cell [145, 150–154]. For graphene/SiC(0001) this effect was observed several times by ARPES

measurements [145, 154–156]. However, studies by Gierz et al. [145] have shown that ARPES measurements using a certain rotation of the polarization vector of the incoming photons, unveil the dark corridor, making the full Dirac cone at the Fermi energy accessible. Another interesting point is that ARPES measurements on graphene/Ir(111) by Starodub et al. [91] suggested a different direction of the horseshoe like replica cones in respect to the main Dirac cone (Fig. 6.11 (b) – ARPES data in chapter 6). This is contrary to earlier observations of the Dirac cone and the replicas in graphene/SiC(0001) by Bostwick et al. [155]. The authors could show that the six replica cones have the same relative orientation towards the Γ point as the main Dirac cone [155]. These differences can be understood, as Bostwick et al. [157] pointed out, that in the case of graphene/SiC(0001) the replicas, showing towards the same direction as the main Dirac cone, emerge as final state diffraction effect in the photoemission process itself. On the other hand, Starodub et al. [91] found that the replicas in graphene/Ir(111) pointing towards different directions than the main cone. The authors suggests that a quantum-mechanical phase term in the initial state process of photoemission is responsible for the observed effect. Another feature in the band structure are so-called “minigaps” [43, 45, 91], emerging at the crossing points of the main Dirac cone with the replica cones. Taken together, these findings are depicted schematically in Fig. 6.12 showing a sketch of the band structure with the main Dirac cone formed by the graphene π band and the associated replica cones. The linear dispersing π band shows the opening of minigaps – indicated as suppression in intensity – at the intersection with the replica cones. These findings are further discussed in the experimental part of the thesis (chapter 6).

6.3 Rotational domains

We generally refer to graphene/Ir(111) as the case where the graphene sheet lies in the same in-plane direction as the underlying Ir(111) substrate. This is not always the case; there are several possible configurations of growth directions for graphene on an Ir(111) substrate.

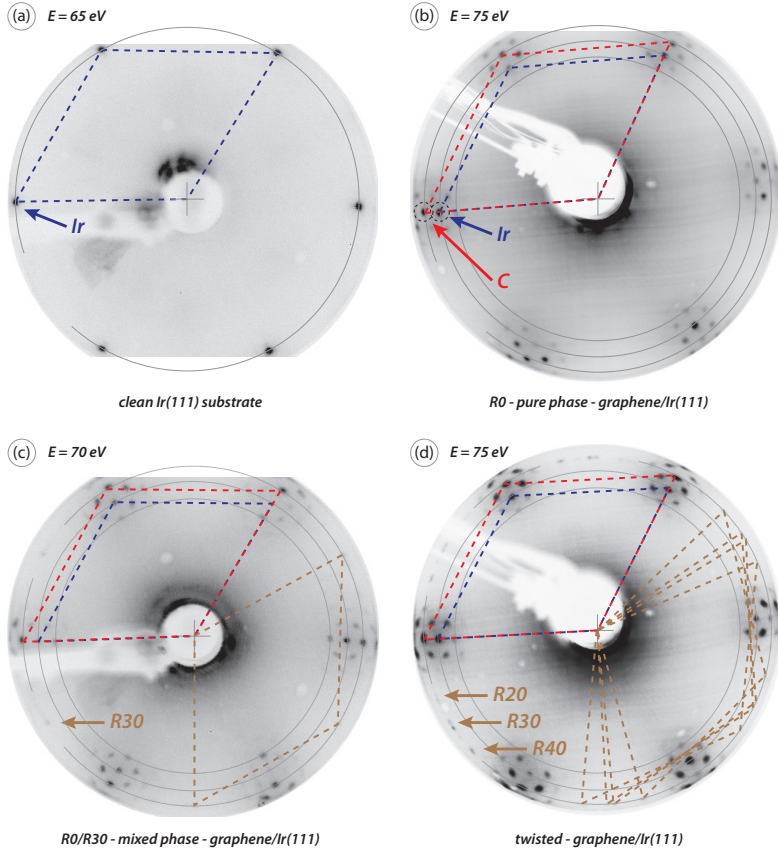


Figure 6.13: LEED images of the clean Ir(111) substrate and different crystallographic phases of graphene/Ir(111). (a) clean Ir(111), (b) “phase pure” $R0^\circ$ -graphene/Ir(111), (c) “mixed phase” $R30^\circ/R0^\circ$ -graphene/Ir(111) and (d) “twisted phase” graphene/Ir(111).

Firstly, graphene can grow during the CVD process with the main azimuth in-line with the underlying substrate as described above ($R0^\circ$ -graphene/Ir(111)). Additional variants of graphene grown on Ir(111) have been reported by Longinova et al. [158] and Hattab et al. [159] – such as $R30^\circ$, $R18.5^\circ$ and $R14^\circ$ – and additionally $R22^\circ$ and $R26^\circ$ found by Starodub et al. [91].

Graphene grown under conditions as described in chapter 4.7 has the $R0^\circ$ -graphene/Ir(111) variant. However, an insufficient number of cleaning cycles and growth steps of graphene/Ir(111) as described by van Gastel et al. [160], or growth temperatures below 1500 K as shown by Hattab et al. [159] can give rise to the formation of rotated graphene domains; these are usually undesirable, especially if the graphene/Ir(111) surface is chemically modified *e. g.*, by intercalation of transition metals as described in chapter 4.9. Since the structural variations by rotational domains can be pinpointed by LEED and ARPES, it is instructive to have a closer look on the way in which rotational domains affect the band structure of graphene. LEED images shown in Fig. 6.13 describe the different crystallographic phases that were observed for various samples in this thesis. Starting from a clean Ir(111) substrate in (a), in the case of “phase pure” $R0^\circ$ -graphene/Ir(111), [Fig. 6.13 (b)] the graphene sheet lies in-line with the underlying substrate along the main azimuth. Additionally, “mixed phase” $R30^\circ/R0^\circ$ -graphene/Ir(111) in Fig. 6.13 (c) is observed in accordance with [158, 159].

Furthermore, a phase with several rotated domains is observed – the “twisted phase” graphene/Ir(111) in Fig. 6.13 (d). The band structure of “phase pure” $R0^\circ$ -graphene/Ir(111) was already described in chapter 6.1 and 6.2. The “mixed phase” $R30^\circ/R0^\circ$ -graphene/Ir(111) variant is discussed by Starodub et al. [91], who showed that the $R30^\circ$ -phase has a slightly lower interaction with the underlying Ir substrate. By doping the sample with potassium, the authors show that no gap-opening between the π - and π^* -band at the K-point is observed. Hence, no replica bands and associated minigaps appear in the band structure of the $R30^\circ$ -phase. Additionally, by employing spatially resolved Raman spectroscopy, the authors claim that the characteristic G and G' peaks, which represent the graphene-related vibrational modes, are only observed for the $R30^\circ$ -phase, while the G

and G' modes are absent for the $R0^\circ$ -phase. Finally, Starodub et al. [91] conclude that the $R30^\circ$ -graphene phase is less strongly bonded to the Ir(111) substrate than the $R0^\circ$ -graphene phase.

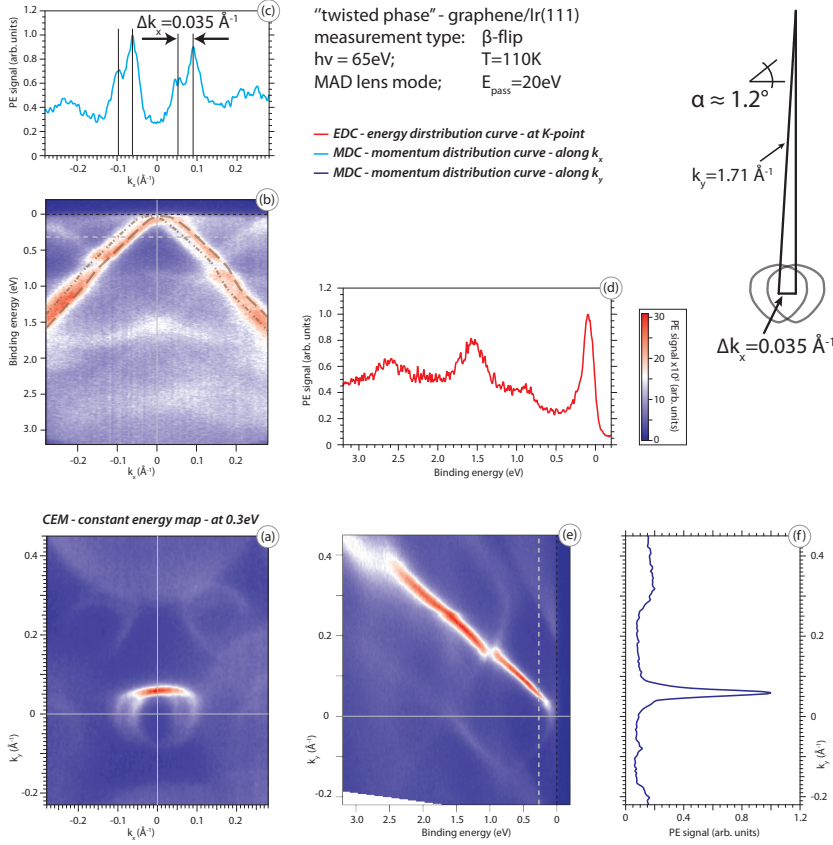


Figure 6.14: 2D- k -space ARPES data from “twisted”-graphene/Ir(111) measured at the BESSY ARPES station. (a) Constant energy maps extracted at energies of 0.3 eV below the Fermi level, indicating rotationally twisted Dirac cones by about 2° . (b) and (e) depict the valence band spectra at the K-point along k_x (b) and k_y (e) direction in k -space, with main contributions from the π -band of graphene and associated replica bands. (d) EDC taken at the K-point. (c) and (f) MDC extracted at the K-point, indicating twisted π bands separated by about 0.035 \AA^{-1} . The right side shows an estimated rotational twisting of $\approx 1.2^\circ$ by simple trigonometric functions.

Finally, samples with several rotational domains beyond the R30°- and R0°-phases are observed and characterized by LEED – Fig. 6.13 (d) and ARPES. Using an ARPES survey scan I could identify for every K-point of the R0°-phase a slightly rotated variant which lies beneath the π band forming the Dirac cone. The angle between both Dirac cones is about 2°. This is reflected in the LEED images of Fig. 6.13 (d). For the main LEED spots related to (1×1) graphene, it is, most likely due to the high intensities of the main spots, not possible to resolve a second component. However, for the rotated phases, *e. g.* , R30° in (d) a rotational twisting of about 2.5° can be identified. To further analyze this behavior in detail, high-resolution ARPES spectra of the sample were measured in a small area around the K-point shown in Fig. 6.14 (a). The high resolution ARPES spectra yield a separation of the two “twisted” Dirac cones of about 0.035 \AA^{-1} , which is near the value of the determined k-space resolution of 0.037 \AA^{-1} (ch. 6.2). Since the two Dirac cones are still distinguishable an even better k-space resolution is suggested. However, the contributions from two π -bands can still be well separated. In order to verify the rotational twisting of the two Dirac cones, observed by LEED in Fig. 6.13(d), simple trigonometric functions are used. As shown on the right side of Fig. 6.14, the estimated twisting of the Dirac cones amounts to $\approx 1.2^\circ$, which agrees with the estimated 2° by LEED. Recent work of Marchenko et al. [161] show similar observations, with a rotational separation of 2.8° obtained from ARPES measurements.

6.4 Line shape analysis on graphene/Ir(111)

Employing a line-shape analysis one can extract information from the measured spectra function by ARPES. Using an automated fitting routine with one or two Lorentzian peaks and an additional linear background along the energy axis and k-axis, one can obtain informations about the peak position, FWHM and amplitude. From the following formula the group velocity can be deduced, which corresponds to the Fermi-velocity at the Fermi-energy.

$$v_g = \frac{\partial \omega}{\partial k} = \frac{1}{\hbar} \cdot \frac{\partial E}{\partial k} \quad (6.2)$$

For graphene/Ir(111) measured at the BESSY, employing a photon energy of $h\nu = 65\text{ eV}$, one obtains $v = 1.050(4) \times 10^6\text{ ms}^{-1}$ evaluating the slope at energies of 2.3 eV . For energies of the π band near the Fermi-energy there is a distinct reduction in dispersion leading to $v = 0.900(3) \times 10^6\text{ ms}^{-1}$ (at 0.8 eV). This observation is in agreement with recent studies by Kralj et al. [28], who report velocities of $1.07 \times 10^6\text{ ms}^{-1}$ and $0.95 \times 10^6\text{ ms}^{-1}$ for the corresponding energy positions. For the direction perpendicular ΓK reduced velocities of $v = 0.840(10) \times 10^6\text{ ms}^{-1}$ at energies of 1.3 eV and $v = 0.700(11) \times 10^6\text{ ms}^{-1}$ at energies of 0.6 eV are observed for measurements at the BESSY machine (Fig. 11.1). In the following I evaluated datasets taken from graphene/Ir(111) using the two different measurement procedures β -flip and φ -rotation. These datasets are shown in chapter 11 (appendix). The derived velocities using the MDC line shape analysis along ΓK are about the same for the laboratory station and the BESSY machine. At 0.8 eV the same velocities of $0.88(1) \times 10^6\text{ ms}^{-1}$ are observed along ΓK (Fig. 11.2). For the perpendicular direction velocities of $v = 0.70(3) \times 10^6\text{ ms}^{-1}$ are found at 0.6 eV . These measurements gave the final confirmation that the new laboratory experiment is successfully commissioned.

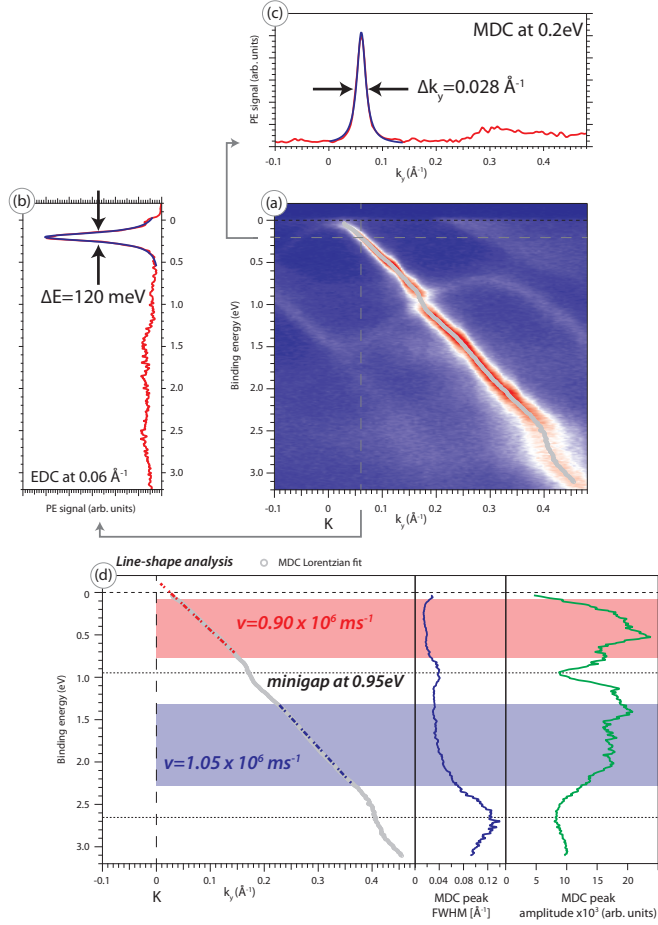


Figure 6.15: The line-shape analysis along $\Gamma - K$ direction. (a) ARPES data from pristine R0-graphene/Ir(111) measured at the BESSY ARPES-station, using $h\nu = 65 \text{ eV}$ photon energy and employing the β -flip. The analyser is set to MAD lens mode. (b) EDC spectra at 0.06 \AA^{-1} . (c) MDC spectra at 0.2 eV (d) Evaluation of the group velocity from the slope of the fitted peak positions. Further, the FWHM and the amplitude of the single Voigt profile, used in the line shape analysis is shown.

Modification of graphene/Ir(111) by copper intercalation

As mentioned in the introduction, understanding the nature of the interaction at the graphene/metal interfaces is the basis for graphene-based electron- and spin-transport devices. The discovery of the unique transport properties of graphene [7, 8] has stimulated the search for practical applications of this material in devices based on the transport of electrical charge or/and spin. In most of these as yet elusive devices, the graphene-metal interfaces will be utilized as a contact for charge or spin injection or filtering. Hence the crystallographic and electronic properties of such interface determine the charge/spin injection efficiency of the corresponding contact, which is one of the main motivations for studies of the graphene-metal interface [24, 114, 162]. In this chapter we investigate the hybridization between graphene- and metal-derived electronic states by studying the changes induced through intercalation of a pseudomorphic monolayer of Cu in between graphene and Ir(111). Copper, which has an electronic configuration of $-\text{Cu} [\text{Ar}] 3d^{10}(4s)^1 -$ is a closed d -shell metal and exhibits sharp d bands in photoemission such that the dispersion can be followed in great detail; in fact, the method of “band mapping” using photoemission was elaborated in many studies of this material in the 1980’s and onwards [163, 164]. The idea here is that the sharp d bands and their

interaction with the π band of graphene may give insight into the open question regarding the interaction mechanism and strength between various metals and graphene, and may be of general importance beyond the specific system. We use scanning tunneling microscopy to gain structural information about graphene/Cu/Ir(111), and photoelectron spectroscopy in combination with density functional theory calculations to establish the interaction mechanism. We observe the modifications in the band structure by the intercalation process and its concomitant changes in the charge distribution at the interface. A state-selective analysis of band hybridization using DFT, is able to determine their contributions to the valence band of graphene giving rise to a gap opening. This reveals the mechanisms that are responsible for the modification of the electronic structure of graphene at the Dirac point, and permits to predict the electronic structure of other graphene-metal interfaces.

From a more fundamental point of view, the study of the bonding mechanism at the graphene-metal interface is a very interesting problem in itself, and up to now such systems are far from being fully understood [117]. Several factors influence the electronic properties of the graphene-metal interface: charge transfer from/onto graphene-derived π states, hybridization of the electronic valence band states of graphene and the metal, and the lattice match between the graphene and metal surface. These factors determine the behavior of the π states in the vicinity of the Fermi level, E_F , (as *e.g.* a deviation from the linear behavior characteristic for free-standing graphene) as well as the appearance of an energy gap in the spectrum of the graphene-derived electronic states at the so-called Dirac point, E_D . Regarding the electronic structure, two scenarios may be distinguished [117]: those in which the characteristic linear dispersion near E_D is largely preserved, such as on Ir(111) [ch. 6], Pt(111), and Cu(111), and those where a massive rearrangement of bands occurs, such as Ni(111) and Co(0001) [ch. 8], for example. Intercalation of metals in between graphene and substrates offers an interesting scientific playground to investigate the metal-graphene interaction. Graphene may become decoupled from strongly interacting substrates, such as in the case of Au or Al intercalation in between graphene and nickel [41, 50, 51, 165]. Such intercalated layers may also change the carrier concentration in graphene, and even

change the carrier type (from electrons to holes) such as in the case of Au intercalation in graphene/SiC(0001) [156]. Intercalated metals may also enhance the magnetic coupling between a ferromagnetic substrate and graphene (ch. 8), with a view to utilizing graphene as a spin filter [166, 167]. Moreover, the passivating, protecting function of graphene may also be used in such systems [111, 112]. The intercalated layer in itself may bring new properties to graphene, such as in the case of lithium where superconductivity has been predicted to occur [168]. The different factors that determine the bonding between graphene and a metal can be analyzed by studying graphene-based intercalation systems. Hence pseudomorphic layers of Co and Ni were intercalated on graphene/Ir(111) [ch. 8] and are compared to recent studies [169–171].

On top of Pt(111) or Ir(111), graphene has properties almost like the free-standing phase, as judged by its electronic structure derived from photoemission and scanning tunneling spectroscopy [43, 172]. Intercalation of 1 ML of Co or Ni leads to a strong buckling of the graphene layer similar to the one formed on Ru(0001) [173], and a large energy gap between π and π^* states around the K-point occurs, due to the broken symmetry for the two carbon sublattices in the graphene unit cell, induced by the strong hybridization of the graphene π and Co, Ni $3d$ valence band states; in both cases the linear dispersion of the graphene-derived states in the vicinity of E_F is not conserved [169–171]. A very different situation is found for intercalation of noble metals (Cu, Ag, Au) and the formation of single close-packed pseudomorphic layers. Here, due to the absence of d states in the close vicinity of E_F and the change of the doping of graphene upon intercalation, the influence of $\pi - d$ hybridization effects on the electronic structure of graphene is much weaker [50, 51, 174, 175], and the linear dispersion of the graphene-derived π states survives. The intercalation of single layers of noble metals is a suitable model system to investigate the interaction between graphene and metals, since it permits to follow the competition between the different (substrate and intercalated layer) electronic states. Apart from the interest in intercalated Cu in graphene/Ir(111) mentioned above, this system is also interesting since it permits the creation of a single layer of Cu under considerable tensile strain, because of the lattice mismatch of 6.2 % between the

two metals. If deposited on top of an Ir (111) surface, this strain leads to de-wetting and the creation of 3D islands/clusters even at low coverages, or to dendritic growth of layers as in the case of Au on Ir(111) [176] or incomplete growth of Cu on Pt(111) [177]. The studies in this chapter have been published in

- H. Vita, S. Böttcher, K. Horn, E. N. Voloshina, R. Ovcharenko, Th. Kampen, A. Thissen and Yu. S. Dedkov (2014).
“Understanding the origin of band gap formation in graphene on metals: graphene on Cu/Ir(111).”
Scientific Reports **4**, Article number: 5704.

with myself as the principal investigator, and the assistance of Stefan Böttcher under the supervision of Karsten Horn. Yuriy Dedkov contributed the STM measurements and a part of the ARPES measurements using He-II radiation. The theoretical calculations were performed by Roman Ovcharenko and Elena Voloshina from the Quantum Chemistry group at the Humboldt-Universität zu Berlin.

7.1 Preparation and spectroscopic methods

Preparation of graphene/Ir(111) and graphene/Cu/Ir(111)

The graphene/Ir(111) system was prepared in a ultra high vacuum system for ARPES experiments, as described in chapter 4.7, according to the recipe given in detail in Refs. [108–110], via cracking of propylene: $T = 1300^\circ\text{C}$; $p = 5 \times 10^{-7}$ mbar; $t = 30$ min. This procedure leads to the single-domain graphene layer on Ir(111) of very high quality as shown in chapter 6. Intercalation of the 1 ML-thick Cu layer and formation of the graphene/Cu/Ir(111) intercalation-like system was achieved via annealing of the graphene/Ir(111) sample with a thin pre-deposited copper layer on top. The process of intercalation was monitored by measuring of the “real-time” C 1s and Ir 4f spectra of the system, and formation of the graphene/Cu/Ir(111) system was detected at 550°C . The quality and cleanness of the system in ARPES experiment was verified by LEED and XPS/ARPES, respectively. The base vacuum was better than 7×10^{-11} mbar during all experiments.

All STM measurements were performed at room temperature in constant current (CC) mode, where the topography of the sample, $z(x, y)$, is studied with the corresponding signal, tunneling current (I_T), used as an input for a feedback loop. The STM images were collected with an SPM Aarhus-150 equipped with the KolibriSensorTM from SPECS [110, 178] with a Nanonis Control system. A sharp W-tip was used which was cleaned *in situ* via Ar⁺-sputtering. In the STM images the tunneling bias voltage, U_T , is referenced to the sample and the tunneling current, I_T , is collected by the tip, which is virtually grounded. In the DFT calculations, the crystallographic model of graphene/Ir(111) and graphene/Cu/Ir(111) presented in Fig. 7.1 is used within the projector augmented plane wave method [179] and a plane wave basis set with a maximum kinetic energy of 400 eV and the PBE exchange-correlation potential [180], as implemented in the VASP program [181]. The long-range van der Waals interactions were accounted for by means of the DFT-D2 approach proposed by Grimme [182]. The studied system is modelled using a supercell which has a (9×9) lateral periodicity and contains one layer of (10×10) graphene on a five-layer slab of metal atoms. Metallic slab replicas are separated by ca. 20 Å in the surface normal direction. To avoid interactions between periodic images of the slab, a dipole correction is applied [183]. The surface Brillouin zone is sampled with a $7 \times 7 \times 1$ k -point mesh centered at the Γ -point.

7.2 Results and electronic structure calculations

STM images of graphene layers on Ir(111) demonstrate the long range ordering of the moiré structure over several hundreds nm, as shown in Fig. 7.1(a), which is an extract of the originally acquired $300 \times 300 \text{ nm}^2$ STM data set. The lower inset shows an atomically resolved STM image of the moiré unit cell of graphene/Ir(111), which demonstrates the periodicity of 10 graphene unit cells over 9 unit cells of Ir(111), consistent with the corresponding low energy electron diffraction (LEED) pattern shown in the upper inset of Fig. 7.1(a) [108, 118, 184]. At the bias voltages used in the experiment ($U_T = +0.3 \text{ V}$ and $U_T = +0.5 \text{ V}$), graphene/Ir(111) is imaged in the so-called *inverted* contrast [108, 110],

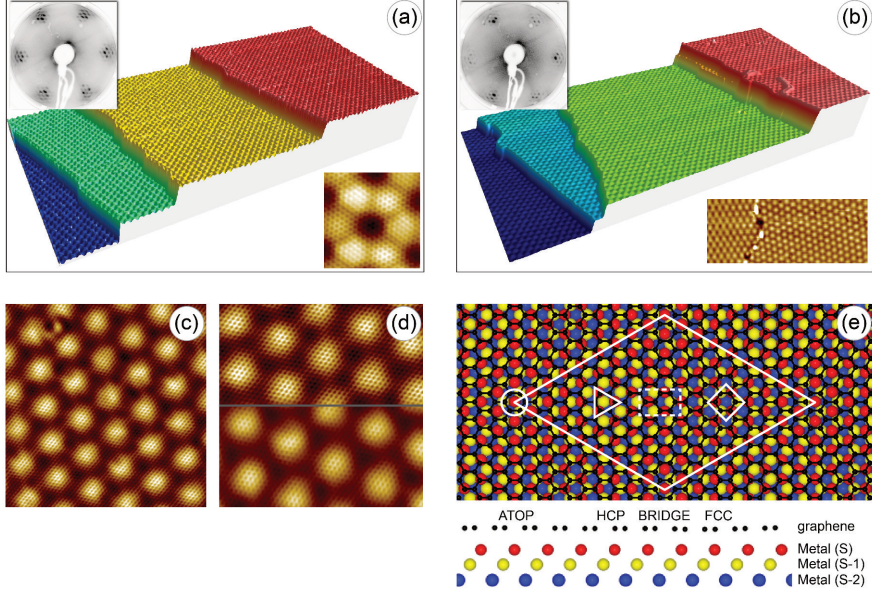


Figure 7.1: STM images of graphene on Ir(111) and pseudomorphic Cu/Ir(111). (a) 3D view of the STM image of graphene/Ir(111) (scanning parameters: $120 \times 56 \text{ nm}^2$, $U_T = +0.3 \text{ V}$, $I_T = 1.6 \text{ nA}$. Upper and lower insets show the LEED image ($E_p = 93 \text{ eV}$) and atomically resolved STM image (scanning parameters: $4.5 \times 4.5 \text{ nm}^2$, $U_T = +0.5 \text{ V}$, $I_T = 10 \text{ nA}$) of this system. (b) 3D view of the STM image of graphene/Cu/Ir(111) (scanning parameters: $175 \times 82 \text{ nm}^2$, $U_T = +0.3 \text{ V}$, $I_T = 1.6 \text{ nA}$. Upper and lower insets show the LEED image ($E_p = 90 \text{ eV}$) and an STM image of two graphene domains (scanning parameters: $60 \times 24 \text{ nm}^2$, $U_T = +0.3 \text{ V}$, $I_T = 1.6 \text{ nA}$). (c) and (d) present atomically resolved images of the graphene/Cu/Ir(111) system obtained at $U_T = +0.3 \text{ V}$ and $U_T = -0.3 \text{ V}$ (top) / -0.9 V (bottom), respectively (scanning parameters: (c) $13.5 \times 13.5 \text{ nm}^2$, (d) $10.1 \times 10.1 \text{ nm}^2$, $I_T = 1.6 \text{ nA}$ for both images). (e) Top and side views of the graphene/metal(111) structure. In case of Ir(111) all layers consist of the same atoms, whereas for the Cu/Ir(111) pseudomorphic system the metal (S) is the copper layer. In the top view, the circle, triangle, rhombus, and rectangular denote the ATOP, HCP, FCC, and BRIDGE positions for the carbon atoms, respectively. The big white rhombus marks the unit cell of the graphene/metal(111) system.

where the crystallographic highest ATOP positions are imaged as dark areas and the lowest HCP and FCC places are imaged as bright ones, demonstrating the strong influence of the electronic structure on STM contrast (for the definitions of the high-symmetry positions of the graphene/metal moiré structure see Fig. 7.2). Intercalation of a

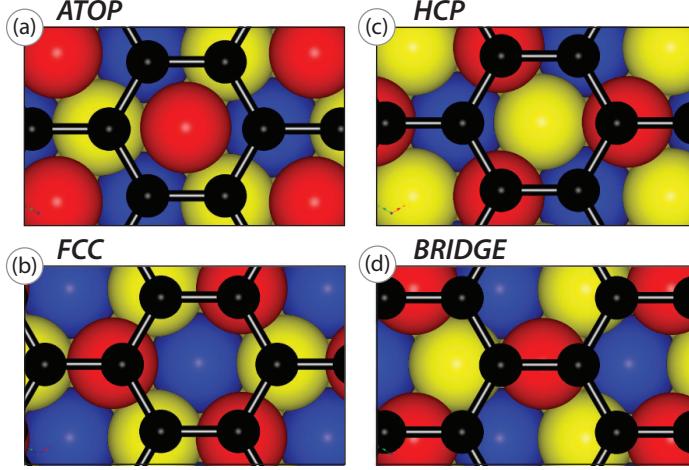


Figure 7.2: Definitions of the high-symmetry positions of the graphene/metal(111) moiré structures as discussed in ch. 4.8: The capital-letters labels are used for the definition of the high-symmetry places in the graphene/metal(111) moiré structure where carbon atoms surround the corresponding adsorption places of the metal(111) surface: (a) ATOP-position – carbon atoms are placed in the *hcp* and *fcc* hollow positions of the metal(111) stack above (S-1) and (S-2) metal-layers, respectively; (b) FCC-position – carbon atoms are placed in the *top* and *hcp* hollow positions of the metal(111) stack above (S) and (S-1) metal-layers, respectively; (c) HCP-position – carbon atoms are placed in the *top* and *fcc* hollow positions of the metal(111) stack above (S) and (S-2) metal-layers, respectively; and (d) BRIDGE-position – carbon atoms are bridged by the metal atom in the (S) layer.

1 ML-thick Cu layer underneath graphene was performed via stepwise annealing of a deposited layer of Cu (with a nominal thickness of 1.5 ML) on graphene/Ir(111). During this procedure, the intensity of the “real-time” C 1s and Ir 4f photoelectron spectra was taken as

the intercalation proceeded as a function of annealing temperature [see Fig. 7.3 (b)]. This method permits to follow the formation of an intercalated Cu layer underneath graphene/Ir(111). The absence of any additional low binding energy (BE) components in the C 1s spectra after intercalation indicates that the Cu layer is completely intercalated. The effective intercalation of a thin Cu layer, and

Table 7.1: Overview of the main C 1s peak position for Cu deposited at sample temperatures of $T = 100$ K on top and the intercalated graphene/Cu/Ir(111) phase, compared to pristine graphene/Ir(111).

	G/Ir(111)	Cu/G/Ir(111)	G/Cu/Ir(111)
	– pristine –	– on top –	– intercalated –
C 1s	284.17 eV	284.17 eV	284.69 eV

the formation of graphene/Cu/Ir(111) occurs at 550 °C, as identified via strong modifications of the C 1s and Ir 4f emission lines [Fig. 7.3 (a) and (b)]. Intercalation leads to a shift of the C 1s peak from 284.170(2) eV towards higher binding energy. The spectra are fitted with two components at 284.70(7) eV and 285.00(6) eV [Fig. 7.3 (c)]. A value of 3σ is taken for the error bar resulting in a negligible deviation from the peak positions. The integral intensity of the C 1s line is restored to the value equivalent to the one for graphene/Ir(111). The C 1s peak shows an additional component at higher binding energy. The components are denoted as (*h*) “hills” (top place) and (*v*) “valleys” (bottom place) of graphene/Cu/Ir(111), which means the “weakly” and “strongly” interacting places of the structure. In case of the Ir 4f spectra, the energy splitting between bulk (*b*) and interface (*i*) components is reduced from about 540 meV towards 460 meV. The intensity of the interface component is strongly suppressed compared to that of graphene/Ir(111) [Fig. 7.3 (d)].

Although the STM data from graphene with an intercalated Cu layer [Fig. 7.1 (b) – (d)] may appear similar at first glance to those from graphene/Ir(111), there are clear differences in detail which reveal the effect of intercalation. The large scale STM image shown in (b) demonstrates the formation of a moiré structure on top of Cu/Ir(111) which has the same periodicity of (10×10) graphene /

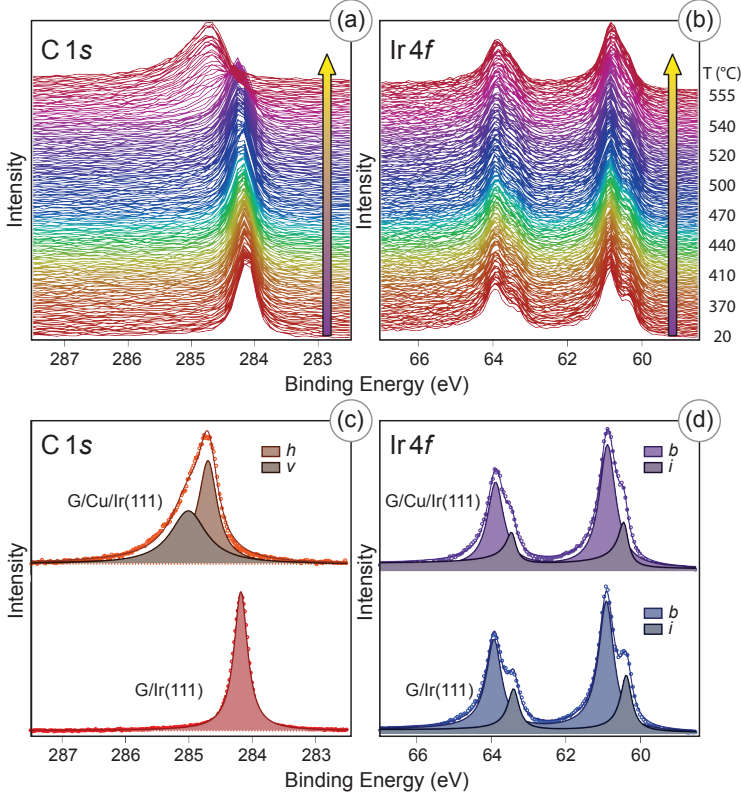


Figure 7.3: (a) and (b) show a series of the C 1s and Ir 4f photoelectron spectra collected in “real-time” during annealing of the thin pre-deposited Cu layer on graphene/Ir(111) indicating the formation of the graphene/Cu/Ir(111) system. Annealing temperature is specified; intercalation appears at 550 °C. (c) and (d) show a fit of the C 1s and Ir 4f photoemission lines acquired before and after intercalation of Cu in graphene/Ir(111). Photon energy is $h\nu = 400$ eV. *b* and *i* label the bulk and interface component of Ir 4f; *h* and *v* the “hills” and “valleys” component of C 1s respectively.

(9 × 9) Cu/Ir(111). Hence we conclude that a pseudomorphic Cu layer on Ir(111) is formed after intercalation. However, contrary to the results for graphene on Ir(111), a variation of the tunneling voltage during STM imaging of graphene/Cu/Ir(111) does not lead to an inversion of the imaging contrast – graphene is here always imaged in

“direct” contrast [Fig. 7.1(c) and (d)]. These results differ significantly from the “inverted” contrast for pristine graphene/Ir(111) [110, 185], where topographically higher places are imaged as dark areas, hence as valleys in the STM experiments. The origin of this behavior was explained recently by Dedkov et al. [116], who assign this effect to the so-called interface states of graphene/Ir(111) formed as a result of the overlap of graphene $2p_z$ and Ir $5d_{z^2}$ orbitals. This indicated that for graphene/Cu/Ir(111) the formation of these interface states is disturbed. The two atomically-resolved STM images were acquired at (c) $U_T = +0.3$ V and (d) $U_T = -0.3$ V (upper part) and $U_T = -0.9$ V (lower part). In Fig. 7.1(d) the tunneling voltage was changed during scanning “on-the-fly”, showing the absence of any change of the contrast in the moiré cell on an atomic scale. Figure 7.1(e) shows the structure of the graphene/Cu/Ir(111) system as derived from DFT calculations. The (10×10) unit cell graphene lattice on the (9×9) five layer Ir(111) oriented slab were allowed to relax; the resulting in-plane lattice constants of graphene are close to those of the free-standing species. For the structural evaluation of the intercalated system, the topmost metal layer (S) in Fig. 7.1(e) was replaced by Cu. The Cu atoms were found to take up the positions of the Ir atoms, and the distance between the topmost metal layer and graphene in the ATOP position was found to be 3.581 Å for graphene on Ir and 3.122 Å for the intercalated Cu layer, a considerable reduction, signaling an enhanced interaction of carbon with the Cu atoms. Other structural parameters are given in Table 7.2. The conservation of long range periodicity of the system after intercalation of Cu is also shown by the LEED images of the graphene/Cu/Ir(111) system [upper inset of Fig. 7.1(b)].

The spot pattern is indicative of the moiré structure, similar to the one observed for graphene on Ir(111). The fact that the pattern symmetry is reduced from sixfold to threefold cannot by itself be taken as evidence for a lowering of local symmetry: first, the reduction occurs mainly on the Ir-related spots, which because of the 3D face-centered cubic character of the substrate by necessity exhibit threefold symmetry. The sixfold symmetry in the LEED pattern in the inset of Fig. 7.1(b) is probably due to the fact that the intensities of the diffracted beams of the two sets of threefold symmetric spots at that particular electron energy are accidentally equal. This may well occur

Table 7.2: Distances (in Å) between graphene and the underlying metal layer, Ir or Cu, for high-symmetry positions in graphene/Ir(111) and graphene/Cu/Ir(111) systems, respectively. See Fig. 7.2 for the explanation of the corresponding notations of the high-symmetry positions of the graphene/metal moiré structures.

Position/System	G/Ir(111)	G/Cu/Ir(111)
ATOP	3.581	3.122
FCC	3.280	2.893
HCP	3.274	3.006
BRIDGE	3.315	3.002

because the peaks in the I/V curves may undergo considerable changes in energy due to the fact that the intercalated Cu layer has a slightly different vertical distance from the topmost Ir layer than an extra Ir layer would have.

This modification is revealed in detail using ARPES and a comparison of the results with our DFT calculations. Such data demonstrate deviations from the band structure expected for free-standing or electronically decoupled graphene, and because of the sharp and well-separated Cu 3*d* band spectral features, permit to identify details of band hybridization. Consider the photoemission intensity maps of graphene/Ir(111) and graphene/Cu/Ir(111) in the vicinity of E_F in Fig. 7.4. For graphene/Ir(111) [Fig. 7.4(a)] a clear linear dispersion of the graphene π states is observed around E_F with energy gaps at higher binding energies, due to avoided crossings among the main π band and the replica bands which appear due to the additional periodicity of the moiré lattice [43], as described in chapter 6. By extrapolation we extract a position of the Dirac point at about 100 ± 20 meV above E_F , corresponding to a slight *p*-doping of the graphene layer, in agreement with earlier ARPES data [28, 43]. Intercalation of the Cu layer underneath graphene leads to a significant modification of the valence band states of the graphene layer [Fig. 7.4(b)]. A collection of the characteristic π band positions for graphene/Cu/Ir(111) is given in Table 7.3. In the following I compare the latter sample to pristine graphene/Ir(111), the graphene/Mn/Ir(111) – (2×2) phase

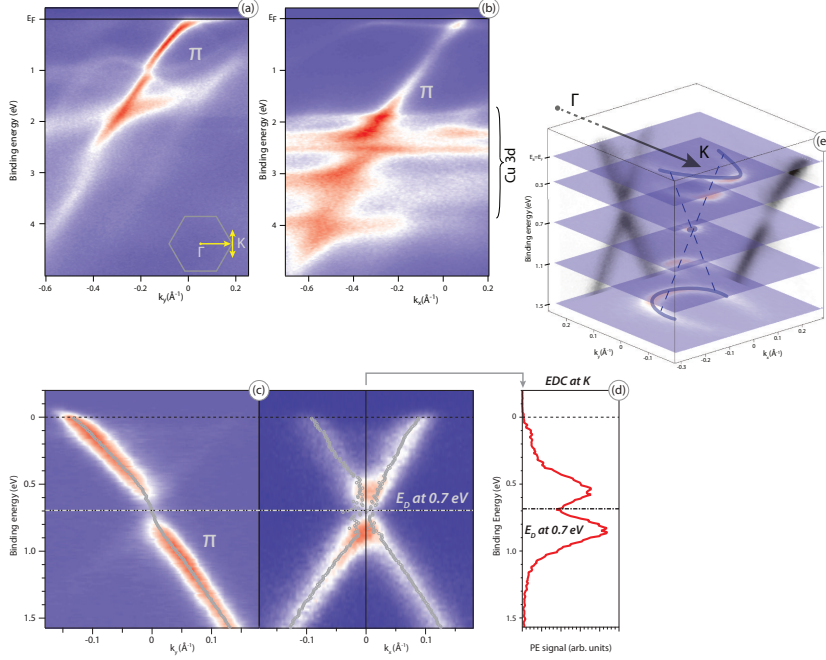


Figure 7.4: Electronic structure of graphene/Ir(111) and graphene/Cu/Ir(111) measured by ARPES. (a) and (b) ARPES intensity maps for the graphene layer on Ir(111) and Cu/Ir(111), respectively, acquired along the Γ -K direction of the BZ of graphene with a photon energy $h\nu = 65$ eV. The inset in (a) shows a graphene-derived BZ with the corresponding directions. (c) ARPES intensity maps acquired along the Γ - K direction of the BZ of graphene (left) and perpendicular to the Γ - K direction (right), using a photon energy of $h\nu = 40.81$ eV. (d) EDC spectrum extracted at the K-point, revealing a gap opening in the π band at the K-point. (e) Overview of the 2-D-k-space dataset of graphene/Cu/Ir(111) measured by ARPES. Depicted is a selection of constant energy surfaces at 400 meV separation in binding energy [blue-red] and ARPES spectra along and perpendicular Γ - K [grey]. The shape of the π band is highlighted [blue line].

Table 7.3: Overview of characteristic positions of graphene's π -band for graphene/Cu/Ir(111), at high symmetric points of the Brillouin zone, compared to pristine graphene/Ir(111), the graphene/Mn/Ir(111) – (2×2) phase (ch. 10.2) and the strongly interacting graphene/Ni/W(110) case (ch. 8.1).

	G/Ir(111)	G/Cu/Ir(111)	G/Mn/Ir(111)	G/Ni/W(110)
			– (2×2) phase –	
Γ	7.8 eV	8.2 eV	9.7 eV	9.9 eV
	$\Delta_{\Gamma M} = 5.2$ eV	$\Delta_{\Gamma M} = 4.5$ eV	$\Delta_{\Gamma M} = 5.8$ eV	$\Delta_{\Gamma M} = 5.4$ eV
M	2.6 eV	3.7 eV	3.9 eV	4.5 eV
	$\Delta_{MK} = 2.7$ eV	$\Delta_{MK} = 3.0$ eV	$\Delta_{MK} = 2.5$ eV	$\Delta_{MK} = 1.9$ eV
K	–0.1 eV	0.7 eV	1.4 eV	2.6 eV

(ch. 10.2), and the strongly interacting graphene/Ni/ W(110) case (ch. 8.1), which are discussed in separate chapters. The difference in the π band positions between the M- and K-point ($\Delta_{MK} = 3.0$ eV) is increased compared to $\Delta_{MK} = 2.7$ eV for the pristine sample. This is unusual compared to other metal intercalates such as Mn, where a reduced value of $\Delta_{MK} = 2.5$ eV is observed in the (2×2) phase (ch. 10.2). This reduction can get as large as for the intercalation of Ni thin films, yielding values of $\Delta_{MK} = 1.9$ eV, as observed for graphene/Ni/W(111). The difference between the Γ - and K-point is affected by the n-type doping as reported for graphene/Cu/Ir(111) and the graphene/Mn/Ir - (2×2) phase. However, the values are reduced towards $\Delta_{\Gamma M} = 4.5$ eV observed for graphene/Cu/Ir(111), as compared to $\Delta_{\Gamma M} = 5.2$ eV for pristine graphene/Ir(111). This is the reverse behavior as seen for the graphene/Mn/Ir - (2×2) phase and the strongly interacting case graphene/Ni/W(110), which both show increased $\Delta_{\Gamma M}$ values. Graphene on Cu/Ir(111) is *n*-doped with a position of the Dirac point at 0.688(10) eV below E_F . Although the π band still has a linear dispersion near E_F , a clear hybridization between the graphene π and Cu $3d$ valence band states in the 2 – 4 eV binding energy region is obvious. This manifests itself as a series of avoided crossing gaps between graphene- and Cu-*d*-derived valence band states [see also Figure 7.8] which is discussed in detail in conjunction with the DFT calculations in section 7.3.

In the spectral function of the graphene π band, an energy gap of 0.36(1) eV appears at the Dirac point. This energy gap is more clearly resolved in photoemission data sets obtained at a photon energy $h\nu = 40.81$ eV presented in Fig. 7.4(c),(d), where ARPES intensity maps around the K point are shown in (c) for the $\Gamma - K$ (left panel) and perpendicular to $\Gamma - K$ (right panel) directions as well as (d) corresponding energy cuts at the respective binding energies marked in the figure. It is surprising that the present values for the energy of the Dirac point E_D and the gap are quite different from those for graphene on bulk Cu(111) ($E_D - E_F = -0.3$ eV; gap = 0.25 eV [186]), and for a single intercalated Cu layer in between graphene and Ni(111) ($E_D - E_F = -0.3$ eV, gap = 0.18 eV, [175]). The different width of the gap for the different graphene/Cu interfaces are likely to be connected with the various periodicities of the corresponding moiré structures as was shown in Ref. [187]. Assuming the pseudomorphic growth of a Cu layer at the interface in all cases, the energy gap has to increase in the row: graphene/Cu/Ni(111) \rightarrow graphene/Cu(111) \rightarrow graphene/Cu/Ir(111).

A line shape analysis depicted in Fig. 9.5 is used in the following to further analyze the band structure with respect to possible quasi-particle interactions. Different coupling mechanisms (electron-phonon, electron-hole pair generation, electron-plasmon and impurity scattering) are considered to influence the spectra [53, 155]. MDC line profiles were extracted from the datasets and a convolution of Lorentzian and Gaussian line profile (Voigt line profile) was used for the analysis of the spectra. Deviations from the linear dispersion of the π band are clearly present. Analyzing the MDC spectra along the ΓK direction, two different strong kinks are apparent, emerging at energies of 0.2 eV and 0.5 eV. Evaluation of the slope of the π band gives a velocity of $v = 0.980(4) \times 10^6$ m s $^{-1}$ for binding energies in the range of (1.1 eV – 1.6 eV), which is only slightly reduced compared to $v = 1.050(4) \times 10^6$ m s $^{-1}$ for pristine graphene/Ir(111) (chapter 6). At energies of 0.5 eV, being above the Dirac energy at 0.7 eV, a significantly reduced velocity with $v = 0.720(3) \times 10^6$ m s $^{-1}$ is observed. A further decrease of the velocity towards $v = 0.580(11) \times 10^6$ m s $^{-1}$ is observed in the region near the Fermi energy at 0.2 eV. The latter reduction in the velocity is most likely due to electron-phonon coupling. Phononic

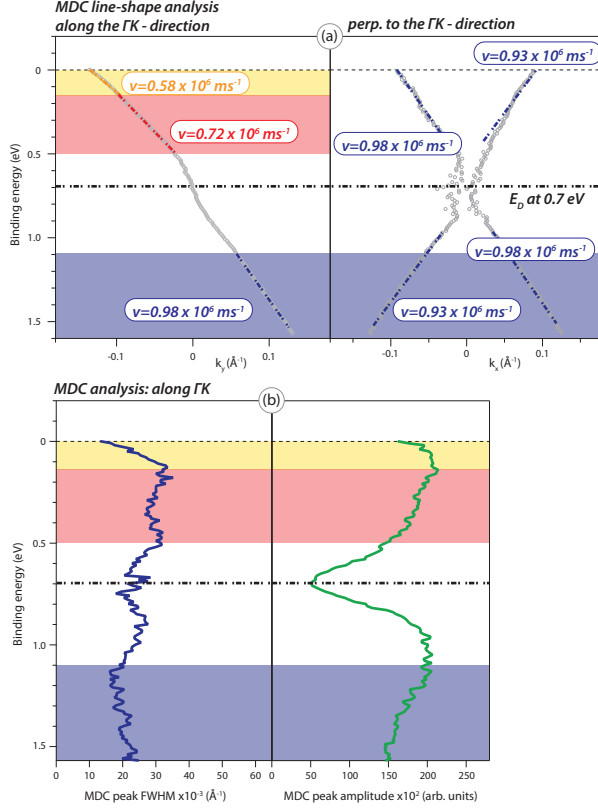


Figure 7.5: MDC line shape analysis of graphene/Cu/Ir(111) around the K-point. (a) Left side: MDC line shape analysis from spectra along the $\Gamma - \text{K}$ direction of the BZ of graphene as depicted in Fig.7.4(c) by Voigt line shapes. Right side: MDC line shape analysis from spectra perpendicular to the $\Gamma - \text{K}$ direction. The derived dispersion regions and corresponding velocities are indicated [blue-red-orange]. (b) Left side: MDC peak line width of the Lorentzian contribution to the Voigt profile; the Gaussian line width is held constant. Right side: MDC amplitude of the Lorentzian.

contributions lead to a kink in the dispersion of graphene, which would emerge at binding energies around $E_{\text{phonon}} = k_B \theta_D = 180 \text{ meV}$, derived from the Debye-temperature θ_D of graphene [188, 189]. Thus in spite of the presence of the metal, which certainly has a screening

influence, the electron-phonon coupling can be clearly discussed, another sign for the fact that graphene on intercalated copper is well decoupled from the substrate.

Regarding the obtained velocities, this behavior is similar to the case of the graphene/Mn/Ir(111) - (2×2) phase, as discussed in chapter 10.2. Here we find, with the Dirac energy at 1.4 eV, a reduced velocity of $v = 0.780(7) \times 10^6 \text{ m s}^{-1}$. Despite the stronger n-type doping and shift of the Dirac energy, promoted by the intercalated Mn thin film acting as electron donor, similar velocities are observed for the region at lower binding energies above E_D . For the direction perpendicular to ΓK the line shape analysis reveals that no distinct kinks in the π band dispersion could be observed. The dispersion of the π band at energies of 1.6 eV yields velocities of $0.930(7) \times 10^6 \text{ m s}^{-1}$ and $0.980(6) \times 10^6 \text{ m s}^{-1}$ for the left and right branch in Fig. 7.5 (a). These values are larger compared to velocities of $0.85(1) \times 10^6 \text{ m s}^{-1}$ derived for pristine graphene/Ir(111) (ch. 6). In the region above the Dirac energy, the dispersion seems to be similar over large ranges for both branches, as compared to velocities obtained for regions below E_D . However, on the right branch of the spectrum some small deviations to the indicated velocity are present. Since this region of the π band is quite far away from the linear behavior near E_D , and trigonal warping effects are likely to be felt, it is probably not surprising that such deviations occur.

7.3 Discussion

The appearance of an energy gap around the K point in the spectrum of the graphene π states is one of the intriguing problems in graphene interface studies, and its existence or absence, for example in graphene on SiC(0001), has been extensively discussed [190, 191]. For single layer graphene on those metals that do not destroy the Dirac cone, *i. e.* the noble metals, Pt, Ru or Ir, gap openings have been observed in photoemission, and this has been attributed to sublattice symmetry breaking induced by a superstructure that couples the states at the K and K' points [192]. As is shown through DFT calculations below, the dominating factor that determines the magnitude of the energy

gap is the strength of hybridization of the graphene-derived π states with the valence band states of the substrate, which leads to a broken symmetry of the two carbon sublattices.

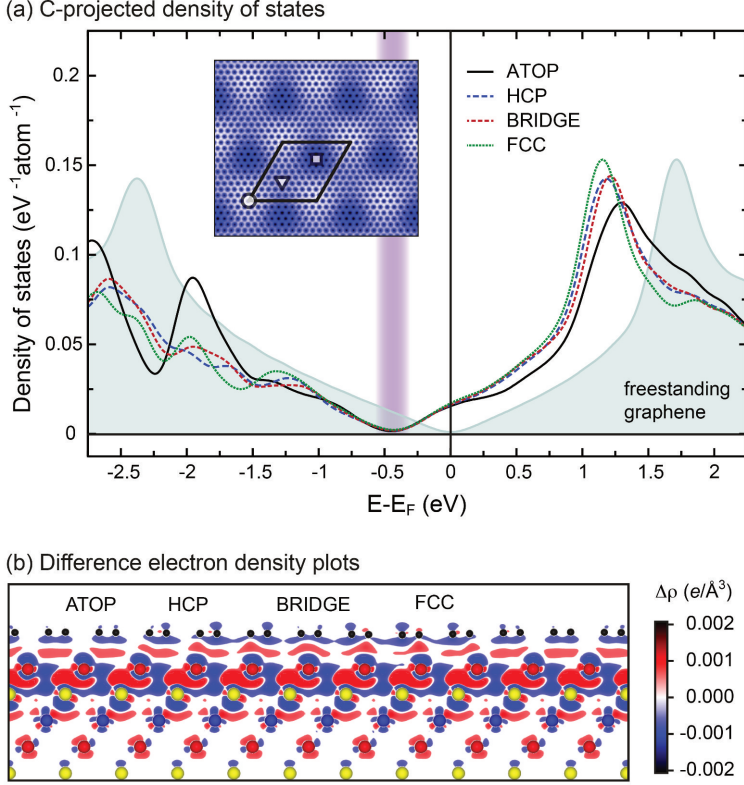


Figure 7.6: Results of the electronic structure DFT modeling for graphene/Cu/Ir(111). (a) Carbon-atom projected site-resolved partial density of states for the graphene-derived π states. The gray area plot shows the corresponding DOS for the free-standing graphene. The band gap region is marked by the shadow area. The inset shows the simulated STM image corresponding to the experimental results obtained at $U_T = -0.3$ V. The high-symmetry positions are marked by the symbols similar to Fig. 7.1. (b) Side view of the graphene/Cu/Ir(111) system with the corresponding difference electron density, $\Delta\rho(r) = \rho_{gr/Cu/Ir(111)}(r) - \rho_{Ir(111)}(r) - \rho_{Cu(111)}(r) - \rho_{gr}(r)$, plotted in units of $e/\text{\AA}^3$.

The analysis of structural features is shown in Fig. 7.1(e). Here the interface metal layer (S) is either Ir or Cu on Ir(111). A pseudomorphic arrangement of the Cu layer on Ir(111) is assumed in the structure optimization procedure, a reasonable assumption in view of the STM data. At the energy minimum, a corrugation of the graphene layer on Cu/Ir(111) of 0.229 Å is found, which is much lower than the one of 0.307 Å for graphene/Ir(111) [110]. The calculated carbon site projected partial density of states (PDOS) for the graphene-derived π states in graphene/Cu/Ir(111) shows that graphene is n-doped with the Dirac point at 0.45 eV binding energy and a band gap of 0.15 eV [Fig. 7.6(a)], whereas the experiments give values of 0.688(10) eV and 0.36(1) eV, respectively [Fig. 7.4(c)]. The computed DOS was obtained by broadening of the originally calculated data for the density of states obtained for the graphene/Cu/Ir(111) supercell in the slab geometry: this broadening gives rise to a reduction of the energy gap, which would be 0.26 eV from the unbroadened data (see Fig. 7.7). The effect of

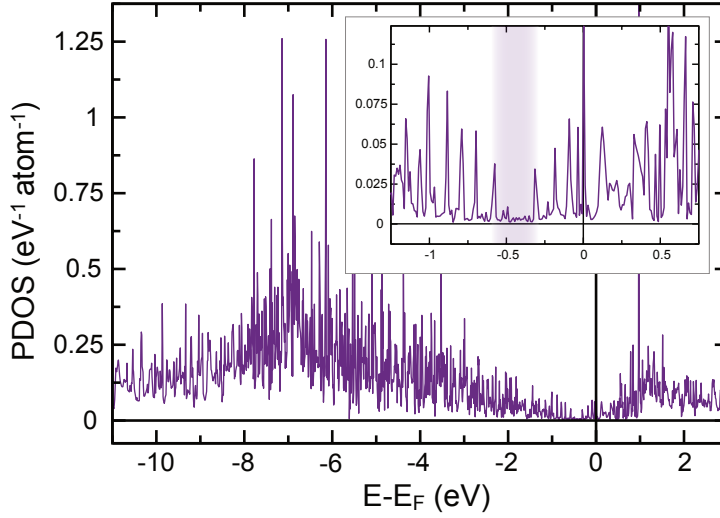


Figure 7.7: Carbon-atom projected total DOS for graphene/Cu/Ir(111). See Vita et al. [193] for details on the calculations. Inset shows the zoom of the DOS plot around band gap and E_F . The band gap region is marked by the shadow area.

hybridization can be visualized in real space in the charge distribution across the moiré unit cell; the corresponding difference in electron density, $\Delta\rho(r)$, defined as a difference of densities for graphene/Cu/Ir(111) and those for the separate layers in the system, is shown in Fig. 7.6(b). The charge distribution picture for the FCC and HCP high symmetry sites is different from the one characteristic for graphene/Ir(111) and similar to the situation for graphene/Ni(111) or graphene/Rh(111) where a strong interaction for these positions is observed. However, here the effect is weaker because the hybridization occurs between the valence states at higher binding energies. This charge distribution was then used to model the STM images. A simulated image corresponding to a bias voltage of $U_T = -0.3$ V is shown as an inset of Fig. 7.6; this is in good agreement with results presented in Fig. 7.1(d). As mentioned above, the ATOP positions of the graphene/Cu/Ir(111) system are imaged as bright areas corresponding to “direct” imaging contrast; this situation prevails over a range from $+0.3$ V and -0.9 V, due to the similarity in the PDOS for different high-symmetry positions in the graphene moiré structure for this system [Fig. 7.6(a)]. In this case the real topography contrast prevails in the STM images of graphene/Cu/Ir(111).

Because of the narrow line widths of the Cu 3*d*-induced bands in photoemission, graphene/Cu/Ir(111) is an excellent example to study the wave vector resolved band hybridization. Five features altogether can be distinguished in the binding energy region from 1.8 eV to 4.0 eV (Fig. 7.8). The avoided crossings of these bands with those derived from the graphene π band are clearly observed [shown enlarged in Fig. 7.8, upper panel, left], and the change of band character at around 2.15 eV, starting from mostly *d*-derived at $k = -0.6 \text{ \AA}^{-1}$ (with respect to the K point) to mostly graphene p_z -derived is evident. Moreover, there are clear differences in the amount of hybridization, reflected in the magnitude of the avoided crossings. Because of the computational cost of deriving the band structure of the complete system (large unit cell of the moiré structure), the calculations were restricted to an assignment of bands calculated for a Cu slab layer with the same lattice constant than graphene, *i. e.* 2.464 Å. These data are shown next to the experimental bands in Fig. 7.8. Because of the slab model, a multitude of bands appear in the calculations; the main weights

of the bands are indicated by color bands. Their relation to the different atomic d states from which they arise is indicated next to the calculation. The calculated bands are close to the experimental bands.

Having shown the occurrence of hybridization of the graphene π and Cu $3d$ valence band states through photoemission, it can be demonstrated that this process is responsible for the appearance of the energy gap in the electronic structure of graphene at the Dirac point. Hybridization leads to an intermixing of the π orbitals with $3d$ orbitals of the corresponding orbital character (symmetry) depending on the carbon atom in the unit cell. According to the picture of Fig. 7.6(b), which shows the charge distribution difference, the most intensive interaction is observed around the FCC and HCP places. Here, one of the carbon atoms is above the interface Cu atom and hybridization between $C^{top} p_z$ and Cu $3d_{z^2}$ orbitals is observed. The second carbon atom is located either above the HCP or FCC hollow site of Cu/Ir(111), and here the hybridization between $C^{fcc,hcp} p_z$ and Cu $3d_{xz,yz}$ orbitals occurs. For free-standing graphene, the electronic states originating from two carbon sublattices are degenerate around the K-point. The interaction of electronic states of carbon atoms with the $3d$ electronic states of different symmetry of the Cu layer then leads to the lifting of this degeneracy and to the opening of the band gap at the K-point. Symmetry breaking is directly reflected in the photoemission data in the region of the Cu d bands. Along the $\Gamma - K$ line, the group of the k -vector in free-standing graphene is C_{3v} , such that carbon p_z -derived bands and those from Cu $d_{xz,yz}$ would not be allowed to interact. However, an avoided crossing between these states, indicative of symmetry reduction, is apparent in the data of (Fig. 7.4). The symmetry must therefore be further reduced on account of the lattice mismatch leading to the moiré structure.

This conclusion is supported by analyzing in DFT the weight of the contributions from different orbitals to the bands below and above the band gap as a function of energy and electron wave vector. The lower panel of Fig. 7.8 shows the weight of the $p_z^{C^{top}} + d_{z^2}^{Cu(S)}$ (top) and the $p_z^{C^{fcc}} + d_{xz,yz}^{Cu(S)}$ (bottom) hybridized states, represented by the thickness of the lines. It is clear that the $p_z + d_{z^2}$ hybrid state dominate the

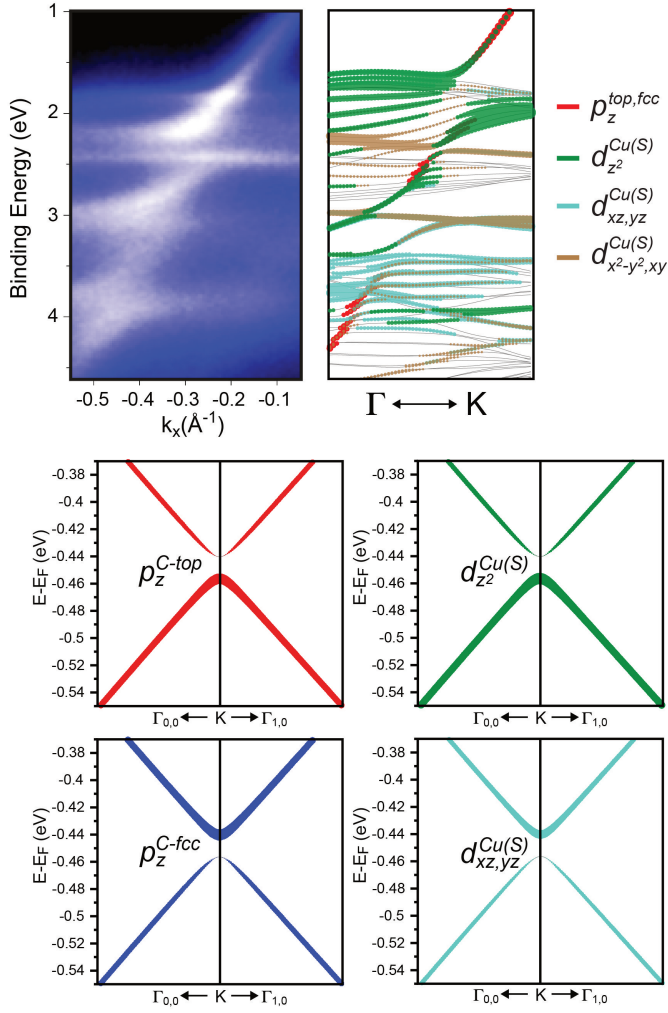


Figure 7.8: Analysis of the electronic structure of graphene/Cu/Ir(111). Upper panel: Comparison of the photoemission images from graphene/Cu/Ir(111) and the calculated electronic structure of graphene/Cu(111), respectively, in the energy and k -vector ranges where hybridization of graphene π and Cu $3d$ states is observed. Lower panel: Orbital character decomposition of the valence band states of graphene in the vicinity of the Dirac point. See Fig. 7.1(e) and Fig. 7.2 with the corresponding text for the definitions of the respective position of the carbon atoms.

bands below the band gap, while the $p_z + d_{xz,yz}$ state dominates the bands above. This clearly shows how hybridization leads to sublattice breaking. Comparing the graphene/Cu/Ir(111) system with the original graphene/Ir(111) interfaces, the interaction or hybridization between graphene valence band states and Ir d orbitals is weaker compared to the Cu d orbitals and hence the sublattice symmetry breaking is more pronounced in the latter case. This is to our knowledge the first case where such a detailed assignment of orbitals contributing to the states around the band gap has been achieved. A similar analysis for graphene on other substrates in which gap opening occurs will permit an understanding of the interplay of substrate and graphene states, and will shed light on the as yet elusive correlation between bonding strength, magnitude of band gap, and its consequences for the structural arrangement.

Thus, STM and photoemission data from an intercalated layer in between graphene and Ir(111), interpreted on the basis of state-of-the-art DFT calculations, permit a detailed analysis of the changes in doping and band gap opening in the graphene π bands upon intercalation of Cu, in terms of state-specific hybridization between the different Cu d and graphene π bands. The strong spatial and energy overlap of the valence band states lead to the lifting of the sublattice symmetry of the carbon atoms which manifests itself as an opening of the band gap at the Dirac point. Analyses of this kind permit to predict the arrangement of the electronic states of graphene in other graphene-metal interfaces [39].

Graphene/Ir(111) – intercalation of cobalt and nickel

As explained in chapter 2.2, an interface of graphene and Co(0001) or Ni(111) may act as spin filter on account of the overlap of only the minority spin states with the electronic states of graphene at the K point of the BZ [11, 12]. Beyond this interesting aspect, there are other reasons why such interfaces may be interesting: first, graphene is known to passivate the reactive ferromagnetic material surface, and hence may render Ni or Co films useful in applications [111]. Second, the graphene film may permit the growth of flat and well-ordered intercalated films of Co and Ni, suppressing their tendency to corrugate and form 3D islands. Finally, the magnetic interaction between Ni or Co and graphene may induce changes in their magnetic anisotropy, compared to films that have an unprotected surface. In this chapter I describe experiments where ultrathin films of Ni and Co – with electronic configuration $[\text{Ar}] 3d^8(4s)^2$ and $[\text{Ar}] 3d^7(4s)^2$ – were intercalated in between Ir(111) and graphene. The intercalation process is examined by means of LEED and core level photoemission, and the changes in the electronic structure of graphene upon intercalation is studied using ARPES. Finally, the magnetic properties (magnitude of spin- and orbital magnetic moments; direction of magnetic coupling either in-plane or out-of-plane) of an evolving Co layer underneath graphene

are measured using XMCD. This study gives a comprehensive view on the graphene/ferromagnet interaction and the emerging magnetic order in the intercalated film.

The growth of high quality films of graphene on transition metals, described in chapter 4.7, is considered as a route towards mass production of large scale transferable graphene [24, 42]. The interaction of graphene with ferromagnetic substrates is also interesting regarding possible spintronic applications. Moreover, ferromagnetic substrates such as Ni(111) and Co(0001) induce a magnetic polarization in graphene [42, 166, 167]. When projected onto the hexagonal surface, only the spin-minority states of the transition metals overlap with graphene valence states at the K-point of the Brillouin zone (BZ) near the Fermi level. Graphene can thus act as a spin filter, and a sizable difference in spin-dependent transmission has been predicted by Karpan et al. [11]. Recent studies by Dedkov and Fonin [42], and Weser et al. [166], show that the proximity of graphene to the ferromagnetic Ni(111) substrate induces a sizable magnetic moment in the carbon π states as determined from C K edge XMCD [42, 166], strengthened when a monolayer of iron is intercalated between the Ni substrate and the graphene layer [167]. Instead of using ferromagnetic single crystals as substrate, we use here the intercalation of magnetic transition metals between graphene and a nonmagnetic substrate [169], as an approach to induce sizable magnetic moments in graphene.

In the following, I describe the influence of thin layers of ferromagnetic Co sandwiched between the non-magnetic Ir(111) and a graphene overlayer. Hence, it becomes possible to examine an emerging ferromagnetic behavior in a thin cobalt film from the monolayer upwards, in a morphology that suppresses islanding, and to study the transfer of magnetic moment from the metal onto the carbon π states. I find that the induced magnetism in the graphene sheet is oriented out-of-plane and exhibits an anti-ferromagnetic coupling with respect to the underlying Co thin film an anti-ferromagnetic coupling. Further, regarding the magnitude of the magnetic coupling, the results of the XMCD studies are complemented by state-of-the art density-functional theory (DFT) calculations. The main parts of the described studies in this section have been published in

- H. Vita, S. Böttcher, P. Leicht, K. Horn, A. B. Shick and F. Máca (2014). “Electronic structure and magnetic properties of cobalt intercalated in graphene on Ir(111).” *Physical Review B* **90**, Article number: 165432.

with myself as the principal investigator, and the assistance of Stefan Böttcher under the supervision of Karsten Horn.

8.1 Intercalation of nickel

Let us first discuss the electronic band structure of graphene on Ni thin films, prepared by intercalation of 2 ML of Ni – graphene/Ni/Ir(111), and compare these measurements with graphene/Ni/W(110) as reference. An amount of 2 ML of Ni is deposited on top of graphene/Ir(111) with the sample kept at room temperature. The intercalation of Ni atoms underneath a graphene sheet occurs upon annealing of the sample to 400 °C, and is monitored by C 1s core level spectra in Fig. 8.1(a) and (b). After the deposition of Ni atoms on top of graphene, the C 1s core level intensity is reduced, following an exponential decay (equation 4.3). As soon as the thermal activation due to annealing of the sample exceeds a certain energy barrier, the intercalation mechanism is initiated, yielding a pronounced chemical shift of the C 1s core level of about 760 meV compared to pristine graphene/Ir(111).

Table 8.1: Overview of the C 1s peak position for the intercalated system graphene/Ni/Ir(111) compared to highly oriented pyrolytic graphite (HOPG) [194, 195], graphene/Ir(111), and for different substrates: graphene/Ni/W(110) and graphene/Ni(111) [196, 197].

	HOPG	G/Ir(111)	G/Ni/Ir(111)	G/Ni/W(110)	G/Ni(111)
C 1s	284.23 eV	284.17 eV	284.90 eV	284.62 eV	285.00 eV

An overview of the C 1s core level positions for the different systems under study as well as for HOPG and graphene/Ni(111) as references is given in Table 8.1. The values for pristine graphene/Ir(111) agree well with previously published data by Preobrajenski et al. [195]. A large chemical shift of 760 meV occurs for the intercalated Ni thin

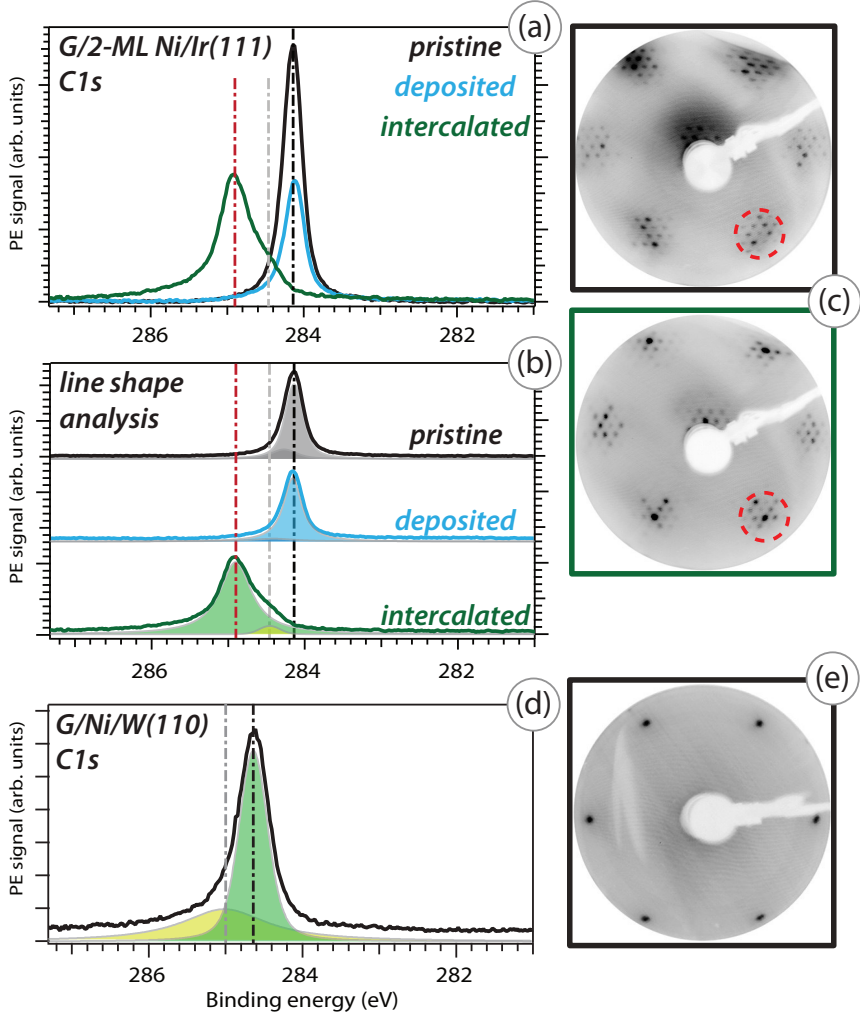


Figure 8.1: Overview of the C 1s core level spectra showing in (a) the intercalation process from graphene/Ir(111) [black] and Ni/graphene/Ir(111) [blue] towards graphene/Ni/Ir(111) [green], using a photon energy of $h\nu = 400$ eV. (b) Line shape analysis of the C 1s core level, showing a shift towards 284.95 eV for the Ni intercalated sample. (c) LEED images for pristine graphene/Ir(111) [black], indicating the moiré structure, and graphene/Ni/Ir(111) [green], showing the pseudomorphic arrangement of Ni. (e) Graphene/Ni/W(110) is given for comparison. All LEED images are taken at 100 eV. (d) Graphene/Ni/W(110) C 1s core level spectra.

films – graphene/Ni/Ir(111) – thus approaching the C 1s core level position of graphene/Ni(111). In graphene/Ni/W(110) a different position of the C 1s core level is found (284.62 eV). This agrees well with studies by Grüneis et al. [198], reporting a similar position of the C 1s core level (284.7 eV). Following the work of Zhao et al. [197] a model of a mixture of HCP and BRIDGE positions of graphene grown on Ni(111) gives a possible explanation for the different position of the C 1s core level for graphene/Ni/W(110) in Fig. 8.1 (d) in the sense that BRIDGE graphene is mainly formed. The BRIDGE orientation could be preferred due to pinning by defects. STM measurements and density functional theory calculations reported recently by Pacilé et al. [171], indicate that the intercalation of thin Ni films underneath graphene yields a pronounced increase in the corrugation of the graphene sheet. The relatively small corrugation of about 0.27 Å, reported for graphene/Ir(111) [115], is increased to values of about 1.51 Å for graphene/Ni/Ir(111) [171]. In the LEED images of Fig. 8.1(c), the diffraction spots of the regular moiré pattern of graphene/Ir(111) show a strongly increased contrast for the graphene/Ni/Ir(111) case, yielding a star-like shape. In contrast to the intercalated Ni film, the preparation of graphene on Ni yields a lattice-matched situation; consequently, a 1×1 LEED pattern is observed in Fig. 8.1(e).

The electronic band structure of graphene/Ni/Ir(111) depicted in Fig. 8.2(a) exhibits distinct differences to pristine graphene/Ir(111) (chapter 6.2). First of all, the electronic band structure associated with the graphene π -band exhibits a strong n-doping, shifting the bottom of the π -band to higher binding energies. Second, the features of graphene/Ir(111), attributed to almost freestanding graphene – a Dirac cone with linear dispersing π -band and low doping – are absent in graphene/Ni/Ir(111). Finally, the replica cones, which are present in graphene/Ir(111), attributed to the lattice-mismatch between graphene and the underlying Ir substrate, are suppressed in graphene/Ni/Ir(111). For comparison, the electronic band structure of graphene/Ni/W(110) is given in Fig. 8.2(b), largely matching the band structure of graphene/Ni/Ir(111).

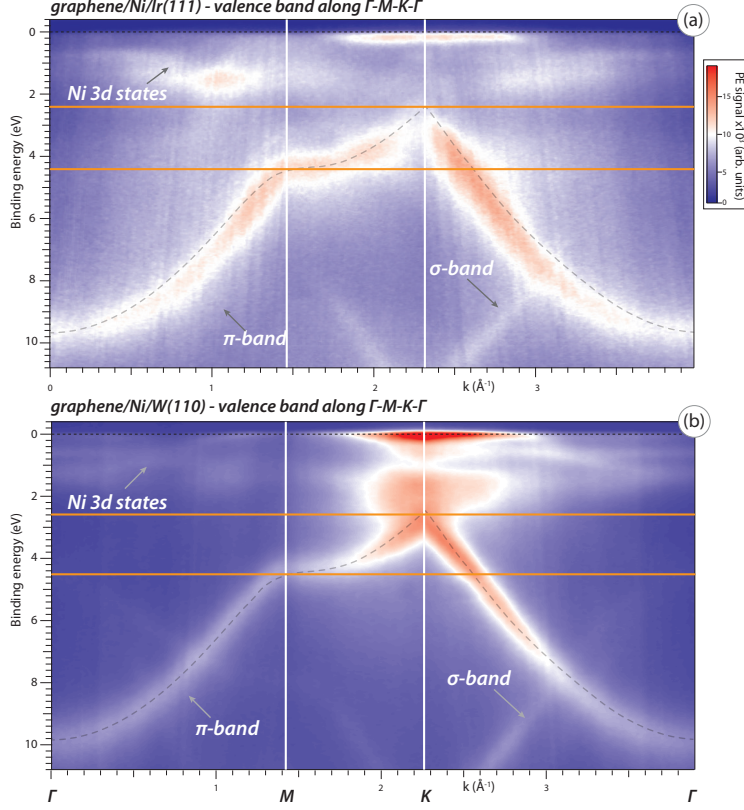


Figure 8.2: ARPES data of graphene/Ni/Ir(111) (a) and graphene/Ni/W(110) (b). Intensity maps acquired along the $\Gamma - M - K - \Gamma$ direction of the first Brillouin zone of graphene using a photon energy of $h\nu = 65$ eV. The orange line gives the π band positions at K and M.

However, the π -band is shifted to slightly higher binding energies; its position at the high symmetric points $\Gamma - M - K - \Gamma$ of the Brillouin zone are summarized in Table 8.2 below. Starting from pristine graphene/Ir(111) a shift in the energy of the π -band at the Γ , M and K-points is apparent, with increasing thickness of the underlying Ni film from graphene/Ni/Ir(111) towards graphene/Ni/W(110) and finally graphene on bulk Ni. The energy difference of the π band at Γ and M ($\Delta_{\Gamma M} \sim 5.3$ eV) is similar for all four cases, but the distance

Table 8.2: Overview of characteristic energetics of graphene’s π -band for graphene/Ni/Ir(111) at high symmetric points of the Brillouin zone, compared to graphene/Ir(111), and different substrates: graphene/Ni/W(110) and graphene/Ni(111) [199].

	G/Ir(111)	G/Ni/Ir(111)	G/Ni/W(110)	G/Ni(111)
Γ	7.8 eV	9.7 eV	9.9 eV	10.1 eV
	$\Delta_{\Gamma\text{M}} = 5.2 \text{ eV}$	$\Delta_{\Gamma\text{M}} = 5.3 \text{ eV}$	$\Delta_{\Gamma\text{M}} = 5.4 \text{ eV}$	$\Delta_{\Gamma\text{M}} = 5.3 \text{ eV}$
M	2.6 eV	4.4 eV	4.5 eV	4.8 eV
	$\Delta_{\text{MK}} = 2.7 \text{ eV}$	$\Delta_{\text{MK}} = 2.0 \text{ eV}$	$\Delta_{\text{MK}} = 1.9 \text{ eV}$	$\Delta_{\text{MK}} = 2.0 \text{ eV}$
K	-0.1 eV	2.4 eV	2.6 eV	2.8 eV

between M point and the K point ($\Delta_{\text{MK}} = 2.7 \text{ eV}$) for graphene/Ir(111) is distinctly different from the latter three Ni substrates ($\Delta_{\text{MK}} \sim 2.0 \text{ eV}$).

The difference in shift of the graphene π -band at the various points in the BZ indicates a behavior beyond a simple rigid shift scenario, observed *e. g.* by doping graphene with potassium [200]. This is most likely due to the hybridization between the electronic states with Ni 3*d* character, located around $E_B = 2.0 \text{ eV}$ and the graphene π -band in the region around the K-point leading to the formation of so-called “interface states” at the K-point, as discussed by Bertoni et al. [40]. Graphene on all three Ni substrates show this strong hybridization between the π -states and Ni 3*d*-states, whereas it is absent in graphene/Ir(111) [43]. A reason for this behavior is that the bulk-related Ir 5*d*-states are absent in the region around the K point. ARPES studies for Ir(111) by Pletikosić et al. [201] show the formation of a band gap around the K point. This is believed to be a prerequisite for the emerging linearly dispersing π band around the K point, as observed in graphene/Ir(111).

Feasibility of XMCD studies on graphene/Ni/Ir(111)

Prior to measuring the magnetic properties of graphene/Ni/Ir(111), it is necessary to find out what the exact limits of XMCD experiments at beamline D1011 are, *i. e.* whether magnetic order in thin Ni and Co films can be achieved at the available magnetic fields (500 Oe)

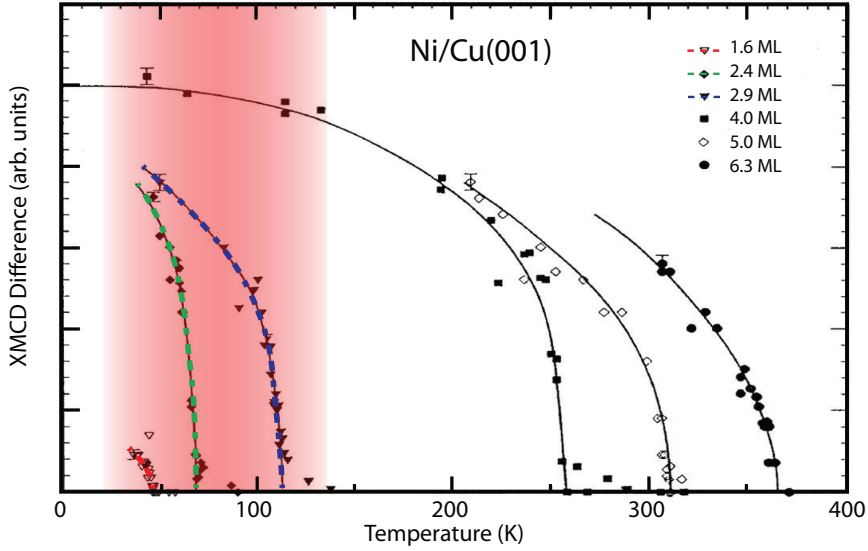


Figure 8.3: Behavior of the XMCD signal, as a function of the temperature for different thickness of Ni thin films on Cu(001), taken from Baberschke [202]. For thin films of about 2 ML of Ni, the magnetic ordering as reflected by the strength of the XMCD signal is strongly quenched around 60 K.

and sample temperature ($T = 90$ K). XMCD studies by Baberschke [202], have shown that in-plane ferromagnetic coupling of Ni/Cu(001) can be obtained at various Ni film thicknesses (Fig. 8.3). Unfortunately, magnetic ordering as reflected by the strength of the XMCD signal is strongly quenched around 60 K for thin Ni films of about 2 ML, indicating a strong decrease in the Curie temperature T_C . Therefore, studying intercalated Ni thin films of graphene/2 ML Ni/Ir(111) does not seem promising. Some estimates information on the magnetic behavior of graphene/Ni/Ir(111) can be derived from a comparison of hysteresis loop measurements of various Ni film thicknesses of Ni/Au(111) by Gundel et al. [203]. Rather thick Ni films (11.5 ML) show a distinct in-plane ferromagnetic behavior, with saturation easily reached by magnetic fields of 500 Oe. The hysteresis loop is almost completely quenched for thinner Ni films (6.7 ML Ni/Au(111)) [203]. This renders the chances for inducing magnetic order and observation in an XMCD experiment on graphene/2 ML Ni/Ir(111) questionable

with the available low magnetic static fields of 500 Oe. However, an alternative path towards studying emerging magnetic behavior in thin metal films intercalated underneath graphene/Ir(111), is to use Co instead of Ni because Co possesses a much higher Curie temperature even at low metal film coverages. This system was thus chosen to study the interactions of thin ferromagnetic films with graphene.

8.2 Intercalation of cobalt

Let us now compare the magnetic behavior of thin Co films deposited on Au(111), in order to consider the feasibility of possible XMCD experiments on graphene/Co/Ir(111). The hysteresis loop of Co on

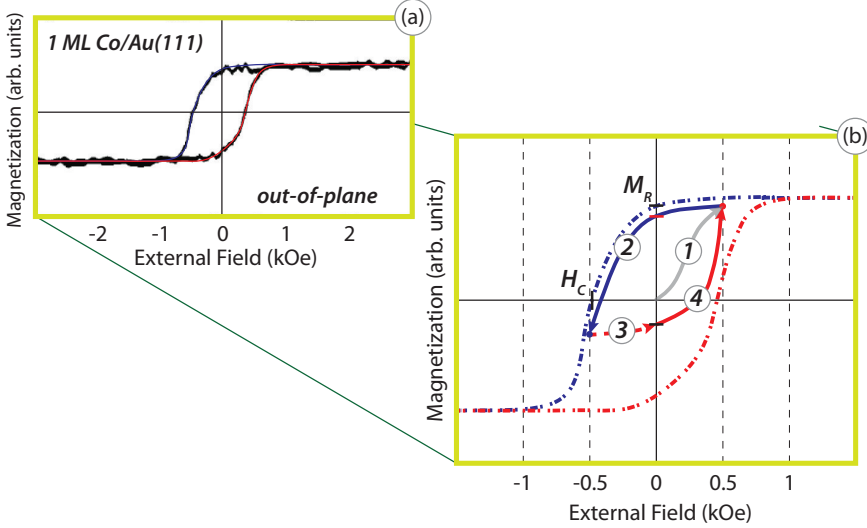


Figure 8.4: (a) Hysteresis loop for different thickness of Co films on Au(111), taken from Gundel et al. [203]. (b) Sketch of the hysteresis loop for 1 ML Co/Au(111) as shown in (a). For thin films (1 ML Co), the system shows a distinct out-of-plane ferromagnetic behavior. However, saturation is not reached by applying magnetic fields of 500 Oe.

Au(111), from Gundel et al. [203] is depicted in Fig. 8.4 (a). For thin films (1 ML Co), the system shows a distinct out-of-plane ferromagnetic behavior. For thicker films of Co, the easy axis is switched towards the

in-plane direction, due to contributions of the shape anisotropy [203]. Figure 8.4 (b) is a sketch of the hysteresis for 1 ML Co/Au(111), using an external field of ± 500 Oe. Different paths are indicated on the hysteresis loop: (1) initial magnetization following the so-called “Neukurve”, using $+500$ Oe. (2) the obtained remanent magnetization – M_R – in the absence of an external field and the partial reversal of the magnetization. A certain value for the external field is needed to bring the magnetization to zero. This value is called coercivity – H_C – and amounts to about -500 Oe. (3) indicates the remanent magnetization obtained by using the switched field. M_R is in this case always smaller compared to the value obtained following the initial magnetization curve (1). (4) Magnetization of the sample using the initial direction for the external field $+500$ Oe. This shows that a reversal of the induced magnetization is only partially possible by external magnetic fields of this magnitude [path (2) in Fig. 8.4 (b)].

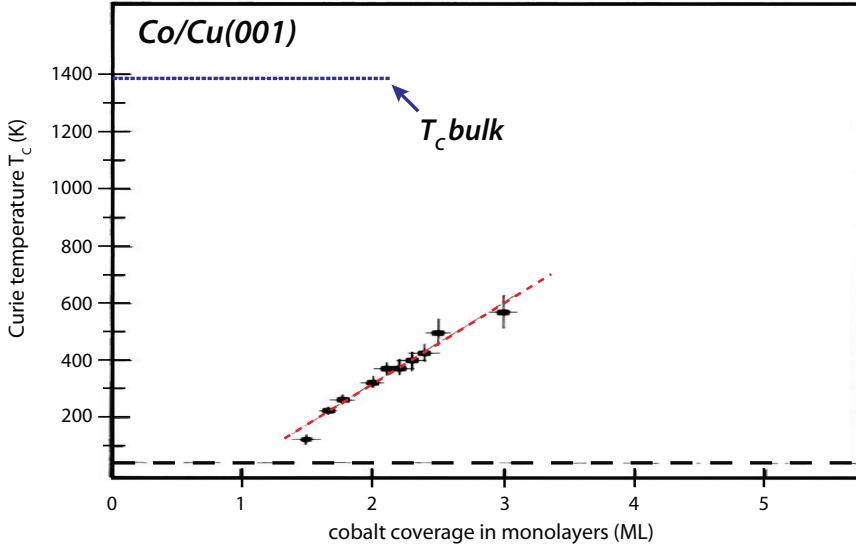


Figure 8.5: Behavior of the Curie temperature for different thicknesses of Co films on Cu(100), compared to the bulk value of $T_C = 1394$ K, taken from Schneider et al. [204].

However, as described in chapter 3.2.3, XMCD data can be obtained using a magnetically oriented sample and changing the direction of polarization of the incoming photons. In this context, an interesting observation is that covering Co thin films by graphene acts as a protecting layer, which increases the perpendicular magnetic anisotropy (PMA) to about twice the value of the uncovered film, as shown by Rougemaille et al. [205] using spin-polarized low energy electron microscopy (SPLEEM). The second important parameter for XMCD studies is the Curie temperature T_C of ferromagnetic materials. The induced magnetism in the sample results from oriented magnetic moments, which persist in remanence. Above T_C this ordering is lost. Fig. 8.5 depicts the behavior of the Curie temperature for Co films of varying thickness on Cu(100), by Schneider et al. [204] using the surface magneto-optical Kerr effect (SMOKE). For 2 ML of Co/Cu(100) a Curie temperature of about 250 K is obtained. This value is well above our sample temperatures of 90 K available at D 1011. That means that the magnetic order in the Co thin film intercalated in graphene/Ir(111), should be maintained during XMCD experiments.

Experimental methods

The experiments were performed at beamline D1011 of MAX-lab, and at beamline UE56/2-PGM1 at BESSY II. In order to preserve the orientation of the magnetic moments, all measurements were performed at a low temperature of $T = 90$ K. The x-ray absorption spectroscopy (XAS) and XMCD spectra were collected at both the Co $L_{2,3}$ and the C K absorption edges in partial electron yield (PEY) and total electron yield (TEY) mode with an energy resolution of 100 meV. After applying a magnetic field of 500 Oe along the out-of-plane direction, circularly polarized light (degree of polarization $P = 75\%$) was used to measure the magnetic dichroism spectra. Performing XMCD measurements by changing the polarization of light means that the accuracy of the degree of circular polarization of the beamline becomes important. This was verified in studies by Dunn et al. [206] and Preobrajenski [207]. The authors find that the theoretical value of the polarization at D1011 is slightly higher compared to the real polarization measured in the experiment. This is taken into account in the evaluation of the magnetic moments derived from the XMCD data by using a pre-

factor. The sample was pre-aligned along the $\Gamma - K$ direction of the graphene Brillouin zone with the angle dispersive data acquired perpendicular to $\Gamma - K$. For the preparation of graphene/Ir(111), the recipe described in chapter 4.7 was used to obtain the high quality single-phase $R0^\circ$ graphene on Ir(111), as characterized by Hattab et al. [159]. Low-energy electron diffraction (LEED) was used to verify the quality of the graphene/Ir(111) sample prior to Co deposition, showing the characteristic hexagonal pattern with sharp main spots, and the satellite spots due to the moiré structure (ch. 6.3) as shown by N'Diaye et al. [108]. The XPS spectra measured at the C 1s core level revealed the high quality of the graphene/Ir(111) sample by a sharp single component line with no additional peaks at higher binding energies, as shown in Fig. 8.6 (a).

Experimental results

For the present case of Co intercalation in graphene/Ir(111) [170, 205, 208–210], a considerable lattice mismatch between Co and Ir occurs, similar to the case of an intercalated Ni monolayer [171]. Since the Co film takes up the lattice constant of Ir, this gives the opportunity to examine the electronic structure of thin metallic films under tensile stress, but also necessitates a close examination of the growth mode at the monolayer stage and beyond. An amount of 2 ML of Co, estimated by calibration with a quartz microbalance prior to the experiment, is deposited on top of graphene/Ir(111). During the deposition C 1s and Ir 4f core-level photoemission spectra were taken [Fig. 8.7 (a) (c)] with the sample kept at $T = 100$ K. To study the temperature dependent behavior of the line shapes C 1s and Ir 4f core-level photoemission spectra are measured during the intercalation process as shown in Fig. 8.7 (a) and (b), reflecting the changes in the system from Co on top of graphene towards the formation of 2 monolayers of Co underneath graphene/Ir(111). The C 1s core level for different steps of sample preparation is shown in Fig. 8.6 (a) for pristine graphene/Ir(111) [black line], towards 2 ML of Co deposited on graphene/Ir(111) [blue line] and finally intercalated graphene/Co/Ir(111) [green line]. A line shape analysis in Fig. 8.6 (b) using Voigt profiles [144] yields a peak position of 284.170(2) eV for the initial C 1s core-level spectra. Assuming a confidence interval of 3σ , one obtains, with 0.002 eV a

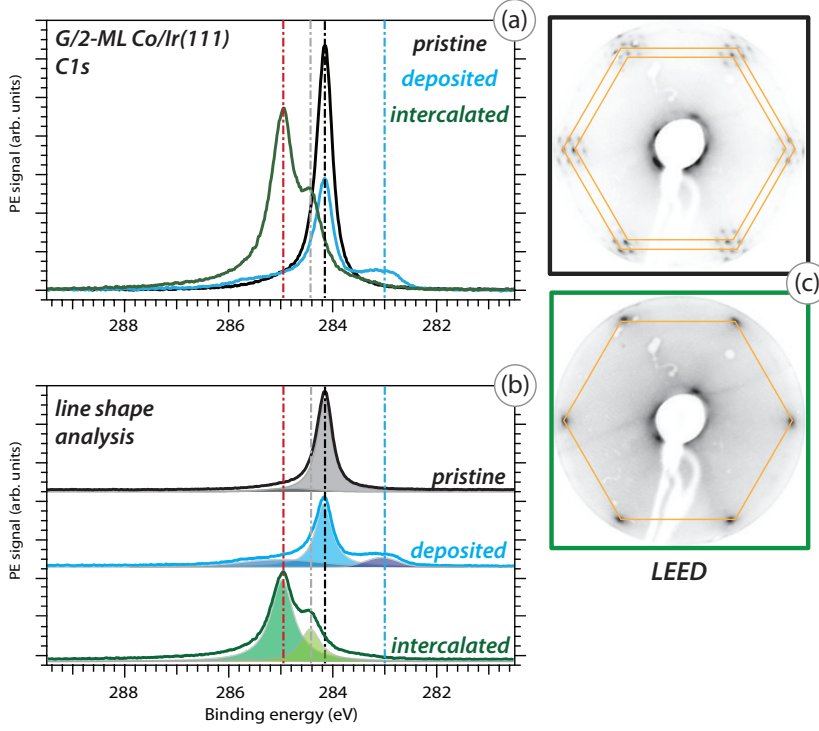


Figure 8.6: Overview of the XPS C 1s core level spectra showing the intercalation process from (a) graphene/Ir(111) [black] and Co/graphene/Ir(111) [blue] towards graphene/Co/Ir(111) [green], measured at the ARPES station at BESSY II, using $h\nu = 400$ eV radiation. (b) Line shape analysis of the C 1s core level. (c) LEED images for graphene/Ir(111) [black] and graphene/Co/Ir(111) [green].

negligible deviation from the peak position. The main peak is reduced in intensity upon Co deposition on top of graphene up to a coverage of 2 monolayers' equivalent. Because of the low sample temperature, we assume that the deposited film grows in a disordered layer wise manner. An additional broad peak around 283.00 eV can be related to the formation of a surface Co-C carbide, as described by Ye et al. [211]. The intercalation of the 2 monolayer (ML)-thick Co layer underneath graphene is performed via stepwise annealing of the deposited layer of

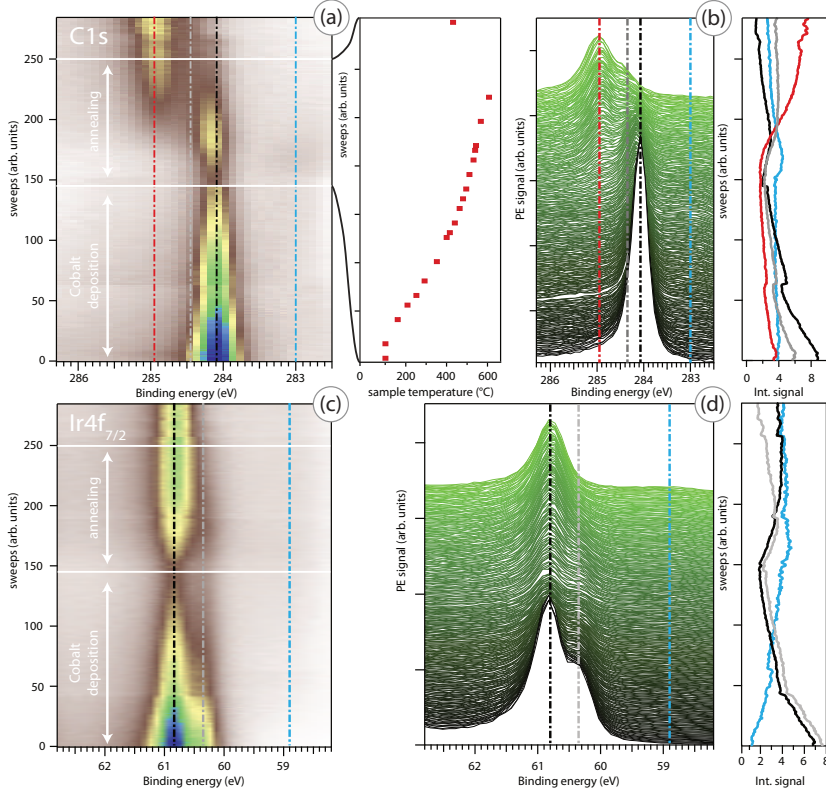


Figure 8.7: (a) and (c) Changes in C 1s and Ir 4f line shape upon deposition (up to sweep 145) and annealing, as false color plots [(a) and (c)] and waterfall plot [(b) and (d)]. Right side of (b) and (d): Extracted intensity at certain energies E_B indicated by dashed lines in the core-level spectra, emphasizing the changes in the C 1s and Ir 4f line shape during intercalation. See text for discussion.

Co on graphene/Ir(111) – depicted in Fig. 8.7. In this procedure, the intensity of the C 1s and Ir 4f lines, observed in “real-time”, is followed to uncover when the temperature required for successful intercalation is reached [Figs. 8.7 (a) and 8.7 (c)] as in the case of Cu intercalation (ch. 7). This method permits to carefully control the formation of an intercalated Co film underneath graphene/Ir(111). Upon intercalation, the Co-C carbide peak vanishes and the main C 1s peak is strongly

Table 8.3: Overview of the main C 1s peak position for the intercalated system graphene/2ML Co/Ir(111) compared to the initial system graphene/Ir(111), and the graphene/15 ML Co/W(110) system mimicking a Co(0001) substrate Pacilé et al. [209].

	G/Ir(111)	G/2 ML Co/Ir(111)	G/15 ML Co/W(110)
C 1s	284.17 eV	284.95 eV	284.6 eV [209]

shifted towards higher binding energies, by 780 meV to 284.95 eV, as shown in Fig. 8.6 (b). Again the error bar is with 0.002 eV negligible for the determination of the peak position. The positions of the C 1s peaks are collected in Table 8.3. It is concluded that the Co film is completely intercalated, since the structure of the C 1s spectra reaches a stable shape with no further intensity changes or shifts in binding energy.

The effective intercalation of a thin Co layer, and the formation of graphene/Co/ Ir(111) occurs at 400 °C, identified by strong modifications of the C 1s emission lines [Figs. 8.6 (a) and 8.7 (a) and (b)]. The C 1s peak now has an additional second component at lower binding energies (284.35 eV) derived from the line shape analysis in Fig. 8.6 (b). This situation seems similar to the case of graphene on bulk Ni(111) as described earlier, where different absorption geometries of the carbon atoms (HCP and BRIDGE) are believed to coexist, leading to a second component in the C 1s spectrum at 284.46 eV as interpreted by Zhao et al. [197]. Shortly after the publication of the main findings of our study in Vita et al. [212], work by Pacilé et al. [209] was published, focusing on the electronic properties of graphene/Co/Ir(111) with different amounts of intercalated Co layers (1 ML up to 4 ML). The authors find about the same positions for the C 1s core level peaks and assign the two main contributions for graphene/Co/Ir(111) to different absorption sites of the carbon atoms in valleys (284.92 eV) and hills (284.42 eV) connected to the corrugation of the graphene layer. Further intercalation up to 4 ML Co lead in their studies [209] to a relaxation of the Co film allowing the formation of a purely commensurate graphene sheet on top. For graphene/2 ML Co/Ir(111) we find an intermediate case between the mismatched moiré phase – 1 ML Co – and the com-

mensurate (1×1) phase – 4 ML Co – since the double peak structure in the C 1s being weak but still present. Hence the LEED image in Fig. 8.6 (c) shows mainly a (1×1) pattern with traces of moiré spots left. My experiments using Ni as intercalant in chapter 8.1 support a similar conclusion. Studies on graphene/Ni/Ir(111) by Pacilé et al. [171] observed a similarly strong asymmetry towards lower binding energy in the C 1s line shape, which also indicates the presence of a second component. The fact that the spectra presented in [171] were measured at room temperature with lower resolution, compared to the presented ones in Fig. 8.6 (a) probably accounts for the line shape with two clearly resolved components in our case. In the Ir 4f spectra, the interface component is suppressed and only the two bulk components of the Ir 4f levels remain. The changes induced by intercalation of Co

Table 8.4: Overview of characteristic positions of the graphene π -band for graphene/2 ML Co/Ir(111) at high symmetric points of the Brillouin zone, compared to the pristine system graphene/Ir(111).

	G/Ir(111)	G/2 ML Co/Ir(111)
Γ -point	7.8 eV	9.7 eV
	$\Delta_{\Gamma M} = 5.2$ eV	$\Delta_{\Gamma M} = 5.2$ eV
M-point	2.6 eV	4.5 eV
	$\Delta_{MK} = 2.7$ eV	$\Delta_{MK} = 2.0$ eV
K-point	-0.1 eV	2.5 eV

are even more strongly reflected in the valence electronic structure, as evident from the angle-resolved photoemission spectroscopy (ARPES) data in Fig. 8.8 (a) and (b) and summarized in Table 8.4. In the top left dispersion plot of Fig. 8.8, which shows the photoemission signal intensity along the high-symmetry directions of the graphene Brillouin zone, the sharp π band, extending from about 7.8 eV binding energy at the Γ point right up to the Fermi energy at the K point is clearly evident. The band exhibits small hybridization gaps where it collides with satellite π bands brought about by the reciprocal lattice vectors of the large moiré structure unit cell, *i. e.* the lattice mismatch between graphene and Ir(111) (chapter 6.2). Sharp features in the

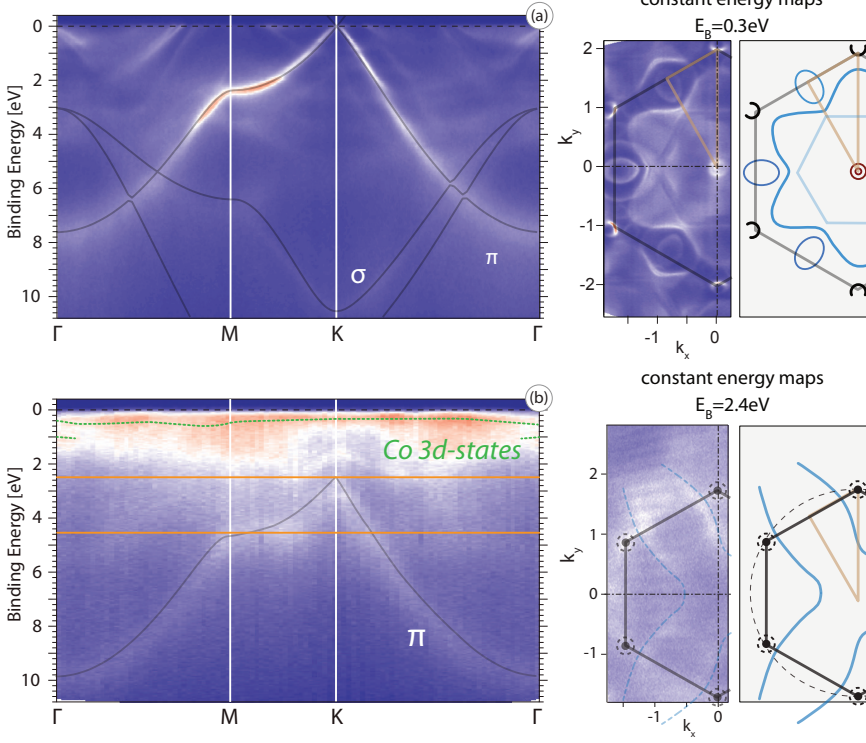


Figure 8.8: (a) ARPES intensity maps for the graphene layer on Ir(111) acquired along the $\Gamma-M-K-\Gamma$ direction of the BZ of graphene with photon energy $h\nu = 65\text{ eV}$. The gray line shows a calculated band structure for a free-standing graphene film [149]. (b) Constant energy surface at $E_B = 0.3\text{ eV}$ extracted from the ARPES measurements. The main features in red are derived from the Ir(111) surface state, the graphene Dirac cones [black], and the Ir bulk bands [blue]. (c) Upon intercalation of 2 ML Co, the graphene π band is shifted to higher binding energy due to strong hybridization effects with Co 3d states (photon energy $h\nu = 94\text{ eV}$). The main features of the Co film intercalated under graphene/Ir(111) are derived from Co 3d states [dashed green line] near the Fermi energy. (d) Constant energy surface at $E_B = 2.4\text{ eV}$ extracted from the ARPES measurements. The sketch of the constant energy surface shows the main features derived from trigonal shaped Ir d states [blue line] of the substrate. π band positions at K and M indicated [orange].

region from E_F to (2 – 3 eV) binding energy are due to iridium bands of d character, also visible in the constant energy cut on the right-hand side, at 0.3 eV binding energy. The sharp features are assigned to Ir surface states (red), graphene Dirac cones (black) including the clearly visible satellite cones, and the bulk Ir bands, in good agreement with literature data [91]. Intercalation reduces the sharp features in the d -band region [Fig. 8.8(c)], or rather masks them through their dominating intensity, in the region from (0 – 2 eV) binding energy. Sharp dispersing features can still be seen here, *e. g.*, between Γ and M and even more so between K and Γ . The π band, which is strongly shifted downwards (its bottom at Γ shifted by about 2 eV), is weaker but can still be followed. It is also clear that the π bands at K end at about 2.5 eV, similar to previously published results for graphene/Co(0001) by Varykhalov and Rader [213]. Altogether, the behavior of the π band in the ARPES data of the graphene/Co/Ir(111) system resembles the valence electronic structure of graphene/Ni/Ir(111) as discussed in chapter 8.1. In the constant energy plot of Fig. 8.8 (c), clear evidence for dispersing Co $3d$ bands is found; this supports our assumption that the Co intercalated layers are well ordered.

Graphene/Co/Ir(111) – XMCD results

Let us now turn to the quantitative investigation of the magnetic properties of the intercalated Co layer for different thicknesses, and a comparison of these data with theoretical predictions. To reveal the magnetic coupling behavior and to quantitatively determine the related magnetic moments of the graphene/2 ML Co/Ir(111) system, x-ray magnetic circular dichroism (XMCD), as explained in chapter 3.2.3, is used. First of all, our XMCD data for a single intercalated Co layer (not shown here) give no magnetic contrast at the Co $L_{2,3}$ edge. This is most likely due to insufficient sample cooling, since the Curie temperature for a single layer is expected to be below our sample temperature of 90 K – see also Fig. 8.5 – in analogy with data from thin Ni films [202]. Moreover, the structural properties of the Co monolayer, yielding a stretched Co layer to match with the underlying Ir lattice [209], as mentioned earlier, could be a further evidence for the absence of magnetic ordering in our XMCD measurements on graphene/1 ML Co/Ir(111). Increasing the amount of intercalated Co,

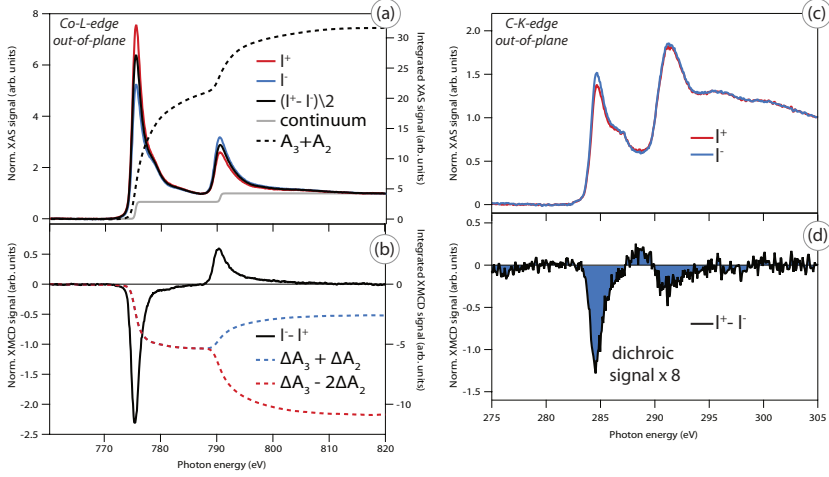


Figure 8.9: (a) XMCD spectra of graphene/2 ML Co/Ir(111) measured in an out-of-plane geometry at the Co $L_{2,3}$ absorption edge for two opposite directions (red and blue). The black line in (b) is the corresponding difference spectrum. The areas under the curves are indicated by broken lines. (c) XMCD spectra of graphene/2 ML Co/Ir(111) measured at the C K absorption edge with the circularly polarized light for two opposite directions (blue and red). The black line in (d) represents the corresponding difference spectrum. The C K edge shows anti-ferromagnetic coupling with respect to the Co $L_{2,3}$ absorption edge.

either in a single deposition/annealing cycle or several cycles, leads to the appearance of magnetic contrast as shown in Fig. 8.9. Quantitative data on the magnetic moments of the cobalt and carbon layers are evaluated from the absorption data, as explained in chapter 5.3. The upper part of Fig. 8.9 (a) shows the XAS intensity at the Co $L_{2,3}$ edge taken with different (right and left), circularly polarized light. The XMCD spectrum [black line in the lower part of Fig. 8.9 (a)] is obtained by the difference $\Delta I = I^+ - I^-$, leading to a negative signal at the Co L_3 edge. The spectra are normalized to the edge jump by subtraction of a Fermi function taken at the center of the L_3 and L_2 edges, as discussed by Chen et al. [138]. This is indicated as gray line in Fig. 8.9 (a).

For a quantitative evaluation of the datasets one needs to evaluate the integrated intensities A_3 and A_2 under the L_3 and L_2 curves. The integrated intensity $A_3 + A_2$ is formed by integrating the averaged XAS intensity $\frac{(I^+ + I^-)}{2}$ (“white line” [black curve in Fig. 8.9(a)]) over the whole range of photon energies in the spectrum. The indices 2, 3 indicate the ranges of photon energy of the Co $L_{2,3}$ edge. The integrals $\Delta A_3 + \Delta A_2$ and $\Delta A_3 - 2\Delta A_2$, which are needed for the evaluation of the magnetic moments below, are formed by integrating the XMCD signal over the range of photon energy in the spectrum. In order to obtain quantitative values from the XMCD spectra, the sum rules [equation (5.7) and (5.8)], as discussed in chapter 5.3 are used. The degree of circular polarization of the incoming photons – P_{circ} – is also included in these equations. The angle ϕ which is defined by the geometry of the experiment, defines the direction between the incidence of photon and the magnetic moment. Since the magnetization of the sample and the \vec{k} vector of the incident photons are collinear for out-of-plane measurements, the factor $\cos \phi$ yields unity. The number of holes in the Co d band is given by n_h . From these sum rules, the ratio of the orbital and spin moment can be derived, which does not require magnetic saturation of the sample, useful for our measurements under reversal of the direction of the magnetic field.

Employing these XMCD sum rules, we extract the following numbers for the magnetic moments, using a value for the $3d$ holes $n_h = 2.9$, according to the theory data presented below, and a degree of polarization of the light $P_{circ} = 75\%$. At a sample temperature of $T = 90$ K, our 2 ML film of Co intercalated between graphene and Ir(111) exhibits an orbital moment of $M_L = 0.17 \mu_B$ and a spin moment of $M_S = 1.57 \mu_B$. This compares well with the values for saturated magnetic moments of bulk Co ($M_L = 0.153 \mu_B$ and $M_S = 1.55 \mu_B$), as reported by Chen et al. [138], with a ratio of $\frac{M_L}{M_S} = 0.1$. These values are slightly smaller compared to the intercalated 2 ML Co thin film stated above, but agree with molecular beam deflection measurements by Billas et al. [214] and XMCD measurements by Gambardella et al. [215], showing increased magnetic moments for the $3d$ -metals when approaching smaller cluster sizes, *i. e.* from the bulk material to 2-D Co monolayers. Thus, the ratio of $\frac{M_L}{M_S} = 0.12$, we obtain, is slightly larger compared to $\frac{M_L}{M_S} = 0.1$

for bulk Co [138]. To further discuss these values, I compare the results above to XMCD studies on 2.1 ML Co/Cu(001) by Wilhelm et al. [216]. They derive values of $M_L = 0.24 \mu_B$ and $M_S = 1.77 \mu_B$, yielding a ratio of $\frac{M_L}{M_S} = 0.136$; this shows good agreement with the ratio of the magnetic moments for the graphene/2 ML Co/Ir(111) system measured here. While the determination of M_S and M_L may be affected by the fact that full magnetic saturation was not achieved under our experimental conditions as discussed earlier, the determination of this ratio does not suffer from such problems. The ratio is thus also significant for a comparison between theory and experiment below.

An interesting finding is observed on the CK edge [Fig. 8.9 (b)]: this shows a fairly large dichroism signal in the leading π^* states around 285 eV photon energy. The evidently large magnetic moment of the intercalated cobalt film is partially transferred onto the graphene states, a prerequisite for spin filtering as discussed by Karpan et al. [11] (ch. 2.2). To quantitatively interpret these findings, one has to consider that there is a transition from non-spin-orbit split $1s$ initial state to $2p$ final states. The analysis of the XMCD data at CK edges thus provides only information about the orbital magnetic moment. Following the description of Huang et al. [87] and Thole et al. [85] one can formulate a sum rule for K -edge absorption, and relate this to orbital magnetic moments deduced from the CK -edge dichroism signal:

$$M_L = -\frac{1}{3} \frac{n_h \mu_B}{P_{circ} \cos \phi} \frac{\Delta A}{A} \quad (8.1)$$

For the CK edge of the graphene/2 ML Co/Ir(111), measured under an angle of $\phi = 40^\circ$, I find a fairly large dichroism signal [Fig. 8.9(d)] and, using equation (8.1) determine a value of $M_L = 0.042 \mu_B$. Studies on carbon nanotubes in contact with a flat ferromagnetic Co substrate yield a magnetic moment transfer of $0.1 \mu_B$ [217]. This value also compares well with the induced magnetic moments in the graphene film by underlying ferromagnetic bulk material observed for the cases graphene/Ni(111)/W(110) [42] and graphene/Fe/Ni(111) [167].

For graphene/Ni(111)/W(110), a magnetic moment in the range $0.05 - 0.1 \mu_B$ [166] was estimated, whereas in the graphene/Fe/Ni(111) system an increase in magnetic moment, compared to the latter case, by a factor of ~ 2.7 was observed [167]. From the measurements on graphene/2 ML Co/Ir(111) an increase in the magnetic moment by a factor of ~ 2.0 compared to graphene/Ni(111)/ W(110) is found. Thus I conclude that for the graphene/Co/Ir(111) system, the strength of the induced magnetic moments at the CK edge lies in between the graphene/Ni(111)/W(110) and graphene/Fe/Ni(111) cases. The dichroism occurs mostly on the π^* absorption edge, with a smaller effect on the σ^* one. It cannot be excluded that the latter is caused by the background subtraction method.

The XMCD data show an out-of-plane anti-ferromagnetic coupling between the intercalated Co thin film and the graphene overlayer (Fig. 8.9), from the sign of the magnetic contrast in XMCD. Just as a reversal of the direction of the circular polarization of the light, reversing the magnetization direction should also induce magnetic circular dichroism. In the present case, a complete reversal of the direction of magnetization could not be achieved, most likely due to the insufficient strength of the magnet used in the experiment. However, the trend showed the correct effect, yielding similar results for the ratio $\frac{M_L}{M_S}$. To understand the magnetic coupling in the intercalated cobalt thin film, related experiments using spin-polarized scanning tunneling microscopy (SP-STM) [170] and spin-polarized low-energy electron microscopy (SP-LEEM) [205] were carried out by other groups.

In SP-STM experiments by Decker et al. [170] it was observed that the intercalated cobalt film induces a magnetic moiré pattern in the graphene sheet, leading to ferromagnetic coupling between graphene and the underlying cobalt thin film at the ATOP sites and to anti-ferromagnetic coupling at the HCP/FCC sites; however, in agreement with our data above, the overall orientation was found to be anti-ferromagnetic. The authors estimated the magnetic coupling by DFT calculations yielding an overall anti-ferromagnetic orientation and magnetic moments of $0.0104 \mu_B$ per carbon atom. In a simplified picture each HCP, FCC and ATOP region in the unit cell contains 200/3 atoms, leading to a magnetic moment of $1.36 \mu_B/130$. The SP-LEEM measurements by Rougemaille et al. [205] showed that the graphene film

induces a perpendicular magnetic anisotropy (PMA) in the underlying Co film. Additionally, the authors observe for Co/Ir(111) a transition between out-of-plane and in-plane magnetization, which emerges at a coverage of about 6 ML Co. This transition increases to about twice the value – about 12 ML Co – for graphene/Co/Ir(111), where the Co thin film is intercalated between graphene and Ir(111). Hence, the perpendicular magnetic anisotropy is increased for graphene/Co/Ir(111) compared to the case of non-passivated Co/Ir(111). However, with both techniques it is not possible to extract quantitative information about the magnitude of the magnetic coupling. The key strength of our XMCD experiments at the Co $L_{2,3}$ and C K edges presented above is that quantitative insight into the magnetic behavior of the complex graphene/Co/Ir(111) system is gained.

8.3 Electronic structure calculations

8.3.1 Monolayer Co/Ir(111) and graphene/Co/Ir(111)

When trying to calculate the electronic and magnetic properties of graphene on intercalated Co on Ir(111), we face a problem due to the moiré superstructure on Ir(111) because of the in-plane lattice mismatch. In order to directly model this superstructure, one would need to consider 10×10 graphene unit cells (with 200 C atoms) placed on a 9×9 Ir(111) mesh (with 81 Ir atoms in each Ir layer), and insert a 9×9 Co layer between the graphene and the Ir(111) substrate. Application of density functional theory to such superstructure is a difficult and expansive task, and while it was achieved for the case of Cu intercalates in chapter 7, the situation is more complex here because of the need for high accuracy relativistic calculations with spin-orbit coupling included for the analysis of the XMCD experimental results. Instead of considering this large superstructure, the calculations reported here are restricted to a more manageable system, by placing two C atoms of the graphene unit cell on the top of a monolayer (ML) Co/Ir(111) [GR/[1 ML Co]/Ir(111)], and considering three different placements for the graphene overlayer, as discussed in chapter 4.8:

- FCC: one of the C atoms is on top of Co, another is over an Ir atom of the interface layer;
- HCP: one of the C atoms is on top of Co, another is over an Ir of the sub-interface layer;
- ATOP: one of the C atoms is on top of the Ir interface layer and another one is over the Ir sub-interface layer.

This supercell model, which consists of a ten-layer Ir(111) substrate and 1 ML of Co on each side of the substrate, covered by a layer of graphene, is shown in Fig. 8.10. In addition, the properties of 1 ML of Co on the Ir(111) surface [1 ML Co]/Ir(111) are calculated in order to analyze the graphene-induced changes in the magnetic properties of the Co atoms. A similar approach was used by Busse et al. [218] and Voloshina et al. [110], to describe the graphene/Ir(111) system compared to graphene/Ni(111), utilizing hybrid states which allow the transfer of magnetic moments. The calculations are performed

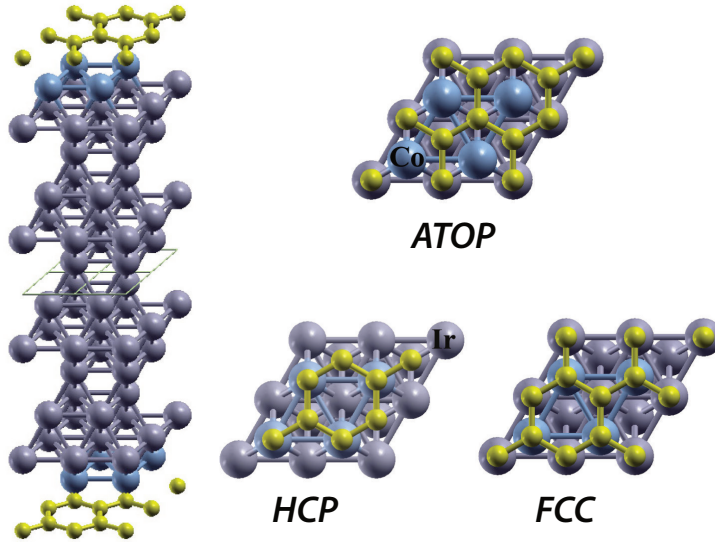


Figure 8.10: A schematic crystal structure used to represent the graphene/Co/Ir(111) surface.

in two separate steps, adapted to the complexity of the task. The structural optimization procedure is performed using the standard VASP-PAW [219–221] program package without spin-orbit coupling (SOC) employing the generalized gradient approximation (GGA) - Perdew-Burke-Ernzerhof (PBE). The in-plane interatomic distance of pure Ir, 5.132 a.u. was adopted and kept fixed in the calculations. For [1 ML Co]/Ir(111), a relatively large -8.4% relaxation of the interlayer distance $d_{[Co-Ir]} = 3.84$ a.u. was obtained. The 2.5% change in the distance between the Ir-interface (Ir-I) and the Ir-sub-interface (Ir-I-1) layers $d_{[(Ir-I)-(Ir-I-1)]} = 4.31$ a.u. is substantial. Very small, practically negligible, changes in the Ir atom positions for the rest of the substrate are found in the calculations. For GR/[1 ML Co]/Ir(111), in the cases of FCC and HCP, graphene is strongly bound to the Co atom, with $d_{[C-Co]} = 3.80$ and 3.72 a.u. respectively. For the ATOP case, the C atoms are much less connected to the substrate, with $d_{[C-Co]} = 4.27$ a.u. Once the structure relaxation is carried out, and the final structure has been established, it is used within the relativistic version of the full-potential linearized augmented plane-wave method (FP-LAPW) [222], in which spin-orbit coupling is included in a self-consistent second-variational procedure [223], and the local-spin-density (LSDA) von Barth Hedin approximation is adopted, to calculate the electronic and magnetic properties. The radii of the atomic muffin-tin (MT) spheres were set to 1.4 a.u. for C atoms, 2.2 a.u. for Co, and 2.5 a.u. for Ir atoms. The parameter $R_{Co} \times K_{max} = 7.7$ defines the basis set size, and the Brillouin zone was sampled with 229 k points. In all calculations the magnetization is directed along the z -axis along the surface normal. The use of the relativistic FP-LAPW method then allows an accurate determination of the element-specific spin (M_S) and orbital (M_L) magnetic moments.

8.3.2 Graphene/2 ML Co/Ir(111)

Now we turn to the comparison between the XMCD experiments and the calculations for two monolayers of Co intercalated in between graphene and Ir(111). The same supercell approach as described above is used (see Fig. 8.10) inserting an extra Co ML into graphene/[1 ML Co]/Ir(111). Again a two-step procedure is used: at first, the relaxed

structure is obtained with the VASP code without spin-orbit coupling; next, the FP-LAPW calculations including SOC are performed. Since it was observed for the case of graphene/[1 ML Co]/Ir(111) that the HCP and FCC placements of graphene yield only minor differences for the Co atom magnetic moments (Vita et al. [212]), only the ATOP and HCP cases are considered. In Table 8.5 the spin M_S , orbital M_L ,

Table 8.5: Spin (M_S), orbital (M_L), and dipole (M_D) magnetic moments (in Bohr magnetons) in the d -shells, and the ratio $R_{LS} = \frac{M_L}{M_S + M_D}$ for a double layer of Co intercalated in between graphene and Ir(111): for the Co monolayer next to the graphene (Co@GR) and the Co monolayer next to the Ir substrate (Co@Ir) for different graphene overlayer placements.

		Co@GR		Co@Ir	
		ATOP	HCP	ATOP	HCP
LSDA	M_S	1.52	1.56	1.69	1.66
	M_L	0.07	0.09	0.09	0.09
	M_D	-0.31	-0.01	-0.08	-0.07
	R_{LS}	0.06	0.06	0.06	0.06
LSDA+U-FLL	M_S	1.73	1.72	1.92	1.90
	M_L	0.20	0.24	0.28	0.27
	M_D	-0.47	-0.10	-0.11	-0.13
	R_{LS}	0.16	0.15	0.16	0.16
LSDA+U-AMF	M_S	1.52	1.48	1.66	1.62
	M_L	0.13	0.19	0.19	0.18
	M_D	-0.32	0.13	0.014	-0.01
	R_{LS}	0.11	0.11	0.11	0.12

and magnetic dipole moment M_D (in μ_B) (note that in our notations, $M_D = 7\langle T_z \rangle$, where the $\langle T_z \rangle = \frac{1}{7}Q_{zz}M_S$ [224, 225], and Q_{zz} is a quadrupole moment), and the ratio R_{LS} for the d -shell of the Co monolayer next to graphene (Co@GR) and the Co monolayer next to the Ir substrate (Co@Ir) are shown. For the hexagonal hollow ATOP position of the graphene overlayer, the LSDA calculations yield

a d -shell occupation of 7.14 for Co@GR, and for the HCP position $n_d = 7.10$, while for Co@Ir, $n_d = 7.03 - 7.04$. It is not surprising that we find the M_S , M_L , and M_D moments to depend on the graphene overlayer placement as well as on the position of the Co atom (Co@GR, Co@Ir). These differences are small except for the Co@GR case where both M_L and M_D are changing. This can be traced to the changes in the electronic structure due to the charge redistribution in the Co atom d -shell. Namely with a change in the graphene overlayer placement from HCP to ATOP (see Fig. 8.10), the occupation for the spin-minority $\{3z^2 - r^2\}$ orbital increases, and Q_{zz} becomes more negative so that the sum $[M_S + M_D]$ is reduced. Simultaneously, the orbital magnetic moment M_L is reduced. Thus, the ratio R_{LS} is less affected by the graphene overlayer placement and remains close to 0.06, *i. e.*, a similar value which is measured by the XMCD experiment.

It is well known that LSDA does not properly account for the orbital polarization in the transitional d metals, and underestimates the values of the orbital magnetic moments [226]. In order to analyze this effect, the rotationally invariant LSDA+ U method was applied in the calculations, which preserves the full local occupation matrix including all spin off-diagonal components. Two flavors of LDA+ U with different choices for the double-counting term, the “fully localized” (FLL) [227] and the “around-mean-field” (AMF) [228], were considered. A Coulomb U of 3 eV was chosen, from an average of the U values commonly used in the LDA+ U calculations of the transitional metals [229]. An exchange J of 0.9 eV was used which corresponds to a choice of the Slater integrals of $F_2 = 7.75$ eV, and $F_4 = 4.85$ eV.

The spin M_S , orbital M_L , and magnetic dipole moment M_D (in μ_B), and the ratio R_{LS} calculated with LSDA+ U -FLL are also shown in Table 8.5. The spin and orbital magnetic moments for both Co@GR and Co@Ir layers found to be enhanced over the LSDA values. The magnetic dipole moments are also increased in magnitude. The d -shell occupation is $n_d = 7.12$ (Co@GR, HCP and ATOP), and $n_d = 7.03 - 7.04$ for (Co@Ir, HCP and ATOP). Similar to LSDA, the ratio R_{LS} is about 0.15–0.16, closer to but now exceeding the experimental XMCD value of 0.12. Note that for the [1 ML Co]/Ir(111) case calculated with LSDA+ U -FLL and the same values of the Coulomb U and exchange J , the values are $n_d = 7.02$, $M_S = 2.07 \mu_B$, $M_L = 0.493 \mu_B$, magnetic

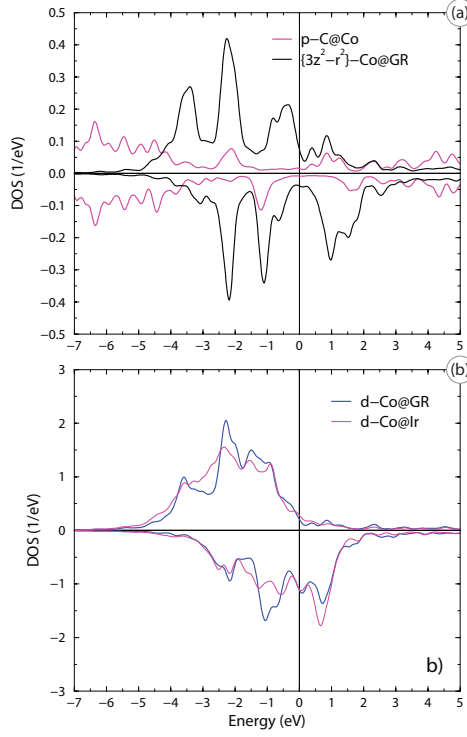


Figure 8.11: (a) Spin-resolved projected DOS for the p states of C atom on top of Co, together with the $\{3z^2 - r^2\}$ projected DOS for the d states of Co@GR atom; (b) spin-resolved DOS for the d states of Co@GR and Co@Ir in HCP case calculated with relativistic LSDA+ U -AMF ($U = 3$ eV).

dipole moment, $M_D = 0.32 \mu_B$, and a ratio R_{LS} is 0.21. Once the LSDA+ U -AMF is applied, this ratio becomes 0.11 – 0.12 in good agreement with the XMCD experiment. The d -shell occupation remains practically unchanged, $n_d = 7.11 - 7.14$ (Co@GR, HCP and ATOP), and $n_d = 7.03 - 7.04$ for (Co@Ir, HCP and ATOP). The values of individual moments are listed in Table 8.5. It is seen that the M_S , M_L , and M_D moments depend on the graphene overlayer placement as well as on the position of the Co atom (Co@GR, Co@Ir). While both the sum $[M_S + M_D]$ and M_L change, the ratio R_{LS} remains unaffected. For a clean [1 ML Co]/Ir(111) calculated with LSDA+ U -AMF and

the same values of the Coulomb U and exchange J , we get a d -shell occupation of 7.03, $M_S = 1.78 \mu_B$, $M_L = 0.29 \mu_B$, magnetic dipole moment, $M_D = 0.29 \mu_B$, and a ratio $R_{LS} = 0.140$. For the ATOP case, relatively small spin moments M_S are induced on the C atoms ($-0.012 \mu_B$, $0.001 \mu_B$). For the HCP case, the moments increase, with $M_S = -0.027 \mu_B$ for the C atom on the top of Co (C@Co), and $M_S = 0.014 \mu_B$ for the C atom over the Ir substrate (C@Ir). These moments are mainly of p -orbital character and originate from spin-dependent hybridization between C π and Co d valence-band states. The spin-resolved projected density of states (DOS) for the p states of the C atom on top of Co (C@Co) is shown in Fig. 8.11. It is seen that the C atom spin polarization follows the spin polarization of the $\{3z^2 - r^2\}$ d states of the Co@GR atom. This spin splitting of the p states is qualitatively consistent with the carbon K -edge XMCD spectra in Fig. 8.9(d). However, the theory does not support the sizable orbital moment M_L of the p states of the C atom. This moment is derived from the XMCD experimental data making use of the orbital moment sum rule Eq. 8.1. The reason for this disagreement is not clear at the moment. It can indicate limitations of the DFT calculations for a proper description of orbital polarization in graphene, and the necessity to go beyond DFT for the C atoms of graphene. Another possibility is that the use of the commensurate in-plane unit cell of graphene instead of a realistic moiré pattern can lead to the neglect of strong interface effects such as charge transfer-induced polarization in the adsorbed graphene. From the computational point of view, the accurate evaluation of a graphene orbital moment in a realistic moiré structure remains a challenge. The spin-resolved DOS for the d states of Co@GR and Co@Ir in the HCP case, calculated with relativistic LSDA+ U -AMF ($U = 3$ eV) are shown in Fig. 8.11. It is seen that the spin splitting of the d states is slightly reduced for Co@GR as compared to Co@Ir. This reduction is consistent with the corresponding reduction of the spin moment M_S seen in Table 8.5. We can interpret it in terms of spin-polarization transfer from the Co layer to graphene, mainly due to hybridization between C π and Co $\{3z^2 - r^2\}$ d states.

8.4 Conclusions

Both Ni and Co behave quite differently from the case of Cu: both metals, when intercalated in between graphene and Ir(111) “destroy” the Dirac cone and the associated linear dispersion, such that high charge carrier mobilities and other special properties of graphene are no longer present. This statement holds irrespective of the ongoing debate whether the band crossing at ≈ 2.4 eV for Ni (Fig. 8.2 (b)) or Co (Fig. 8.8) can be identified with the Dirac cone as postulated by Varykhalov and Rader [213]. Even if this assignment would hold, the specific band structure would be so far removed from the Fermi level that it could not play a role in the transport properties. So just as in the case of graphene grown on bulk Co(0001), the present system is another example of a metal/graphene interface where the relative position in energy and wave vector of the metal d and carbon π states near the Fermi level causes a massive rearrangement of the bands and the removal of the band structure specific to graphene. Concerning magnetic ordering in thin intercalated ferromagnetic layers and their magnetic interaction with graphene, two results have been achieved. First, under the conditions of our experiment (field strength, sample temperature) we observe clear indications of magnetic ordering in Cobalt intercalated films of 2 ML thickness, with values for the spin and orbital moment close to those of bulk Co. This is a somewhat surprising result since the first Co layer, adjacent to the Ir(111) substrate, does not possess the structure of a closed packed hexagonal Co layer; only the second layer assumes that structure. The results agree with our DFT-based calculations which, however assume a different structure. The transfer of magnetic moment onto the graphene π states is quite strong, as evidenced by the clear XMCD signal at the carbon K edge (Fig. 8.9 (d)). With respect to a spin filter action proposed by Karpan et al. [11, 12] (shown in Fig. 2.4 of ch. 2.2), we can state that, due to the absence of a Dirac cone in the graphene layer, the graphene/Co system is not suitable. It would be interesting to study whether the decoupling of Co from graphene through an interlayer of gold for example (Sánchez-Barriga et al. [230]), which restores the Dirac cone, would not weaken the magnetic coupling between the Co and graphene too much such that no moment is transferred to the graphene layer.

Intercalation of ytterbium in graphene/Ir(111)

9.1 Experimental results

The study of graphene modified by intercalation of rare-earth elements seems promising from a technological point of view. Rare-earth materials exhibit magnetic properties which may be exploited in possible applications as magnetic storage devices. Early studies have reported on the modification of the electronic structure of graphite by incorporation of layers of various rare earth atoms in the so-called graphite intercalation compounds (GICs)[231–233]. Ytterbium, which has an electron configuration of $[\text{Xe}]4f^{14}(6s)^2$, is chosen as an example representing the class of rare earth metals, since it exhibits an s-type valence band, making it possible to compare the electronic structure to the widely studied cases of alkali metals used as intercalates in GICs [234]. Early examples of research into Yb intercalation include work by Molodtsov et al. [232]. The authors used PES to compare the electronic structure of pristine graphite with GICs modified by incorporation of Yb atoms, leading to valence bands shifts towards higher binding energy. A mechanism beyond the simple rigid band model was suggested to account for the different behavior of the bands with π and σ character. More recently, reports have proposed the exis-

tence of superconductivity in the intercalation compounds C_6Yb [235]. The authors observed a considerably higher superconducting transition temperature (6.5 K), than in the first reported superconducting GICs, which was C_8K [236, 237] with a transition temperature of 0.15 K.

The specific objective of this chapter is to investigate the electronic structure of intercalated Yb thin films into the graphene/Ir(111) interface by ARPES. Additional information on the intercalation process itself is gained from “real-time” XPS at the C 1s core level and the valence band region near the Fermi edge. LEED is used in order to obtain further information on the structural properties on the sample *e.g.* on the arrangement of the Yb atoms with respect to the underlying Ir(111) substrate. High resolution static XPS spectra were obtained in order to perform a detailed shape analysis of the core level lines (Fig. 9.1 (a)) for the pristine graphene/Ir(111) sample, as reference, and graphene/Yb/Ir(111) after the finished intercalation process. An amount of 1 ML of Yb, estimated by calibration to a quartz microbalance prior to the experiment, is deposited on top of pristine graphene/Ir(111) with the sample kept at a temperature of 110 K. Special attention was given to the vacuum conditions during the preparation of the sample. The partial pressure in the experimental chamber never exceeded 7×10^{-11} mbar. In order to rule out possible oxidation of the highly reactive Yb thin films on the sample surface, O 1s core level spectra were taken.

The line shape analysis of the C 1s core level depicted in Fig. 9.1 (b), indicates that the Yb atoms intercalate underneath the graphene sheet, visible as a strong chemical shift of the C 1s core level from 284.170(2) eV for pristine graphene/Ir(111) towards 284.950(2) eV (see ch. 8.1 and ch. 8.2) Ni and Co intercalated layers, show a similar shift in the C 1s level. Thus it can be concluded that the Yb thin film is completely intercalated. Further, a broad shoulder at higher binding energy is visible in the C 1s peak after intercalation, most possibly due to contributions from disordered carbon atoms in the graphene sheet. The energies of the C 1s core level after deposition and intercalation are collected in Table 9.1. In the LEED images [Fig. 9.1 (c)] a restructuring of the intercalated Yb thin film is seen, by the formation of a $(\sqrt{3} \times \sqrt{3})R30^\circ$ phase, additionally to the hexagonal moire pattern caused by graphene. The $(\sqrt{3} \times \sqrt{3})R30^\circ$ lattice is

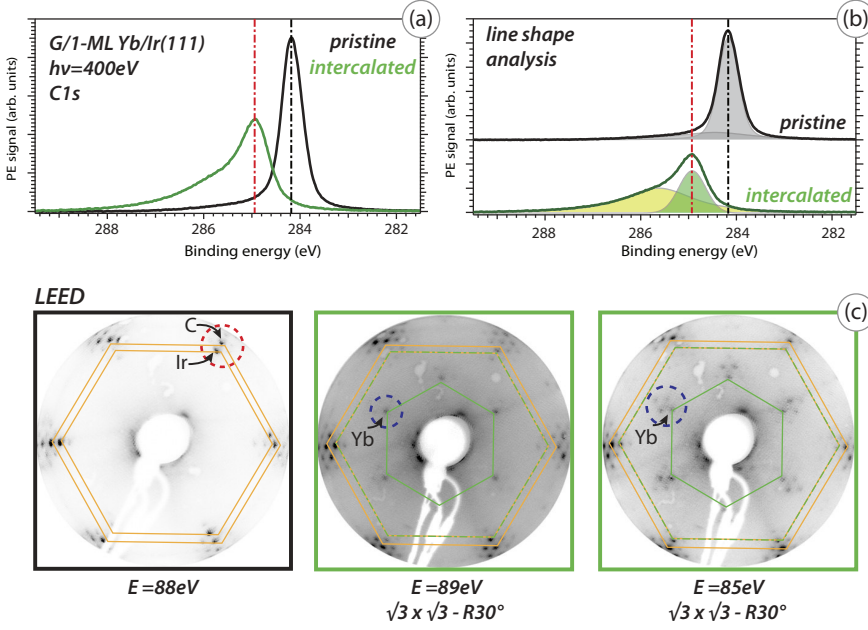


Figure 9.1: Overview of the XPS C 1s core level spectra showing in (a) the intercalation process from graphene/Ir(111) [black] towards graphene/Yb/Ir(111) [green]. (b) Line shape analysis of the C 1s core level, showing a shift towards 284.95 eV for the Yb intercalated sample. (c) LEED images for pristine graphene/Ir(111) [black], obtained with $E = 88\text{ eV}$ indicating the moiré structure, and graphene/Yb/Ir(111) [green], obtained with $E = 89\text{ eV}$ and 85 eV , showing an additional $(\sqrt{3} \times \sqrt{3})R30^\circ$ structure relative to the Ir substrate.

Table 9.1: Overview of the main C 1s peak position for Yb deposited on top and the intercalated graphene/Yb/Ir(111) phase, compared to pristine graphene/Ir(111).

	G/Ir(111) – pristine	Yb/G/Ir(111) – on top	G/Yb/Ir(111)
C 1s	284.17 eV	284.70 eV	284.95 eV

aligned with respect to the spots of the underlying Ir substrate, which becomes clear from the different lattice distances of graphene and Ir in LEED. Images obtained at different energies of 85 eV and 89 eV reveal that there are not only single but multiple Yb spots. The evaluation of the characteristic C 1s and Yb 4f core levels during deposition and annealing is followed in “real-time” by measuring photoelectron spectra iteratively (Fig. 9.2). During the deposition process with the sample kept at low temperature, a relatively strong shift of 500 meV changes the position of the C 1s core level peak from 284.170(2) eV for pristine graphene/Ir(111), towards 284.700(3) eV (Fig. 9.2 (a)). This is, as in similar cases such as the intercalation of Cu atoms described in chapter 7, due to Yb atoms acting as electron donors with respect to the graphene sheet, leading to an n-doping effect of the π band.

The intercalation process as observed by “real-time” XPS spectra in Fig. 9.2 (a) differs significantly from the cases of Ni and Co atoms (chapter 8), since no partial recovery in the intensity of the shifted C 1s lineshape after the suppression of the signal due to deposition of metal atoms is apparent. This behavior is highlighted by a waterfall plot in Fig. 9.2 (b), showing several spectra extracted at different sweeps, stacked above each other. The spectra in the valence band region (Fig. 9.2 (b)) show the emergence of two distinct peaks which can be identified as (strongly localized) Yb 4f_{5/2}; 4f_{7/2} core levels. This observation is in agreement with studies by Mårtensson and Nilsson [238], Dedkov et al. [239], who showed that for Yb coverages in the regime below 1 ML on top of Mo(110), only two separate Yb 4f peaks were observed. For higher Yb coverages the peak structure of the spectrum develops into four single peaks with two separate doublets emerging from Yb 4f_{5/2} and Yb 4f_{7/2}.

The intercalation process is initiated by approaching a temperature of 300 °C, and becomes visible as a chemical shift in the “real-time” C1s spectra (Fig. 9.2 (a), (b)). This temperature regime coincides with early photoelectron and Auger-electron spectroscopy studies by Shikin et al. [240], who found that the intercalation of 1 ML Yb into the graphene/Ni(111) interface is accomplished at annealing temperatures of 300 – 400 °C. Using temperatures higher than 450 °C is reported to yield a undesired increase in the desorption rate of Yb atoms from the surface. The observation of the relatively low intercalation

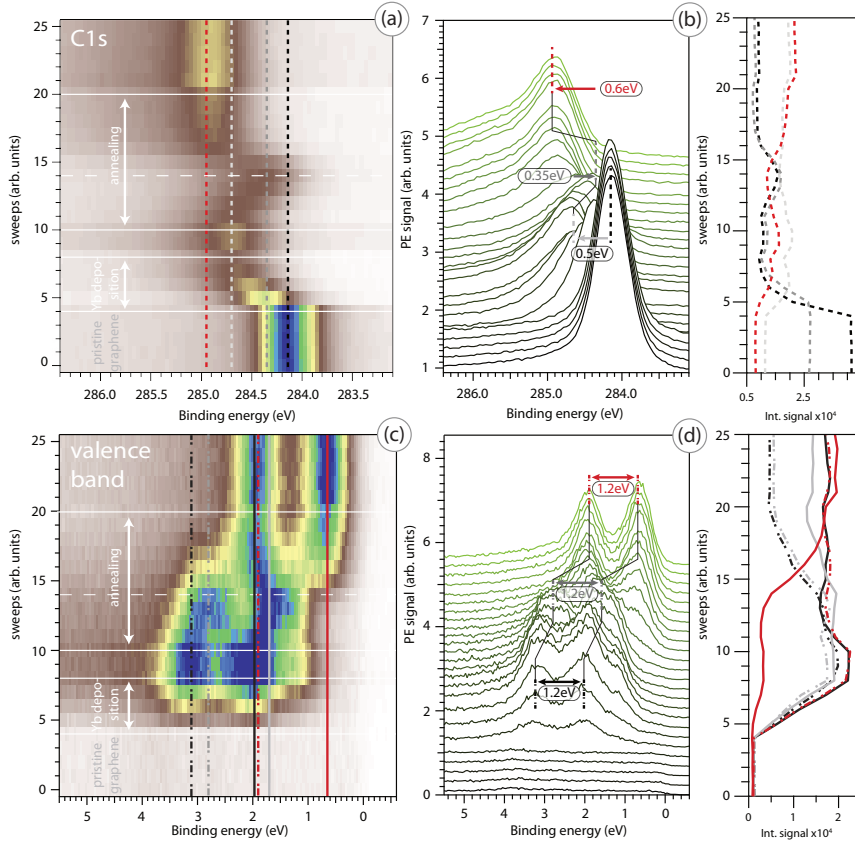


Figure 9.2: (a) and (c) Changes in C 1s line shape and Yb 4f valence band region ($5.5 \text{ eV} - E_F$) upon deposition (sweep 4 to 8) and annealing (sweep 10 to 20), as false color plots [(a) and (c)] and waterfall plot [(b) and (d)]. The core levels are marked by dashed lines. Right side of (b) and (d): Extracted intensity at certain energies E_B indicated by dashed lines in the core-level spectra, emphasizing the changes in the C 1s shape and valence band region during deposition and intercalation. See text for discussion.

temperature of 300°C is in contrast to the intercalation of *e.g.* Cu atoms into the graphene/Ir(111) interface, as reported in chapter 7, where significantly higher temperatures of 550°C are necessary. Another, rather unusual observation is seen during the intercalation

process leading to non-monotonic changes in the energy positions of the Yb $4f$ spin-orbit-doublet, upon slowly increasing the sample temperature. This is visible from Fig. 9.2 (a) and (b), starting from the cold sample surface ($T = 110$ K) at sweep 10, with increasing annealing of the surface up to $T = 300$ °C at sweep 20. The C $1s$ shows a back-shift of 350 meV in binding energy from 284.70(1) eV at sweep 10, towards lower binding energy of 284.35(1) eV at sweep 14.

A similar behavior is present in the valence band spectra near the Fermi edge. Here, a 300 meV shift of the Yb $4f$ spin-orbit-doublet from 3.10 eV; 1.95 eV towards 2.80 eV; 1.65 eV is present. This could be due to a re-distribution of atomic Yb-clusters, which were formed upon deposition on the surface, with the sample kept at $T = 110$ K. Before a sufficient temperature for the initiation of the intercalation process is reached, an intermediate phase of Yb may be formed, which is accompanied by the observed back-shift in binding energy. However, upon reaching a temperature of 300 °C, the C $1s$ level is shifted back towards higher binding energy of 284.95(1) eV at sweep 20. A different behavior is present in the Yb $4f$ level leading to a shift towards 1.95 eV; 0.65 eV. No further changes in the line shapes could be observed in the following, which is an indication that the intercalation process is complete.

In order to evaluate the electronic band structure and the formation of the $(\sqrt{3} \times \sqrt{3})R30^\circ$ phase, ARPES data (Fig. 9.3) are compared with pristine graphene/ Ir(111). The band structure of pristine graphene/Ir(111) identified in the constant energy maps (Fig. 9.3 (c)) shows – Ir(111) surface state (red), graphene Dirac cones (black), and Ir bulk bands (blue). Upon Yb intercalation, a strong n-type doping effect of the graphene π band is apparent from Fig. 9.3 (b): the π band at the K-point is strongly shifted to higher binding energy, with E_D at 1.5 eV. This gives a large shift of the π band at the K-point of about 1.6 eV, compared to the case of pristine graphene/Ir(111), which is slightly p-doped. Interestingly, the observed shift of the Dirac energy towards higher binding energy, is similar to the case of the high temperature graphene/Mn/Ir(111) – (2×2) phase (ch. 10.2), with $E_D = 1.4$ eV (Fig. 10.7). A collection of the characteristic π band positions for graphene/Yb/Ir(111) is given in Table 9.2. In the following I compare the latter sample to the cases of pristine graphene/Ir(111),

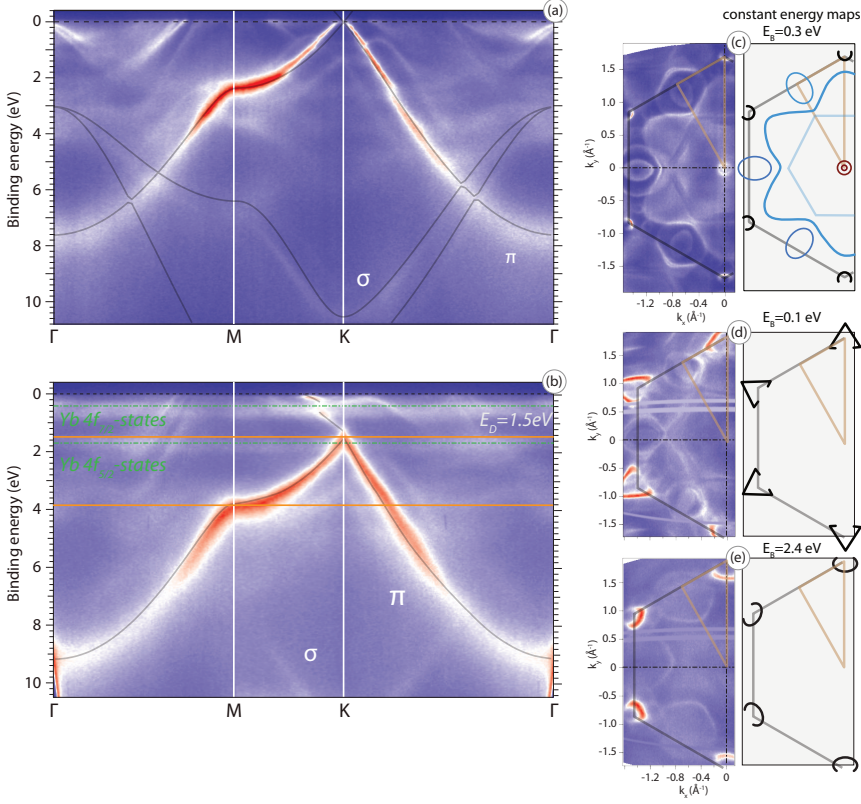


Figure 9.3: ARPES data for the electronic structure of graphene/Ir(111) (a) and intercalated graphene/Yb/Ir(111) (b). (a) Left side: ARPES intensity maps for graphene/Ir(111) acquired along the $\Gamma - M - K - \Gamma$ at $h\nu = 65$ eV. The gray line shows a calculated band structure for a free-standing graphene film [149]. (c) Right side: constant energy surface at $E_B = 0.3$ eV extracted from the ARPES measurements. (b) Left side: ARPES intensity map for graphene/Yb/Ir(111) – additional features are derived from Yb $4f_{5/2}$; $4f_{7/2}$ states (green line) located around $E_B = 1.7$ eV and $E_B = 0.4$ eV. Orange lines give π band position at K and M. (d) and (e) Right side: constant energy surface at $E_B = 0.1$ eV (top) and $E_B = 2.4$ eV (bottom) extracted from the ARPES measurements.

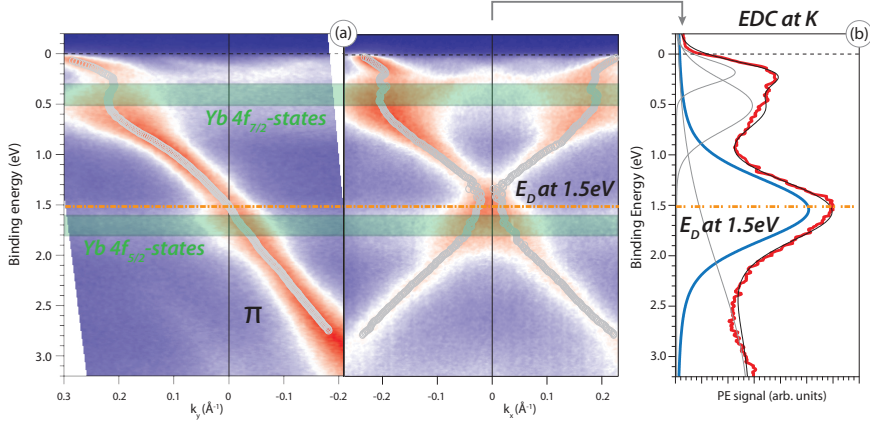


Figure 9.4: (a) ARPES intensity maps from graphene/Yb/Ir(111) along $\Gamma - K$ (left) and perpendicular to it (right). The position of the π band at the K-point, indicated as Dirac energy E_D , is shifted to 1.5 eV. The Yb $4f_{5/2}$ and $4f_{7/2}$ states are located around $E_B = 0.4$ eV and $E_B = 1.7$ eV and labeled [green]. The peak position derived from a MDC line shape analysis is marked by [gray circles]. (b) EDC spectrum extracted at the K point. A multi-component peak fit using four Gaussian peaks is used to determine the position of the Dirac energy E_D [orange].

the graphene/Mn/Ir(111) - (2×2) phase (ch. 10.2) and the strongly interacting graphene/Ni/ W(110) case (ch. 8.1). The difference in the π band positions at the M- and K-point ($\Delta_{MK} = 2.4$ eV) is reduced compared to $\Delta_{MK} = 2.7$ eV for the pristine sample. A similar value of $\Delta_{MK} = 2.4$ eV is observed for graphene/Mn/Ir(111) in the (2×2) phase. This contrasts with the strong reduction of this value towards $\Delta_{MK} = 1.9$ eV, for graphene/Ni/W(111). The difference in band energy at Γ and K is, generally speaking, less affected by the strong n-type doping reported for graphene/Yb/Ir(111) and graphene/Mn/Ir - (2×2) . Therefore, values around $\Delta_{\Gamma M} = 5.3$ eV observed for graphene/Yb/Ir(111) are close to $\Delta_{\Gamma M} = 5.2$ eV for pristine graphene/Ir(111). A similar value ($\Delta_{\Gamma M} = 5.4$ eV) is observed for the strongly interacting case graphene/Ni/W(110). In order to provide better insight into the region around the K-point, detailed ARPES spectra were obtained along and perpendicular to the $\Gamma - K$

Table 9.2: Overview of characteristic positions of the graphene π band for graphene/Yb/Ir(111), at high symmetric points of the Brillouin zone, compared to graphene/Ir(111), graphene/Mn/Ir(111) in the (2×2) phase and strongly interacting graphene/Ni/W(110).

	G/Ir(111)	G/Yb/Ir(111)	G/Mn/Ir(111) – (2×2) phase –	G/Ni/W(110)
Γ	7.8 eV	9.2 eV	9.7 eV	9.9 eV
	$\Delta_{\Gamma\text{M}} = 5.2$ eV	$\Delta_{\Gamma\text{M}} = 5.3$ eV	$\Delta_{\Gamma\text{M}} = 5.8$ eV	$\Delta_{\Gamma\text{M}} = 5.4$ eV
M	2.6 eV	3.9 eV	3.9 eV	4.5 eV
	$\Delta_{\text{MK}} = 2.7$ eV	$\Delta_{\text{MK}} = 2.4$ eV	$\Delta_{\text{MK}} = 2.5$ eV	$\Delta_{\text{MK}} = 1.9$ eV
K	–0.1 eV	1.5 eV	1.4 eV	2.6 eV

direction as shown in Fig. 9.4 (a). An overview of the 2-D-k-space data set of graphene/Yb/Ir(111) is depicted in Fig. 9.4 (b), as a selection of constant energy surfaces at 400 meV separation in binding energy. EDC spectra extracted at the K-point and depicted in Fig. 9.4 (c), show a rather broad contribution of π states around the K-point, which makes it difficult to judge if there is a band gap opening. A line shape analysis (Fig. 9.5), is used to further analyze the band structure with respect to possible quasi-particle interactions. Deviations from the linear dispersion of the π band are obviously present. An evaluation of the slope of the π band gives a velocity of $v = 1.00(3) \times 10^6 \text{ m s}^{-1}$ for binding energies at 2.8 eV, which is only slightly reduced compared to $v = 1.050(4) \times 10^6 \text{ m s}^{-1}$ for pristine graphene/Ir(111) (chapter 6). For energies at 1.0 eV, well above the Dirac energy at 1.5 eV, a significantly reduced velocity with $v = 0.520(6) \times 10^6 \text{ m s}^{-1}$ is observed. Upon passing the range of the low lying Yb $4f_{7/2}$ states at 0.4 eV, a hybridization gap occurs in the π band. This can be explained using the concept of avoided crossings of valence band states for the case of Cu in ch. 7, which leads to a further reduction in the velocity $v = 0.330(14) \times 10^6 \text{ m s}^{-1}$, in the region near the Fermi energy ($E_F - 0.2$ eV). This behavior is distinctly different from the case of graphene/Mn/Ir(111), as discussed in chapter 10.2. Here, no additional hybridization gaps were observed - only strong n-type doping promoted by the intercalated Mn thin film acting as electron donor. However,

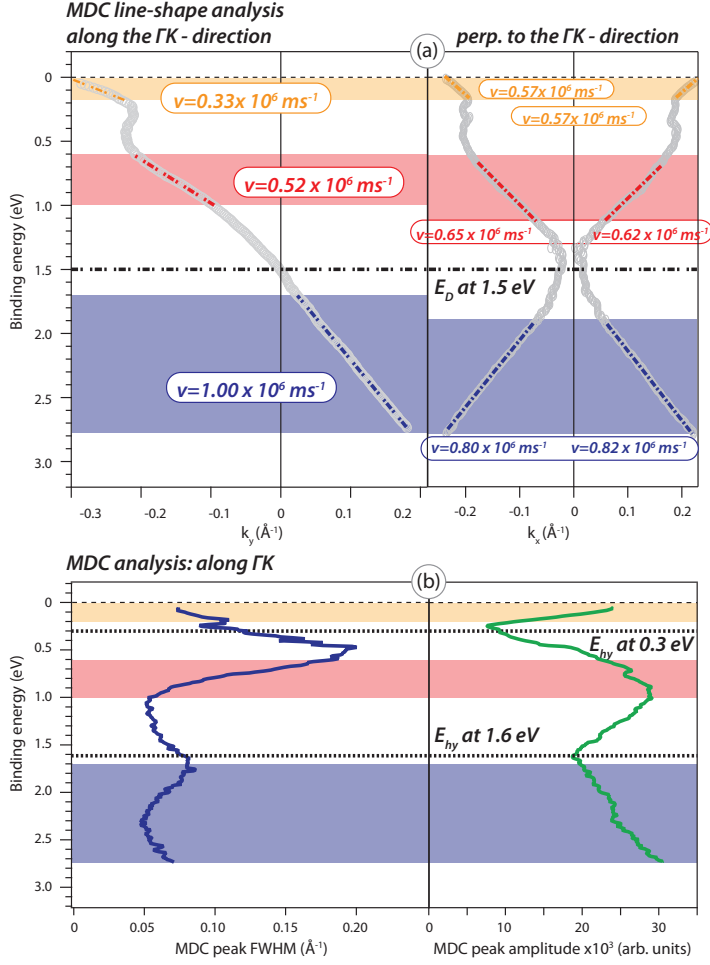


Figure 9.5: (a) MDC line shape analysis from spectra along $\Gamma - K$, (Fig.9.4), by Voigt line shapes (left). MDC line shape analysis perpendicular to the $\Gamma - K$ direction (right). The derived dispersion regions and corresponding velocities are indicated [blue-red-orange]. The Dirac energy is marked at $E_D = 1.5 \text{ eV}$. (b) MDC peak line width of the Lorentzian contribution to the Voigt profile (left); the Gaussian line width is held constant. MDC amplitude of the Lorentzian (right).

a similar effect is present in the data of graphene/Cu/Ir(111) (ch. 7), leading to a series of hybridization gaps in the region of (1.8 – 4.2 eV), due to avoided crossing mechanism of the localized Cu 3*d* states and the graphene π band discussed in detail in ch. 7. For the direction perpendicular to ΓK , the line shape analysis reveals that there are similar kinks present in the π band. The dispersion of the π band in the region (1.9 eV – 2.8 eV), yields similar velocities of $0.800(4) \times 10^6 \text{ m s}^{-1}$ and $0.820(5) \times 10^6 \text{ m s}^{-1}$ for the left and right branch in Fig. 9.5 (a). These values are in good agreement with velocities derived for the pristine graphene/Ir(111) system (chapter 6). A similar reduction in the velocity is observed in the region above the Dirac energy (0.6 eV – 1.2 eV) with a velocity of $0.650(3) \times 10^6 \text{ m s}^{-1}$ and $0.620(7) \times 10^6 \text{ m s}^{-1}$. Finally, the region near the Fermi energy shows a reduction of the velocity to $0.570(7) \times 10^6 \text{ m s}^{-1}$ for both branches.

In order to clarify the question whether a Yb 4*f* – π hybridization gap is induced, spectra were taken at different photon energy using a so-called “photon scan”, as discussed in the appendix (Fig. 11.5). We chose a comparison of ARPES spectra obtained with $h\nu = 65 \text{ eV}$ and $h\nu = 100 \text{ eV}$ (Fig. 9.6). Since the spectra were taken in the same sample geometry, the different photoionization cross-section of π states and Yb 4*f* states should become the only factor for the different intensities in the ARPES spectra. By increasing the photon energy from $h\nu = 65 \text{ eV}$ to $h\nu = 100 \text{ eV}$, the cross section of the carbon 2*p* level is significantly reduced compared to an increase in the cross section for the Yb 4*f* levels [241–243]. Therefore, the ARPES data presented in Fig. 9.6 (a), taken at $h\nu = 65 \text{ eV}$, indicate weaker contributions of the Yb 4*f* levels. The EDC spectrum extracted at the K-point gives no clear indication for a band gap opening. A different situation occurs for $h\nu = 100 \text{ eV}$ (Fig. 9.6 (b)). The Yb 4*f* levels become dominant, highlighting a suppression in the dispersion of the graphene π band around (1.0 – 1.7 eV) at the K-point, which is a clear indication of a hybridization-induced band gap. Similar studies regarding the deposition and intercalation of Yb thin films have been carried out, but with graphene/SiC(0001) using a different substrate [244–246]. Recently, Hwang et al. [246] observe signatures of two coexisting phases: on the one hand, parts resemble as-grown graphene/SiC(0001) with $E_D = 0.4 \text{ eV}$ [247], nearly unchanged in position of the Dirac

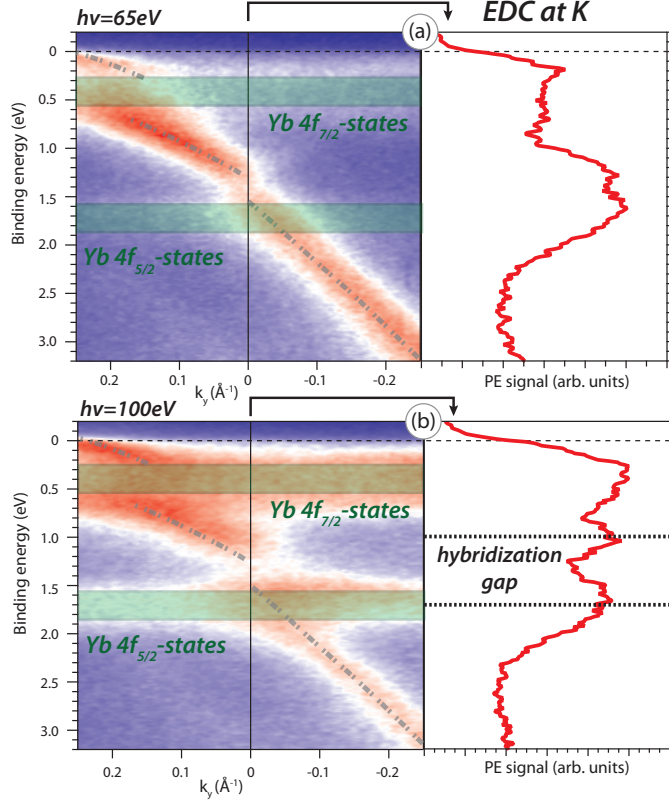


Figure 9.6: (a) ARPES intensity maps acquired along $\Gamma - K$ (left) measured with $h\nu = 65 \text{ eV}$. The position of the π band at the K-point, indicated as Dirac energy E_D , is shifted to 1.5 eV, as indicated from the EDC spectrum extracted at the K-point (right). The Yb $4f_{5/2}$ and $4f_{7/2}$ states are located around $E_B = 0.4 \text{ eV}$ and $E_B = 1.7 \text{ eV}$ [green]. The dispersion of the graphene π band is sketched as dashed line [gray]. (b) ARPES intensity maps acquired along $\Gamma - K$ measured with $h\nu = 100 \text{ eV}$ (left). The EDC spectra suggest the opening of a gap around the K-point (right).

energy, whereas other parts show signatures of highly n-doped graphene with a shifted Dirac energy towards $E_D = 1.4 \text{ eV}$ [248]. The study of the intercalation of thin films of the rare-earth metal Yb into the graphene/Ir(111) interface gives the following results. The band

structure of the graphene π band is strongly affected by the Yb thin film: an n-type doping effect, driven by the Yb atoms acting as a electron donor and the graphene as acceptor, shifts the π band at the K-point to higher binding energy (1.5 eV), similar to the case of alkali metals [155, 249]. Band gaps are observed for the graphene π band in the region around the K point. These gaps occur at binding energies of 0.3 eV and 1.6 eV; they open up at energies close to the positions of the strongly localized Yb $4f_{5/2}$; $4f_{7/2}$ levels at 0.4 eV and 1.7 eV. We thus have a situation that exhibits some similarities with the case of intercalated Cu (ch. 7), in that these gaps are due to a hybridization between Yb $4f$ and graphene π states, *i. e.* an avoided crossing phenomenon. The astonishing fact is that this hybridization also occurs with a $4f$ state, since these are thought to be core-like and thus a state mixing would be less likely to occur. Also surprising is the large difference in the magnitude of the thus-induced gaps, which is much larger for the one close to E_F . LEED studies identify the structural arrangement of the intercalated Yb thin film upon intercalation. A $(\sqrt{3} \times \sqrt{3})R30^\circ$ phase is observed, which is oriented relative to the Ir(111) substrate. During the intercalation process, a rather unusual back shift in the C $1s$ and Yb $4f$ level is observed, which suggest the formation of an intermediate phase of the Yb clusters after the deposition on top of the graphene/Ir(111) surface. This phase vanishes as soon as the temperature is high enough to promote the intercalation and restructuring of the Yb atoms underneath the graphene sheet.

Chapter 10

Manganese as intercalate in graphene/Ir(111)

As we have seen in chapter 8, transition metals such as Ni and Co, intercalated underneath graphene/Ir(111), show a rather strong interaction with graphene, yielding pronounced modifications of the graphene π band [42, 51, 111, 213]. Now, I will describe the modification of graphene/Ir(111) by intercalation of Mn thin films. This topic is interesting in this context since Mn has, with the electronic configuration – Mn [Ar] $3d^5(4s)^2$ – a half filled $3d$ shell and thus the interaction may be weaker. Further, the intercalation of Mn thin films seems promising from the point of view of spintronic applications, as pointed out by Gao et al. [250]. The authors studied the intercalation of Mn layers underneath epitaxial graphene on SiC(0001) using STM, LEED and XPS. They report that the Mn atoms can intercalate between the carbon-rich interface layer, as well as underneath the graphene monolayer situated above the interface layer. A small n-doping effect by 30 meV peak shift in the XPS spectrum was observed at the K-point upon intercalation of 0.1 ML Mn. However, the Dirac cone vanishes here for larger amounts of Mn above a coverage of 0.6 ML. Investigations of intercalation of Mn thin films on metallic substrates were performed by Zhang et al. [251], who studied the morphology of the intercalation of Mn in graphene/Rh(111) by STM. The authors report the formation

of intercalated Mn islands, which show the same contrast in the moire superstructure as the surrounding graphene/Rh(111) areas. Another interesting point is the formation of “surface alloys”, which is widely discussed in the books of Woodruff [252] and Wuttig and Liu [253]. Surface alloys are observed for Mn thin films grown directly on Ni or Cu single crystal substrates [254–256]. In particular, O’Brien and Tonner [256] claim that the surface alloys MnNi and MnCu indicate significantly different magnetic behavior compared to the bulk properties. However, these samples are vulnerable to oxidation due to the reactive half-filled Mn $3d$ shell. Our study was thus also motivated by the idea that the graphene sheet may act as an inert and passivating cover, preventing oxidation of a possible novel surface alloy. Here I investigate graphene/Mn/Ir(111), by deposition of Mn thin films on top of graphene/Ir(111), and follow the intercalation process by annealing at moderate temperatures of 350 °C using XPS. Investigating the band structure by high resolution ARPES shows a preserved Dirac cone, and a trigonal suppression of the replica Dirac cones. I will refer to this preparation as the “trigonal phase” – graphene/Mn/Ir(111). A totally different situation occurs if the intercalation process is performed at higher temperatures (550 °C), which leads to the (2×2) “high temperature phase” in the following. Strong changes in the band structure emerge, with a π band shifted to higher binding energies, and a chemical shift of the C $1s$ core level. Additionally, a restructuring of the intercalated Mn thin film is observed by LEED. Additional information on the (2×2) phase where obtained by STM experiments, which revealed the occurrence of enhanced corrugation comparing the (2×2) “high temperature phase” phase and the graphene/Mn/Ir(111) “trigonal phase”.

10.1 Intercalation of manganese – trigonal phase

As in previous and subsequent chapters, Mn deposition and intercalation was examined using core-level XPS, LEED and valence-level ARPES. A novel aspect here is that also the changes in the valence band during deposition were followed in “real-time”. Upon intercalation of Mn at moderate temperatures, a pseudomorphic phase of graphene/Mn/Ir(111) emerges which shows a preserved π band at the K-point. For reasons that become clear later, this phase is called “trigonal phase” in the following; it is obtained by annealing the sample at temperatures of 350 °C. This temperature is significantly lower compared to the “high-temperature” (2×2)-phase, which is formed by annealing at 550 °C. This process leads to the intercalation of Mn atoms as well, but is accompanied by the formation of a structural (2×2) phase (see ch. 10.2).

During the deposition of Mn and subsequently intercalation into the graphene/Ir(111) interface, the sample is characterized by C 1s core level photoemission, ARPES at the K-point, and LEED (Fig. 10.1). Intercalation is performed at medium temperatures of 350 °C, showing the characteristic suppression and partially recovery of the line intensity of the C 1s core level, as observed for the intercalation Cu in ch. 7. Moreover a shift in the peak position is observed. ARPES spectra recorded in “real-time” during the deposition of Mn, as shown in Fig. 10.1 (d) and (e), indicate a shift of the graphene π band of 500 meV towards higher binding energy. The Mn atoms acting as electron donors cause a strong n-doping of the π band. This shift is also partially visible in the C 1s core level spectra in Fig. 10.1 (a) which indicate a chemical shift from 284.170(2) eV for pristine graphene/Ir(111) towards 284.470(7) eV for Mn/graphene/Ir(111).

The intercalation process is initiated by slowly increasing the temperature up to 350 °C. I infer from the data in Fig. 10.1 (a) and (b) that the Mn atoms intercalate underneath the graphene sheet, because of the nearly full recovery in the C 1s intensity upon annealing. This process is accompanied by a minor decrease in the total chemical shift to 250 meV with the C 1s level located at 284.420(4) eV. Reasons for this behavior could be *e. g.* re-evaporation of Mn atoms from the surface during intercalation.

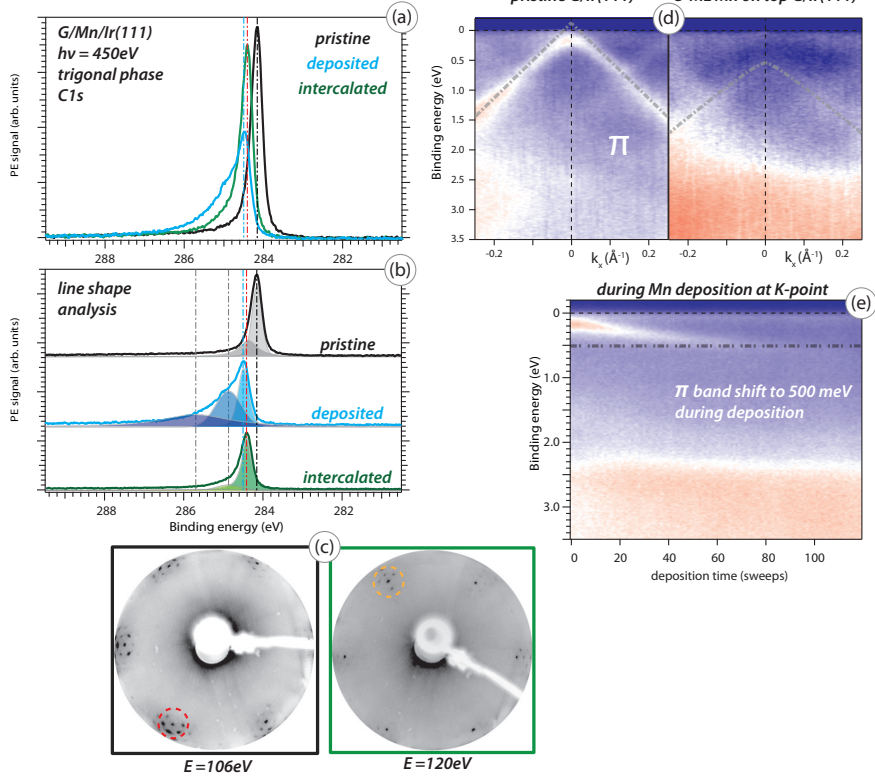


Figure 10.1: Overview of the XPS C 1s core level spectra showing (a) the evolution of the C 1s line during the intercalation process from graphene/Ir(111) [black] and Mn/graphene/Ir(111) [blue] towards graphene/Mn/Ir(111) [green]. (b) Line shape analysis of the C 1s core level. (c) LEED images for graphene/Ir(111) [black] and Mn intercalated [green]. (e) “Real-time” ARPES measurements during Mn deposition at the graphene K-point, leading to a 500 meV shift of the top of the π band towards lower binding energy. (d) Valence band taken at the K-point before and after Mn deposition. The intensity of the graphene π bands emission increase significantly after annealing (Fig. 10.2).

Table 10.1: Overview of the main C 1s peak position for the intercalated system graphene/Mn/Ir(111) – trigonal phase, compared to Mn/graphene/Ir(111) and the initial system graphene/Ir(111).

	G/Ir(111)	Mn/G/Ir(111)	G/Mn/Ir(111) – trigonal phase –
C 1s	284.17 eV	284.47 eV	284.42 eV

A collection of the C 1s core level positions is given in Table 10.1. A line shape analysis of the core level lines in Fig. 10.1 (b) reveals that a shoulder is apparent at higher binding energies of 284.95 eV after Mn deposition. This shoulder is significantly reduced in intensity upon annealing. The C 1s line of the intercalated sample is sharpened and increased in intensity after the intercalation of the Mn thin film.

LEED images in Fig. 10.1 (c), show a pseudomorphic structure of the intercalated Mn atoms underneath graphene, accompanied by a suppression of every second replica spot related to the moiré superstructure. This is significantly different from the cases of Cu, Ni and Co intercalates (ch. 7, 8), and will be discussed in detail below. The characteristic π band positions are obtained from survey ARPES data over a large range of graphene’s Brillouin zone (not shown). A collection of these values is given in Table 10.2 below.

Table 10.2: Overview of characteristic positions of graphene’s π -band for graphene/Mn/Ir(111) – trigonal phase, at high symmetric points of the Brillouin zone, compared to pristine graphene/Ir(111) and the strongly interacting graphene/Ni/W(110).

	G/Ir(111)	G/Mn/Ir(111) – trigonal phase –	G/Ni/W(110)
Γ	7.8 eV	7.8 eV	9.9 eV
	$\Delta_{\Gamma\text{M}} = 5.2 \text{ eV}$	$\Delta_{\Gamma\text{M}} = 5.1 \text{ eV}$	$\Delta_{\Gamma\text{M}} = 5.4 \text{ eV}$
M	2.6 eV	2.7 eV	4.5 eV
	$\Delta_{\text{MK}} = 2.7 \text{ eV}$	$\Delta_{\text{MK}} = 2.4 \text{ eV}$	$\Delta_{\text{MK}} = 1.9 \text{ eV}$
K	–0.1 eV	0.2 eV	2.6 eV

In the following I compare the trigonal phase with the cases of pristine graphene/Ir(111) and the strongly interacting graphene/Ni/W(110). First of all, the Dirac cone formed by graphene's π band around the K-point is much less affected by the intercalated Mn film. The result is an n-doped π band with a total shift of 0.3 eV as compared to graphene/Ir(111); the position of the π band at the Γ -point is unaffected. The difference in the π band positions between the M- and K-points is, with $\Delta_{\text{MK}} = 2.4$ eV, significantly reduced compared to $\Delta_{\text{MK}} = 2.7$ eV for the pristine sample. A strong reduction of this value towards $\Delta_{\text{MK}} = 1.9$ eV, as observed for graphene/Ni/W(111), is not found. The π band positions between the Γ - and K-point is ($\Delta_{\Gamma\text{M}} = 5.1$ eV), about the same as for the pristine sample. For graphene/Ni/W(110) $\Delta_{\Gamma\text{M}} = 5.4$ eV is found, a significantly increased difference, as discussed in section 8.1.

In order to verify the exact position of the π band at the K-point, close-up ARPES spectra were obtained (Fig. 10.2 (a)) along and perpendicular to ΓK . For the latter direction, one can see that the replica band of the main π band is suppressed. This is also visible in constant energy surfaces extracted at energies of 0.6 eV in Fig. 10.2 (b). A trigonal suppression of the replica Dirac cones *i. e.* suppression of every second replica can be derived from the spectra; hence the name of this phase. Due to the structural arrangement of the Mn atoms on Ir(111) the symmetry is reduced to threefold, as compared to unperturbed graphene/Ir(111) which exhibits sixfold symmetry (six replica cones).

A similar behavior was observed in recent studies by Rusponi et al. [45], where Ir clusters were deposited on graphene/Ir(111). The authors observe the formation of a self-assembled Ir metal cluster superlattice on top of the moiré pattern of graphene/Ir(111), during room temperature evaporation of Ir atoms. A similar threefold symmetry with trigonal suppression of the replica cones is apparent, accompanied by small n-doping to 0.2 eV below E_F . The authors argue that a symmetry breaking between the A and B sublattices of graphene's BZ is the reason for this observation, due to preferential nucleation of the Ir cluster at the HCP stacking areas. This interpretation obviously does not apply here; rather, the structural arrangement of the Mn atoms on Ir(111) must be of importance as explained below.

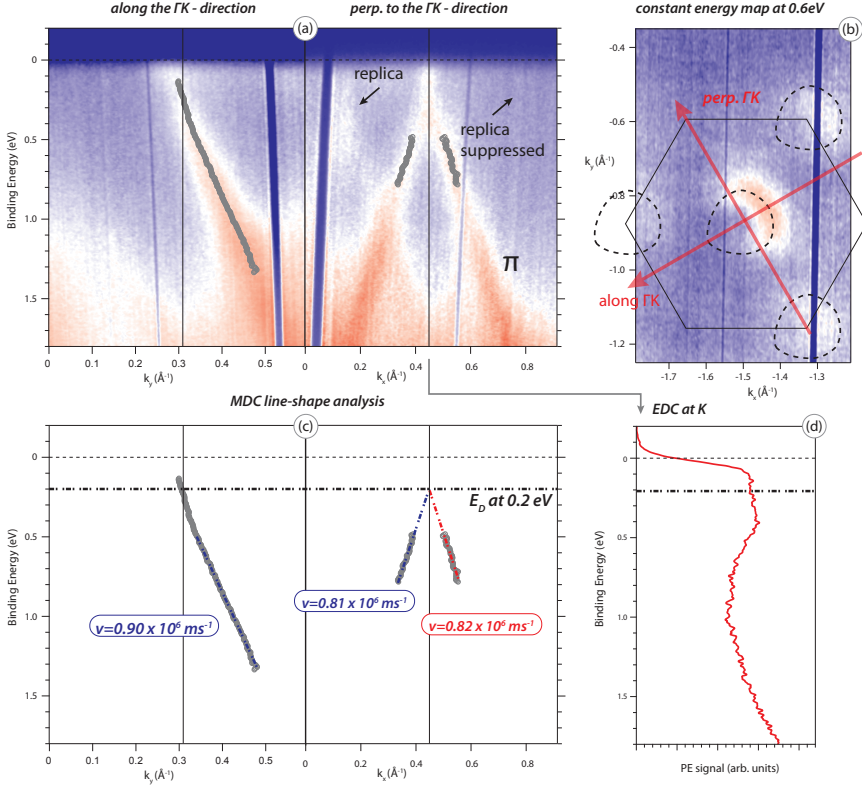


Figure 10.2: (a) ARPES intensity maps acquired along and perpendicular to the $\Gamma - \text{K}$ direction of the BZ of graphene with photon energy $h\nu = 65 \text{ eV}$. (b) Constant energy surface at $E_B = 0.6 \text{ eV}$ extracted from the ARPES measurements. The main feature is the trigonal suppression of the replica cones. (c) MDC line shape analysis from spectra depicted in (a) by Voigt line shapes. The derived dispersion is indicated [gray] with the associated velocities. The Dirac energy is shifted towards $E_D = 0.2 \text{ eV}$. (d) EDC extracted at the K-point, giving no indication for a bandgap.

A line shape analysis of the MDC spectra is used in order to evaluate the dispersion of the π band (Fig. 10.2 (c)). Perpendicular to $\Gamma - \text{K}$, the line shape analysis is limited to the range as far as the two branches of the π band can be well distinguished. First of all, from analyzing the MDC spectra along and perpendicular to the ΓK direction, I

conclude that the π band disperses linearly up to a binding energy of 0.2 eV. Extracting EDC spectra at the K-point, shown in Fig. 10.2 (d) indicates rather broad contributions in the valence band states without a band gap opening. Evaluating the slope of the π band along ΓK , as described in chapter 6.4, I derive a velocity of $v = 0.90(2) \times 10^6 \text{ m s}^{-1}$ up to binding energies of 0.2 eV. The dispersion is slightly decreased compared to pristine graphene/Ir(111) as shown in Fig. 6.15. The minigaps, present for the pristine sample, are suppressed for graphene/Mn/Ir(111) in the trigonal phase. For the direction perpendicular to ΓK , the line shape analysis reveals that there is no kink present in the π band. The derived velocities of $0.81(3) \times 10^6 \text{ m s}^{-1}$ and $0.82(3) \times 10^6 \text{ m s}^{-1}$ show similar dispersion of both arches of the π band. These values are in good agreement with measurements on the pristine graphene/Ir(111) system as discussed in section 6.4.

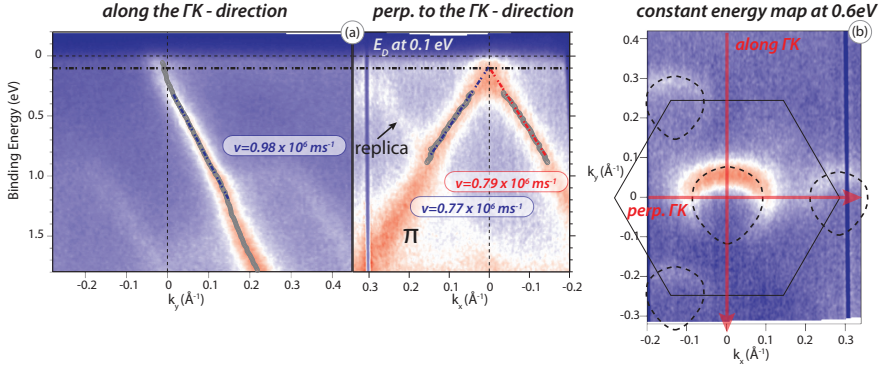


Figure 10.3: graphene/Mn/Ir(111) - trigonal phase, measured around the K-point of the second sublattice compared to Fig. 10.2. (a) ARPES intensity maps acquired along and perpendicular to the $\Gamma - K$ direction of the BZ of graphene with photon energy $h\nu = 65 \text{ eV}$. MDC line shape analysis and derived dispersion is indicated [gray], with associated velocities. The Dirac cone is shifted towards $E_D = 0.1 \text{ eV}$. (b) Constant energy surface at $E_B = 0.6 \text{ eV}$ extracted from the ARPES measurements. The main feature is the trigonal suppression of the replica cones.

One may ask whether, the observed trigonal suppression of the replica cones (Fig.10.2 (b)) shows the same behavior for both K- and K'-points of the different sublattices in graphene. Hence additional ARPES measurements were obtained around the K'-point (Fig.10.3), which is located along the k_y -axis, being the second sublattice B, as compared to Fig. 10.2, where the K-point from sublattice A is measured. Evaluation of the spectra shows exactly the same pattern in the trigonal suppression with about the same values for the associated velocities [Fig. 10.3 (a) and (b)]. Hence the trigonal suppression shows always the same pattern on both sublattices *i. e.* at K- and K'-points. The latter case shows a slightly smaller n-doping of the π band at the K-point towards 0.1 eV [Fig. 10.3 (a)] which is explained due to a smaller amount of deposited Mn atoms.

In order to obtain structural information about the trigonal phase – graphene/Mn/Ir(111), STM experiments were obtained in a joint study with Stefan Böttcher. The discussion of the morphological structure is based on the doctoral thesis of Stefan Böttcher [257]. I restrict myself to a short summary of the informations regarding the morphology. From the STM experiments it becomes clear that Mn nanoislands intercalate underneath the graphene sheet already during the deposition process. The kinetic energy of the evaporated metal atoms is apparently sufficient to initiate intercalation of the atoms, probably at defect sites. Annealing the sample to a temperature of about 300 °C yields a complete intercalation of the Mn atoms, with graphene/Mn/Ir(111) in the trigonal phase. A 3D representation of the STM measurements for a complete intercalated sample is shown in Fig. 10.4, together with a LEED image. Detailed scans are shown in Fig. 10.4 (b) and (c), representing smaller areas on the surface. Various structures appear on the surface – I(a) double and I(b) single atomic step edge; non-intercalated areas appearing as small holes (II); multilayer intercalated islands (III); and defects, such as unoccupied atop sites [IV(a)] or, for example, manganese clusters and structural defects [IV(b)].

The comparison of the morphology (Fig. 10.4), with the pristine sample graphene/Ir(111), yields the following results: At first, an enhanced corrugation of about 1 Å is observed, which is significantly larger than the values of 0.3 Å as reported for graphene/Ir(111) [258].

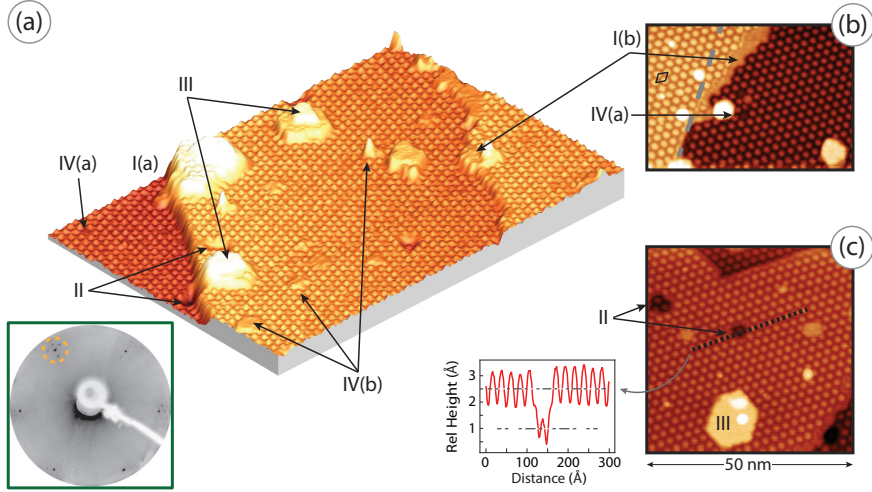


Figure 10.4: Morphology of graphene/Mn/Ir(111) – trigonal phase, obtained by STM measurements, taken from Böttcher [257]. (a) 3D representation of a large area of graphene/Mn/Ir(111) with $1500 \times 900 \text{ \AA}$, acquired at $U_T = 0.65 \text{ V}$ and $I_T = 0.36 \text{ nA}$; (b) shows a closeup scan of $500 \times 350 \text{ \AA}$, acquired at $U_T = 0.3 \text{ V}$ and $I_T = 1.3 \text{ nA}$. (c) indicates a closeup scan with $500 \times 500 \text{ \AA}$, acquired at $U_T = 0.3 \text{ V}$ and $I_T = 1.15 \text{ nA}$, together with a height profile corresponding to the black line. The labels indicate double [I(a)], and single atomic step edges [I(b)]. Non-intercalated areas appearing as small holes (II), multilayer intercalated islands (III), and defects, such as unoccupied atop sites [IV(a)], or for example manganese clusters and structural defects [IV(b)]. The LEED image ($E = 120 \text{ eV}$) in the inset of panel (a) is obtained from separate ARPES experiment of the corresponding structure.

Similar effects of increased corrugation are found for the intercalation of $3d$ transition metals, like Ni (ch. 8.1), into the graphene/Ir(111) interface, as shown by Pacilé et al. [171]. The authors explain the enhanced corrugation by a “strong” interaction between graphene adsorbed on the intercalated $3d$ metal. The results presented in this section indicate that graphene/Mn/Ir(111) in the trigonal phase shows an intact and only slightly shifted Dirac cone with trigonal suppression of the replicas, despite the fact that an enhanced corrugation of the graphene sheet is observed by STM. This offers the unique possibility

to study the behavior of the π band for a strongly corrugated graphene intercalation system. This is usually not possible, as shown previously for the cases of intercalated Ni and Co thin films (ch. 8), where the Dirac cone is mostly destroyed due to hybridization between the metal $3d$ states and the π band. Hence the graphene/Mn/Ir(111) trigonal phase takes an intermediate position in terms of interaction strength between the “strongly” interacting cases of Ni and Co and the rather “weakly” interacting case of Cu.

10.2 The high temperature phase

The high temperature phase of graphene on Mn thin films, intercalated in graphene/ Mn/Ir(111) is characterized by a restructuring of the Mn film, different to the pseudomorphic phases in section 10.1 and the previously discussed examples for the intercalation of Ni and Co thin films in chapter 8. An amount of 3 ML of Mn, estimated by calibration with a quartz microbalance prior to the experiment, was deposited on top of graphene/Ir(111) with the sample kept at room temperature. The comparatively large amount was necessary since the high temperatures during the annealing process results in a partial loss of manganese, *e. g.* due to re-evaporation. The intercalation process is initiated by slowly approaching temperatures up to 550 °C, which is close to the vapor pressure of Mn (507 °C at 1.3×10^{-8} mbar) [113]. As shown from the intensities of the C 1s core level in Fig. 10.5 (a) and (b), the Mn atoms intercalate underneath the graphene sheet. This process is accompanied by a strong chemical shift of the C 1s core level, from 284.170(2) eV for pristine graphene/Ir(111) to 284.950(12) eV, similar to the cases of strongly interacting Ni and Co thin films intercalated underneath graphene/Ir(111) (chapter 8). A line shape analysis of the core level lines reveals that the C 1s line is already shifted by 300 meV after the deposition of Mn with the sample kept at room temperature. This suggests a partial intercalation of hot Mn clusters directly after hitting the surface in agreement with the STM data discussed later. This is supported by the fact that the C 1s shows a broad shoulder around 284.95 eV after Mn deposition, which is significantly sharpened and increased in intensity after the intercalation of the Mn thin film.

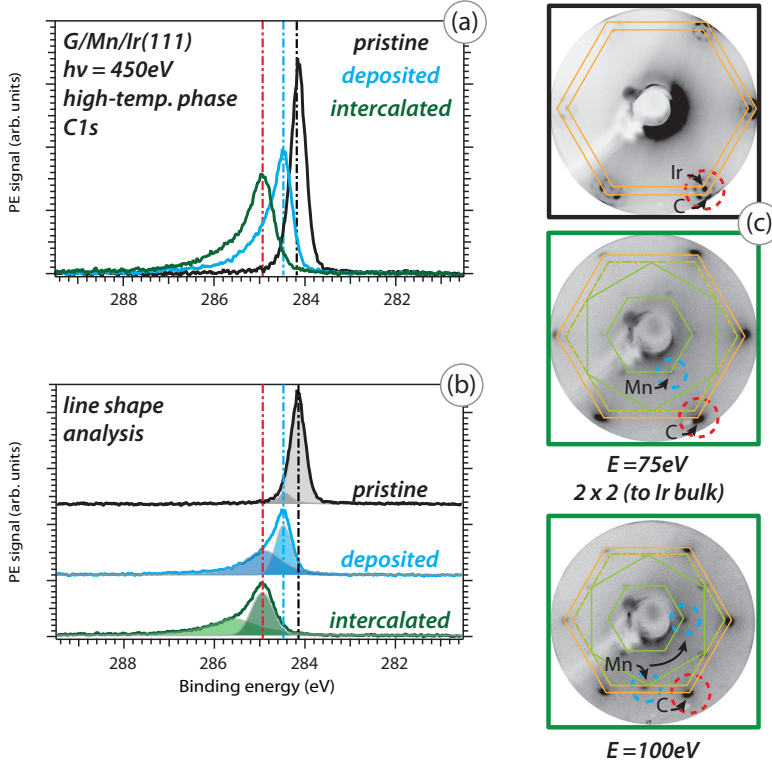


Figure 10.5: Overview of the C 1s core level spectra showing in (a) the intercalation process from graphene/Ir(111) [black] and Mn/graphene/Ir(111) [blue] towards graphene/Mn/Ir(111) – high temperature phase [green]. (b) Line shape analysis of the C 1s core level. (c) LEED images for pristine graphene/Ir(111) [black], obtained with $E = 75\text{eV}$ indicating the moiré structure, and graphene/Mn/Ir(111) – high temperature phase [green], obtained with $E = 75\text{eV}$ and 100eV , showing a (2×2) structure relative to the Ir substrate.

From the LEED images in Fig. 10.5 (c) a loss of the characteristic moiré pattern and a restructuring of the intercalated Mn into the high temperature (2×2) phase is observed. The LEED pattern exhibits this phase and the spots from the (1×1) pattern caused by graphene. The (2×2) lattice is aligned with respect to the underlying Ir spots. This becomes clear from the LEED images obtained at 100eV , at which

Table 10.3: Overview of the main C 1s peak position for Mn deposited on top and the intercalated graphene/Mn/Ir(111) – (2×2) phase, compared to pristine graphene/Ir(111).

	G/Ir(111) – pristine –	Mn/G/Ir(111) – on top –	G/Mn/Ir(111) – (2×2) –
C 1s	284.17 eV	284.45 eV	284.95 eV

energy reflexes of higher order are visible (Fig. 10.5). Hence, the spots from the Ir substrate are suppressed by the reconstructed Mn film and are no longer visible in the LEED images. The only similar case leading to a (2×2) LEED pattern was observed by Petrović et al. [125] for the intercalation of Cs alkali atoms into the graphene/Ir(111) interface. However, in this case the pattern is arranged relative to the graphene lattice vectors and not to the Ir bulk. Hence, the intercalated Mn atoms in the high temperature phase seem to form a unique surface alloy with the Ir bulk, from the observed LEED spot arrangement, relative to the Ir lattice vectors.

In order to evaluate the findings above, let us compare the observed (2×2) LEED pattern to the pseudomorphic growth of Mn atoms on top of the hexagonal Ir surface lattice. Andrieu et al. [259] studied the growth of Mn on Ir by using reflection high-energy electron diffraction (RHEED). For a Mn thickness up to 3 ML the authors report pseudomorphic growth of Mn on Ir, whereas above 3 ML of Mn a $(\sqrt{3} \times \sqrt{3})R30^\circ$ superstructure is observed, which is maintained up to a thickness of 100 Å. Similar observations are reported by LEED studies of O’Brien and Tonner [260], who find a direct phase transition from the pseudomorphic (1×1) pattern towards the $(\sqrt{3} \times \sqrt{3})R30^\circ$ superstructure at 4 ML Mn coverage. This comparison suggests that the intercalated Mn film in graphene/Mn/Ir(111) occupies with (2×2) a rather unusual structural arrangement, which is promoted by annealing. Recent theoretical studies by Chen et al. [261] reveal that Mn_3Ir , which is a high-temperature antiferromagnet and typically used in spin-valve devices, could match to the observed (2×2) phase discussed in this chapter. As shown in Fig. 10.6, Mn_3Ir can be understood as an *fcc* crystal with Mn atoms on three of the four cubic sublattices.

Therefore, the Mn atoms form a so-called “kagome” lattice, which shows a trihexagonal tiling with two triangles and two hexagons in alternating positions. The arrangement of Mn atoms in Mn_3Ir could then lead to the observed (2×2) structure in LEED.

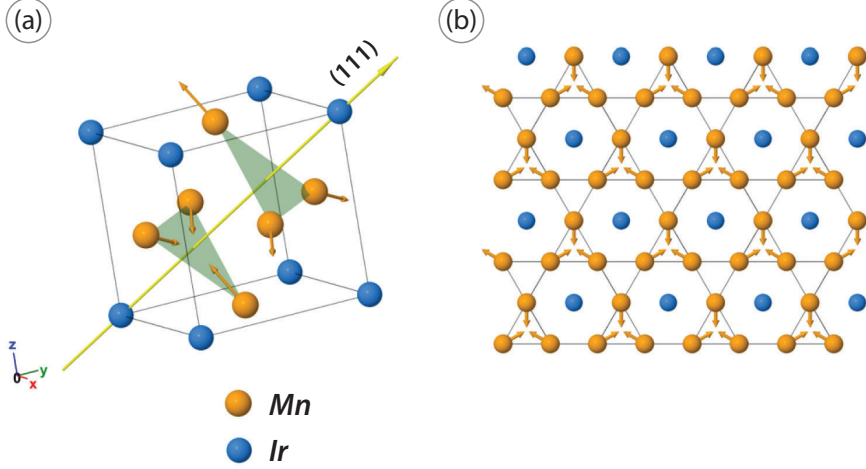


Figure 10.6: Structure of Mn_3Ir taken from Chen et al. [261]. (a) Unit cell of Mn_3Ir with triangular anti-ferromagnetic order. (b) An individual (111) plane of Mn_3Ir . The Mn atoms form a “kagome” lattice.

In order to evaluate how the electronic band structure is affected by the intercalation of Mn and the formation of the (2×2) high temperature phase, ARPES measurements (Fig. 10.7) are compared with pristine graphene/Ir(111) (ch. 6).

Upon intercalation of Mn, the graphene π band is shifted by 1.5 eV with the Dirac energy at $E_D = 1.4$ eV to higher binding energy at K [Fig. 10.7 (b)]. This equals a total shift of the π band at the K-point of about 1.5 eV, compared to the case of pristine graphene/Ir(111) [Fig. 10.7 (a)]. The main features of the Mn film intercalated under graphene/Ir(111) are derived from Mn $3d$ states (green line) located around $E_B = 2.4$ eV. A restructuring of the Dirac cone with a triangular inverted shape near the Fermi energy is apparent from constant energy maps [Fig. 10.7 (d)]. A collection of the characteristic π band positions for graphene/Mn/Ir(111) – (2×2) high tempera-

ture phase, is given in Table 10.4 below. In the following I compare this sample to pristine graphene/Ir(111) and the strongly interacting graphene/Ni/W(110) case. The difference in the π band positions between the M and K point ($\Delta_{\text{MK}} = 2.5 \text{ eV}$) is significantly reduced compared to $\Delta_{\text{MK}} = 2.7 \text{ eV}$ for the pristine sample. However, a strong reduction of this value towards $\Delta_{\text{MK}} = 1.9 \text{ eV}$, as observed for graphene/Ni/W(111), is not found. Comparable values of $\Delta_{\text{MK}} = 2.0 \text{ eV}$ were reported in chapter 8. Here I find that the intercalation of Ni and Co thin films into the graphene/Ir(111) interface induces similarly strong modifications of the graphene π band, connected with the absence of the Dirac cone at the K-point as in the case of graphene/Ni/W(110).

Table 10.4: Overview of characteristic positions of the graphene π -band for the graphene/Mn/Ir(111) – (2×2) phase, at high symmetric points of the Brillouin zone, compared to graphene/Ir(111) and strongly interacting graphene/Ni/W(110).

	G/Ir(111)	G/Mn/Ir(111) – (2×2) –	G/Ni/W(110)
Γ	7.8 eV	9.7 eV	9.9 eV
	$\Delta_{\Gamma\text{M}} = 5.2 \text{ eV}$	$\Delta_{\Gamma\text{M}} = 5.8 \text{ eV}$	$\Delta_{\Gamma\text{M}} = 5.4 \text{ eV}$
M	2.6 eV	3.9 eV	4.5 eV
	$\Delta_{\text{MK}} = 2.7 \text{ eV}$	$\Delta_{\text{MK}} = 2.5 \text{ eV}$	$\Delta_{\text{MK}} = 1.9 \text{ eV}$
K	–0.1 eV	1.4 eV	2.6 eV

In order to provide better insight into the region around the K-point, ARPES spectra were obtained along and perpendicular to the $\Gamma - \text{K}$ direction in a small range near the K-point, as shown in Fig. 10.8 (a). First of all, the trigonal suppression of the replica cones, reported in section 10.1, is absent in the (2×2) high temperature phase. EDC spectra extracted at the K-point and depicted in Fig. 10.8 (b), show a rather broad contribution of states around the K-point, indicating the absence of a band gap. A line shape analysis, depicted in Fig. 10.9, is used in the following to further analyze the band structure. A convolution of a Lorentzian and Gaussian line profile (Voigt line profile) is used for the procedure of fitting the MDC spectra.

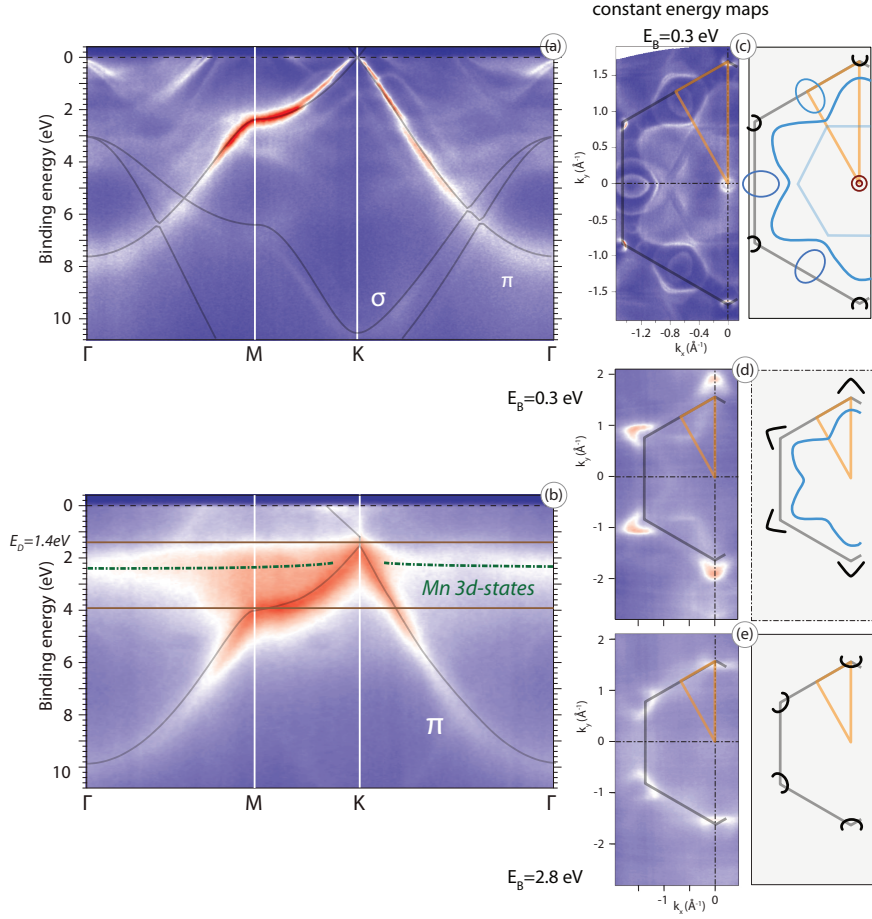


Figure 10.7: ARPES intensity maps for (a) graphene/Ir(111) and (b) intercalated graphene/Mn/Ir(111) – (2×2) high temperature phase, acquired along the $\Gamma - M - K - \Gamma$ direction of the BZ of graphene with photon energy $h\nu = 65$ eV (a) and $h\nu = 120$ eV (b). The gray line shows a calculated band structure for a free-standing graphene film [149]. Main features of the intercalated Mn film are derived from Mn 3d states (green line) located around $E_B = 2.4$ eV (b). (c) Constant energy maps at $E_B = 0.3$ eV extracted from the ARPES measurements. The main features in red are derived from the Ir(111) surface state, graphene Dirac cones (black), and Ir bulk bands (blue). (d) and (e) constant energy maps at $E_B = 0.3$ eV (top) and $E_B = 2.4$ eV (bottom) extracted from the ARPES measurements.

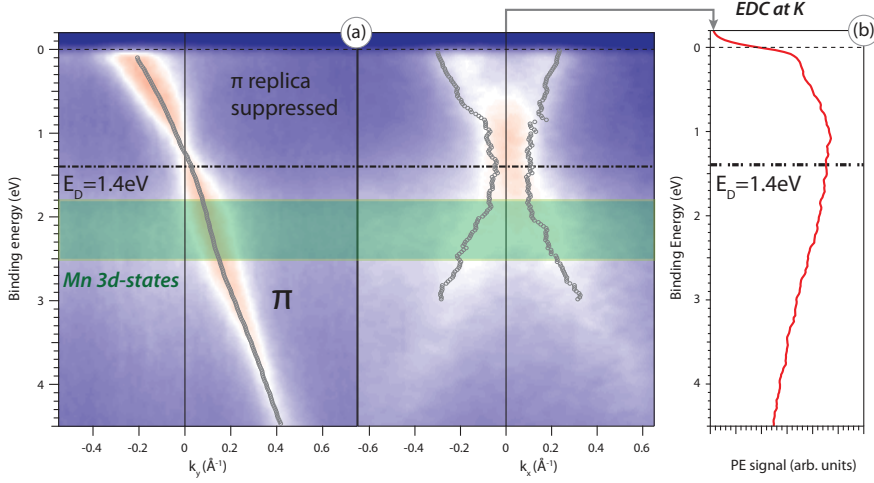


Figure 10.8: ARPES data for graphene/Mn/Ir(111) – 2×2 phase around the K-point. ARPES intensity maps acquired along (left) and perpendicular $\Gamma - K$ (right). The position of the π band at the K-point, indicated as Dirac energy E_D , is shifted to 1.4 eV. The peak position, derived from a MDC line shape analysis is marked [gray circles]. Weakly dispersing Mn 3d states emerge around 1.8 – 2.5 eV [green] (b) EDC spectrum extracted at the K-point. The broad contributions of the π band around the K-point indicate the absence of a band gap.

Following the discussion regarding the line shape analysis of the MDC spectra for pristine graphene/Ir(111) (ch. 6.4), we note that in the MDC spectra along the ΓK direction, a kink is apparent in the range of $(E_F - 0.8 \text{ eV})$ (Fig. 10.9 (a)). An evaluation of the slope of the π band gives a velocity of $v = 1.080(5) \times 10^6 \text{ m s}^{-1}$ for binding energies of 4.0 eV and $v = 0.780(7) \times 10^6 \text{ m s}^{-1}$ for energies of 0.8 eV; a rather large difference. This dispersion shows a partly similar behavior as for pristine graphene/Ir(111) in Fig. 6.15. Here, a similar slope of the graphene π band with a velocity of $v = 1.050(4) \times 10^6 \text{ m s}^{-1}$ for binding energies of 2.3 eV and a slightly reduced velocity of $v = 0.900(3) \times 10^6 \text{ m s}^{-1}$ for energies of 0.8 eV is found. Hence the observed kink visible in the π band for the graphene/Mn/Ir(111) – (2×2) high temperature phase is more pronounced, yielding a smaller velocity as compared to the intrinsic

sic kink for graphene/Ir(111). However, the minigaps present for the pristine sample are suppressed for graphene/Mn/Ir(111) – (2×2) high temperature phase, due to the formation of the Mn film underneath graphene.

For the direction perpendicular to ΓK the line shape analysis reveals that there is no kink present in the π band. The derived velocities of $0.800(22) \times 10^6 \text{ m s}^{-1}$ and $0.780(22) \times 10^6 \text{ m s}^{-1}$ show only small differences in the dispersion of the π band for the left and right branch. For pristine graphene/Ir(111) a velocity of $v = 0.85 \times 10^6 \text{ m s}^{-1}$ was obtained for binding energies of 1.3 eV (ch. 6.4). Hence, the velocities are slightly reduced in the direction perpendicular to ΓK for the intercalated Mn thin film. Therefore, I conclude that the observed kink in the dispersion of graphene/Mn/Ir(111), occurs partly due to the intrinsic dispersion of graphene/Ir(111), as discussed in chapter 6.4.

These result leads to the question, what kind of quasi-particle interactions could be reason for the observed kink? Phononic contributions, leading to a kink in the dispersion of graphene would emerge at binding energies around $E_{\text{phonon}} = k_B \theta_D = 180 \text{ meV}$ [188, 189], as discussed in chapter 7. The observed energy regime ($E_F - 0.7 \text{ eV}$) is certainly too large for phononic interactions. For the weakly interacting graphene/SiC(0001) case, Bostwick et al. [155] find an increased line width in the MDC spectra between the Dirac energy and the Fermi level, suggesting interactions due to electron-hole pair generation. On the other hand, plasmonic interactions would have a growing impact only near the Dirac energy, which is in this case with 1.4 eV far away from the observed kink. Additionally, plasmonic interactions would be quenched by the screening effect of the metallic substrate. As previously shown for pristine graphene/Ir(111) (Fig. 6.15), the line width and peak amplitude decreases in the range of $(E_F - 0.7 \text{ eV})$, as the π band approaches the Fermi level. Bostwick et al. [155] associate this decay at least in the region of $(E_F - 0.2 \text{ eV})$ with phononic interactions. In the case presented here one can see the reverse behavior – an increase in MDC peak amplitude and line width as the π band approaches E_F , as shown in Fig. 10.9 (b). Although the decrease in the velocity seems to be similar as in the case of graphene/Ir(111), the behavior of the line width and amplitude of the MDC peak is different. A similar broadening of the MDC lineshape was already observed

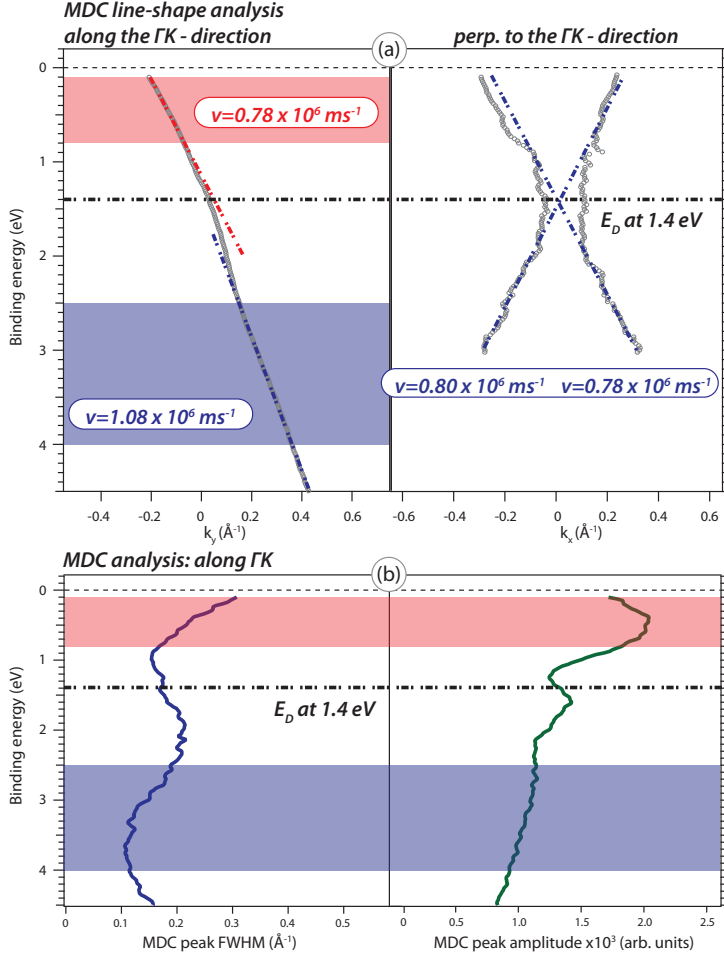


Figure 10.9: (a) Left side: MDC line shape analysis of the (2×2) high temperature phase from spectra along $\Gamma - K$ in Fig.10.8 by Voigt line shapes. Right side: MDC line shape analysis perpendicular to $\Gamma - K$. The derived dispersion regions and corresponding velocities are indicated [blue-red]. (b) Left side: MDC peak line width of the Lorentzian contribution to the Voigt profile; the Gaussian line width is held constant. Right side: MDC amplitude of the Lorentzian.

by Bostwick et al. [262] in hydrogen intercalated graphene/SiC(0001). The authors report that the observed broadening in the MDC spectra is due to defect scattering, an explanation that may also apply here.

STM studies on graphene/Mn/Ir(111)

The studies of Mn intercalates in graphene/Mn/Ir(111) in chapter 10.1 and 10.2 showed the existence of two different cases – the trigonal and the (2×2) high temperature phase – for a Mn thin film arranged underneath graphene/Mn/Ir(111). This indicates the

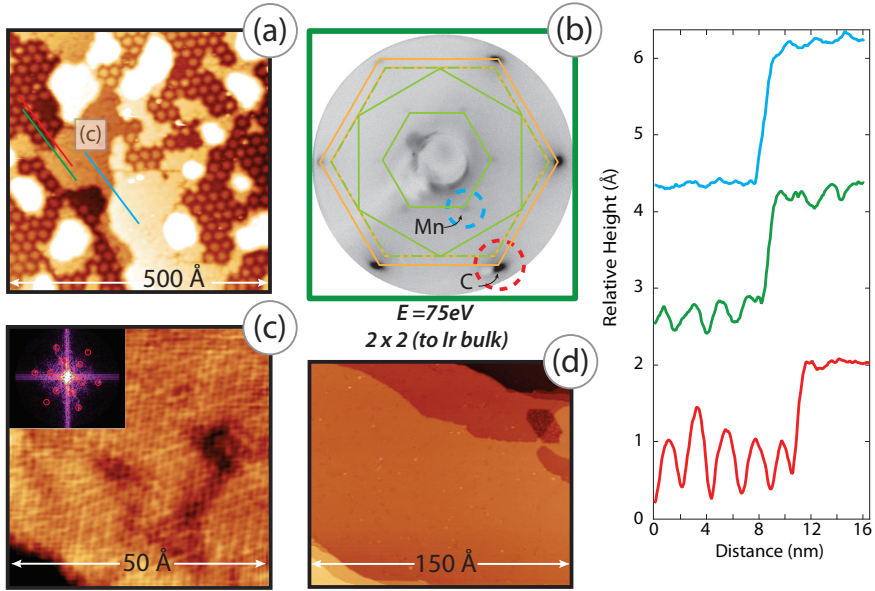


Figure 10.10: STM spectra of intercalated graphene/Mn/Ir(111) taken from Böttcher [257]. (a) presents an survey image over 500 Å, acquired at $U_T = 1.25$ V and $I_T = 1$ nA. Extracted height profiles, indicated as colored lines are presented in panel (e). High resolution spectra are acquired in a small area, shown as inset (c). The spectra in (c) are measured at $U_T = 0.3$ V and $I_T = 1.86$ nA. (d) shows an survey spectrum over 150 Å for the phase pure (2×2) surface, obtained at $U_T = 2.35$ V and $I_T = 0.27$ nA. A LEED image, shown in (b), correspond to the sample measured with APRES, depicted in Fig. 10.7 and 10.8.

need to clarify the structural properties of graphene/Mn/Ir(111) using further experimental techniques. To shed light upon the question how the different phases of graphene/Mn/Ir(111) arise, STM experiments were obtained (see the doctoral thesis of Stefan Böttcher [257]). The occurrence of the (2×2) high temperature phase can be identified also in STM measurements; Fig. 10.10 (a) show a mixed phase sample with patches of (2×2) phase and moiré-type graphene/Mn/Ir(111). The moiré-type graphene/Mn/Ir(111) was labeled in chapter 10.1 as the trigonal phase, due to the associated suppression in the replica cones. The (2×2) phase is distinctly different compared to the surrounding moiré-type structures. The intercalation of Mn realized by annealing the sample to 550°C , leads to the agglomerated formation of the (2×2) phase in certain areas. By extracting height profiles, indicated as colored lines in panel (a) and (e), information on the corrugation and the height difference between the newly formed (2×2) phase and the adjacent graphene/Mn/Ir(111) moiré phase can be derived. The green line represents the profile starting between ATOP hills of the lower steps. For comparison, the red line shows the profile along the ATOP hills of the moiré pattern. A significant reduction in the corrugation is apparent in both profiles by crossing from the moiré phase towards the (2×2) phase. Further, multilayer intercalation areas, *e. g.* defects of type III (Fig. 10.4), are also apparent from Fig. 10.10 (a) and the blue line in (e). These areas show an increased step height of almost 2 \AA . The flat areas of the graphene/Mn/Ir(111) – (2×2) phase lie on the same terrace as the moiré-type graphene/Mn/Ir(111) areas and are shown in a closeup image in Fig. 10.10 (c). Evaluation of the acquired image using fast Fourier transform (FFT) leads to the same (2×2) pattern relative to the Ir bulk seen in LEED. Further annealing of the sample leads to the destruction of the moiré type phase and a complete coverage of the sample with the (2×2) phase. On the basis of these results, we conclude that the underlying substrate is in both cases – moiré-type and (2×2) -type – an intercalated Mn layer. However, the different corrugation suggests a change in the adsorption distance of the carbon layer to the Mn film. A reason for this behavior could originate from a different interaction of the carbon atoms with the new substrate structure or by changes in the substrate superpotential affecting the carbon layer and leading to the formation of a surface

alloy. The results for the (2×2) high temperature phase from STM and photoemission yield a consistent picture of *d*-metal intercalation which has similarities to the cases of Co and Ni in chapter 8. The new observation is here that the Mn atoms do not just take positions of the Ir lattice, but induce a re-structuring of the interface which is interpreted as a surface alloy. The case of the (1×1) trigonal phase is more difficult to interpret, in particular with respect to the induced trigonal symmetry breaking. Here more structural data are clearly needed to arrive at a conclusive interpretation.

Conclusions and outlook

The studies contained in this thesis cover a wide range of metal-graphene interfaces, from those where the interaction with the metal has only a small effect on the specific electronic structure of graphene, such as iridium, copper, and ytterbium, to those cases where a massive influence is observed, as in the cases of nickel, cobalt, and to some extent manganese. As we have seen, each of these has its own specific aspects: intercalated layers of copper, with only $s - p$ derived states near the Fermi level, and a range of well-resolved d band signatures in photoemission. This provides a system, in reference to DFT calculations, in which the mechanisms that lead to band hybridization and band gap opening can be pinpointed. This model system can provide a general view of graphene-metal interaction. Graphene on Ir(111) exhibits similarities and differences: on the one hand, it is the prime example for a large lattice-mismatched interface, giving rise to the moiré patterns that in the context of graphene on insulating substrates, have revealed features in electronic transport that had long been predicted [263] but only became accessible recently [264] through the possibility to handle graphene and related 2-dimensional systems. Cobalt and nickel, on the other hand, are cases where a massive influence of the d bands in the region near the Fermi level is observed, by the removal of the linear dispersion. A special aspect here relates to the magnetic properties that emerge in a cobalt layer

as a function of the thickness of the intercalated film, the emergence of ferromagnetic ordering, and the transfer of magnetic moment from the cobalt onto graphene's π states. Ytterbium, shows considerable similarities with copper, which is plausible in view of the fact that in both metals, the region near the Fermi level is exclusively occupied by $s - p$ type states. Finally, intercalated manganese is a case in between: for an intercalated layer, the Dirac cone is preserved despite the fact that Mn has occupied d -derived states near E_F . It also exhibits a difference to other intercalated metals since a surface alloy is formed, with the topmost layer of the Ir substrate affecting the shape of the graphene bands. As for future developments, what is the situation for graphene-metal interfaces, and where do we go from here? First, there are still a few "white spots on the landscape", *i. e.* graphene interfaces with some common and some less common metals are still unexplored. However, their properties can be estimated on the basis of the examples in this thesis as well as many other publications, and DFT calculations. Among the ferromagnet-graphene interfaces, further studies that may prove fruitful is the examination of ferromagnet-graphene-ferromagnet sandwich structures. For a suitable choice of materials, such as a nickel – monolayer graphene – cobalt sandwich, the transfer of magnetic moment, and the predicted spin filter action can be measured by XMCD, because this is an element-sensitive method that can distinguish between the magnetic behavior of the constituent metals. As far as the electronic structure of graphene on cobalt or nickel is concerned, the destruction of the Dirac cone with its possible detrimental effect on spin filtering can be suppressed by the intercalation of a noble metal. Such experiments were already performed well before the current rush of activities [50, 51, 265]. The aspect that is still open is whether the magnetic coupling between the ferromagnetic substrate and graphene survives the insertion of a noble metal. Finally, the use of graphene to study electronic state entanglement, for which encouraging signs have recently been found [266] also involves graphene-metal interaction. That graphene-metal systems are all important for a practical use of graphene, and issues such as contact resistance and metal-induced doping effects need to be examined in detail, is also obvious. These fundamental as well as practical aspects of metal-graphene interaction will thus remain a very active and exciting field for future research.

Appendix

Line shape analysis on graphene/Ir(111)

Employing a line shape analysis one can extract information from the measured spectral function by ARPES. Using an automated fitting routine with one or two Lorentzian peaks and an additional linear background along the energy axis and k-axis, one can obtain informations about the peak position, FWHM and amplitude. From equation (6.2) the group velocity can be deduced, which corresponds to the Fermi velocity at E_F . Datasets taken from graphene/Ir(111) are shown in the following (Fig. 11.1, 11.2, 11.3) using the different measurement procedures β -flip and φ -rotation. These datasets are used to obtain further informations on graphene/Ir(111), and to compare datasets measured at BESSY II with datasets from the laboratory machine. The derived velocities using the MDC line shape analysis along and perpendicular ΓK are similar for both stations, which gave the final confirmation that the new laboratory experiment is successfully commissioned.

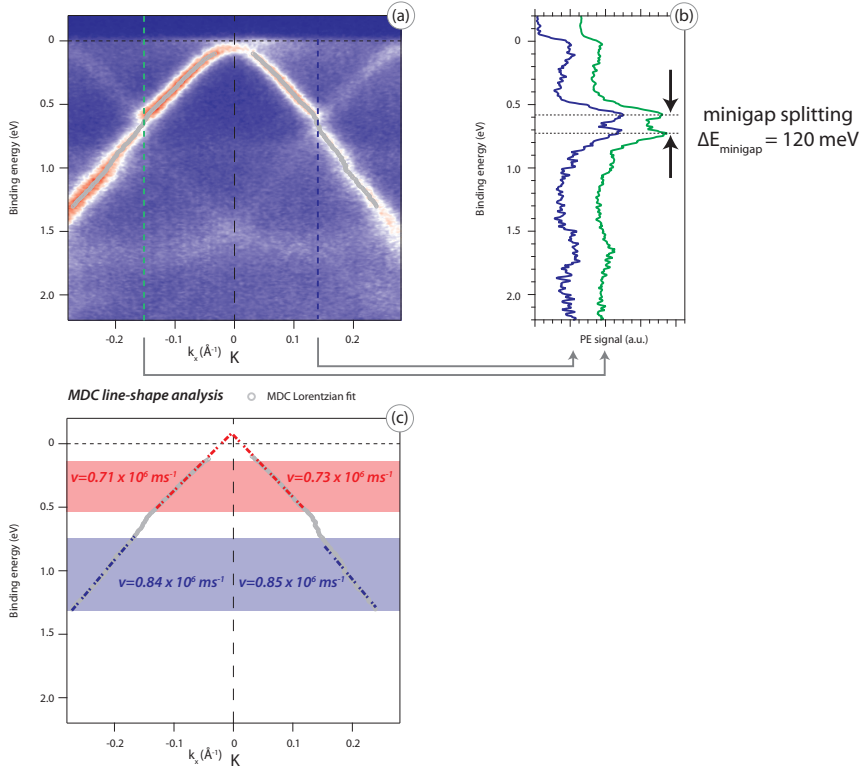


Figure 11.1: The line-shape analysis perpendicular to the $\Gamma - \text{K}$ direction. (a) ARPES data from graphene/Ir(111) measured at the BESSY ARPES-station, using $h\nu = 65 \text{ eV}$ photon energy and employing the β -flip. The analyzer is set to MAD lens mode. (b) EDC spectra extracted at -0.15 \AA^{-1} and 0.15 \AA^{-1} yielding a equal minigap spitting of 120 meV . (c) Evaluation of the group velocity from the slope of the fitted peak positions.

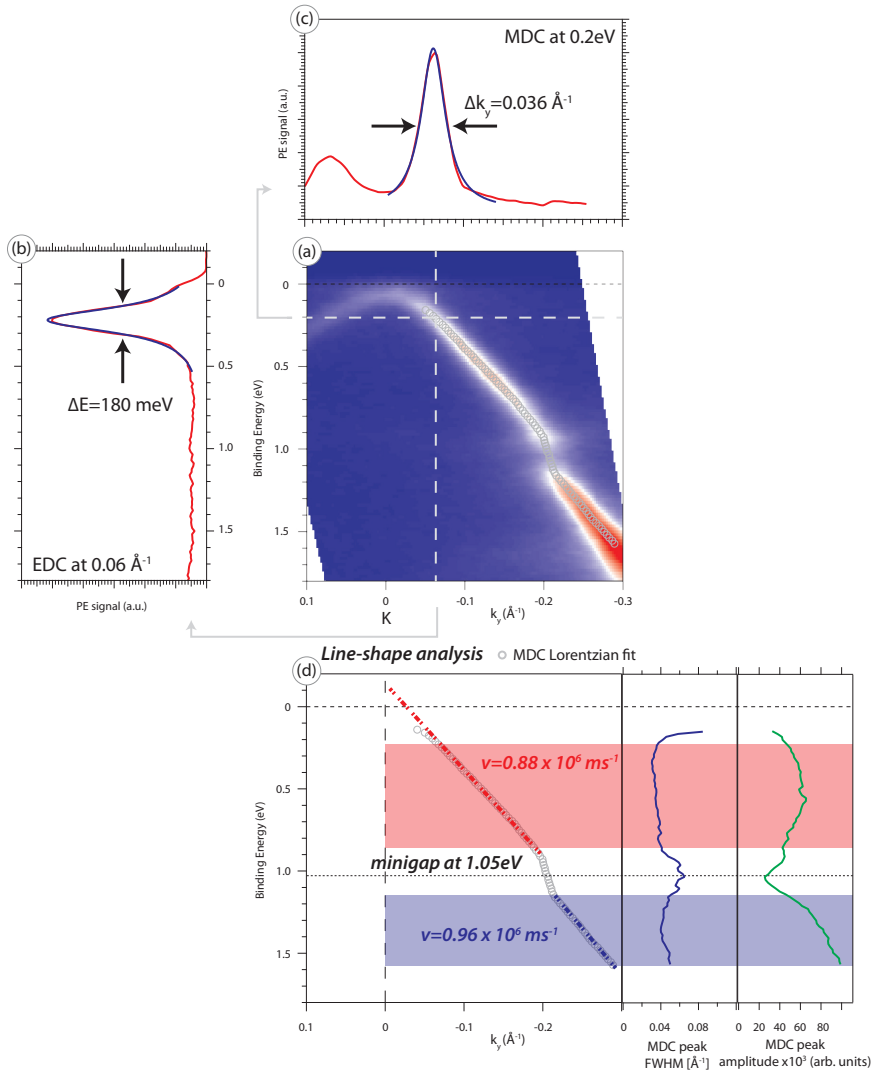


Figure 11.2: Line-shape analysis of ARPES data from graphene/Ir(111) measured at the Lab ARPES-station, using the Helium discharge lamp with $h\nu = 21.21 \text{ eV}$ radiation and employing the β -flip. The analyzer is set to LAD lens mode. The analysis is performed extracting spectra along the ΓK direction.

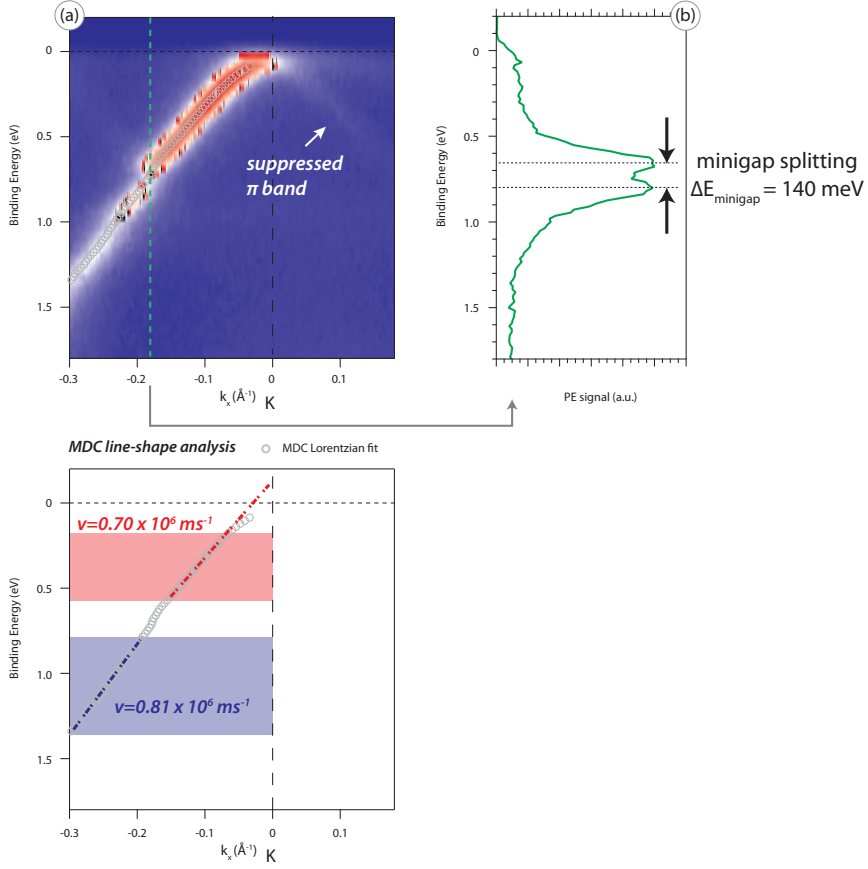


Figure 11.3: Line-shape analysis of ARPES data from graphene/Ir(111) measured at the Lab ARPES-station, using the Helium discharge lamp with $h\nu = 21.21 \text{ eV}$ radiation and employing the β -flip. The analyzer is set to LAD lens mode, to obtain high resolution spectra of the area around the K-point. The analysis is performed extracting spectra perpendicular to the Γ K direction. Due to the rotated “dark corridor” the second “branch” of the π band is suppressed.

Polarization dependence

Beyond the possibility to vary the photon energy over a large range, most of the modern synchrotron light sources offer the possibility to change type and direction of polarization of the electromagnetic radiation through the use of APPLE-type undulators, as described in chapter 4.4. Thus, it becomes possible to study how dipole and polarization selection rules of the different electronic states effect the photoemission intensity. All ARPES measurements shown in chapter 6 – 10 are obtained using linear horizontal polarized radiation. ARPES spectra using linear vertical polarization are shown in Fig. 11.4, highlighting the distinct geometrical orientation of the π states of graphene pointing out-of-plane, whereas the associated σ states are arranged in-plane of the graphene sheet. Hence the π band is suppressed over the whole range of the BZ (Fig. 11.4 (a) and (d)), while the σ band is enhanced.

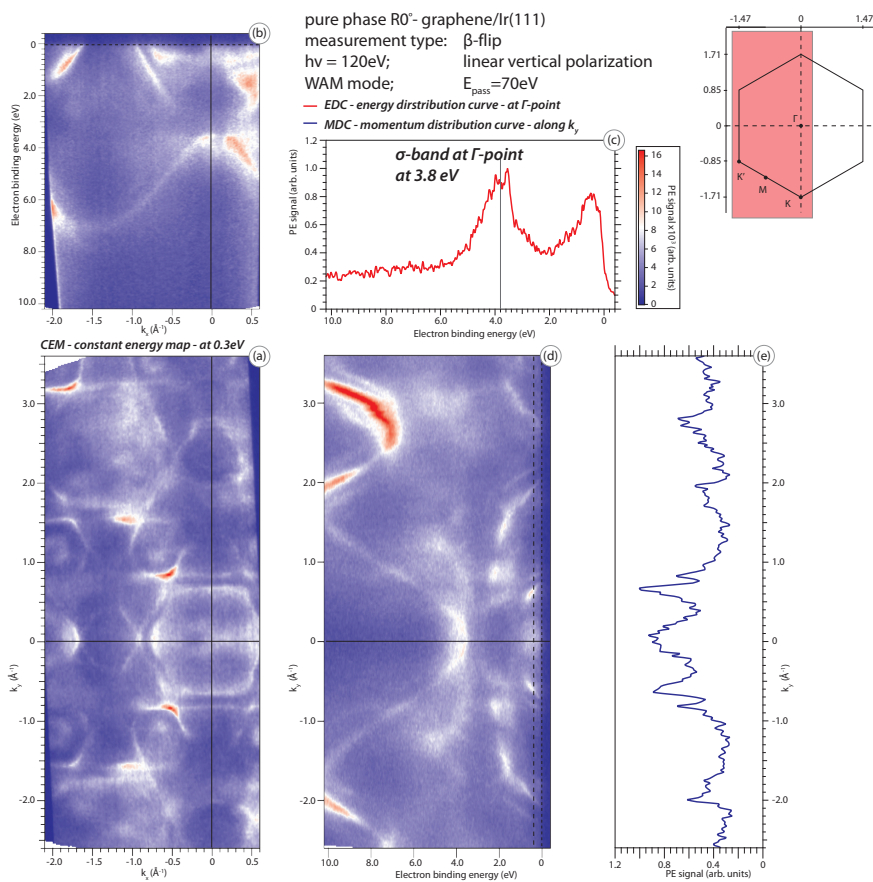


Figure 11.4: 2D-k-space ARPES data from graphene/Ir(111) measured at the BESSY ARPES station, with $h\nu = 120$ eV radiation with **linear vertical polarization**, employing the β -flip. (a) Constant energy maps extracted at energies of 0.3 eV below the Fermi level. (b) and (d) depict the valence band spectra at the K-point along k_x (b) and k_y (d) direction in k-space, with main contributions from the σ -band of graphene. The graphene π -band is effectively suppressed. (c) EDC at the Γ -point. (e) MDC along Γ K direction.

Photon energy dependence

In order to gain more information about the behavior of the dominating band character of features in the photoemission images of graphene/Ir(111) – graphene π –, σ – band and Ir related sp –, $5d$ – and surface–states, it is instructive to measure ARPES spectra for different excitation energies. ARPES data of graphene/Ir(111) are obtained at different photon energies in the range of 65 eV – 155 eV and using linear horizontal polarization are shown in Fig. 11.5. Such “photon scans” are used in chapter 9 on graphene/Yb/Ir(111), to specify that the apparent band gaps above E_D , are caused by hybridization between Yb $4f$ and graphene π states, *i. e.* an avoided crossing phenomenon. Data on two photon energies 65 eV and 100 eV where extracted from a photon scan and depicted in Fig. 9.6.

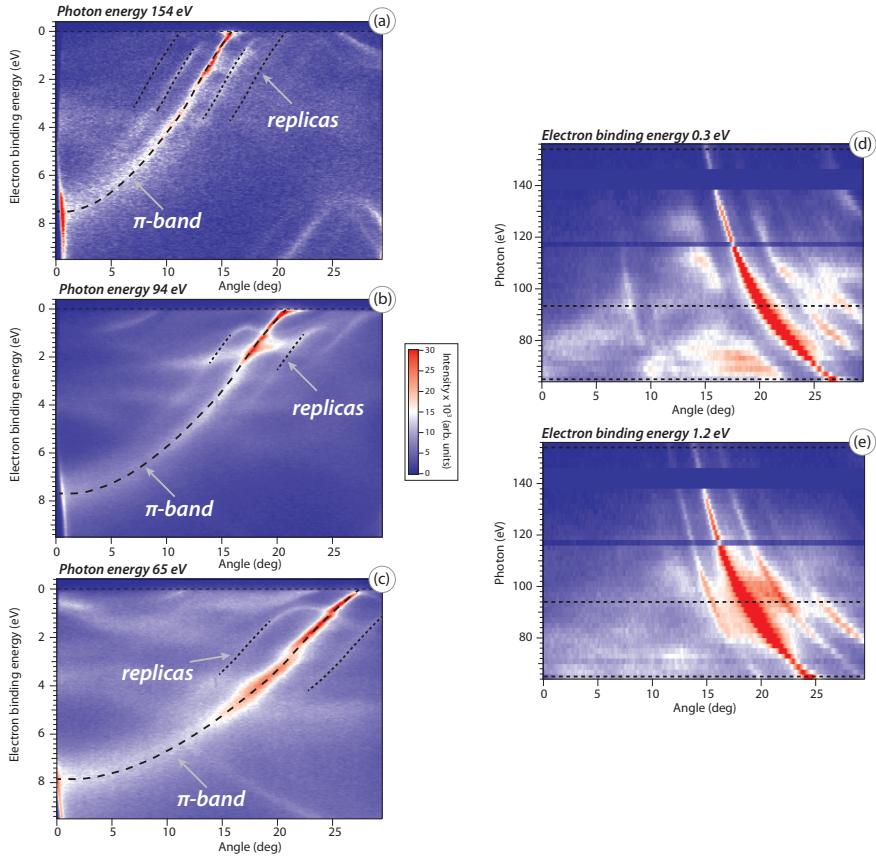


Figure 11.5: ARPES data from graphene/Ir(111) measured at the BESSY ARPES station, successively changing the photon energy $h\nu = 65 \text{ eV} - 155 \text{ eV}$ and using linear horizontal polarization. (a), (b) and (c) valence band spectra for photon energies of 154 eV, 94 eV and 65 eV. (d) and (e) depict spectra at binding energies of 0.3 eV and 1.2 eV, as a function of the acceptance angle and the photon energy for a fixed sample geometry along the Γ -K direction. Due to compression of the Brillouin-zone at higher photon energies, the graphene π band emerges at lower take-off angles.

Bibliography

- [1] K. S. Novoselov, D. Jiang, F. Schedin, T. J. Booth, V. V. Khotkevich, S. V. Morozov, and A. K. Geim. Two-dimensional atomic crystals. *Proceedings of the National Academy of Sciences of the United States of America*, 102(30):10451–10453, 2005.
- [2] P. R. Wallace. The Band Theory of Graphite. *Physical Review*, 71(9), 1947.
- [3] G. W. Semenoff. Condensed-Matter Simulation of a 3-Dimensional Anomaly. *Physical Review Letters*, 53(26):2449–2452, 1984.
- [4] D. P. DiVincenzo and E. J. Mele. Self-consistent effective-mass theory for intralayer screening in graphite intercalation compounds. *Physical Review B*, 29(4):1685–1694, 1984.
- [5] R. Peierls. Quelques propriétés typiques des corps solides. *Annales de l'institut Henri Poincaré*, 5(3):177–222, 1935.
- [6] L. D. Landau. Zur Theorie der Phasenumwandlungen II. *Phys. Z. Sowjetunion*, 11:26–35, 1937.
- [7] K. S. Novoselov, A. K. Geim, S. V. Morozov, D. Jiang, M. I. Katsnelson, I. V. Grigorieva, S. V. Dubonos, and A. A. Firsov. Two-dimensional gas of massless Dirac fermions in graphene. *Nature*, 438(7065):197–200, 2005.
- [8] Y. B. Zhang, Y. W. Tan, H. L. Stormer, and P. Kim. Experimental observation of the quantum Hall effect and Berry's phase in graphene. *Nature*, 438(7065):201–204, 2005.

- [9] Nobel Media AB. The Nobel Prize in Physics 2010, 2015. Available online at http://www.nobelprize.org/nobel_prizes/physics/laureates/2010/.
- [10] Graphene Flagship. “Extras” about Graphene Flagship, 2013. Available online at http://graphene-flagship.eu/wp-content/uploads/2013/11/EXTRAS_Graphene_Flagship.pdf.
- [11] V. Karpan, G. Giovannetti, P. Khomyakov, M. Talanana, A. Starikov, M. Zwierzycki, J. van den Brink, G. Brocks, and P. Kelly. Graphite and Graphene as Perfect Spin Filters. *Physical Review Letters*, 99(17):176602, 2007.
- [12] V. M. Karpan, P. A. Khomyakov, A. A. Starikov, G. Giovannetti, M. Zwierzycki, M. Talanana, G. Brocks, J. van den Brink, and P. J. Kelly. Theoretical prediction of perfect spin filtering at interfaces between close-packed surfaces of Ni or Co and graphite or graphene. *Physical Review B*, 78(19):195419, 2008.
- [13] M. Tokman, X. Yao, and A. Belyanin. Generation of Entangled Photons in Graphene in a Strong Magnetic Field. *Physical Review Letters*, 110(7):077404, 2013.
- [14] Andreas Hirsch. The era of carbon allotropes. *Nature Materials*, 9:868–871, 2010.
- [15] R. Gross. *Festkörperphysik*. Walther-Meissner-Institut, Garching, 2004. Available online at <http://www.wmi.badw.de/teaching/Lecturenotes/index.html>.
- [16] T. Ohta, A. Bostwick, T. Seyller, K. Horn, and E. Rotenberg. Controlling the electronic structure of bilayer graphene. *Science*, 313(5789):951–954, 2006.
- [17] A. K. Geim and K. S. Novoselov. The rise of graphene. *Nature Materials*, 6(3):183–191, 2007.
- [18] K. V. Emtsev, A. Bostwick, K. Horn, J. Jobst, G. L. Kellogg, L. Ley, J. L. McChesney, T. Ohta, S. A. Reshanov, J. Rohrl, E. Rotenberg, A. K. Schmid, D. Waldmann, H. B. Weber, and Th. Seyller. Towards wafer-size graphene layers by atmospheric pressure graphitization of silicon carbide. *Nature Materials*, 8(3):203–207, 2009.

-
- [19] E. McCann. Epitaxial Graphene on Metals. In H. Raza, editor, *Graphene Nanoelectronics*, pages 237–275. Springer, Berlin-Heidelberg, 2012.
 - [20] R. Saito, M. S. Dresselhaus, and G. Dresselhaus. *Physical Properties of Carbon Nanotubes*, (Imperial College Press, London, 1998). Imperial College Press, London, 1998.
 - [21] H. Aoki and M. S. Dresselhaus. *Physics of Graphene*. Springer, Berlin-Heidelberg, 2014.
 - [22] J. Fuchs and M. Goerbig. Introduction to the Physical Properties of Graphene, 2015. Available online at https://www.lps.u-psud.fr/IMG/pdf_CoursGraphene2008.pdf.
 - [23] P. B. Atienza. *Superconductivity in Graphene and Carbon Nanotubes*. Springer Theses. Springer International Publishing, Switzerland, 2014.
 - [24] Y. S. Dedkov, K. Horn, A. B. Preobrajenski, and M. Fonin. Epitaxial Graphene on Metals. In H. Raza, editor, *Graphene Nanoelectronics*, pages 189–234. Springer, Berlin-Heidelberg, 2012.
 - [25] S. Reich, J. Maultzsch, C. Thomsen, and P. Ordejón. Tight-binding description of graphene. *Physical Review B*, 66(3):035412, 2002.
 - [26] Felix Bloch. Über die Quantenmechanik der Elektronen in Kristallgittern. *Zeitschrift für Physik*, 52(7-8):555–600, 1929.
 - [27] W. Nolting. *Grundkurs Theoretische Physik 7 – Viel-Teilchen-Theorie*. Springer Spektrum, Berlin-Heidelberg, 2015.
 - [28] M. Kralj, I. Pletikosić, M. Petrovic, P. Pervan, M. Milun, A. T. N’Diaye, C. Busse, T. Michely, J. Fujii, and I. Vobornik. Graphene on Ir(111) characterized by angle-resolved photoemission. *Physical Review B*, 84(7):075427, 2011.
 - [29] W. Nolting. *Grundkurs Theoretische Physik 5/2 – Quantenmechanik: Methoden und Anwendungen*. Springer Spektrum, Berlin-Heidelberg, 2015.
 - [30] T. Ohlsson. *Relativistic Quantum Physics: From Advanced Quantum Mechanics to Introductory Quantum Field Theory*. Cambridge University Press, 2011.

- [31] Wavemetrics Inc. Igor Pro 6.36 Software, 2015. Available online at <http://www.wavemetrics.com/>.
- [32] Claire Berger, Zhimin Song, Xuebin Li, Xiaosong Wu, Nate Brown, Cécile Naud, Didier Mayou, Tianbo Li, Joanna Hass, Alexei N. Marchenkov, Edward H. Conrad, Phillip N. First, and Walt A. de Heer. Electronic Confinement and Coherence in Patterned Epitaxial Graphene. *Science*, 312(5777):1191–1196, 2006.
- [33] J. H. Chen, M. Ishigami, C. Jang, D. Hines, M. Fuhrer, and E. Williams. Printed Graphene Circuits. *Advanced Materials*, 19(21):3623–3627, 2007.
- [34] Wei Han, K. Pi, K. M. McCreary, Yan Li, Jared J. I. Wong, A. G. Swartz, and R. K. Kawakami. Tunneling Spin Injection into Single Layer Graphene. *Physical Review Letters*, 105(16):167202, 2010.
- [35] Nikolaos Tombros, Csaba Jozsa, Mihaita Popinciuc, Harry T. Jonkman, and Bart J. van Wees. Electronic spin transport and spin precession in single graphene layers at room temperature. *Nature*, 448(7153):571–574, 2007.
- [36] Changgu Lee, Xiaoding Wei, Jeffrey W. Kysar, and James Hone. Measurement of the Elastic Properties and Intrinsic Strength of Monolayer Graphene. *Science*, 321(5887):385–388, 2008.
- [37] K. S. Kim, Y. Zhao, H. Jang, S. Y. Lee, J. M. Kim, K. S. Kim, J. H. Ahn, P. Kim, J. Y. Choi, and B. H. Hong. Large-scale pattern growth of graphene films for stretchable transparent electrodes. *Nature*, 457(7230):706–10, 2009.
- [38] S. Bae, H. Kim, Y. Lee, X. Xu, J. S. Park, Y. Zheng, J. Balakrishnan, T. Lei, H. R. Kim, Y. I. Song, Y. J. Kim, K. S. Kim, B. Ozyilmaz, J. H. Ahn, B. H. Hong, and S. Iijima. Roll-to-roll production of 30-inch graphene films for transparent electrodes. *Nature Nanotechnology*, 5(8):574–8, 2010.
- [39] E. N. Voloshina and Yu. S. Dedkov. General approach to understanding the electronic structure of graphene on metals. *Materials Research Express*, 1(3):035603, 2014.

-
- [40] Giovanni Bertoni, Lionel Calmels, Anne Altibelli, and Virginie Serin. First-principles calculation of the electronic structure and EELS spectra at the graphene/Ni(111) interface. *Physical Review B*, 71(7):075402, 2005.
- [41] A. Varykhalov, J. Sanchez-Barriga, A. M. Shikin, C. Biswas, E. Vescovo, A. Rybkin, D. Marchenko, and O. Rader. Electronic and Magnetic Properties of Quasifreestanding Graphene on Ni. *Physical Review Letters*, 101(15):157601, 2008.
- [42] Y. S. Dedkov and M. Fonin. Electronic and magnetic properties of the graphene-ferromagnet interface. *New Journal of Physics*, 12:125004, 2010.
- [43] I. Pletikosić, M. Kralj, P. Pervan, R. Brako, J. Coraux, A. T. N'Diaye, C. Busse, and T. Michely. Dirac Cones and Minigaps for Graphene on Ir(111). *Physical Review Letters*, 102(5):056808, 2009.
- [44] R. Balog, B. Jorgensen, L. Nilsson, M. Andersen, E. Rienks, M. Bianchi, M. Fanetti, E. Laegsgaard, A. Baraldi, S. Lizzit, Z. Sljivancanin, F. Besenbacher, B. Hammer, T. G. Pedersen, P. Hofmann, and L. Hornekaer. Bandgap opening in graphene induced by patterned hydrogen adsorption. *Nature Materials*, 9(4):315–319, 2010.
- [45] S. Rusponi, M. Papagno, P. Moras, S. Vlaic, M. Etzkorn, P. Sheverdyeva, D. Pacilé, H. Brune, and C. Carbone. Highly Anisotropic Dirac Cones in Epitaxial Graphene Modulated by an Island Superlattice. *Physical Review Letters*, 105(24), 2010.
- [46] M. N. Baibich, J. M. Broto, A. Fert, F. Nguyen Van Dau, F. Petroff, P. Etienne, G. Creuzet, A. Friederich, and J. Chazelas. Giant Magnetoresistance of (001)Fe/(001)Cr Magnetic Superlattices. *Physical Review Letters*, 61(21):2472–2475, 1988.
- [47] G. Binasch, P. Grünberg, F. Saurenbach, and W. Zinn. Enhanced magnetoresistance in layered magnetic structures with antiferromagnetic interlayer exchange. *Physical Review B*, 39(7):4828–4830, 1989.
- [48] Nobel Media AB. The Nobel Prize in Physics 2007, 2015. Available online at http://www.nobelprize.org/nobel_prizes/physics/laureates/2007/.

- [49] J. Stöhr. *Magnetism*. Springer, Berlin – Heidelberg, 2010.
- [50] A. M. Shikin, G. V. Prudnikova, V. K. Adamchuk, F. Moresco, and K. H. Rieder. Surface intercalation of gold underneath a graphite monolayer on Ni(111) studied by angle-resolved photoemission and high-resolution electron-energy-loss spectroscopy. *Physical Review B*, 62(19):13202–13208, 2000.
- [51] Y. S. Dedkov, A. M. Shikin, V. K. Adamchuk, S. L. Molodtsov, C. Laubschat, A. Bauer, and G. Kaindl. Intercalation of copper underneath a monolayer of graphite on Ni(111). *Physical Review B*, 64(3):035405, 2001.
- [52] S. Hüfner. *Photoelectron Spectroscopy*. Springer, Berlin-Heidelberg, 2003.
- [53] S. Hüfner. *Very High Resolution Photoelectron Spectroscopy*. Springer, Berlin-Heidelberg, 2007.
- [54] A. Damascelli. Probing the electronic structure of complex systems by ARPES. *Physica Scripta*, T109:61–74, 2004.
- [55] H. Vita. *Polarisationsabhängige winkelaufgelöste Photoemissionsspektroskopie am Kupratsupraleiter $\text{Bi}_{2-x}(\text{Pb}_x)\text{Sr}_2\text{CaCu}_2\text{O}_{8+\delta}$* . Diplomarbeit, Humboldt-Universität zu Berlin, 2009.
- [56] St. Thürmer. *Der Einfluss von Wasseradsorption auf die elektronische Struktur der Titan-Dichalkogenide*. Diplomarbeit, Humboldt-Universität zu Berlin, 2009.
- [57] H. Hertz. Über den Einfluss des ultravioletten Lichts auf die elektrische Entladung. *Annalen der Physik*, 31:983–1000, 1887.
- [58] P. Lenard. Erzeugung von Kathodenstrahlen durch ultraviolettes Licht. *Annalen der Physik*, 307:359–375, 1900.
- [59] A. Einstein. Über einen die Erzeugung und Verwandlung des Lichtes betreffenden heuristischen Gesichtspunkt. *Annalen der Physik*, 17:132–148, 1905.
- [60] D. Cahen and A. Kahn. Electron energetics at surfaces and interfaces: Concepts and Experiments. *Advanced Materials*, 15(4):271–277, 2003.

-
- [61] SPECS Surface Nano Analysis GmbH. PHOIBOS 100/150 Hemispherical Energy Analyzer Series – Technical Manual, 2008.
- [62] C. N. Berglund and W. E. Spicer. Photoemission Studies of Copper and Silver - Theory. *Physical Review A - General Physics*, 136(4A):A 1030 – A 1044, 1964.
- [63] M. P. Seah and W. A. Dench. Quantitative electron spectroscopy of surfaces: A standard data base for electron inelastic mean free paths in solids. *Surface and Interface Analysis*, 1(1):2–11, 1979.
- [64] A. Damascelli, Z. Hussain, and Z. X. Shen. Angle-resolved photoemission studies of the cuprate superconductors. *Reviews of Modern Physics*, 75(2):473–541, 2003.
- [65] P. D. Johnson and T. Valla. Photoemission as a Probe of the Collective Excitations in Condensed Matter Systems. In *Very High Resolution Photoelectron Spectroscopy*, book section 3, pages 55–84. Springer, Berlin-Heidelberg, 2007.
- [66] J. Minár. Theoretical Description of ARPES: The One-Step Model. In E. Pavarini, E. Koch, D. Vollhardt, and A. Lichtenstein, editors, *Lecture Notes of the Autumn School on Correlated Electrons*, Jülich, 2014. Forschungszentrum Jülich GmbH.
- [67] A. Kaminski and H. M. Fretwell. On the extraction of the self-energy from angle-resolved photoemission spectroscopy. *New Journal of Physics*, 7(1):98, 2005.
- [68] S. Raimes. *Many-Electron Theory*. North-Holland Publishing Company, Amsterdam-London, 1972.
- [69] M. Randeria, H. Ding, J. C. Campuzano, A. Bellman, G. Jennings, T. Yokoya, T. Takahashi, H. Katayama-Yoshida, T. Mochiku, and K. Kadowaki. Momentum Distribution Sum Rule for Angle-Resolved Photoemission. *Physical Review Letters*, 74(24):4951–4954, 1995.
- [70] A. Kaminski, J. Mesot, H. Fretwell, J. C. Campuzano, M. R. Norman, M. Randeria, H. Ding, T. Sato, T. Takahashi, T. Mochiku, K. Kadowaki, and H. Hoechst. Quasiparticles in the superconducting state of $\text{Bi}_2\text{Sr}_2\text{CaCu}_2\text{O}_{8+\delta}$. *Physical Review Letters*, 84(8):1788–1791, 2000.

- [71] T. Valla, A. V. Fedorov, P. D. Johnson, J. Xue, K. E. Smith, and F. J. DiSalvo. Charge-density-wave-induced modifications to the quasiparticle self-energy in $2\text{H} - \text{TaSe}_2$. *Physical Review Letters*, 85(22):4759–4762, 2000.
- [72] C. Brouder. Angular dependence of X-ray absorption spectra. *Journal of Physics-Condensed Matter*, 2(3):701, 1990.
- [73] A. Lehnert. *Magnetism of Individual Adatoms and of Epitaxial Monolayers*. PhD thesis, École Polytechnique Fédérale de Lausanne, 2009.
- [74] M. Bernien. *X-Ray Absorption Spectroscopy of Fe Complexes on Surfaces: Electronic Interactions and Tailoring of the Magnetic Coupling*. PhD thesis, Freie Universität, Berlin, 2009.
- [75] M. Bernien. *Spinfluktuationen in gekoppelten, magnetischen Schichten: eine temperaturabhängige Röntgenzirkulardichroismus-Studie*. Diplomarbeit, Freie Universität, Berlin, 2004.
- [76] J. H. Hubbell, H. A. Gimm, and I. Overbo. Pair, Triplet, and Total Atomic Cross-Sections (and Mass Attenuation Coefficients) for 1 MeV-100 GeV Photons in Elements $Z=1$ to 100. *Journal of Physical and Chemical Reference Data*, 9(4):1023–1147, 1980.
- [77] Nobel Media AB. The Nobel Prize in Physics 1924, 2014. Available online at http://www.nobelprize.org/nobel_prizes/physics/laureates/1924/index.html.
- [78] W. Demtröder. *Experimentalphysik Band 3 - Atome, Moleküle und Festkörper*. Springer, Berlin Heidelberg New York, 2010.
- [79] J. L. Erskine and E. A. Stern. Calculation of M_23 Magneto-Optical Absorption-Spectrum of Ferromagnetic Nickel. *Physical Review B*, 12(11):5016–5024, 1975.
- [80] F. De Groot and A Kotani. *Core Level Spectroscopy of Solids*. CRC Press; Taylor and Francis Group, Boca Raton – London – New York, 2008.
- [81] C. Cohen-Tannoudji, B. Diu, and F. Laloë. *Quantum Mechanics - Volume 2*. Hermann and John Wiley and Sons, 1977.

-
- [82] T. Regan. *X-ray Absorption Spectroscopy and Microscopy study of Ferro- and Antiferromagnetic thin films, with Applications to Exchange Anisotropy*. PhD thesis, Stanford University, 2001.
- [83] J. Stöhr and Y. Wu. *New Directions in Research with Third-Generation Soft X-Ray Synchrotron Radiation Sources*, pages 221–251. Kluwer Academic Publishers, Dordrecht, Boston and London, 1992.
- [84] P. Carra, B. T. Thole, M. Altarelli, and X. Wang. X-ray circular dichroism and local magnetic fields. *Physical Review Letters*, 70(5):694–697, 1993.
- [85] B. T. Thole, P. Carra, F. Sette, and G. van der Laan. X-ray circular dichroism as a probe of orbital magnetization. *Physical Review Letters*, 68(12):1943–1946, 1992.
- [86] G. Schütz, W. Wagner, W. Wilhelm, P. Kienle, R. Zeller, R. Frahm, and G. Materlik. Absorption of Circularly Polarized X-Rays in Iron. *Physical Review Letters*, 58(7):737–740, 1987.
- [87] D. J. Huang, H. T. Jeng, C. F. Chang, G. Y. Guo, J. Chen, W. P. Wu, S. C. Chung, S. G. Shyu, C. C. Wu, H. J. Lin, and C. T. Chen. Orbital magnetic moments of oxygen and chromium in CrO_2 . *Physical Review B*, 66(17):174440, 2002.
- [88] N. Mårtensson, P. Baltzer, P. A. Brühwiler, J. O. Forsell, A. Nilsson, A. Stenborg, and B. Wannberg. A very high resolution electron spectrometer. *Journal of Electron Spectroscopy and Related Phenomena*, 70(2):117–128, 1994.
- [89] C. Enderlein. *Graphene and its Interaction with Different Substrates Studied by Angular-Resolved Photoemission Spectroscopy*. PhD thesis, Freie Universität, Berlin, 2010.
- [90] H. D. Polaschegg. Optimization of the Parameters of the Ideal 180° Spherical Analyzer. *Applied Physics*, 9:223–227, 1976.
- [91] E. Starodub, A. Bostwick, L. Moreschini, S. Nie, F. El Gabaly, K. F. McCarty, and E. Rotenberg. In-plane orientation effects on the electronic structure, stability, and Raman scattering of monolayer graphene on $\text{Ir}(111)$. *Physical Review B*, 83:125428, 2011.

- [92] Helmholtz-Zentrum Berlin. Funktionsweise BESSY II, 2014. Available online at <http://www.helmholtz-berlin.de/quellen/bessy/elektronenspeicherring/>.
- [93] Albert C. Thompson. *X-Ray Data Booklet*. Lawrence Berkeley National Laboratory, University of California, Berkeley, 2009.
- [94] F. Hinterberger. *Physik der Teilchenbeschleuniger und Ionenoptik*. Springer, Berlin-Heidelberg, 2003.
- [95] D. Atwood. Synchrotron Radiation for Materials Science Applications, 2014. Available online at <http://ast.coe.berkeley.edu/srms/2007/Intro2007>.
- [96] Helmholtz-Zentrum Berlin. BESSY II Top-Up Operation, 2014. Available online at <http://www.helmholtz-berlin.de/forschung/oe/fg/beschleunigerphysik>.
- [97] T. Atkinson, V. Dürr, M. Helmecke, D. Schüler, D. Jousse, J.-L. Pastre, A. Setty, and E. Weihrer. Commissioning of the 50 MeV Preinjector LINAC for the BESSY II facility. *Proceedings of IPAC2011, San Sebastian, Spain*, THPC108:3140–3142, 2011.
- [98] H. Winick. Synchrotron radiation sources - Present capabilities and future directions. *J. Synchrotron Radiat.*, 5(24):168–175, 1998.
- [99] K. J. S. Sawhney, F. Senf, M. Scheer, F. Schafers, J. Bahrddt, A. Gaupp, and W. Gudat. A novel undulator-based PGM beam-line for circularly polarised synchrotron radiation at BESSY II. *Nuclear Instruments and Methods in Physics Research Section A - Accelerators Spectrometers Detectors and Associated Equipment*, 390(3):395–402, 1997.
- [100] R. Follath and F. Senf. New plane-grating monochromators for third generation synchrotron radiation light sources. *Nuclear Instruments and Methods in Physics Research Section A*, 390(3): 388–394, 1997.
- [101] S. Sasaki, K. Miyata, and T. Takada. A New Undulator for Generating Variably Polarized Radiation. *Japanese Journal of Applied Physics Part 2-Letters*, 31(12B):L1794–L1796, 1992.

-
- [102] W. Mahler. Flux measurement at UE56/2-PGM-1 by GaAs-Diode, 2012. private communication.
- [103] LumaSense Technologies GmbH. *IMPAC-Pyrometer IGA 8 pro – Technical Manual*, 2013.
- [104] R. Nyholm, S. Svensson, J. Nordgren, and A. Flodström. A Soft-X-Ray Monochromator for the Max Synchrotron Radiation Facility. *Nuclear Instruments and Methods in Physics Research Section A*, 246:267–271, 1986.
- [105] N. Vinogradov. *Controlling Electronic and Geometrical Structure of Honeycomb-Lattice Materials Supported on Metal Substrates*. PhD thesis, Uppsala University, 2013.
- [106] MAX IV Laboratory. D1011 station at MAX-lab, 2014. Available online at <https://www.maxlab.lu.se/node/501>.
- [107] Mika Hirsimäki. MAX-lab beamline D1011 panorama, 2014. Available online at <https://www.flickr.com/photos/finnbiff/5418158233/in/photostream/>.
- [108] A. T. N’Diaye, J. Coraux, T. N. Plasa, C. Busse, and T. Michely. Structure of epitaxial graphene on Ir(111). *New Journal of Physics*, 10:043033, 2008.
- [109] J. Coraux, A. T. N’Diaye, M. Engler, C. Busse, D. Wall, N. Buckanie, F. J. M. Z. Heringdorf, R. van Gastel, B. Poelsema, and T. Michely. Growth of graphene on Ir(111). *New Journal of Physics*, 11:023006, 2009.
- [110] E. N. Voloshina, E. Fertitta, A. Garhofer, F. Mittendorfer, M. Fonin, A. Thissen, and Y. S. Dedkov. Electronic structure and imaging contrast of graphene moiré on metals. *Scientific Reports*, 3:1072, 2013.
- [111] Y. S. Dedkov, M. Fonin, and C. Laubschat. A possible source of spin-polarized electrons: The inert graphene/Ni(111) system. *Applied Physics Letters*, 92(5):052506, 2008.
- [112] Y. S. Dedkov, M. Fonin, U. Rüdiger, and C. Laubschat. Graphene-protected iron layer on Ni(111). *Applied Physics Letters*, 93(2):022509, 2008.

- [113] Kurt J. Lesker Company. Material Deposition Table, 2014. Available online at http://www.lesker.com/newweb/deposition_materials/materialdeposition.cfm?pgid=0.
- [114] J. Wintterlin and M. L. Bocquet. Graphene on metal surfaces. *Surface Science*, 603(10-12):1841–1852, 2009.
- [115] A. T. N’Diaye, S. Bleikamp, P. J. Feibelman, and T. Michely. Two-dimensional Ir cluster lattice on a graphene moire on Ir(111). *Physical Review Letters*, 97(21):215501, 2006.
- [116] Y. S. Dedkov, E. Voloshina, and M. Fonin. Scanning probe microscopy and spectroscopy of graphene on metals. *physica status solidi (b)*, pages 1–18, 2015.
- [117] E. Voloshina and Y. Dedkov. Graphene on metallic surfaces: problems and perspectives. *Physical Chemistry Chemical Physics*, 14(39):13502–13514, 2012.
- [118] S. K. Hamalainen, M. P. Boneschanscher, P. H. Jacobse, I. Swart, K. Pussi, W. Moritz, J. Lahtinen, P. Liljeroth, and J. Sainio. Structure and local variations of the graphene moire on Ir(111). *Physical Review B*, 88(20):201406(R), 2013.
- [119] A. Y. Cho and J. R. Arthur. Molecular beam epitaxy. *Progress in Solid State Chemistry*, 10, Part 3(0):157–191, 1975.
- [120] H. Lüth. *Solid Surfaces, Interfaces and Thin Films*. Springer, Berlin-Heidelberg, 2010.
- [121] R. E. Honig and D. A. Kramer. Vapor Pressure Data for Solid and Liquid Elements. *RCA Review*, 30(2):285–305, 1969.
- [122] Omicron Vakuumphysik GmbH. UHV Evaporator EFM3 – Technical Manual, 1993.
- [123] NIMS. Database of electron inelastic mean free path for elemental solids, 2014. Available online at <http://www.nims.go.jp/research/organization/hdfqf1000000isjt-att/hdfqf1000000ispa.pdf>.
- [124] M. Sicot, S. Bouvron, O. Zander, U. Rudiger, Y. S. Dedkov, and M. Fonin. Nucleation and growth of nickel nanoclusters on graphene Moireacute on Rh(111). *Applied Physics Letters*, 96(9), 2010.

-
- [125] M. Petrović, I. Šrut Rakić, S. Runte, C. Busse, J. T. Sadowski, P. Lazić, I. Pletikosić, Z. H. Pan, M. Milun, P. Pervan, N. Atodiresei, R. Brako, D. Šokčević, T. Valla, T. Michely, and M. Kralj. The mechanism of caesium intercalation of graphene. *Nature Communications*, 4:2772, 2013.
- [126] J. F. van der Veen, F. J. Himpsel, and D. E. Eastman. Structure-Dependent 4f Core-Level Binding Energies for Surface Atoms on Ir(111), Ir(100)-(5x1), and Metastable Ir(100)-(1x1). *Physical Review Letters*, 44(3):189–192, 1980.
- [127] A. Varykhalov, D. Marchenko, M. R. Scholz, E. D. L. Rienks, T. K. Kim, G. Bihlmayer, J. Sanchez-Barriga, and O. Rader. Ir(111) Surface State with Giant Rashba Splitting Persists under Graphene in Air. *Physical Review Letters*, 108(6):066804, 2012.
- [128] S. Tougaard and B. Jorgensen. Absolute background determination in XPS. *Surface and Interface Analysis*, 7:17–21, 1985.
- [129] S. Tougaard, W. Braun, E. Holub-Krappe, and H. Saalfeld. Test of algorithm for background correction in xps under variation of xps peak energy. *Surface and Interface Analysis*, 13(4):225–227, 1988.
- [130] S. Tougaard. Universality Classes of Inelastic Electron Scattering Cross-sections. *Surface and Interface Analysis*, 25:137–154, 1997.
- [131] M. P. Seah. Background subtraction: I. General behaviour of Tougaard-style backgrounds in AES and XPS. *Surface Science*, 420(2-3):285–294, 1999.
- [132] R. Hesse and R. Denecke. Improved Tougaard background calculation by introduction of fittable parameters for the inelastic electron scattering cross-section in the peak fit of photoelectron spectra with UNIFIT 2011. *Surface and Interface Analysis*, 43(12):1514–1526, 2011.
- [133] S. Doniach and M. Sunjic. Many-Electron Singularity in X-ray Photoemission and X-ray Line Spectra From Metals. *Journal of Physics Part C Solid State Physics*, 3:285–291, 1970.
- [134] W. H. Press, S. A. Teukolsky, W. T. Vetterling, and B. P. Flannery. *Numerical Recipes - The Art of Scientific Computing*. Cambridge University Press, New York, 2007.

- [135] D. Pacilé, M. Papagno, A. F. Rodriguez, M. Grioni, and L. Papagno. Near-edge x-ray absorption fine-structure investigation of graphene. *Physical Review Letters*, 101(6):066806, 2008.
- [136] J. Stöhr. NEXAFS Spectroscopy. In G. Ertl, R. Gomer, D. Mills, and H. Lotsch, editors, *Springer Series in Surface Science*. Springer-Verlag, Berlin, Heidelberg, New York, 1996.
- [137] A. Schöll, Y. Zou, Th Schmidt, R. Fink, and E. Umbach. Energy calibration and intensity normalization in high-resolution NEXAFS spectroscopy. *Journal of Electron Spectroscopy and Related Phenomena*, 129(1):1–8, 2003.
- [138] C. T. Chen, Y. U. Idzerda, H.-J. Lin, N. V. Smith, G. Meigs, E. Chaban, G. H. Ho, E. Pellegrin, and F. Sette. Experimental Confirmation of the X-Ray Magnetic Circular Dichroism Sum Rules for Iron and Cobalt. *Physical Review Letters*, 75(1):152–155, 1995.
- [139] R. Wu, D. Wang, and A. Freeman. First principles investigation of the validity and range of applicability of the x-ray magnetic circular dichroism sum rule. *Physical Review Letters*, 71(21):3581–3584, 1993.
- [140] A. Scherz. *Spin-dependent X-ray Absorption Spectroscopy of 3d Transition Metals: Systematics and Applications*. PhD thesis, Freie Universität, Berlin, 2003.
- [141] P. Lacovig, M. Pozzo, D. Alfe, P. Vilmercati, A. Baraldi, and S. Lizzit. Growth of Dome-Shaped Carbon Nanoislands on Ir(111): The Intermediate between Carbide Clusters and Quasi-Free-Standing Graphene. *Physical Review Letters*, 103:166101, 2009.
- [142] J. Moulder, W. Stickle, P. Sobol, and K. Bomben. *Handbook of X-ray Photoelectron Spectroscopy*. Physical Electronics Inc., Eden Prairie, Minnesota, USA, 1995. A Reference Book of Standard Spectra for Identification and Interpretation of XPS Data.
- [143] S. Lizzit and A. Baraldi. High-resolution fast X-ray photoelectron spectroscopy study of ethylene interaction with Ir(111): From chemisorption to dissociation and graphene formation. *Catalysis Today*, 154:68–74, 2010.

-
- [144] S. Evans. Curve synthesis and optimization procedures for X-ray photoelectron spectroscopy. *Surface and Interface Analysis*, 17: 85–93, 1991.
 - [145] I. Gierz, J. Henk, H. Hochst, C. R. Ast, and K. Kern. Illuminating the dark corridor in graphene: Polarization dependence of angle-resolved photoemission spectroscopy on graphene. *Physical Review B*, 83(12):121408(R), 2011.
 - [146] SPECS Surface Nano Analysis GmbH. Ultraviolet Source UVS 300, UV Monochromator TMM 304 – Technical Manual, 2009.
 - [147] R. Koch and Th. Seyller. High resolution ARPES measurements on QFMLG at the ARPES-station at BESSY II – personal communication, 2012.
 - [148] C. Riedl, C. Coletti, T. Iwasaki, A. A. Zakharov, and U. Starke. Quasi-Free-Standing Epitaxial Graphene on SiC Obtained by Hydrogen Intercalation. *Physical Review Letters*, 103(24):246804, 2009.
 - [149] St. Böttcher. *Functionalization of Graphene: A Theoretical and Experimental Study of Water and Ammonia Adsorbed on Graphene/Ni(111)*. Master thesis, Freie Universität, Berlin, 2010.
 - [150] E. L. Shirley, L. J. Terminello, A. Santoni, and F. J. Himpsel. Brillouin-Zone-Selection Effects in Graphite Photoelectron Angular-Distributions. *Physical Review B*, 51(19):13614–13622, 1995.
 - [151] M. Mucha-Kruczynski, O. Tsyplyatyev, A. Grishin, E. McCann, V. I. Fal’ko, A. Bostwick, and E. Rotenberg. Characterization of graphene through anisotropy of constant-energy maps in angle-resolved photoemission. *Physical Review B*, 77(19):195403, 2008.
 - [152] F. Kuemmeth and E. I. Rashba. Giant spin rotation under quasiparticle-photoelectron conversion: Joint effect of sublattice interference and spin-orbit coupling. *Physical Review B*, 80(24): 241409(R), 2009.
 - [153] W. S. Jung, C. S. Leem, Chul Kim, S. R. Park, S. Y. Park, B. J. Kim, E. Rotenberg, and C. Kim. Imaging the electron density in solids by using multi-Brillouin-zone angle resolved photoelectron spectroscopy. *Physical Review B*, 82(23):235105, 2010.

- [154] I. Gierz, M. Lindroos, H. Hocht, C. R. Ast, and K. Kern. Graphene Sublattice Symmetry and Isospin Determined by Circular Dichroism in Angle-Resolved Photoemission Spectroscopy. *Nano Letters*, 12(8):3900–3904, 2012.
- [155] A. Bostwick, T. Ohta, T. Seyller, K. Horn, and E. Rotenberg. Quasiparticle dynamics in graphene. *Nature Physics*, 3(1):36–40, 2007.
- [156] I. Gierz, T. Suzuki, R. T. Weitz, D. S. Lee, B. Krauss, C. Riedl, U. Starke, H. Hochst, J. H. Smet, C. R. Ast, and K. Kern. Electronic decoupling of an epitaxial graphene monolayer by gold intercalation. *Physical Review B*, 81:235408, 2010.
- [157] A. Bostwick, T. Ohta, J. L. McChesney, K. V. Emtsev, T. Seyller, K. Horn, and E. Rotenberg. Symmetry breaking in few layer graphene films. *New Journal of Physics*, 9:385, 2007.
- [158] E. Longinova, S. Nie, K. Thurmer, N. C. Bartelt, and K. F. McCarty. Defects of graphene on Ir(111): Rotational domains and ridges. *Physical Review B*, 80:085430, 2009.
- [159] H. Hattab, A. T. N’Diaye, D. Wall, G. Jnawali, J. Coraux, C. Busse, R. van Gastel, B. Poelsema, T. Michely, F. J. M. Z. Heringdorf, and M. Horn-von Hoegen. Growth temperature dependent graphene alignment on Ir(111). *Applied Physics Letters*, 98(14):141903, 2011.
- [160] R. van Gastel, A. T. N’Diaye, D. Wall, J. Coraux, C. Busse, N. M. Buckanie, F. J. M. zu Heringdorf, M. H. von Hoegen, T. Michely, and B. Poelsema. Selecting a single orientation for millimeter sized graphene sheets. *Applied Physics Letters*, 95: 121901, 2009.
- [161] D. Marchenko, J. Sanchez-Barriga, M. R. Scholz, O. Rader, and A. Varykhalov. Spin splitting of Dirac fermions in aligned and rotated graphene on Ir(111). *Physical Review B*, 87(11), 2013.
- [162] M. Batzill. The surface science of graphene: Metal interfaces, CVD synthesis, nanoribbons, chemical modifications, and defects. *Surface Science Reports*, 67(3-4):83–115, 2012.

-
- [163] R. Courths. Absolute determination of electronic band structure of copper by angle-resolved photoemission. *Solid State Communications*, 40(5):529–533, 1981.
- [164] R. Courths, B. Cord, H. Wern, and S. Hufner. Angle-Resolved Photoemission and Band Structure of Copper. *Physica Scripta*, 1983(T4):144, 1983.
- [165] E. N. Voloshina, A. Generalov, M. Weser, S. Böttcher, K. Horn, and Y. S. Dedkov. Structural and electronic properties of the graphene/Al/Ni(111) intercalation system. *New Journal of Physics*, 13:113028, 2011.
- [166] M. Weser, Y. Rehder, K. Horn, M. Sicot, M. Fonin, A. B. Preobrajenski, E. N. Voloshina, E. Goering, and Y. S. Dedkov. Induced magnetism of carbon atoms at the graphene/Ni(111) interface. *Applied Physics Letters*, 96(1):012504, 2010.
- [167] M. Weser, E. N. Voloshina, K. Horn, and Y. S. Dedkov. Electronic structure and magnetic properties of the graphene/Fe/Ni(111) intercalation-like system. *Physical Chemistry Chemical Physics*, 13(16):7534–7539, 2011.
- [168] G. Profeta, M. Calandra, and F. Mauri. Phonon-mediated superconductivity in graphene by lithium deposition. *Nature Physics*, 8(2):131–134, 2012.
- [169] M. Gyamfi, T. Eelbo, M. Wasniowska, and R. Wiesendanger. Impact of intercalated cobalt on the electronic properties of graphene on Pt(111). *Physical Review B*, 85(20):205434, 2012.
- [170] R. Decker, J. Brede, N. Atodiressei, V. Caciuc, S. Blugel, and R. Wiesendanger. Atomic-scale magnetism of cobalt-intercalated graphene. *Physical Review B*, 87(4):041403(R), 2013.
- [171] D. Pacilé, P. Leicht, M. Papagno, P. M. Sheverdyaeva, P. Moras, C. Carbone, K. Krausert, L. Zielke, M. Fonin, Y. S. Dedkov, F. Mittendorfer, J. Doppler, A. Garhofer, and J. Redinger. Artificially lattice-mismatched graphene/metal interface: Graphene/Ni/Ir(111). *Physical Review B*, 87(3):035420, 2013.

- [172] P. Sutter, J. T. Sadowski, and E. Sutter. Graphene on Pt(111): Growth and substrate interaction. *Physical Review B*, 80(24): 245411, 2009.
- [173] S. Marchini, S. Gunther, and J. Winterlin. Scanning tunneling microscopy of graphene on Ru(0001). *Physical Review B*, 76(7): 075429, 2007.
- [174] Y. S. Dedkov, M. Poygin, D. Vyalikh, A. Starodubov, A. M. Shikin, and V. K. Adamchuk. Modification of the valence band electronic structure under Ag intercalation underneath graphite monolayer on Ni(111). *pre-print*, 2003. <http://arxiv.org/abs/cond-mat/0304575v1>.
- [175] A. Varykhalov, M. R. Scholz, T. K. Kim, and O. Rader. Effect of noble-metal contacts on doping and band gap of graphene. *Physical Review B*, 82(12):121101, 2010.
- [176] S. Ogura, K. Fukutani, and M. Okada. Structure of gold thin films grown on Ir(111). *Topics in Catalysis*, 44(1-2):65–71, 2007.
- [177] P. Moras, P. M. Sheverdyeva, C. Carbone, D. Topwal, L. Ferrari, G. Bihlmayer, S. Ouazi, S. Rusponi, A. Lehnert, and H. Brune. Electronic states of moire modulated Cu films. *Journal of Physics-Condensed Matter*, 24(33):335502, 2012.
- [178] S. Torbrugge, O. Schaff, and J. Rychen. Application of the KolibriSensor® to combined atomic-resolution scanning tunneling microscopy and noncontact atomic-force microscopy imaging. *Journal of Vacuum Science and Technology B*, 28(3), 2010.
- [179] P. E. Blochl. Projector Augmented-Wave Method. *Physical Review B*, 50(24):17953–17979, 1994.
- [180] J. P. Perdew, K. Burke, and M. Ernzerhof. Generalized gradient approximation made simple. *Physical Review Letters*, 77(18): 3865–3868, 1996.
- [181] G. Kresse and J. Hafner. Norm-Conserving and Ultrasoft Pseudopotentials for First-Row and Transition-Elements. *Journal of Physics-Condensed Matter*, 6(40):8245–8257, 1994.

-
- [182] S. Grimme. Semiempirical GGA-type density functional constructed with a long-range dispersion correction. *Journal of Computational Chemistry*, 27(15):1787–1799, 2006.
- [183] J. Neugebauer and M. Scheffler. Adsorbate-Substrate and Adsorbate-Adsorbate Interactions of Na and K Adlayers on Al(111). *Physical Review B*, 46(24):16067–16080, 1992.
- [184] H. Hattab, A. T. N’Diaye, D. Wall, C. Klein, G. Jnawali, J. Coraux, C. Busse, R. van Gastel, B. Poelsema, T. Michely, F. J. M. Z. Heringdorf, and M. Horn-von Hoegen. Interplay of Wrinkles, Strain, and Lattice Parameter in Graphene on Iridium. *Nano Letters*, 12(2):678–682, 2012.
- [185] Y. Dedkov and E. Voloshina. Multichannel scanning probe microscopy and spectroscopy of graphene moire structures. *Physical Chemistry Chemical Physics*, 16(9):3894–3908, 2014.
- [186] A. L. Walter, S. Nie, A. Bostwick, K. S. Kim, L. Moreschini, Y. J. Chang, D. Innocenti, K. Horn, K. F. McCarty, and E. Rotenberg. Electronic structure of graphene on single-crystal copper substrates. *Physical Review B*, 84(19):195443, 2011.
- [187] J. C. W. Song, A. V. Shytov, and L. S. Levitov. Electron Interactions and Gap Opening in Graphene Superlattices. *Physical Review Letters*, 111(26):266801, 2013.
- [188] Dmitri Efetov and Philip Kim. Controlling Electron-Phonon Interactions in Graphene at Ultrahigh Carrier Densities. *Physical Review Letters*, 105(25):256805, 2010.
- [189] E. Rotenberg and A. Bostwick. microARPES and nanoARPES at diffraction-limited light sources: opportunities and performance gains. *Journal of Synchrotron Radiation*, 21(5):1048–1056, 2014.
- [190] S. Y. Zhou, D. A. Siegel, A. V. Fedorov, F. El Gabaly, A. K. Schmid, A. H. C. Neto, D. H. Lee, and A. Lanzara. Origin of the energy bandgap in epitaxial graphene - Reply. *Nature Materials*, 7(4):259–260, 2008.
- [191] E. Rotenberg, A. Bostwick, T. Ohta, J. L. McChesney, T. Seyller, and K. Horn. Origin of the energy bandgap in epitaxial graphene. *Nature Materials*, 7(4):258–259, 2008.

- [192] C. Enderlein, Y. S. Kim, A. Bostwick, E. Rotenberg, and K. Horn. The formation of an energy gap in graphene on ruthenium by controlling the interface. *New Journal of Physics*, 12:033014, 2010.
- [193] H. Vita, S. Böttcher, K. Horn, E. N. Voloshina, R. E. Ovcharenko, T. Kampen, A. Thissen, and Y. S. Dedkov. Understanding the origin of band gap formation in graphene on metals: graphene on Cu/Ir(111). *Scientific Reports*, 4:5704, 2014.
- [194] K. C. Prince, I. Ulrych, M. Peloi, B. Ressel, V. Cháb, C. Crotti, and C. Comicioli. Core-level photoemission from graphite. *Physical Review B*, 62(11):6866–6868, 2000.
- [195] A. B. Preobrajenski, M. L. Ng, A. S. Vinogradov, and N. Mårtensson. Controlling graphene corrugation on lattice-mismatched substrates. *Physical Review B*, 78(7):073401, 2008.
- [196] A. Nagashima, N. Tejima, and C. Oshima. Electronic States of the Pristine and Alkali-Metal-Intercalated Monolayer Graphite/Ni(111) Systems. *Physical Review B*, 50(23):17487–17495, 1994.
- [197] Wei Zhao, Sergey M. Kozlov, Oliver Höfert, Karin Gotterbarm, Michael P. A. Lorenz, Francesc Vines, Christian Papp, Andreas Görling, and Hans-Peter Steinrück. Graphene on Ni(111): Coexistence of Different Surface Structures. *The Journal of Physical Chemistry Letters*, 2(7):759–764, 2011.
- [198] A. Grüneis, K. Kummer, and D. V. Vyalikh. Dynamics of graphene growth on a metal surface: a time-dependent photoemission study. *New Journal of Physics*, 11(7):073050, 2009.
- [199] R. J. Koch. *Doping, Metal Contacts And Phonon Plasmon Coupling In Graphene Investigated With Electron Spectroscopies*. PhD thesis, Friedrich-Alexander-Universität Erlangen-Nürnberg, Erlangen, 2014.
- [200] A. Bostwick, T. Ohta, J. L. McChesney, Th. Seyller, K. Horn, and E. Rotenberg. Renormalization of graphene bands by many-body interactions. *Solid State Communications*, 143(1-2):63–71, 2007.

-
- [201] I. Pletikosić, M. Kralj, D. Šokčević, R. Brako, P. Lazić, and P. Pervan. Photoemission and density functional theory study of Ir(111); energy band gap mapping. *Journal of Physics-Condensed Matter*, 22(13):135006, 2010.
- [202] K. Baberschke. The magnetism of nickel monolayers. *Applied Physics A-Materials Science and Processing*, 62(5):417–427, 1996.
- [203] A. Gundel, L. Cagnon, C. Gomes, A. Morrone, J. Schmidt, and P. Allongue. In-situ magnetic measurements of electrodeposited ultrathin Co, Ni and Fe/Au(111) layers. *Physical Chemistry Chemical Physics*, 3(16):3330–3335, 2001.
- [204] C. M. Schneider, P. Bressler, P. Schuster, J. Kirschner, J. J. de Miguel, and R. Miranda. Curie temperature of ultrathin films of fcc-cobalt epitaxially grown on atomically flat Cu(100) surfaces. *Physical Review Letters*, 64(9):1059–1062, 1990.
- [205] N. Rougemaille, A. T. N'Diaye, J. Coraux, C. Vo-Van, O. Fruchart, and A. K. Schmid. Perpendicular magnetic anisotropy of cobalt films intercalated under graphene. *Applied Physics Letters*, 101(14):142403, 2012.
- [206] J. Hunter Dunn, A. Hahlin, O. Karis, D. Arvanitis, G. LeBlanc, Å. Andersson, and L. J. Lindgren. Elliptically polarised soft x-rays produced using a local bump in MAX II – Characterisation of the degree of polarisation. *AIP Conference Proceedings*, 705(1):65–68, 2004.
- [207] A. B. Preobrajenski. Estimation of real (65 %) versus theoretical value for the degree of circular polarization at D1011 – personal communication, 2014.
- [208] J. Coraux, A. T. N'Diaye, N. Rougemaille, C. Vo-Van, A. Kimouche, H. X. Yang, M. Chshiev, N. Bendiab, O. Fruchart, and A. K. Schmid. Air-protected epitaxial graphene/ferromagnet hybrids prepared by chemical vapor deposition and intercalation. *Journal of Physical Chemistry Letters*, 3(15):2059–2063, 2012.
- [209] D. Pacilé, S. Lisi, I. Di Bernardo, M. Papagno, L. Ferrari, M. Pisarra, M. Caputo, S. K. Mahatha, P. M. Sheverdyeva, P. Moras, P. Lacovig, S. Lizzit, A. Baraldi, M. G. Betti, and C. Carbone. Electronic structure of graphene/Co interfaces. *Physical Review B*, 90(19):195446, 2014.

- [210] S. Vlaic, A. Kimouche, J. Coraux, B. Santos, A. Locatelli, and N. Rougemaille. Cobalt intercalation at the graphene/iridium(111) interface: Influence of rotational domains, wrinkles, and atomic steps. *Applied Physics Letters*, 104(10), 2014.
- [211] D. X. Ye, S. Pimanpang, C. Jezewski, F. Tang, J. J. Senkevich, G. C. Wang, and T. M. Lu. Low temperature chemical vapor deposition of Co thin films from $\text{Co}_2(\text{CO})_8$. *Thin Solid Films*, 485(1–2):95–100, 2005.
- [212] H. Vita, S. Böttcher, P. Leicht, K. Horn, A. B. Shick, and F. Máca. Electronic structure and magnetic properties of cobalt intercalated in graphene on Ir(111). *Physical Review B*, 90(16):165432, 2014. PRB.
- [213] A. Varykhalov and O. Rader. Graphene grown on Co(0001) films and islands: Electronic structure and its precise magnetization dependence. *Physical Review B*, 80(3):035437, 2009.
- [214] I. M. L. Billas, A. Chatelain, and W. A. Deheer. Magnetism from the atom to the bulk in iron, cobalt, and nickel clusters. *Science*, 265(5179):1682–1684, 1994.
- [215] P. Gambardella, A. Dallmeyer, K. Maiti, M. C. Malagoli, W. Eberhardt, K. Kern, and C. Carbone. Ferromagnetism in one-dimensional monatomic metal chains. *Nature*, 416(6878):301–304, 2002.
- [216] F. Wilhelm, P. Srivastava, H. Wende, A. Ney, N. Haack, G. Ceбалlos, M. Farle, and K. Baberschke. Magnetism of thin films and in fe/ni, co/fe bilayers on cu(001). *Journal of synchrotron radiation*, 6(3):699–700, 1999.
- [217] O. Céspedes, M. S. Ferreira, S. Sanvito, M. Kociak, and J. M. D. Coey. Contact induced magnetism in carbon nanotubes. *Journal of Physics-Condensed Matter*, 16(10):L155, 2004.
- [218] C. Busse, P. Lazic, R. Djemour, J. Coraux, T. Gerber, N. Atodiresei, V. Caciuc, R. Brako, A. T. N’Diaye, S. Blugel, J. Zegenhagen, and T. Michely. Graphene on ir(111): Physisorption with chemical modulation. *Physical Review Letters*, 107(3):036101, 2011.

-
- [219] G. Kresse and J. Hafner. Ab-initio Molecular-Dynamics for Liquid-Metals. *Physical Review B*, 47(1):558–561, 1993.
 - [220] G. Kresse and J. Furthmuller. Efficiency of ab-initio total energy calculations for metals and semiconductors using a plane-wave basis set. *Computational Materials Science*, 6(1):15–50, 1996.
 - [221] G. Kresse and D. Joubert. From ultrasoft pseudopotentials to the projector augmented plane wave method. *Physical Review B*, 59(3):1758–1775, 1999.
 - [222] D. J. Singh. *Plane waves, Pseudopotentials and the PW Method*. Kluwer Academic, Boston, 1994.
 - [223] A. B. Shick, D. L. Novikov, and A. J. Freeman. Relativistic spin-polarized theory of magnetoelastic coupling and magnetic anisotropy strain dependence: Application to Co/Cu(001). *Physical Review B*, 56(22):14259–14262, 1997.
 - [224] J. Stöhr and H. König. Determination of Spin- and Orbital-Moment Anisotropies in Transition Metals by Angle-Dependent X-Ray Magnetic Circular Dichroism. *Physical Review Letters*, 75(20):3748–3751, 1995.
 - [225] G. van der Laan. Microscopic origin of magnetocrystalline anisotropy in transition metal thin films. *Journal of Physics-Condensed Matter*, 10(14):3239, 1998.
 - [226] J. Trygg, B. Johansson, O. Eriksson, and J. M. Wills. Total Energy Calculation of the Magnetocrystalline Anisotropy Energy in the Ferromagnetic 3d Metals. *Physical Review Letters*, 75(15):2871–2874, 1995.
 - [227] A. B. Shick and W. E. Pickett. Magnetism, spin-orbit coupling, and superconducting pairing in UGe₂. *Physical Review Letters*, 86(2):300–303, 2001.
 - [228] A. B. Shick, V. Drchal, and L. Havela. Coulomb-U and magnetic-moment collapse in δ -Pu. *Europhysics Letters*, 69(4):588–594, 2005.
 - [229] M. Cococcioni and S. de Gironcoli. Linear response approach to the calculation of the effective interaction parameters in the LDA+U method. *Physical Review B*, 71(3), 2005.

- [230] J. Sánchez-Barriga, A. Varykhalov, M. R. Scholz, O. Rader, D. Marchenko, A. Rybkin, A. M. Shikin, and E. Vescovo. Chemical vapour deposition of graphene on Ni(111) and Co(0001) and intercalation with Au to study Dirac-cone formation and Rashba splitting. *Diamond and Related Materials*, 19(7-9):734–741, 2010.
- [231] A. M. Shikin, S. L. Molodtsov, C. Laubschat, and G. Kaindl. Electronic-Structure of La-Intercalated Graphite. *Physical Review B*, 51(19):13586–13591, 1995.
- [232] S. L. Molodtsov, C. Laubschat, M. Richter, T. Gantz, and A. M. Shikin. Electronic structure of Eu and Yb graphite intercalation compounds. *Physical Review B*, 53(24):16621–16630, 1996.
- [233] S. L. Molodtsov, T. Gantz, C. Laubschat, A. G. Viatkine, J. Avila, C. Casado, and M. C. Asensio. Electron-energy bands in single-crystalline La-intercalated graphite. *Zeitschrift Für Physik B-Condensed Matter*, 100(3):381–385, 1996.
- [234] M. S. Dresselhaus and G. Dresselhaus. Intercalation Compounds of Graphite. *Advances in Physics*, 30(2):139–326, 1981.
- [235] T. E. Weller, M. Ellerby, S. S. Saxena, R. P. Smith, and N. T. Skipper. Superconductivity in the intercalated graphite compounds C_6Yb and C_6Ca . *Nature Physics*, 1(1):39–41, 2005.
- [236] N. B. Hannay, T. H. Geballe, B. T. Matthias, K. Andres, P. Schmidt, and D. MacNair. Superconductivity in Graphitic Compounds. *Physical Review Letters*, 14(7):225–226, 1965.
- [237] Y. Koike, H. Suematsu, K. Higuchi, and S. Tanuma. Superconductivity in graphite-alkali metal intercalation compounds. *Physica B+C*, 99(1-4):503–508, 1980.
- [238] N. Mårtensson and A. Nilsson. *High-Resolution Core-Level Photoelectron Spectroscopy of Surfaces and Adsorbates*. Italy, Trieste, 1997. School on the Use of Synchrotron Radiation in Science and Technology.
- [239] Y. S. Dedkov, D. V. Vyalikh, M. Holder, M. Weser, S. L. Molodtsov, C. Laubschat, Y. Kucherenko, and M. Fonin. Electronic structure of thin ytterbium layers on W(110). *Journal of Physics: Conference Series*, 100(7):072023, 2008.

- [240] A. M. Shikin, M. V. Poigin, Y. S. Dedkov, S. L. Molodtsov, and V. K. Adamchuk. Formation of intercalate-like systems of graphite-ytterbium monolayers on the Ni(111) surface. *Physics of the Solid State*, 42(6):1170–1175, 2000.
- [241] J. J. Yeh and I. Lindau. Atomic subshell photoionization cross sections and asymmetry parameters: $1 < Z < 103$. *Atomic Data and Nuclear Data Tables*, 32(1):1–155, 1985.
- [242] J. J. Yeh. *Atomic Calculation of Photoionization Cross-Sections and Asymmetry Parameters*. Gordon and Breach Science Publishers, Langhorne, PE (USA), 1993.
- [243] Scientific Computing Group, Sincrotrone Trieste SCpA. Atomic Calculation of Photoionization Cross-Sections and Asymmetry Parameters, 2015. Available online at <http://ulisse.elettra.trieste.it/services/elements/WebElements.html>.
- [244] S. Watcharinyanon, L. I. Johansson, C. Xia, I. Flege, A. Meyer, J. Falta, and C. Virojanadara. Ytterbium Intercalation of Epitaxial Graphene Grown on Si-Face SiC. *Graphene*, 2(2):66–73, 2013.
- [245] S. Watcharinyanon, L. I. Johansson, C. Xia, and C. Virojanadara. Ytterbium oxide formation at the graphene-SiC interface studied by photoemission. *Journal of Vacuum Science and Technology A*, 31(2):020606, 2013.
- [246] C. Hwang, D. Y. Kim, D. A. Siegel, K. T. Chan, J. Noffsinger, A. V. Fedorov, Marvin L. Cohen, B. Johansson, J. B. Neaton, and A. Lanzara. Ytterbium-driven strong enhancement of electron-phonon coupling in graphene. *Physical Review B*, 90(11):115417, 2014.
- [247] C. Hwang, C.-H. Park, D. A. Siegel, A. V. Fedorov, S. G. Louie, and A. Lanzara. Direct measurement of quantum phases in graphene via photoemission spectroscopy. *Physical Review B*, 84(12):125422, 2011.
- [248] J. L. McChesney, A. Bostwick, T. Ohta, Emtsev K. V., T. Seyller, K. Horn, and E. Rotenberg. Massive enhancement of electron-phonon coupling in doped graphene by an electronic singularity. *pre-print*, 2007. <http://arxiv.org/ftp/arxiv/papers/0705/0705.3264.pdf>.

- [249] J. H. Chen, C. Jang, S. Adam, M. S. Fuhrer, E. D. Williams, and M. Ishigami. Charged-impurity scattering in graphene. *Nature Physics*, 4(5):377–381, 2008.
- [250] Teng Gao, Yabo Gao, Cuizu Chang, Yubin Chen, Mengxi Liu, Shubao Xie, Ke He, Xucun Ma, Yanfeng Zhang, and Zhongfan Liu. Atomic-Scale Morphology and Electronic Structure of Manganese Atomic Layers Underneath Epitaxial Graphene on SiC(0001). *ACS Nano*, 6(8):6562–6568, 2012.
- [251] Yu Zhang, Yanfeng Zhang, Donglin Ma, Qingqing Ji, Wei Fang, Jianping Shi, Teng Gao, Mengxi Liu, Yabo Gao, Yubin Chen, Limei Xu, and Zhongfan Liu. Mn atomic layers under inert covers of graphene and hexagonal boron nitride prepared on Rh(111). *Nano Research*, 6(12):887–896, 2013.
- [252] D. P. Woodruff. Surface Alloys and Alloy Surfaces. In *The Chemical Physics of Solid Surfaces*. Elsevier, 2002.
- [253] M. Wuttig and X. Liu. *Ultrathin Metal Films*. Springer Berlin Heidelberg, Berlin, 2004.
- [254] T. Flores, M. Hansen, and M. Wuttig. Structure and Growth of Mn on Cu(100). *Surface Science*, 279(3):251–264, 1992.
- [255] M. Wuttig, Y. Gauthier, and S. Blügel. Magnetically driven buckling and stability of ordered surface alloys: Cu(100) $c(2 \times 2)$ Mn. *Physical Review Letters*, 70(23):3619–3622, 1993.
- [256] W. O’Brien and B. Tonner. Magnetic properties of Mn/Cu(001) and Mn/Ni(001) $c(2 \times 2)$ surface alloys. *Physical Review B*, 51(1):617–620, 1995.
- [257] St. Böttcher. *Adsorption und Funktionalisierung von Graphen auf Metalloberflächen*. PhD thesis, Freie Universität, 2014.
- [258] E. Loginova, S. Nie, K. Thurmer, N. C. Bartelt, and K. F. McCarty. Defects of graphene on Ir(111): Rotational domains and ridges. *Physical Review B*, 80:085430, 2009.
- [259] S. Andrieu, H. Fischer, M. Piecuch, A. Traverse, and J. Mimault. Structure of Mn films grown on (111) and (001) fcc Ir determined by EXAFS and the multiple-scattering approach. *Physical Review B*, 54(4):2822–2829, 1996.

-
- [260] W. L. O'Brien and B. P. Tonner. Magnetic and structural properties of ultrathin Mn and Fe films on Ir(111). *Journal of Vacuum Science and Technology A*, 13(3):1544–1548, 1995.
- [261] Hua Chen, Qian Niu, and A. H. MacDonald. Anomalous Hall Effect Arising from Noncollinear Antiferromagnetism. *Physical Review Letters*, 112(1):017205, 2014.
- [262] A. Bostwick, J. L. McChesney, K. V. Emtsev, T. Seyller, K. Horn, S. D. Kevan, and E. Rotenberg. Quasiparticle Transformation during a Metal-Insulator Transition in Graphene. *Physical Review Letters*, 103(5), 2009.
- [263] Douglas R. Hofstadter. Energy levels and wave functions of Bloch electrons in rational and irrational magnetic fields. *Physical Review B*, 14(6):2239–2249, 1976.
- [264] C. R. Dean, L. Wang, P. Maher, C. Forsythe, F. Ghahari, Y. Gao, J. Katoch, M. Ishigami, P. Moon, M. Koshino, T. Taniguchi, K. Watanabe, K. L. Shepard, J. Hone, and P. Kim. Hofstadter's butterfly and the fractal quantum Hall effect in moiré superlattices. *Nature*, 497(7451):598–602, 2013.
- [265] D. Farias, A. M. Shikin, K. H. Rieder, and Y. S. Dedkov. Synthesis of a weakly bonded graphite monolayer on Ni(111) by intercalation of silver. *Journal of Physics-Condensed Matter*, 11(43):8453–8458, 1998.
- [266] Z. Tan, D. Cox, T. Nieminen, P. Lähteenmäki, D. Golubev, G. Lesovik, and P. Hakonen. Cooper pair splitting by means of graphene quantum dots. *Physical Review Letters*, 114(9):096602, 2015.

List of Abbreviations and Symbols

β -Flip	Flip of the Sample – Axis k_y in k-space
φ -Rotation	Azimuthal Rotation of the Sample – Rotation of the k_x/k_y Plane
ϑ -Rotation	Polar Rotation of the Sample – Axis k_x in k-space
AFM	Atomic Force Microscopy
APPLE-type	Advanced Planar Polarized Light Emitter
ARPES	Angular Resolved Photoemission Spectroscopy
CEM	Constant Energy Map
CVD	Chemical Vapor Deposition
E_F	Fermi Energy
EDC	Energy Distribution Curve
EXAFS	Extended X-ray Absorption Fine Structure
FFT	Fast Fourier Transform

FWHM	Full Peak Width at Half Maximum
GICs	Graphite Intercalation Compounds
GMR	Giant Magnetoresistance
HM	High Magnification Mode – Detection Mode
ID	Insertion Device
IMFP	Inelastic Mean Free Path
LAD	Low Angle Dispersion – Detection Mode
LEED	Low Energy Electron Diffraction
LINAC	Linear Particle Accelerator
MAD	Medium Angular Dispersion – Detection Mode
MBE	Molecular Beam Epitaxy
MDC	Momentum Distribution Curve
NEXAFS	Near Edge X-ray Absorption Fine Structure
PES	Photoemission Spectroscopy
PEY	XAS Partial Electron Yield
PGM	Plane Grating Monochromator
PVD	Physical Vapor Deposition
QFMLG	Quasi Free-Standing Monolayer Graphene
RHEED	Reflection High-Energy Electron Diffraction
TEY	XAS Total Electron Yield
UHV	Ultra High Vacuum
UPS	Ultraviolet Photoemission Spectroscopy
WAM	Wide Angle Mode – Detection Mode

XAS	X-ray Absorption Spectroscopy
XMCD	X-ray Magnetic Circular Dichroism
XPS	X-ray Photoemission Spectroscopy

Acknowledgments

During the last years at the Fritz-Haber-Institut, I had the opportunity to meet many inspiring people, who all have a share in the successful complementation of this thesis. My special gratitude goes to Prof. Dr. Karsten Horn for taking me into his group and the continuous support during all these years. He had always an open mind for my ideas even if there were obstacles to cope with and challenges to overcome – “per aspera ad astra”. Being a member of his group gave me the possibility and privilege to do excellent scientific work at various synchrotron facilities either at BESSY, MAX-lab or ELETTRA. Besides the demanding beamtimes, there was also work to be done in the “peaceful atmosphere of the lab”.

Prof. Dr. Helmut Winter for his supervision and reviewing my thesis; especially for the invitation to his group seminars. Prof. Dr. Philip Hofmann for external review. Dr. Yuriy Dedkov, Martin Weser and Stefan Böttcher for explaining me so much about graphene, surface science and vacuum physics. Many thanks to Yuriy for his encouragement and push to the limit. Special thanks to Stefan, who I struggled with through most of the numerous beamtimes either at BESSY or MAX-lab. Seeing the “real-time” intercalation for the first time was amazing. Thanks to Alexander Generalov, who I joined in the beginning in the old ARPES-lab.

For the theoretical calculations presented in this thesis I would like to thank Elena Voloshina, Alexander Shick and František Máca. Sergey Peredkov, Nicolai Vinogradov and Alexei Preobajnski for the great support they always gave us during our stay at MAX-lab in Lund. Federico Bisti, visitor at our institute for one year joined me for some time in the lab. Greetings to his colleges Maurizio Donarelli

and Fabrizio Perrozzi who made our stay at ELETTRA pleasant and successful. Thanks goes to Chris Nicholson who got started in the preparation of nanowires in our lab on “ultra slow timescales”. His supervisor Claude Monney who gave me always ideas and feedback when some parts were not “cooperating”.

The team of AG Seyller with Roland Koch, Markus Ostler and Felix Fromm for their work during our shared beamtimes at the BESSY-machine. Special thanks to Birgit Zada and Willy Mahler who were in charge of the UE56 beamline. Henrik Haak for patiently explaining me how to develop CAD files in a time-efficient way. Björn Frietsch for all the work he invested in the first plans on the lab-ARPES machine and his Solid Edge skills. I still remember the two of us unpacking the new chambers during my first days at the Fritz. I gave my best in setting up the new machine – finally every component perfectly matched. Sven Mähl and Thorsten Kampen of SPECS GmbH, for repairs and improvements on our “little” analyzer of the BESSY-machine, despite its high age. The mechanical workshop with Petrik Bishoff, Jörg Wagatha, Heike Dargies, Thorsten Nemes – without them, it would not have been possible to get the lab-machine and the 6-axis-manipulator running. Thanks also for many maintenance repairs on our “workhorse”, the BESSY-machine. Kai Hartlieb for maintenance on vacuum pumps of any kind. The ELAB and especially Harald Fischer who always found a solution, when I came around his office with broken equipment. Wilko Genz and Christian Vietzke, especially for the Peltier cooling of our CCD-cameras and a lot of other work they realized. Georg Hammer for the numerous efforts in fixing several small problems in the lab. Dirk for driving our equipment either to SPECS (hopefully not too often) or to BESSY. My best regards to all the people from the old MP department. Christian Schewe for the Friday evenings and the coffee sessions. Many thanks to Christian Kerpel and Nadja Heine. Simon Merz, who shared the neighboring lab and helped me initially to assemble the chambers of the lab-machine. Inga von Dölln and Andrea Braaker for their caring support during my stay at the Fritz-Haber-Institut. Thanks to friends and family “outside of the physics cloud” Simona, Milena, Julien, Robert, Petra and Gerd. Many thanks to Stephan for all the help, support and answers to my questions concerning XAS, software-wise or equipment related topics.

Sadly we never met at MAX-lab for beamtime, but more often at BESSY to have a chat about the good old times. Last but not least I would like to thank my parents for their continuous support and their endless trust in me. Sophie – for everything.

Eigenständigkeitserklärung

Hiermit versichere ich, dass die vorliegende Arbeit mit dem Titel “Interaction of magnetic and non-magnetic metals with graphene” selbstständig und nur unter Verwendung der angegebenen Hilfen und Hilfsmittel gemäß § 7 Absatz 3 der Promotionsordnung der Mathematisch-Naturwissenschaftlichen Fakultät der Humboldt-Universität zu Berlin vom 06.07.2009 angefertigt worden ist. Die Dissertation wurde unter der wissenschaftlichen Betreuung von Prof. Dr. K. Horn am Fritz-Haber-Institut der Max-Planck-Gesellschaft angefertigt.

Hiermit erkläre ich weiterhin, dass ich mich nicht anderwärts um einen Doktorgrad beworben habe, sowie keinen Doktorgrad führe. Die dem angestrebten Verfahren zugrunde liegende Promotionsordnung der Mathematisch-Naturwissenschaftlichen Fakultät der Humboldt-Universität zu Berlin vom 06.07.2009 nehme ich hiermit zur Kenntnis.

Berlin, den 17.03.2015

Curriculum Vitae

Hendrik Vita, born April 20th, 1983 in Staaken, Germany

04/2010 – present Ph.D. student at the Department of
Physical Chemistry of the
Fritz-Haber-Institut der Max-Planck-Gesellschaft
under the supervision of Prof. Karsten Horn

04/2003 – 09/2009 Studies of physics at
Humboldt-Universität zu Berlin
Diploma thesis in the group
“Elektronische Eigenschaften und Supraleitung”
of Prof. Dr. R. Manzke

Title of the thesis:
“Polarisationsabhängige winkelaufgelöste
Photoemissionsspektroskopie am
Kupratsupraleiter $\text{Bi}_{2-x}(\text{Pb}_x)\text{Sr}_2\text{CaCu}_2\text{O}_{8+\delta}$ ”
Diploma graduation with overall grade
“sehr gut”(1,4)

06/2002 Abitur with focus on physics and chemistry
Lise-Meitner-Gymnasium in Falkensee

